Doctoral Dissertation

Numerical investigation on combustion and emission characteristics in an ammonia co-combustion furnace using detailed chemistry and conjugate heat transfer methods

Yinan Yang

January 2025

Department of Mechanical Engineering,
Graduate School of Engineering,
Osaka University

Abstract

Ammonia co-firing is increasingly recognized as a promising strategy for achieving carbon neutrality, as it not only mitigates carbon emissions but also enhances the stability of ammonia combustion. However, controlling NO emissions during ammonia co-combustion remains a significant challenge. In response to this issue, this study presents a systematic numerical investigation of a 10-kW ammonia co-combustion furnace. A customized solver was developed within the OpenFOAM framework to facilitate fast and accurate numerical analysis. Specifically, to enhance the computational acceleration capabilities of the solver, a novel integrated acceleration strategy was introduced. This strategy incorporates a sparse analytical Jacobian approach using the SpeedCHEM library to enhance the efficiency of the ordinary differential equation solver. Additionally, the dynamic load balancing code was employed to evenly distribute computational workloads across multiple processes. Further optimization was achieved through the integration of an open multi-processing method and a local time-stepping scheme, improving parallel computing efficiency and maximizing the time step for each computational cell.

The effectiveness and robustness of the customized solver were first validated using numerical simulations of Sandia flames D-F as benchmarks. Results demonstrated that following the introduction of the integrated acceleration strategy, the solver demonstrated improved strong scaling characteristics and achieved a speedup of up to 30 times in two-dimensional simulations of Sandia flame D. The numerical predictions for temperature and species distribution closely matched the experimental trends, confirming the prediction accuracy of the solver. Furthermore, the two-dimensional validation results indicated that the application of the integrated acceleration strategy significantly enhanced computational efficiency with minimal impact on predictive accuracy, laying the foundation for subsequent three-dimensional numerical analysis.

A subsequent three-dimensional numerical study examined combustion characteristics in the 10-kW ammonia co-combustion furnace under various secondary injection configurations and ammonia co-firing ratios. The conjugate heat transfer model, accounting for solid and reacting flow regions, was employed to accurately represent thermal boundary conditions at the furnace walls. Regarding the computational acceleration achieved through the integrated acceleration strategy, while the computational acceleration was reduced due to increased communication overhead, a speed-up of 7.06 times was still observed. However, as the size of the reaction mechanism increased, the introduction of the SpeedCHEM chemistry solver facilitated more effective computational acceleration. Additionally, the numerical predictions closely replicated

experimental trends, effectively capturing NO emission characteristics within the ammonia co-combustion furnace.

Regarding the influence of different parameters in the secondary injection system, results indicate that at lower ammonia co-firing ratios, with a constant total air ratio of 1.2, simply reducing the primary air ratio to enhance fuel-rich combustion in the primary air zone does not result in a linear decrease in NO emissions. Instead, NO emissions exhibit a V-shaped trend, reaching a minimum when the primary air ratio equals 0.6. An analysis of combustion characteristics reveals two distinct combustion modes appear as the primary air ratio varies, which is the primary reason for this phenomenon. Regarding the influence of the air nozzle distance and the secondary nozzle diameter, results found that increasing their values effectively promotes NO reduction reactions within the furnace, thereby reducing NO emissions.

Under different ammonia co-firing ratios, as the co-firing ratio increased from 0% to 100%, NO emissions at the furnace outlet first increased and then decreased, peaking at a co-firing ratio of 50%. Within the furnace, fuel NO began to dominate NO formation upon the introduction of ammonia for co-firing, while thermal NO became negligible at co-firing ratios higher than 40%. Further analysis of the rate of production of NO revealed that at higher ammonia co-firing ratios, ammonia acts both as a reducing agent and as a fuel for heat release. These findings provide valuable insights for the development and industrial application of ammonia-based combustion systems.

Keywords: RANS; Sandia flames; Ammonia co-combustion furnace; NO formation prediction; Secondary injection system; Ammonia co-firing ratio.

Contents

1. Introduction 1
1.1 Research background 1
1.2 Ammonia for power 5
1.2.1 Interest in ammonia for power 5
1.2.2 Physicochemical and combustion characteristics of ammonia 7
1.2.3 Emission characteristics of ammonia/air flame 10
1.2.4 Ammonia combustion methods and applications 12
(a) Flame enhancement of ammonia/air flames 12
(b) NO emission control technologies 13
1.3 Numerical calculations in ammonia combustion furnaces 16
1.3.1 Modeling methods 17
1.3.2 Wall boundary condition in combustion furnace simulation 18
1.3.3 Prediction accuracy and calculation speed 19
1.4 Problem statement 22
1.5 Dissertation layout 23
References 25
2. Computational modeling 32
2.1 Introduction 32
2.2 Governing equations 33
2.2.1 Governing equations for turbulent combustion 33
2.2.2 RANS governing equations 35
2.3 Calculation models selection 36
2.3.1 Turbulence model 36
(a) Standard k-ε model 36
(b) Re-Normalization Group k-ε model 37
(c) Reynolds stress equation model 38
2.3.2 Combustion model 39
(a) Eddy dissipation concept 39
(b) Partially stirred reactor model 40
2.3.3 Radiation model 41
2.4 Conjugate heat transfer method 43
2.5 Reaction mechanism 44

2.6 Integrated acceleration strategy 45
2.6.1 SpeedCHEM chemistry solver 46
2.6.2 Dynamic load balancing 48
2.6.3 Open multi-processing method and local time stepping scheme 50
2.7 Implementation details 51
2.8 Summary 52
References 54
3. Model validation 59
3.1 Introduction 59
3.2 Sandia flames D-F 60
3.2.1 Experimental setup 60
3.2.2 Computational domain details 61
3.3 Computational efficiency comparison 62
3.4 Accuracy prediction 65
3.4.1 Inlet boundary conditions 65
3.4.2 Central axis prediction 67
3.4.3 Radial distribution prediction 71
3.5 LRR model constant assessment 75
3.6 Computational model evaluation 77
3.6.1 Turbulence-combustion models 77
3.6.2 Turbulent Prandtl number 79
3.7 Influence of the integrated acceleration method on prediction results 80
3.8 Summary 81
References 83
4. Development of low-NO ammonia co-combustion furnace 85
4.1 Introduction 85
4.2 10-kW combustion furnace 86
4.2.1 Combustion furnace specifications 86
4.2.2 Experimental and modeling conditions 88
4.3 Computational efficiency comparison 91
4.4 Influence of the primary air ratios on NO emission 92
4.4.1 Trends and model validation of NO emissions 92
4.4.2 Temperature and NO distribution within the combustion furnace 96

4.4.3 Mechanisms of NO formation and reduction 100
(a) The effectiveness of air-staged strategy 100
(b) The effect of primary air ratios 103
4.4.4 Discussion on emission variations 106
4.5 Influence of the nozzle distances on NO emission 107
4.5.1 Trends and model validation of NO emissions 107
4.5.2 Combustion characteristics analysis 108
4.6 Secondary nozzle diameter selection 111
4.7 Summary 112
References 114
5. Ammonia co-firing at different ratios 116
5.1 Introduction 116
5.2 Experimental and modeling conditions 117
5.3 NO emission under various ammonia co-firing ratios 119
5.3.1 Trends and model validation of NO emissions 119
5.3.2 Nitrogen origin determination 120
5.4 Effect of ammonia co-firing ratio 122
5.4.1 Temperature distribution 122
5.4.2 NO distribution 125
5.4.3 Combustion characteristics analysis 127
5.5 Summary 130
References 132
6. Conclusions and recommendations 133
6.1 Research conclusions 133
6.2 Future recommendations 136
Appendix 137
A.1 Prediction accuracy under different ammonia co-firing ratios 137
Publications related to this thesis 138
Acknowledgment 140

Chapter 1

Introduction

1.1 Research background

Since the Industrial Revolution, combustion has been the primary energy conversion method for human activities, including power generation and transportation [1]. Fossil fuels such as coal and oil have supported the rapid and sustained development of the global economy and society, providing a comfortable and modern lifestyle while also causing severe global environmental issues. For example, a significant portion of greenhouse gas emissions is produced through industrial applications, undermining efforts to combat climate change [2]. **Figure 1.1** shows the trend in global carbon dioxide (CO_2) emissions and global temperature anomalies (relative to the 1961-1990 average) since 1850 [3,4]. The figure indicates a notable rise in annual global average temperatures is directly correlated with the rapid increase in CO_2 emissions. Despite multiple international conferences aimed at controlling global climate change, such as the "Kyoto Protocol" signed in 1997 at the Conference of Parties III (COP3), which attempted to maintain greenhouse gas levels in the atmosphere at an appropriate level [5]. Nevertheless, global CO_2 emissions have continued to rise significantly in the 21st century, and humanity still faces increasingly severe global climate change.

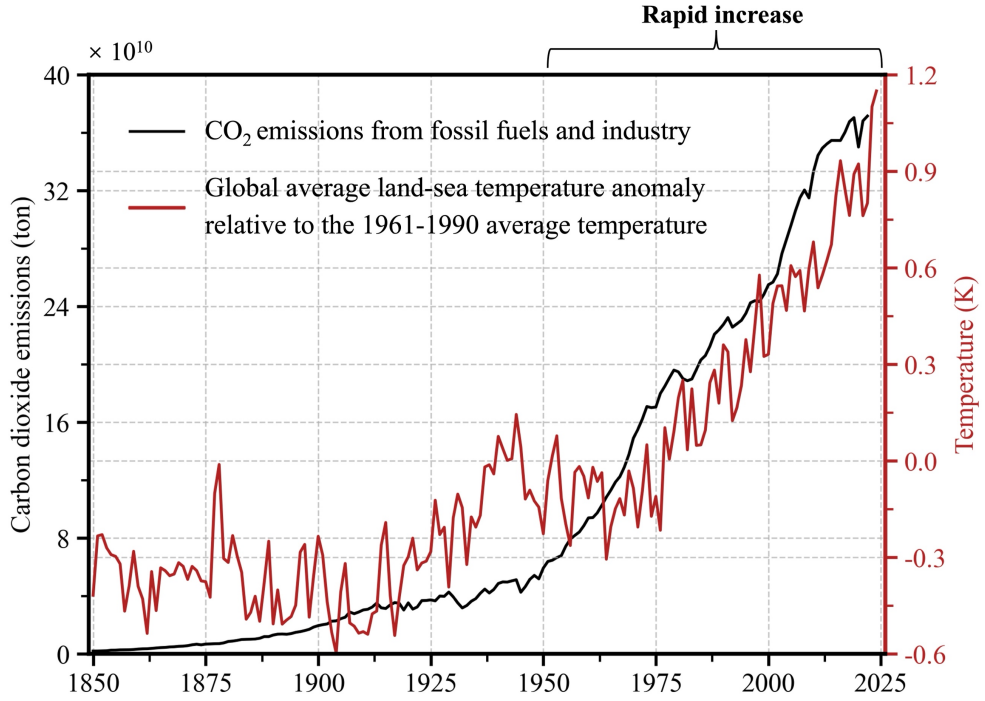

Figure 1.1 Global annual carbon dioxide emissions and average temperature anomaly.

Apart from carbon dioxide, nitrous oxide (N_2O) concentrations in the atmosphere have also sharply increased due to human industrial activities. This gas, along with carbon dioxide, encapsulates the Earth and absorbs heat from the sun, constituting the major greenhouse gases [6]. **Figure 1.2** presents data on the direct consumption of various types of primary energy globally in 2022, as recorded by the Global Change Data Lab [7]. As can be observed, the current global energy structure is still predominantly reliant on traditional fossil fuels such as coal, natural gas, and oil. This reliance is a primary reason for the persistently high levels of global greenhouse gas emissions. The continuously rising temperatures are also altering global weather patterns, disrupting the usual balance of nature. **Figure 1.3** outlines eight potential risks to the Earth as listed by the United Nations due to climate change [8]. Notably, with the rise in environmental temperatures, increased water evaporation can significantly heighten the risk of extreme rainfall and flooding. Additionally, ocean warming, and sea-level rise pose threats to coastal islands and communities. Therefore, to mitigate global climate change, there is an urgent requirement for the reduction of traditional hydrocarbon fuels [9].

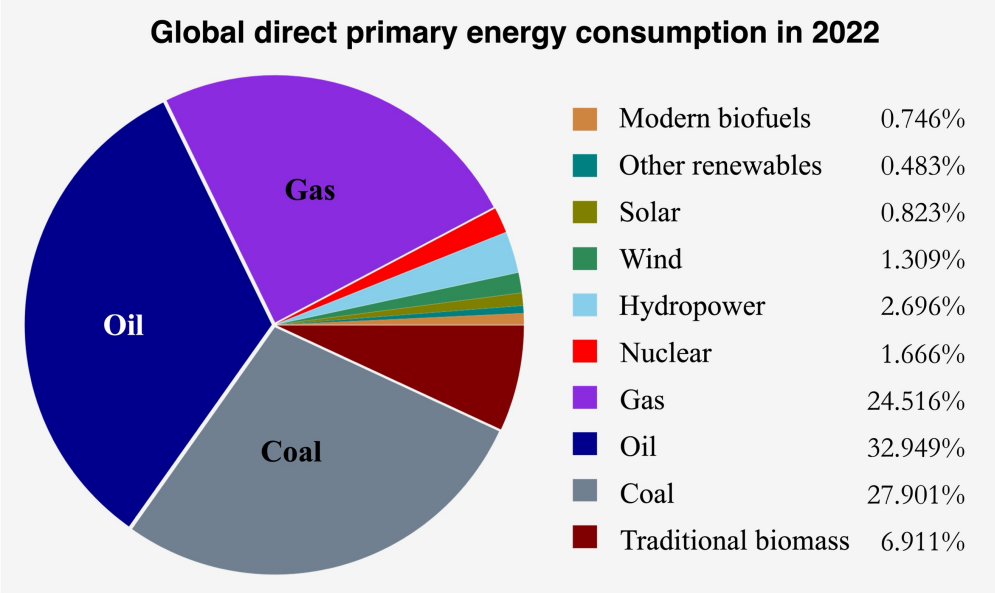

Figure 1.2 Global direct primary energy consumption in 2022.

The Paris Agreement, which came into force in November 2016, is the first legally binding global accord addressing climate change [10]. Over 190 countries have joined this agreement, which aims to limit the increase in global temperatures to within 2 °C above pre-industrial levels, achieving a decarbonized society by the mid to late 21st century. Specifically, it proposes that renewable energy should become the primary source of power, significantly reducing the reliance on fossil fuels. In Japan, the Ministry of Economy, Trade, and Industry also highlighted this issue in the 6th Strategic Energy Plan proposed in 2021. The plan mandates a substantial

reduction in the share of traditional fossil fuels by 2030 and aims to cut greenhouse gas emissions by 46% from 2013 levels [11]. Currently, both academia and industry are striving towards this goal.

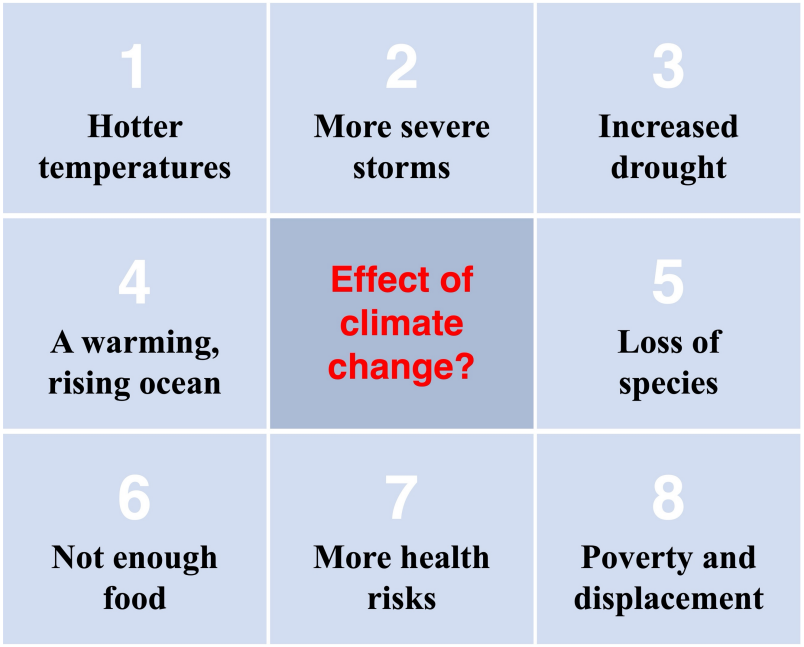

Figure 1.3 Possible effect of the climate change.

As the most stable primary non-fossil fuel in power generation systems, nuclear energy, with its high energy density and minimal greenhouse gas emissions during operation, was once highly anticipated [12]. However, following the Fukushima Daiichi nuclear disaster caused by the Great East Japan Earthquake, public criticism of heavy reliance on nuclear energy has surged. Consequently, it has become extremely challenging to continue the large-scale promotion of nuclear power generation. Therefore, to achieve the intended carbon neutrality goals, it is highly significant to actively research and introduce solar, wind, tidal energy, or other non-carbon fuels to replace traditional fossil fuels [13].

However, when discussing renewable energies such as wind, solar, and tidal energy, the intermittency and instability of energy production are always concerning issues [14]. For instance, in wind power generation, the inability to control wind speed can lead to inconsistent output power, making it a significant challenge to maintain the continuous balance between power supply and demand, as well as the stability of the power system. Additionally, wind turbines generate noise during operation and have a visual impact on the surrounding landscape, affecting the local environment and nearby residents [15,16]. Similarly, solar power generation is influenced by weather and sunlight availability, and current installation and initial investment costs of solar panels remain relatively high, limiting their broader application [17,18].

To address the instability of energy production, some scholars have combined photovoltaic or wind power generation with energy storage systems to achieve longer-term storage and utilization of electricity. **Figure 1.4** presents various energy storage methods, ranging from high-power superconducting storage that manages reasonable energy power (less than 5-MW) within limited time frames (seconds) to pumped hydro or chemical storage that can store thousands of gigawatts of power for extended periods (months or years) [14]. Unlike traditional battery or mechanical storage methods that may cause secondary pollution during manufacturing or disposal, chemical storage offers high flexibility and is easier to move, store, and distribute [19]. Among these chemical storage fuels, hydrogen (H_2), ammonia (NH_3), and hydrazine (N_2H_4) are effective non-carbon fuels with significant potential under the carbon neutrality framework. However, due to toxicity and reactivity issues, hydrazine is challenging to use on a large scale and is currently employed mainly as auxiliary power in the aerospace sector during emergencies [20].

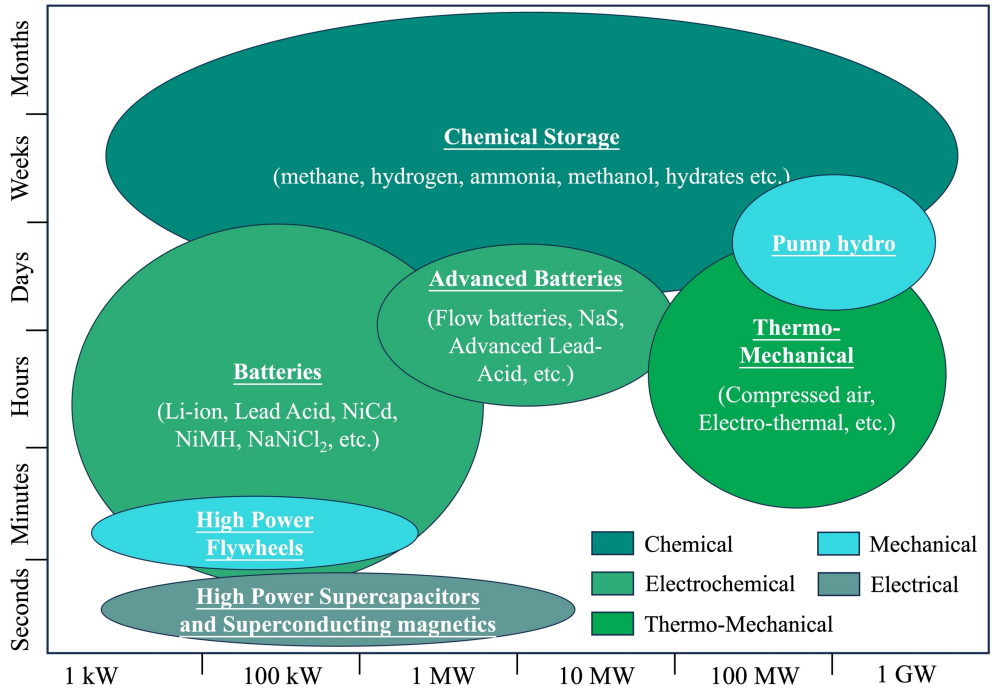

Figure 1.4 Comparison between different energy storage technologies [14].

Hydrogen is the most common molecule in the universe and an effective energy carrier. Hydrogen gas has a high specific energy of approximately 120 MJ/kg, significantly higher than the 44 MJ/kg of oil, and its complete combustion product is only water, making it an environmentally friendly, ideal clean energy source [21]. However, hydrogen is not freely available in nature, so its production requires primary energy sources (traditional hydrocarbon fuels, solar energy, wind energy, biomass energy, tidal energy, etc.) or secondary energy sources like electricity and thermal energy [22]. The practical application of hydrogen also faces

significant challenges. First, while hydrogen has a high specific energy, its volumetric energy density at standard temperature and pressure is relatively low, about 10.8 MJ/Nm^3. This means that the energy content per unit volume is limited, often necessitating high-pressure storage or liquefaction, which increases storage and transportation costs [23,24]. Second, the safety of hydrogen is a major concern due to its wide flammability range (4% - 75%), low ignition energy, and colorless, odorless nature, making it difficult to detect leaks and prone to explosions [14]. Additionally, the current high production costs of hydrogen present significant challenges for large-scale development and application [25]. Thus, given current technological limitations, it is essential to explore more effective fuels.

In contrast, ammonia is also a carbon-free compound that does not produce carbon dioxide during combustion and can serve as an effective fuel and energy carrier. It has a higher energy density and can be stored and transported under simpler conditions (e.g., refrigerated at -33 °C in atmospheric pressure or at 0.8-1.0 MPa at room temperature) [14,26]. Moreover, ammonia has lower flammability and is less prone to explosions, enhancing safety during storage and transportation [9]. In current practical industrial applications, global ammonia production is abundant, with over 100 years of development leading to mature production technology. For example, blue NH_3 can be produced in large quantities using the well-established Haber-Bosch process, and new technologies are being developed and evaluated to produce green NH_3 using renewable energy and direct electrochemical nitrogen reduction reaction [27–29]. The well-established infrastructure and superior transportation characteristics of ammonia make it a promising transitional renewable fuel candidate where hydrogen energy cannot be widely adopted [19,30].

Considering this context, the present study will investigate the practical feasibility of using ammonia in combustion systems against the background of carbon neutrality goals. The aim is to explore the optimal combustion conditions for ammonia to facilitate the transition to a carbon-free combustion industry.

1.2 Ammonia for power

1.2.1 Interest in ammonia for power

Historically, since the discovery of synthetic ammonia after the Industrial Revolution, ammonia has been widely used in agriculture, particularly as a component of fertilizers, to promote crop growth and increase agricultural yields. Dating back to the 20th century, with breakthroughs in industrial ammonia production methods, Belgian researchers began experimenting with liquid ammonia as a fuel for motor buses due to the shortage of traditional automotive fuels in 1945. They powered these vehicles with a mixture of ammonia and coal

gas for over a year [31]. This experiment led to some fundamental research on ammonia in the 1960s. For example, in 1963, Verkamap et al. [32] investigated the ignition and combustion characteristics of ammonia/air mixtures to determine their feasibility for gas turbines. Results showed that under stoichiometric conditions, the quenching distance of the ammonia/air flame was about 7 mm, 3.44 times that of a propane/air flame. They also found that at an equivalence ratio of 0.9, the minimum ignition energy for ammonia was about 8 mJ, significantly higher than the 0.5 mJ for propane, and that the combustion speed and flame stability for ammonia were lower than those of traditional hydrocarbon fuels. Pratt [33] attributed the difficulty in burning ammonia primarily to the slower chemical reaction between ammonia and air. Compared to traditional hydrocarbon fuels, ammonia has much lower mixing efficiency, posing challenges for its pure combustion in practical applications. These early experiments helped establish some basic concepts and the feasibility of using ammonia as a fuel.

Since the early 21st century, the increasing global carbon dioxide emissions and deteriorating climate conditions have led to renewed interest in finding suitable carbon-free fuels to reduce greenhouse gas emissions. Research on ammonia has been revived and is gradually gaining international attention. Japan is currently at the forefront of global ammonia energy utilization and has ambitious plans to extensively apply this chemical in future combustion systems for industrial applications [9,34]. For example, the New Energy and Industrial Technology Development Organization (NEDO) has announced several ammonia production and industrial application development projects in recent years to reduce carbon emissions in electricity, transportation, heating, and other systems, supporting the achievement of carbon neutrality goals [35]. With government support, Japanese power utility JERA has also launched an international bidding process, planning to procure 500,000 tons of fuel ammonia annually from 2027 to 2040 for the Hekinan power plant. The goal is to gradually increase the ammonia co-firing ratio and achieve 50% co-firing ratio power generation by 2030, with plans to eventually expand this to coal-fired power plants across Japan [36].

China shares a similar vision and has officially joined the ammonia energy industry in recent years. In January 2022, the Chinese government, along with the National Development and Reform Commission (NDRC) and the National Energy Administration (NEA), released the "14th Five-Year Plan for New Energy Storage Development Implementation Plan," announcing several research and development projects to study the fundamental ammonia combustion characteristics and to develop ammonia co-firing technology. This marks a significant step towards promoting new energy development [37]. Similarly, the South Korean government has outlined its plans to achieve carbon neutrality by 2050. It announced that by 2030, hydrogen

and ammonia will account for 2.1% of the total power generation, with a further increase to 7.1% by 2036 [34]. Additionally, Steel and cement industries in South Korea are conducting feasibility studies on ammonia combustion and are directly participating in government research and development projects.

European and American countries have also shown interest in the production and application of ammonia. Given that most companies currently produce gray ammonia, which is derived from traditional fossil fuels but involves the separation and recovery of a portion of the CO_2 emitted during production. In contrast, renewable ammonia plants remain relatively scarce. Therefore, in 2016, Cardiff University, Oxford University, Siemens, and the Technology Funding Council in the UK developed and designed the first "Green Ammonia Decoupled" device of the word, which converts wind energy into ammonia for storage and further utilizes the energy through internal combustion engines [38]. Regarding the application of ammonia combustion furnaces, the Department of Energy Security and Net Zero (DESZN) is actively seeking to develop ammonia mixtures to replace propane gas in industrial boilers to reduce greenhouse gas emissions [34]. The US Department of Energy has also committed to gradually adopting ammonia as an energy carrier while advancing the production and utilization technologies for ammonia and promoting its application in the aerospace sector [14]. This feasibility was validated in a report by Reaction Engines in August 2020, which indicated that with certain technological developments, the cost of flying with ammonia fuel could approximate that of traditional jet fuel. Thus, from an environmental impact perspective, the ammonia route based on renewable energy is the most desirable choice with significant application potential [39].

In summary, in recent years, many countries and international institutions have gradually recognized the potential of ammonia as an effective carbon-free fuel. Research projects and investments in the clean production and application of ammonia are also increasing. The implementation of these policies is expected to promote related research on ammonia in combustion systems and contribute to the achievement of global carbon neutrality goals.

1.2.2 Physicochemical and combustion characteristics of ammonia

Ammonia is a colorless, toxic, and pungent gas. It is perceptible at concentrations of 5-30 ppm in air, can cause coughing or throat swelling at 1700 ppm, and exposure to concentrations between 2500 and 4500 ppm for 30 minutes can be life-threatening. Therefore, detecting ammonia leaks is crucial in industrial applications [40]. **Table 1.1** compares some key properties of ammonia with hydrogen and other common hydrocarbon fuels [9,34]. It can be observed that the gravimetric and volumetric energy densities of ammonia are significantly

lower than those of traditional hydrocarbon fuels, being only about one-seventh of the volumetric energy density of propane. However, compared to another carbon-free fuel, hydrogen, the volumetric energy density of ammonia is at least 20% higher, meaning that more energy can be stored in the same volume. Additionally, its higher autoignition temperature provides better anti-explosion performance, making storage and transportation more convenient in practical applications [38].

Table 1.1 Key properties of ammonia and other common fuels at standard conditions [9,34].

Properties	Ammonia (NH_3)	Hydrogen (H_2)	Methane (CH_4)	Propane (C_3H_8)	Methanol (CH_3OH)
Density (kg/m^3, 298 K, 1 atm, gaseous state)	0.73	0.0813	0.648	1.808	1.31
Lower heating value (gravimetric, MJ/kg)	18.6	120	50	46.4	19.9
Lower heating value (volumetric, MJ/Nm^3)	13.2	10.8	35.8	93.2	15.6
Minimum autoignition temperature (K)	924	858	813	723	743
Adiabatic flame temperature (K)	2073	2383	2223	2273	2223
Flammability limit (φ)	0.63-1.4	0.1-7.1	0.5-1.7	0.51-2.5	0.25-2.18
Maximum laminar burning velocity (m/s)	0.07	2.91	0.37	0.43	0.50

Figure 1.5 presents the experimentally measured unstretched laminar burning velocities (S_L) of ammonia/air premixed flames at different equivalence ratios [41–50]. Laminar burning velocity is a crucial parameter for evaluating fuel combustion characteristics and determining combustion efficiency and stability [51]. It is observed that the S_L of ammonia reaches its maximum value at an equivalence ratio of φ = 1.1, with an average value of about 7 cm/s. Deviating from this equivalence ratio leads to a sharp decline in S_L, approaching the flammability limit at φ = 0.6 under lean fuel conditions, indicating a narrow flammability range. In comparison, **Table 1.1** shows that the S_L of traditional hydrocarbon fuels such as methane can be five times that of ammonia, with propane and methanol approaching six and seven times, respectively. The lower laminar burning velocity of ammonia makes it more prone to flame extinction during combustion, especially under low temperature and low flow rate conditions, leading to unstable combustion, incomplete reaction, and inefficient energy utilization. From an emissions perspective, low S_L can also lead to incomplete combustion and ammonia leakage, increasing atmospheric pollution [13].

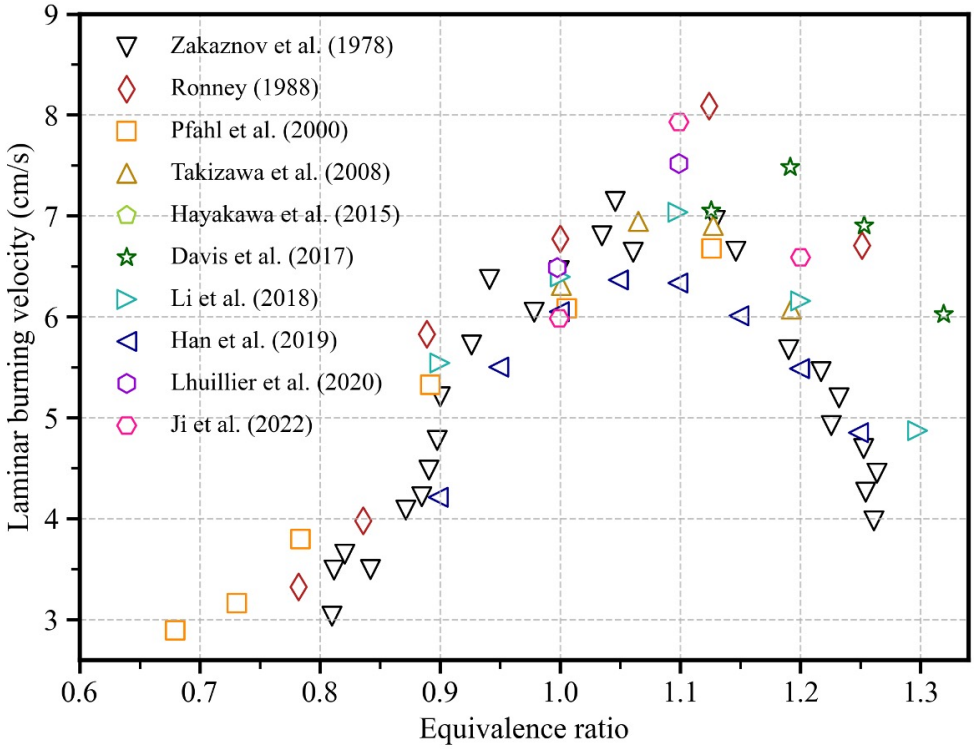

Figure 1.5 Laminar burning velocity of ammonia/air at 303 K, 0.1 MPa [41–50].

Therefore, compared with other hydrocarbon fuels, it is evident that although ammonia can serve as an effective carbon-free fuel, it still has drawbacks such as lower adiabatic flame temperature, weaker flammability, and narrower combustion range, limiting its practical industrial application to some extent. Kane [52] attributed these characteristics to two main reasons. First, the thermal radiation between soot particles formed during combustion and the absorption spectra from carbon species significantly affect heat exchange during combustion [53]. In ammonia/air combustion, the absence of chemical carbon means that little carbon dioxide, which is active in heat exchange, is produced, resulting in reduced radiative heat transfer in the flame and lowering the flame propagation rate.

Secondly, the weaker flammability is possibly due to the chemical stability of the ammonia molecule. Similar to methane combustion, the strong hydrogen bonding to the central atom requires high activation energies to initiate the reaction. However, ammonia releases 63% less energy during complete combustion than methane in the same volume. Since heat release is crucial for raising reaction temperature and promoting flame propagation, the lower heat release significantly reduces ammonia flame propagation speed. However, existing experimental studies indicate that despite the laminar burning velocity of ammonia being lower than that of traditional hydrocarbon fuels, it is still sufficient to ensure the effective operation of burners and engines [13,34]. With appropriate modifications to burners, its practical industrial

application can be anticipated.

Overall, in the context of achieving carbon neutrality, ammonia is a promising carbon-free fuel that could replace traditional hydrocarbon fuels. However, it has certain drawbacks in terms of physicochemical and combustion properties. Therefore, practical applications must consider these factors. Customizing burners for ammonia flame characteristics or using other methods to enhance its combustion intensity are necessary to fully utilize the energy and carbon-free combustion properties it offers.

1.2.3 Emission characteristics of ammonia/air flame

Ideally, the complete combustion of ammonia produces only nitrogen and water, as shown in **Eq. (1.1)**. However, due to actual combustion conditions and application scenarios, this type of combustion is practically impossible to achieve. On the other hand, since the mass fraction of nitrogen in the ammonia molecule is very high, exceeding 82%, using ammonia as a fuel inevitably increases nitrogen oxide (NOx, which mainly constitutes NO and NO_2) emissions when it does not fully react. Excess NOx gases in the air can lead to acid rain, photochemical smog, and fine dust (specifically, particulate matter PM2.5), which are currently under strict regulation globally [54]. In addition to nitric oxide (NO) and nitrogen dioxide (NO_2), ammonia used as fuel also produces small amounts of nitrous oxide (N_2O), which is currently considered a potent greenhouse gas with a global warming potential significantly higher than CO_2 [6]. This means that its emissions can offset the environmental benefits of reduced CO_2 from ammonia combustion. Therefore, it is crucial to implement scientifically effective emission reduction methods to control the generation of these harmful gases during the combustion process of ammonia as a fuel.

$$4NH_3 + 3O_2 = 2N_2 + 6H_2O \quad (1.1)$$

Regarding the relative quantities of the three types of nitrogen oxide emissions, research by Okafor et al. [55] on a micro gas turbine indicates that most nitrogen oxides emitted in an ammonia combustion system appear primarily as NO, with NO_2 and N_2O emissions being one to two orders of magnitude lower. Hence, the present study will focus mainly on investigating the characteristics of NO generation during the ammonia combustion process. NO originates from the fuel-bound nitrogen and nitrogen in the air used in the combustion process and is produced through three mechanisms: thermal NO, prompt NO, and fuel NO [6,56].

Figure 1.6 summarizes the reaction mechanisms for the generation of the three types of NO. Firstly, the formation of thermal NO mainly originates from the reaction of nitrogen and oxygen, and their radicals (O, OH) in the combustion air at high temperatures (typically above 1700 K). This reaction mechanism is also known as the extended Zeldovich mechanism. In this

mechanism, the first reaction, $N_2 + O = NO + N$, is highly sensitive to high temperatures due to the need to break the covalent N-N bond in N_2. Comparatively, the reaction $N + O_2 = NO + O$ is relatively less sensitive to temperature. Therefore, Kobayashi et al. [9] believe that the extended Zeldovich mechanism will also be active in the relatively lower temperature ammonia flames. However, in ammonia combustion systems, thermal NO is not the primary contributor to NO emissions; it is typically a significant mechanism for NO generation in the combustion of traditional nitrogen-free hydrocarbon fuels. Controlling the combustion reaction temperature is the most critical factor in suppressing the formation of thermal NO.

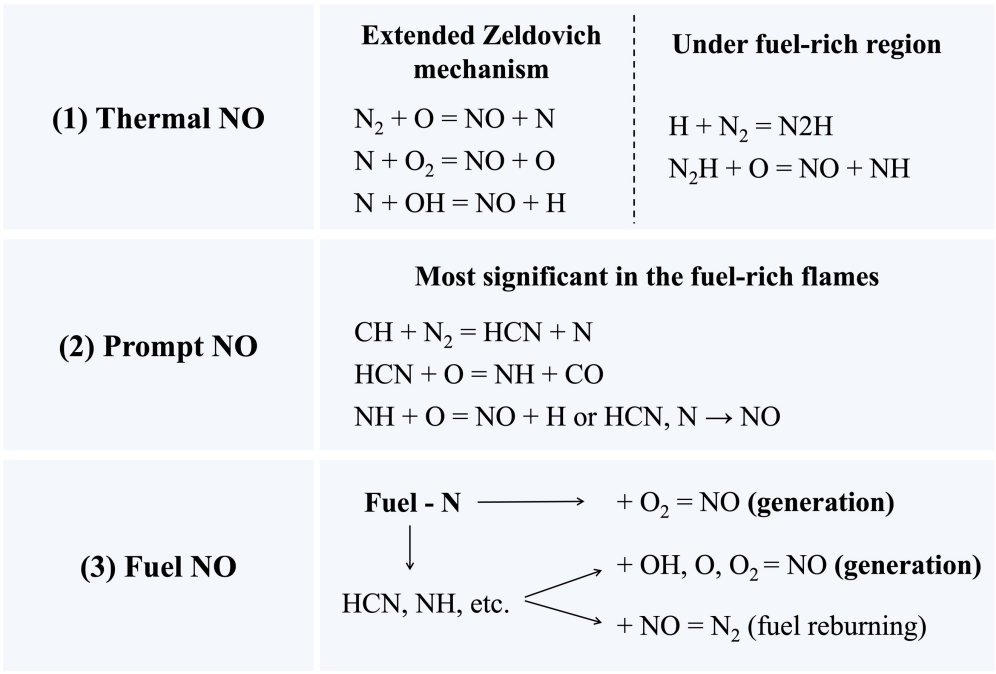

Figure 1.6 Classification and generation mechanism of NO.

Prompt NO is usually generated at the early stage of combustion through the rapid reaction of fuel and nitrogen in the air, and its proportion is very low among the three types of NO formation. In fuel-rich flames, the generation of prompt NO is more significant [56]. However, since the formation of prompt NO does not depend on temperature, occurs quickly, and cannot be eliminated completely during the reaction, most studies pay little attention to prompt NO, focusing primarily on the other two mechanisms for controlling NO formation.

Fuel NO primarily originates from the oxidation of fuel-N in the fuel during combustion. For ammonia combustion flames, its formation follows two different paths: one is the direct reaction of fuel-N with oxygen to form NO; the other is the formation of nitrogen-containing intermediates such as HCN and NH during combustion, which are further oxidized to form NO. However, the fuel NO generated by this mechanism is unstable and may react with NH radicals

to form N_2 again. Therefore, in practical power generation systems, adding secondary fuel can act as an effective reducing agent to reduce the formation of fuel NO [6]. In combustion systems using ammonia as fuel, the rate of fuel NO formation is much higher than that of thermal NO, and it dominates [57].

In conclusion, the application of ammonia in combustion systems will also produce some undesirable nitrogen oxide emissions. To achieve widespread application and promotion of ammonia as fuel, it is also necessary to develop emission reduction technologies that can appropriately control nitrogen oxide emissions based on the ammonia/air combustion characteristics, without producing by-products.

1.2.4 Ammonia combustion methods and applications

Previous studies have shown that while ammonia has many advantages as a carbon-free fuel, there are still two main challenges to its large-scale use in power generation systems: first, the relatively low combustion intensity and energy density of ammonia, and second, the emission of harmful NO gases during combustion. Numerous studies have optimized ammonia combustion scenarios to address these two issues. The present section will review existing methods for enhancing ammonia combustion intensity and reducing NO emissions.

(a) Flame enhancement of ammonia/air flames

Due to the relatively low laminar burning velocity and energy density of ammonia, maintaining the operation of burners at a fixed power requires a combustion chamber with a larger volume compared to traditional hydrocarbon fuels. To address this issue, recent research in thermal power plants focuses on gradually replacing hydrocarbon fuels with ammonia, typically by blending a proportion of ammonia during the combustion process, thus adopting a co-firing approach. By using this co-firing method, it is possible to enhance the combustion characteristics of ammonia flames while effectively reducing carbon emissions [58].

Regarding fundamental research on ammonia co-firing, as early as 1972, Bockhorn et al. [59] measured the laminar burning velocity of C_3H_8/NH_3 co-firing flames and found that the laminar burning velocity decreased as the ammonia co-firing ratio increased. Henshaw et al. [60] and Okafor et al. [61] conducted more detailed studies, measuring the laminar burning velocity of CH_4/NH_3 mixtures at different equivalence ratios. Results showed that at an equivalence ratio of 1.1 and an ammonia co-firing ratio of 10%, the laminar burning velocity increased by nearly 3.8 times compared to pure ammonia combustion. When the co-firing ratio increased to 30%, it still achieved twice the level of pure ammonia combustion. Extending to practical industrial applications, Kurata et al. [62] investigated the NO emission characteristics of CH_4/NH_3 under different ammonia co-firing ratios based on a 50-kW micro gas turbine. The results indicated

that as the ammonia co-firing ratio increased, NO emissions initially increased and then decreased. Similarly, Okafor et al. [63] and Xie et al. [64] explored the combustion state and NO emission trends under different equivalence ratios and co-firing ratios using experimental and numerical methods. Tamura et al. [65] achieved effective control of NO formation in a 1.2-MW ammonia co-combustion furnace by adjusting the ammonia injection method, ensuring no ammonia leakage. Therefore, the ammonia co-firing method has a promising industrial application prospect.

(b) NO emission control technologies

Although the ammonia co-firing strategy can effectively enhance the laminar flame speed and flame stability, NO emissions resulting from the introduction of ammonia for co-firing remain an unavoidable issue. Jójka and Slefarski [66] and Valera-Medina et al. [67] measured the emission characteristics of CH_4/NH_3/air flames. They found that even with the addition of only 4-5% ammonia (by volume) for co-firing, the NO concentration in the exhaust gases increased by one to two orders of magnitude. In light of this, it is of great significance to develop effective strategies to address the above challenge.

Table 1.2 Common NO control technologies.

Technology	Description	Advantage	Disadvantage
Selective Catalytic Reduction (SCR)	Use a catalyst to convert NO into N_2 and H_2O using a reductant like ammonia	• High NO removal	• High capital cost • Possibility of secondary pollution
Selective Non-Catalytic Reduction (SNCR)	Use chemicals (typically urea or ammonia) to reduce NO to N_2 without a catalyst	• Moderate NO removal with non-toxic chemical	• Lower efficiency compared to SCR • Require high temperature operation
Sorbent injection	Use some chemicals or adsorbents to capture and reduce NO	• Controls NO emissions while also adsorbing some other pollutants	• Space and cost for the sorbent storage and handling
Combustion state optimization	Increase the reaction initial pressure	• Moderate cost	• Modifications to the furnace are required • Cost for the furnace maintenance
Rich combustion	Reduction of O and OH radicals during reactions by rich fuel combustion	• Effectively reduces NO generation	• Increased risk of ammonia leakage • Low combustion efficiency

Table 1.2 Common NO control technologies (continue).

Technology	Description	Advantage	Disadvantage
Fuel-reburning technology	Using fuel as the reducing agent to convert NO to N_2	• Moderate cost	• Increased risk of ammonia leakage
Air-staged strategy	Inject the air into the burner in stages to create a fuel-rich region	• Effectively reduces peak temperatures, thus lowering NO formation	• Lead to incomplete combustion if not properly controlled

Unlike sulfur or other easily removable minerals in coal, the nitrogen in ammonia fuel cannot be easily removed or reduced. Therefore, the current technologies to control NO emissions during ammonia combustion in power systems can be categorized into two types. The first is post-combustion treatment, which involves treating the combustion flue gas. This method uses physical and chemical means to remove NO from the flue gas at the furnace outlet. The second is combustion modification, which involves modifying the burners or adjusting the combustion conditions to reduce NO formation. **Table 1.2** summarizes some of the common NO control technologies found in current research [56].

Firstly, post-combustion treatment technology involves a series of chemical reactions to convert NO in flue gas into nitrogen or water. Currently, Selective Catalytic Reduction (SCR) and Selective Non-Catalytic Reduction (SNCR) are two commonly studied strategies in this field. In particular, SCR technology has proven effective across various operating conditions and has been widely applied in traditional power plants. SCR technology primarily uses ammonia as a reducing agent to convert NOx in flue gas into N_2 and H_2O without consuming excess oxygen, as shown in **Eqs. (1.2) – (1.6)** [68,69]. Additionally, other recently developed post-combustion flue gas treatment technologies include Non-Selective Catalytic Reduction (NSCR) and hybrid SCR/SNCR technologies, although they have not been widely adopted or applied [6].

$$4NO + 4NH_3 + O_2 = 4N_2 + 6H_2O \quad (1.2)$$

$$2NO_2 + 4NH_3 + O_2 = 3N_2 + 6H_2O \quad (1.3)$$

$$4NO + 4NH_3 = 5N_2 + 6H_2O \quad (1.4)$$

$$6NO_2 + 8NH_3 = 7N_2 + 12H_2O \quad (1.5)$$

$$NO + NO_2 + 2NH_3 = 2N_2 + 3H_2O \quad (1.6)$$

Besides the aforementioned traditional chemical methods to remove NO generated during combustion, adjusting the combustion process or modifying the furnace is also a highly feasible

approach. For instance, Somarathne et al. [70] found through numerical methods that increasing the initial pressure of combustion under fuel-rich conditions can effectively suppress the formation and emission of NO and ammonia leakage in ammonia/air combustion systems. However, high-pressure combustion applications significantly increase maintenance costs and safety concerns. Therefore, research on controlling NO formation at atmospheric pressure is also meaningful.

In combustion systems using ammonia as fuel, setting up a fuel-rich combustion zone within the furnace or implementing secondary fuel injection to reduce O and OH radicals during the reaction process is the most effective low-cost option for controlling NO formation and reducing fuel-NO. However, due to the physical and chemical properties of ammonia, combustion efficiency under fuel-rich conditions significantly decreases, and excessive fuel input greatly increases the risk of fuel leakage. For ammonia, in particular, this poses a risk of secondary environmental pollution [26].

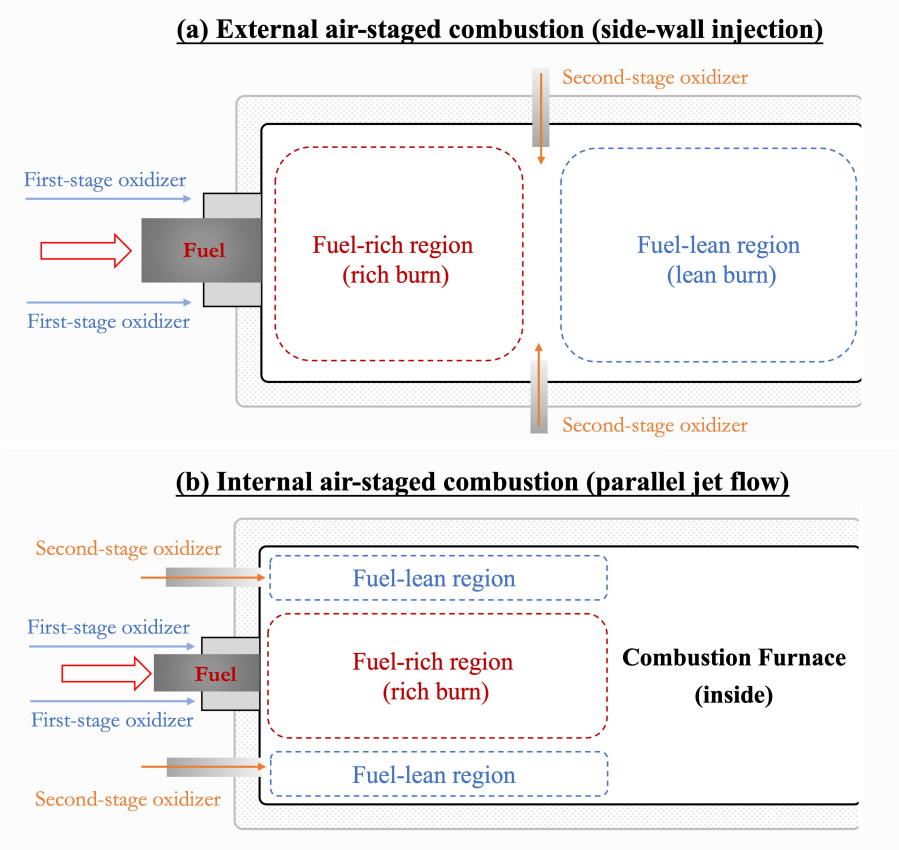

Figure 1.7 Schematic diagram of (a) external air-staged combustion and (b) internal air-staged combustion.

Air-staged combustion, also known as two-stage combustion, is another approach to control NO formation by creating a fuel-rich region within the furnace. Unlike the previously

mentioned fuel-rich combustion method, this approach also involves injecting secondary air to consume the excess fuel, effectively preventing ammonia leakage. Air-staged combustion can be categorized into external air-staged combustion (side-wall injection) and internal air-staged combustion (parallel injection), as shown in **Fig. 1.7**. External air-staged combustion is commonly used in pulverized coal boilers and is adaptable to both wall-fired and tangentially fired boilers. This method involves staging the air injection at the burner entrance and mid-to-lower sections of the furnace, allowing the fuel to first burn in a fuel-rich environment to maximize NO suppression. Subsequently, secondary air is injected into the mid-to-lower sections to consume the excess fuel and prevent ammonia leakage [71]. Internal air-staged combustion differs slightly in the position of secondary air injection but shares the concept of air-staging to create a fuel-rich region in the combustion chamber, utilizing the characteristics of ammonia as an effective NO reduction agent to achieve NO reduction [72]. Therefore, in ammonia co-firing research, equipping burners with a secondary injection system for air-staging is necessary.

In practical industrial applications, large combustion furnaces sometimes feature multiple burners. In such cases, implementing external air-staged combustion, which involves supplying secondary air from the side walls of the combustion chamber, becomes challenging. Consequently, for certain specific furnace designs, employing internal air-staged combustion is a more economical and effective strategy. This approach involves the application of a parallel injection system, enabling the simultaneous injection of secondary air and fuel from the same wall of the burner into the furnace [73]. Therefore, research on internal air-staged combustion is also meaningful, and the present study will focus on exploring the air-staged strategy with the parallel injection system.

1.3 Numerical calculations in ammonia combustion furnaces

Experimental research is the most fundamental and effective method for exploring the combustion and emission characteristics of ammonia co-firing systems. Through practical operation and observation, reliable experimental data can be obtained, which plays a crucial role in verifying and calibrating theoretical models. For example, in an early experimental study on ammonia co-firing furnaces, Kikuchi et al. [73] investigated the combustion and NO emission characteristics within a 10-kW lab-scale combustion furnace under different ammonia co-firing ratios, air-staging ratios, and secondary nozzle diameters. They were the first to validate the effectiveness of using a parallel injection system in air-staged combustion, providing valuable reference data for parameter selection in the practical industrial application of ammonia co-firing systems. However, due to limitations in current experimental

measurement conditions, when using thermocouples for temperature measurements along the axial part of the furnace, the introduction of measurement points significantly impacted the temperature distribution in the central region, resulting in considerable measurement errors. Consequently, an accurate assessment of combustion characteristics under different ammonia co-firing conditions within the furnace could not be made. To address these limitations and better understand NO generation and combustion characteristics, the application of Computational Fluid Dynamics (CFD) analysis becomes necessary. Therefore, the following section will provide a brief introduction to some numerical simulation studies.

1.3.1 Modeling methods

In the industrial application of power generation systems using ammonia as a co-firing fuel, combustion equipment mostly adopts turbulent combustion, where the interaction mechanisms between combustion and turbulence are highly complex and an important research topic. Currently, CFD research primarily relies on the Navier-Stokes equations for fluid flow calculations and is divided into three modeling methods based on the scale of turbulence treatment: Direct Numerical Simulation (DNS), Large Eddy Simulation (LES), and Reynolds-Averaged Navier-Stokes (RANS), as shown in **Fig. 1.8** [74].

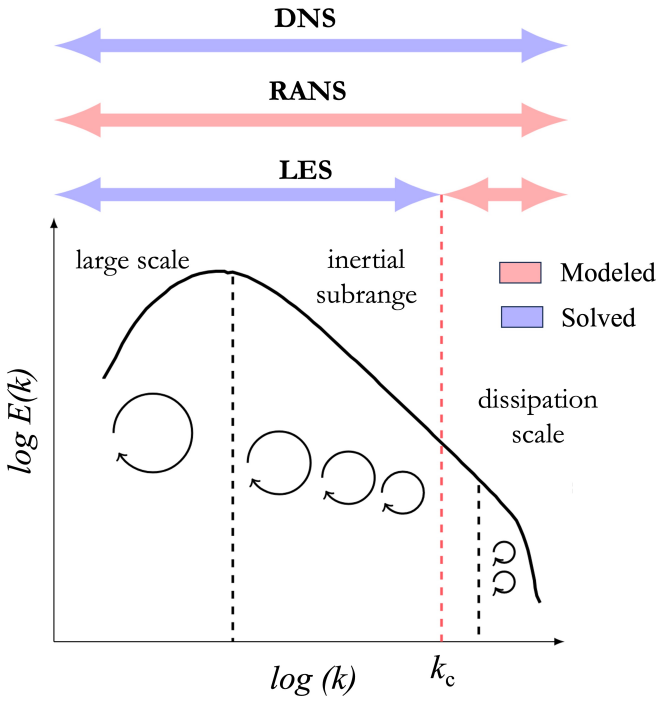

Figure 1.8 Turbulent energy spectrum and modeling methods (k_c is the LES cut-off wave number).

Firstly, the DNS method directly solves the transient control equations for the fluid region without any additional turbulence or combustion models, resulting in highly reliable numerical

results. However, applying the DNS method to numerical simulations requires a grid number roughly proportional to the Reynolds number (Re) to the 12th power, consuming vast computational resources. Therefore, DNS can only be used for small-scale studies, model research, or low-Reynolds-number combustion calculations. In the current research context, it is commonly used as a tool for understanding the turbulence mechanisms in reactions.

LES is a relatively intermediate method that differentiates the eddies in turbulent flow through a filtering function, filtering them into larger-scale and smaller-scale eddies. Larger eddies are directly solved, while smaller eddies are modeled and numerically solved. Compared to DNS, LES has lower computational costs and has been applied to small-scale industrial ammonia combustion equipment in recent years [58,70]. However, for larger-scale combustion equipment, introducing detailed reaction mechanisms still leads to prohibitive computational costs and complexity.

The RANS method simplifies the turbulent flow solution process through time-averaging, breaking down instantaneous flow quantities into time-averaged values and fluctuating components. Specifically, the RANS method decomposes instantaneous velocity into average and fluctuating velocities, then time-averages the Navier-Stokes equations to obtain a set of Reynolds-averaged equations. These equations describe the average flow characteristics of the fluid, with the turbulent fluctuation part modeled through turbulence models. Consequently, RANS has lower computational accuracy compared to LES and DNS but significantly reduces computational costs, making it widely applicable to large-scale, long-term flow and combustion problems in engineering. Therefore, considering the industrial application background of ammonia combustion in the present study, the RANS method will be applied for numerical investigation. The governing equations and calculation models related to the RANS method will be introduced in detail in the second chapter.

1.3.2 Wall boundary condition in combustion furnace simulation

When applying the RANS method for numerical simulation of industrial furnaces, aside from turbulence and combustion models significantly influencing the results, accurately determining thermal boundary conditions at the furnace walls is also critical for the precise prediction of temperature and species distributions [58]. There are several methods representing boundary conditions at the furnace walls. For example, common methods include using adiabatic boundary conditions (for adiabatic materials or ideally insulated situations), fixed wall temperatures, or fixed heat flux. These three methods are relatively simple and require fewer parameters, but they often deviate significantly from actual conditions. Using convective boundary conditions that consider ambient temperature and convective heat transfer

coefficients or further considering the effects of thermal radiation are closer to actual conditions but could introduce more computational parameters and uncertainties [75]. Additionally, an important point often overlooked in these studies is that they only investigate fluid domain calculations, often neglecting the heat transfer process between the fluid and solid domains, making it difficult to obtain the reaction temperature of the solid domain [76].

This concern has been underscored by the work of Xie et al. [64]. They investigated an ammonia co-firing furnace considering the heat transfer process between the fluid and solid domains and found that neglecting the heat transfer effect could lead to negative heat transfer in some regions of the furnace. This implies that heat could be transferred from the furnace side wall towards the fuel gas, which is contrary to actual conditions. Therefore, to more accurately define the boundary conditions at the furnace walls, it is necessary to introduce the Conjugate Heat Transfer (CHT) method. This method considers the thermal interactions between the solid and fluid domains and has recently been regarded as an effective method for representing thermal boundary conditions in combustion simulations. In the present study, the CHT model will also be introduced for the numerical calculation of ammonia combustion furnaces.

1.3.3 Prediction accuracy and calculation speed

In CFD applications, computational speed and accuracy are often the primary concerns for many researchers. For example, in the context of industrial research, constraints related to computational expenses and work progress usually necessitate using coarse meshes, along with lower-fidelity sub-models [77]. These simulations can provide valuable insights into trends during the transition of experimental conditions. Nevertheless, they fall short in providing accurate quantitative predictions of combustion characteristics and emissions, owing to the compromises made on mesh resolution. Additionally, as described in **Sec. 1.3.2**, introducing the CHT method significantly increases the number of computational grids and the complexity of calculations for the solid domain. Therefore, considering these factors, developing a fast and accurate CFD solver is of great importance.

In recent years, advancements in science and technology have significantly accelerated computer processing speeds. Also, there has been a growing depth of understanding regarding ammonia, leading to the proposal of increasingly detailed reaction mechanisms for ammonia combustion [61,78]. This development provides promising prospects for more accurate predictions of flow fields and species distributions within furnaces. However, it is important to note that introducing detailed reaction mechanisms also significantly increases computational costs. In finite-rate chemistry calculations, it is necessary to solve differential equations for the evolution of individual species in each computational cell, in addition to solving the Navier-

Stokes equations for momentum and energy. This computational load escalates with the increasing number of reactive species, resulting in higher computational costs and storage requirements[79]. Therefore, even within the realm of industrial applications employing RANS simulations, the incorporation of detailed reaction mechanisms remains prohibitively costly.

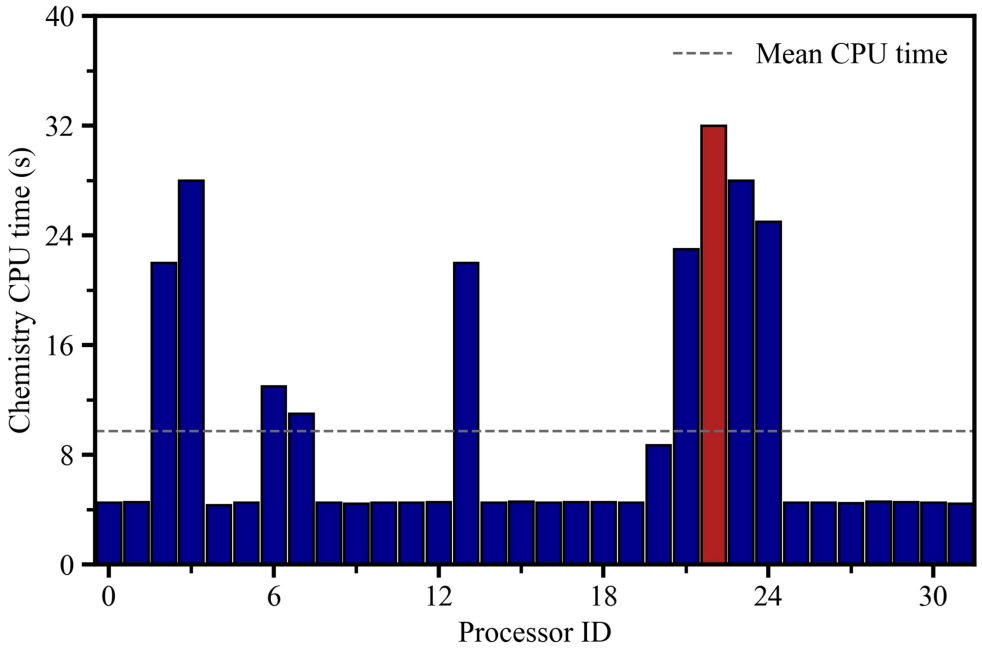

Figure 1.9 An illustration of the computational imbalance in reactive CFD simulation.

Generally speaking, chemistry evaluation comprises the most computationally demanding part of the simulations. In finite-rate chemistry simulations employing detailed chemical reaction mechanisms, the computational cost primarily arises from three key factors: the size of the reaction mechanism, the load imbalance issue in multi-processor applications, and the grid dimensions [80,81]. First of all, as mentioned previously, using detailed reaction mechanisms increases the number of advection equations, diffusion coefficient calculations, and the stiffness of chemical-reaction Ordinary Differential Equations (ODEs). The computational cost of solving the associated stiff ODEs scales quadratically with the number of involved species [82], posing a significant challenge for the application of detailed reaction mechanisms. The secondary issue lies in the imbalanced computational load distribution in parallel calculations. In CFD numerical calculations, parallelization is achieved through geometric domain decomposition. However, with the introduction of combustion reactions, the thermochemical state vector values between different grids change over time, leading to an imbalance in computational load among different sub-domains, as shown in **Fig. 1.9** [83]. Sub-domains with high computational loads significantly increase the calculation time per step. Thirdly, the resolution of the computational grid also affects computational speed. In

computational modeling, an increase in the number of grid cells will significantly increase the number of equations to be solved, meaning that the number of grid cells is directly proportional to the computational workload. Despite most CFD software packages implementing the parallel computing strategy to partition the computational domain into multiple sub-domains, excessive domain partitioning can lead to communication bottlenecks among processors, ultimately diminishing the overall efficiency of the solver [84]. In addition to the factors mentioned above, combustion furnace simulations often require grid refinement in specific locations, such as the inlet nozzle and main reaction area, to accurately capture the flow characteristics and species distribution. However, since the global time step is determined by the smallest cell size in calculations, these refined grids significantly lower the global time step for reactions. This increases reaction convergence time, thereby reducing computational efficiency [85].

To address the potential deficiencies in the computational process mentioned above, researchers have proposed various computational acceleration strategies and have made substantial improvements. For example, for solving ODE systems, Lu et al. [86] reported that using analytically computed Jacobians can effectively enhance computational performance. Safta et al. [87] developed TChem, one of the first programs to solve Jacobian matrices using analytical methods, providing interfaces for solving Jacobian matrices for reaction mechanisms of different sizes. Perini et al. [88] developed a Jacobian matrix computation program for constant volume combustion, systematically implementing the sparse expression and related algorithms of the Jacobian matrix which significantly improved computation speed, especially for the detailed reaction mechanisms. Niemeyer et al. [82] developed the pyJac program for NVIDIA GPU applications, optimizing the evaluation order to minimize computational and memory operations, achieving high computational stability and efficiency. On the other hand, to address the issue of computational load imbalance in parallel calculations, Antonelli et al. [89] developed a Message Passing Interface (MPI) based parallel solver that utilizes a cell distribution-based load balancing algorithm, effectively solving this problem. Building on this research, dynamic load balancing codes have been increasingly applied to various computational programs [83,90]. Additionally, the recently introduced OpenMP and Local Time Stepping (LTS) methods can effectively address communication bottlenecks between processors and global time step issues during calculations [85,91].

However, most of the aforementioned studies focus on specific optimizations for one issue in the computational process. In practical industrial applications, to better enhance computational speed, these acceleration strategies are often combined [92,93]. Therefore, it is of great significance to explore a robust and efficient integrated acceleration strategy.

1.4 Problem statement

As a promising carbon-free fuel, ammonia holds great potential for combustion applications in power generation. However, summarizing previous studies, using ammonia as a fuel in current power systems still faces challenges in controlling NO emissions and addressing weak combustion properties. Therefore, the development and design of low-NO ammonia combustion furnaces are necessary. Additionally, while CFD analysis is an effective tool for developing ammonia combustion furnaces and investigating internal combustion characteristics, its computational efficiency is still limited when applied to large-scale reactive simulations, significantly prolonging the development cycle and time. Hence, there is still room for optimization in numerical computation speed and prediction accuracy, as detailed below:

(1) Combustion characteristic and NO control in parallel injection system

As mentioned in **Sec. 1.2.3**, using an air-staged strategy to create a fuel-rich region near the primary nozzle outlet is an economical and effective method for controlling NO emissions in ammonia combustion furnaces. However, most current studies focus on furnaces where secondary air is injected from the side wall, with relatively few studies on parallel injection systems. Therefore, it is essential to investigate the effectiveness of NO control and the combustion characteristics inside the furnace under different ammonia co-firing ratios when using parallel injection systems.

Additionally, the impact of various burner parameters on NO emissions in parallel injection systems remains unclear. For instance, there is no definitive conclusion on adjusting the primary and secondary air ratios to maximize the suppression of NO formation. Secondly, the diameter of the secondary nozzle affects the velocity of the secondary air entering the furnace and indirectly influences the flow field distribution inside the furnace, thereby impacting NO formation and emission. Moreover, the distance between the secondary and primary nozzles affects the formation of the fuel-rich region, thus also influencing NO emissions. In summary, this study will also systematically investigate the above three parameters to provide references for the future development and design of low-NO ammonia combustion furnaces.

(2) Conjugate heat transfer in CFD application

As discussed in **Sec. 1.3.2**, accurately predicting the thermal boundary conditions at the furnace walls is crucial for predicting the internal temperature and species distribution within the combustion furnace. However, most three-dimensional (3D) numerical simulation studies on combustion furnaces typically use fixed temperature or heat flux boundary conditions, emphasizing fluid calculations while neglecting the heat transfer process between the fluid and solid. This leads to significant deviations from actual conditions. Therefore, integrating the

CHT method in numerical calculations is necessary. Presently, there are few studies using this type of thermal boundary condition, and the present research aims to fill this gap.

(3) Acceleration of the computational speed

In three-dimensional ammonia combustion furnace simulations, introducing detailed reaction mechanisms and the CHT method (due to the inclusion of solid domain, increasing the number of computational grids) significantly increases computational costs and time. This poses substantial challenges when using native CFD computational models. Therefore, in the context of industrial combustion furnace applications, it is necessary to introduce corresponding acceleration strategies based on the computational challenges as discussed in **Sec. 1.3.3**. Specifically, developing a fast and stable integrated acceleration strategy is essential for applying large-scale 3D numerical simulations of ammonia combustion furnaces.

1.5 Dissertation layout

Based on the shortcomings of existing research mentioned previously, **Fig. 1.10** illustrates the technical route and framework of this thesis. Specifically, the present study will focus on the application of ammonia industrial combustion furnaces, optimizing the computational solver and systematically exploring the effects of different co-firing ratios and parameters in parallel injection systems on combustion characteristics through numerical analysis. The goal is to provide references for the future development of low-NO ammonia combustion furnaces.

Regarding the structure, this thesis will be divided into six chapters for discussion:

Chapter 1 introduces the research background, motivation, existing research shortcomings, and the research objectives of this thesis.

Chapter 2 describes the details of the numerical modeling. The calculations will be based on the OpenFOAM platform, further optimizing the solver and introducing an integrated acceleration strategy to achieve faster, more stable, and more accurate numerical prediction.

Chapter 3 selects Sandia flames D-F as benchmark experiments for two-dimensional (2D) analysis to explore the performance of the customized solver. First, in terms of computational acceleration, the study investigates the improvement in scaling performance and acceleration capability after introducing the integrated acceleration strategy. Subsequently, based on the optimized solver, the study examines the effects of different turbulence models and Prandtl numbers on numerical prediction results and identifies the optimal model configuration for predicting temperature and species distribution at various axial and radial positions. The optimal model configuration obtained in this chapter will be applied in the subsequent 3D combustion furnace calculations.

Chapter 4 discusses a 10-kW ammonia co-firing furnace. In the 3D numerical calculations, the CHT method is introduced to describe the thermal boundary conditions of the furnace walls. This Chapter explores the effects of the air-staging ratio, secondary nozzle diameters, and the distance between the primary and secondary nozzles on NO emissions and combustion characteristics within the furnace at low ammonia co-firing ratios with the parallel injection system. Additionally, the effectiveness of the parallel injection system in controlling NO emissions is numerically investigated. Based on the ROP analysis results, the main reasons for NO emission control using the air-staged strategy are discussed.

Chapter 5 examines the combustion and emission characteristics within the 10-kW ammonia combustion furnace under different ammonia co-firing ratios. The Sako reaction mechanism is introduced to analyze fuel NO and thermal NO emissions under different conditions. Based on the ROP analysis results, the main reasons for NO emission under different co-firing ratios are explored, providing references for the future application of high ammonia co-firing ratios.

Chapter 6 summarizes the entire thesis. Finally, it provides some recommendations on the selection of secondary injection system parameters for low-NO ammonia co-firing furnaces.

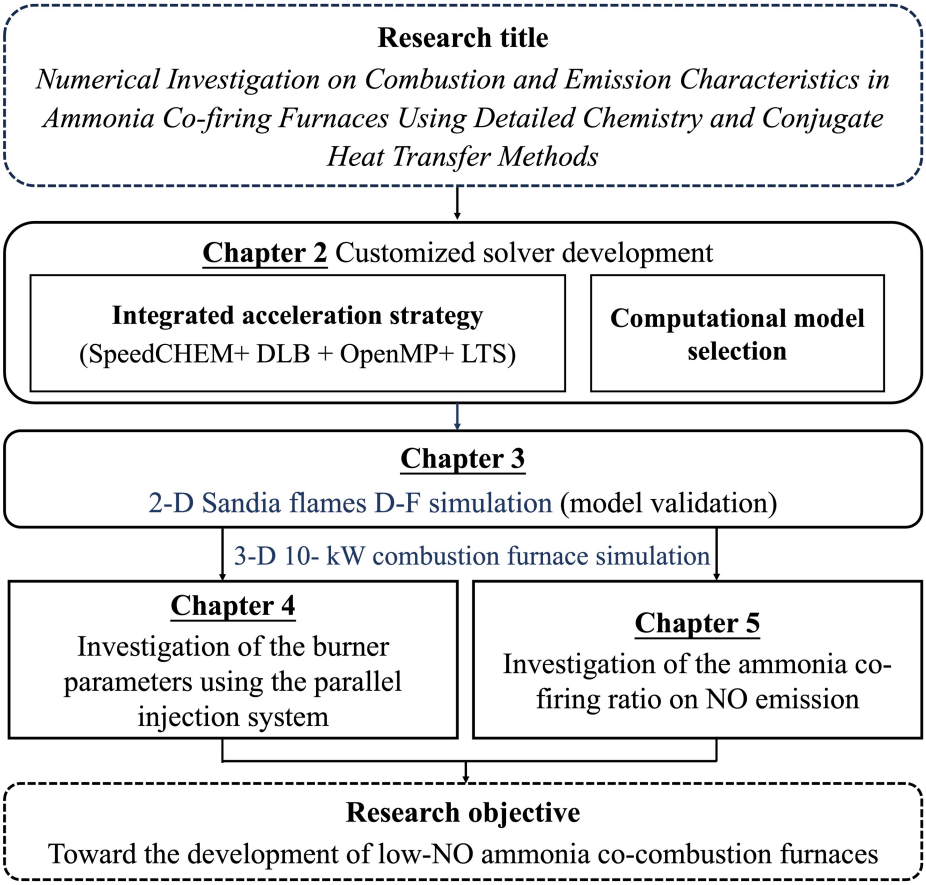

Figure 1.10 Description of research structure and technical roadmap.

References

[1] T. Cai, D. Zhao, E. Gutmark, Overview of fundamental kinetic mechanisms and emission mitigation in ammonia combustion. *Chemical Engineering Journal*, 2023, 458: 141391.

[2] H. Ritchie, P. Rosado, Fossil fuels. *Our World in Data*, 2022, available from: https://ourworldindata.org/fossil-fuels.

[3] H. Ritchie, M. Roser, CO_2 emissions. *Our World in Data*, 2020, available from: https://ourworldindata.org/co2-emissions.

[4] H. Ritchie, P. Rosado, M. Roser, CO_2 and greenhouse gas emissions. *Our World in Data*, 2024, available from: https://ourworldindata.org/co2-and-greenhouse-gas-emissions#research-writing.

[5] United Nations, Kyoto Protocol to the United Nations framework convention on climate change. 1998, available from: https://unfccc.int/kyoto_protocol.

[6] Y. Park, B. Kim, Catalytic removal of nitrogen oxides (NO, NO_2, N_2O) from ammonia-fueled combustion exhaust: A review of applicable technologies. *Chemical Engineering Journal*, 2023, 461: 141958.

[7] Energy Institute, Global direct primary energy consumption. *Our World in Data*, 2023, available from: https://ourworldindata.org/grapher/global-primary-energy.

[8] United Nations, Causes and effects of climate change, available from: https://www.un.org/en/climatechange/science/causes-effects-climate-change.

[9] H. Kobayashi, A. Hayakawa, K.D.K.A. Somarathne, E.C. Okafor, Science and technology of ammonia combustion. *Proceedings of the Combustion Institute*, 2019, 37: 109–133.

[10] United Nations, Paris agreement. 2015, available from: https://unfccc.int/files/essential_background/convention/application/pdf/english_paris_agreement.pdf.

[11] The 6th Strategic Energy Plan. Agency for Natural Resources and Energy, 2021, available from: https://www.enecho.meti.go.jp/en/category/others/basic_plan/.

[12] T.E. Rehm, Advanced nuclear energy: the safest and most renewable clean energy. *Current Opinion in Chemical Engineering*, 2023, 39: 100878.

[13] J. Tian, L. Wang, Y. Xiong, Y. Wang, W. Yin, G. Tian, Z. Wang, Y. Cheng, S. Ji, Enhancing combustion efficiency and reducing nitrogen oxide emissions from ammonia combustion: A comprehensive review. *Process Safety and Environmental Protection*, 2024, 183: 514–543.

[14] A. Valera-Medina, F. Amer-Hatem, A.K. Azad, I.C. Dedoussi, M. De Joannon, R.X. Fernandes, P. Glarborg, H. Hashemi, X. He, S. Mashruk, J. McGowan, C. Mounaim-Rouselle, A. Ortiz-Prado, A. Ortiz-Valera, I. Rossetti, B. Shu, M. Yehia, H. Xiao, M. Costa, Review on ammonia as a potential fuel: From synthesis to economics. *Energy & Fuels*, 2021, 35: 6964–7029.

[15] H. Holttinen, Wind integration: experience, issues, and challenges. *WIREs Energy and Environment*, 2012, 1: 243–255.

[16] G.M. Shafiullah, A. M.T. Oo, A.B.M. Shawkat Ali, P. Wolfs, Potential challenges of integrating large-scale wind energy into the power grid–A review. *Renewable and Sustainable Energy Reviews*, 2013, 20: 306–321.

[17] E. Kabir, P. Kumar, S. Kumar, A.A. Adelodun, K. Kim, Solar energy: Potential and future prospects. *Renewable and Sustainable Energy Reviews*, 2018, 82: 894–900.

[18] K. Ukoba, K.O. Yoro, O. Eterigho-Ikelegbe, C. Ibegbulam, T. Jen, Adaptation of solar energy in the Global South: Prospects, challenges and opportunities. *Heliyon*, 2024, 10: e28009.

[19] M. Tawalbeh, S.Z.M. Murtaza, A. Al-Othman, A.H. Alami, K. Singh, A.G. Olabi, Ammonia: A versatile candidate for the use in energy storage systems. *Renewable Energy*, 2022, 194: 955–977.

[20] O. Elishav, B. Mosevitzky Lis, E.M. Miller, D.J. Arent, A. Valera-Medina, A. Grinberg Dana, G.E. Shter, G.S. Grader, Progress and prospective of nitrogen-based alternative fuels. *Chemical Reviews*, 2020, 120: 5352–5436.

[21] W.S. Chai, Y. Bao, P. Jin, G. Tang, L. Zhou, A review on ammonia, ammonia-hydrogen and ammonia-methane fuels. *Renewable and Sustainable Energy Reviews*, 2021, 147: 111254.

[22] M. Ji, J. Wang, Review and comparison of various hydrogen production methods based on costs and life cycle impact assessment indicators. *International Journal of Hydrogen Energy*, 2021, 46: 38612–38635.

[23] Y. Ma, X.R. Wang, T. Li, J. Zhang, J. Gao, Z.Y. Sun, Hydrogen and ethanol: Production, storage, and transportation. *International Journal of Hydrogen Energy*, 2021, 46: 27330–27348.

[24] Y.H. Teoh, H.G. How, T.D. Le, H.T. Nguyen, D.L. Loo, T. Rashid, F. Sher, A review on production and implementation of hydrogen as a green fuel in internal combustion engines. *Fuel*, 2023, 333: 126525.

[25] O. Faye, J. Szpunar, U. Eduok, A critical review on the current technologies for the generation, storage, and transportation of hydrogen. *International Journal of Hydrogen Energy*, 2022, 47: 13771–13802.

[26] P. Berwal, S. Kumar, B. Khandelwal, A comprehensive review on synthesis, chemical kinetics, and practical application of ammonia as future fuel for combustion. *Journal of the Energy Institute*, 2021, 99: 273–298.

[27] Y. Bicer, I. Dincer, C. Zamfirescu, G. Vezina, F. Raso, Comparative life cycle assessment of various ammonia production methods. *Journal of Cleaner Production*, 2016, 135: 1379–1395.

[28] S. Giddey, S.P.S. Badwal, C. Munnings, M. Dolan, Ammonia as a renewable energy transportation media. *ACS Sustainable Chemistry & Engineering*, 2017, 5: 10231–10239.

[29] A. Sánchez, M. Martín, Optimal renewable production of ammonia from water and air. *Journal of Cleaner Production*, 2018, 178: 325–342.

[30] D.R. MacFarlane, P.V. Cherepanov, J. Choi, B.H.R. Suryanto, R.Y. Hodgetts, J.M. Bakker,

F.M. Ferrero Vallana, A.N. Simonov, A roadmap to the ammonia economy. *Joule*, 2020, 4: 1186–1205.

[31] E. Kroch, Ammonia– A fuel for motor buses. *Journal of Institute Petroleum*, 1945, 31: 213–223.

[32] F.J. Verkamp, M.C. Hardin, J.R. Williams, Ammonia combustion properties and performance in gas-turbine burners. *Symposium (International) on Combustion*, 1967, 11: 985–992.

[33] D.T. Pratt, Performance of ammonia-fired gas-turbine combustors. *Defense Technical Information Center*, 1967, available from: https://apps.dtic.mil/sti/citations/AD0657585.

[34] A. Valera-Medina, M.O. Vigueras-Zuniga, H. Shi, S. Mashruk, M. Alnajideen, A. Alnasif, J. Davies, Y. Wang, X. Zhu, W. Yang, Y.B. Cheng, Ammonia combustion in furnaces: A review. *International Journal of Hydrogen Energy*, 2024, 49: 1597–1618.

[35] NEDO, Fuel ammonia supply chain establishment. 2024, available from: https://green-innovation.nedo.go.jp/en/project/building-fuel-ammonia-supply-chain/scheme/.

[36] J. Atchison, JERA opens tender for long-term ammonia supply contract. *Ammonia energy association*, 2022, available from: https://ammoniaenergy.org/articles/jera-opens-tender-for-long-term-ammonia-supply-contract/.

[37] China, 14th five-year plan: New energy storage development implementation plan (2021-2025). 2022, available from: https://climate-laws.org/document/14th-five-year-plan-for-new-energy-storage-development-implementation-plan_3960.

[38] A. Valera-Medina, H. Xiao, M. Owen-Jones, W.I.F. David, P.J. Bowen, Ammonia for power. *Progress in Energy and Combustion Science*, 2018, 69: 63–102.

[39] T. Brown, Zero emission aircraft: ammonia for aviation. *Ammonia energy association*, 2020, available from: https://ammoniaenergy.org/articles/zero-emission-aircraft-ammonia-for-aviation/.

[40] M. Chorowski, M. Lepszy, K. Machaj, Z. Malecha, D. Porwisiak, P. Porwisiak, Z. Rogala, M. Stanclik, Challenges of application of green ammonia as fuel in onshore transportation. *Energies*, 2023, 16: 4898.

[41] V.F. Zakaznov, L.A. Kursheva, Z.I. Fedina, Determination of normal flame velocity and critical diameter of flame extinction in ammonia-air mixture. *Combustion, Explosion, and Shock Waves*, 1978, 14: 710–713.

[42] P.D. Ronney, Effect of chemistry and transport properties on near-limit flames at microgravity. *Combustion Science and Technology*, 1988, 59: 123–141.

[43] U.J. Pfahl, M.C. Ross, J.E. Shepherd, K.O. Pasamehmetoglu, C. Unal, Flammability limits, ignition energy, and flame speeds in H_2–CH_4–NH_3–N_2O–O_2–N_2 mixtures. *Combustion and Flame*, 2000, 123: 140–158.

[44] K. Takizawa, A. Takahashi, K. Tokuhashi, S. Kondo, A. Sekiya, Burning velocity measurements of nitrogen-containing compounds. *Journal of Hazardous Materials*, 2008, 155: 144–152.

[45] A. Hayakawa, T. Goto, R. Mimoto, Y. Arakawa, T. Kudo, H. Kobayashi, Laminar burning

velocity and Markstein length of ammonia/air premixed flames at various pressures. *Fuel*, 2015, 159: 98–106.

[46] S.G. Davis, J.L. Pagliaro, T.F. Debold, M. Van Wingerden, K. Van Wingerden, Flammability and explosion characteristics of mildly flammable refrigerants. *Journal of Loss Prevention in the Process Industries*, 2017, 49: 662–674.

[47] Y. Li, M. Bi, B. Li, W. Gao, Explosion behaviors of ammonia–air mixtures. *Combustion Science and Technology*, 2018, 190: 1804–1816.

[48] X. Han, Z. Wang, M. Costa, Z. Sun, Y. He, K. Cen, Experimental and kinetic modeling study of laminar burning velocities of NH_3/air, NH_3/H_2/air, NH_3/CO/air and NH_3/CH_4/air premixed flames. *Combustion and Flame*, 2019, 206: 214–226.

[49] C. Lhuillier, P. Brequigny, N. Lamoureux, F. Contino, C. Mounaïm-Rousselle, Experimental investigation on laminar burning velocities of ammonia/hydrogen/air mixtures at elevated temperatures. *Fuel*, 2020, 263: 116653.

[50] C. Ji, Z. Wang, D. Wang, R. Hou, T. Zhang, S. Wang, Experimental and numerical study on premixed partially dissociated ammonia mixtures. Part I: Laminar burning velocity of $NH_3/H_2/N_2$/air mixtures. *International Journal of Hydrogen Energy*, 2022, 47: 4171–4184.

[51] L. Kang, W. Pan, J. Zhang, W. Wang, C. Tang, A review on ammonia blends combustion for industrial applications. *Fuel*, 2023, 332: 126150.

[52] S.P. Kane, Thermochemical recuperation and catalytic strategies for anhydrous ammonia in combustion systems, Doctoral thesis, University of Minnesota, 2021.

[53] R. Viskanta, Radiation heat transfer in combustion systems. *Progress in Energy and Combustion Science*, 1987, 13: 97–160.

[54] A. Islam, S.H. Teo, C.H. Ng, Y.H. Taufiq-Yap, S.Y.T. Choong, M.R. Awual, Progress in recent sustainable materials for greenhouse gas (NOx and SOx) emission mitigation. *Progress in Materials Science*, 2023, 132: 101033.

[55] E.C. Okafor, K.D.K.A. Somarathne, A. Hayakawa, T. Kudo, O. Kurata, N. Iki, H. Kobayashi, Towards the development of an efficient low-NOx ammonia combustor for a micro gas turbine. *Proceedings of the Combustion Institute*, 2019, 37: 4597–4606.

[56] B. Miller, Nitrogen oxides formation and control, in *Fossil Fuel Emissions Control Technologies*, Elsevier, 2015, pp. 243–280.

[57] J.A. Miller, C.T. Bowman, Mechanism and modeling of nitrogen chemistry in combustion. *Progress in Energy and Combustion Science*, 1989, 15: 287–338.

[58] K.D.K.A. Somarathne, E. C. Okafor, A. Hayakawa, T. Kudo, O. Kurata, N. Iki, H. Kobayashi, Emission characteristics of turbulent non-premixed ammonia/air and methane/air swirl flames through a rich-lean combustor under various wall thermal boundary conditions at high pressure. *Combustion and Flame*, 2019, 210: 247–261.

[59] H. Bockhorn, F. Fetting, J.C. Mende, The laminar flame velocities of propane/ammonia mixtures. *Combustion and Flame*, 1972, 18: 471–473.

[60] P.F. Henshaw, T. D'Andrea, K.R.C. Mann, D. Ting, Premixed ammonia-methane-air combustion. *Combustion Science and Technology*, 2005, 177: 2151–2170.

[61] E.C. Okafor, Y. Naito, S. Colson, A. Ichikawa, T. Kudo, A. Hayakawa, H. Kobayashi, Experimental and numerical study of the laminar burning velocity of CH_4–NH_3–air premixed flames. *Combustion and Flame*, 2018, 187: 185–198.

[62] O. Kurata, N. Iki, T. Matsunuma, T. Inoue, T. Tsujimura, H. Furutani, H. Kobayashi, A. Hayakawa, Performances and emission characteristics of NH_3–air and NH_3-CH_4–air combustion gas-turbine power generations. *Proceedings of the Combustion Institute*, 2017, 36: 3351–3359.

[63] E.C. Okafor, K.D.K.A. Somarathne, R. Ratthanan, A. Hayakawa, T. Kudo, O. Kurata, N. Iki, T. Tsujimura, H. Furutani, H. Kobayashi, Control of NOx and other emissions in micro gas turbine combustors fuelled with mixtures of methane and ammonia. *Combustion and Flame*, 2020, 211: 406–416.

[64] M. Xie, Y. Tu, Q. Peng, Numerical study of NH_3/CH_4 MILD combustion with conjugate heat transfer model in a down-fired lab-scale furnace. *Applications in Energy and Combustion Science*, 2023, 14: 100144.

[65] M. Tamura, T. Gotou, H. Ishii, D. Riechelmann, Experimental investigation of ammonia combustion in a bench scale 1.2 MW-thermal pulverised coal firing furnace. *Applied Energy*, 2020, 277: 115580.

[66] J. Jójka, R. Ślefarski, Dimensionally reduced modeling of nitric oxide formation for premixed methane-air flames with ammonia content. *Fuel*, 2018, 217: 98–105.

[67] A. Valera-Medina, R. Marsh, J. Runyon, D. Pugh, P. Beasley, T. Hughes, P. Bowen, Ammonia–methane combustion in tangential swirl burners for gas turbine power generation. *Applied Energy*, 2017, 185: 1362–1371.

[68] L. Han, S. Cai, M. Gao, J. Hasegawa, P. Wang, J. Zhang, L. Shi, D. Zhang, Selective catalytic reduction of NOx with NH_3 by using novel catalysts: State of the art and future prospects. *Chemical Reviews*, 2019, 119: 10916–10976.

[69] T. Andana, K.G. Rappé, F. Gao, J. Szanyi, X. Pereira-Hernandez, Y. Wang, Recent advances in hybrid metal oxide–zeolite catalysts for low-temperature selective catalytic reduction of NOx by ammonia. *Applied Catalysis B: Environmental*, 2021, 291: 120054.

[70] K.D.K.A. Somarathne, S. Hatakeyama, A. Hayakawa, H. Kobayashi, Numerical study of a low emission gas turbine like combustor for turbulent ammonia/air premixed swirl flames with a secondary air injection at high pressure. *International Journal of Hydrogen Energy*, 2017, 42: 27388–27399.

[71] H. Liu, W. Qian, M. Zhu, S. Li, Kinetics modeling on NOx emissions of a syngas turbine combustor using rich-burn, quick-mix, lean-burn combustion method. *Journal of Engineering for Gas Turbines and Power*, 2020, 142: 021005.

[72] X. Wang, W. Fan, J. Chen, G. Feng, X. Zhang, Experimental study on effects of air-staged strategy and NH_3 co-firing ratios on NO formation characteristics in ammonia/coal co-firing process. *Fuel*, 2023, 332: 126217.

[73] K. Kikuchi, R. Murai, T. Hori, F. Akamatsu, Fundamental study on ammonia low-NOx combustion using two-stage combustion by parallel air jets. *Processes*, 2021, 10: 23.

[74] M.F. Ferraro, Hybrid LES/conditional RANS-PDF approach for turbulent non-premixed combustion, Doctoral thesis, University of the Bundeswehr Munich, 2017.

[75] S. Yadav, P. Yu, K. Tanno, H. Watanabe, Large eddy simulation of coal-ammonia flames with varied ammonia injection locations using a flamelet-based approach. *Energy*, 2023, 276: 127546.

[76] M. Abbassi, D. Lahaye, K. Vuik, Modelling turbulent combustion coupled with conjugate heat transfer in OpenFOAM, in *Numerical Mathematics and Advanced Applications ENUMATH 2019*, Springer, Cham, 2021, pp. 1137–1145.

[77] J. Kodavasal, K. Harms, P. Srivastava, S. Som, S. Quan, K. Richards, M. García, Development of a stiffness-based chemistry load balancing scheme, and optimization of input/output and communication, to enable massively parallel high-fidelity internal combustion engine simulations. *Journal of Energy Resources Technology*, 2016, 138: 052203.

[78] Z. Tian, Y. Li, L. Zhang, P. Glarborg, F. Qi, An experimental and kinetic modeling study of premixed $NH_3/CH_4/O_2$/Ar flames at low pressure. *Combustion and Flame*, 2009, 156: 1413–1426.

[79] C.P. Stone, A.T. Alferman, K.E. Niemeyer, Accelerating finite-rate chemical kinetics with coprocessors: Comparing vectorization methods on GPUs, MICs, and CPUs. *Computer Physics Communications*, 2018, 226: 18–29.

[80] F. Perini, A. Krishnasamy, Y. Ra, R.D. Reitz, Computationally efficient simulation of multicomponent fuel combustion using a sparse analytical Jacobian chemistry solver and high-dimensional clustering. *Journal of Engineering for Gas Turbines and Power*, 2014, 136: 091515.

[81] I. Morev, B. Tekgül, M. Gadalla, A. Shahanaghi, J. Kannan, S. Karimkashi, O. Kaario, V. Vuorinen, Fast reactive flow simulations using analytical Jacobian and dynamic load balancing in OpenFOAM. *Physics of Fluids*, 2022, 34: 021801.

[82] K.E. Niemeyer, N.J. Curtis, C.-J. Sung, pyJac: Analytical Jacobian generator for chemical kinetics. *Computer Physics Communications*, 2017, 215: 188–203.

[83] B. Tekgül, P. Peltonen, H. Kahila, O. Kaario, V. Vuorinen, DLBFoam: An open-source dynamic load balancing model for fast reacting flow simulations in OpenFOAM. *Computer Physics Communications*, 2021, 267: 108073.

[84] S. Zou, Y.F. Lin, J. Chen, Q. Wang, Y. Cao, The performance analysis and parallel optimization of the OpenFOAM-based viscoelastic solver for heterogeneous HPC platforms. *Applied Mechanics and Materials*, 2014, 670–671: 873–880.

[85] L. Krivodonova, An efficient local time-stepping scheme for solution of nonlinear conservation laws. *Journal of Computational Physics*, 2010, 229: 8537–8551.

[86] T. Lu, C.K. Law, Toward accommodating realistic fuel chemistry in large-scale computations. *Progress in Energy and Combustion Science*, 2009, 35: 192–215.

[87] C. Safta, H. Najm, O. Knio, TChem - A software toolkit for the analysis of complex kinetic models. *Sandia National Laboratories*, 2011, available from:

https://www.osti.gov/servlets/purl/1113874.

[88] F. Perini, E. Galligani, R.D. Reitz, An analytical Jacobian approach to sparse reaction kinetics for computationally efficient combustion modeling with large reaction mechanisms. *Energy & Fuels*, 2012, 26: 4804–4822.

[89] L. Antonelli, P. D'Ambra, Dynamic load balancing for high-performance simulations of combustion in engine applications, in *19th International Euromicro Conference on Parallel, Distributed and Network-Based Processing*, IEEE, 2011, pp. 133–140.

[90] J. Muela, R. Borrell, J. Ventosa-Molina, L. Jofre, O. Lehmkuhl, C.D. Pérez-Segarra, A dynamic load balancing method for the evaluation of chemical reaction rates in parallel combustion simulations. *Computers & Fluids*, 2019, 190: 308–321.

[91] A. Amritkar, S. Deb, D. Tafti, Efficient parallel CFD-DEM simulations using OpenMP. *Journal of Computational Physics*, 2014, 256: 501–519.

[92] V. Hiremath, S.R. Lantz, H. Wang, S.B. Pope, Computationally-efficient and scalable parallel implementation of chemistry in simulations of turbulent combustion. *Combustion and Flame*, 2012, 159: 3096–3109.

[93] S. Yang, R. Ranjan, V. Yang, S. Menon, W. Sun, Parallel on-the-fly adaptive kinetics in direct numerical simulation of turbulent premixed flame. *Proceedings of the Combustion Institute*, 2017, 36: 2025–2032.

Chapter 2

Computational modeling

2.1 Introduction

As introduced in **Sec. 1.3** of the introduction, in the measurement process of industrial combustion furnaces, it is usually challenging to observe the combustion conditions inside the furnace in real time due to the outer layer of insulation and refractory material. Additionally, limited by the current measurement experimental conditions, using thermocouples for temperature measurement can also affect the combustion conditions inside the furnace, leading to measurement errors. Therefore, in addition to the experimental measurements, it is also necessary to use CFD tools to estimate the actual flow and emission characteristics inside the combustion furnace under different operating conditions [1].

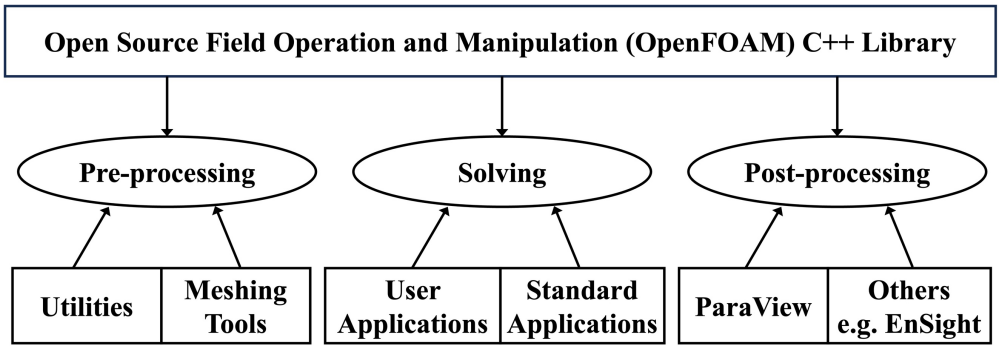

Figure 2.1 Overview of the OpenFOAM structure [2].

Open Field Operation and Manipulation (OpenFOAM) is the largest free open-source software for computational fluid dynamics in the world. It is based on C++ and operates on the Linux platform, using an object-oriented approach. It offers high flexibility and scalability, making it widely used in fluid dynamics and combustion research fields [2]. The overview structure of OpenFOAM is shown in **Fig. 2.1**, which includes not only the computational solving part but also the pre-processing part for mesh generation and the post-processing part for visualization. Therefore, it is very suitable as an effective CFD tool for developing low-NO ammonia co-firing furnaces.

In summary, the numerical analysis part of this study will be based on the OpenFOAM-2.4.0 environment. The governing equations, selection of computational models, and choice of computational parameters in the numerical analysis will be described in detail in this chapter.

2.2 Governing equations

2.2.1 Governing equations for turbulent combustion

In the numerical simulation of a reactive flow containing n_s species, to describe turbulence, it is first necessary to consider the conservation of mass and momentum. In the case of non-adiabatic flow, the conservation of energy equation also needs to be considered. Moreover, because the numerical simulation in the present research also includes combustion reactions, it is necessary to introduce the species conservation equation. The specific forms of the four governing equations are shown below:

(1) Conservation equation of mass:

The mass conservation equation describes the conservation of mass in a fluid, stating that the difference between the mass entering and leaving the control volume equals the rate of change of mass within the control volume, as shown in **Eq. (2.1)**:

$$\frac{\partial(\rho)}{\partial t} + \nabla \cdot (\rho \boldsymbol{u}) = 0 \tag{2.1}$$

where ρ represents the fluid density while t denotes time, and u represents velocity. Since mass does not change during the combustion process, the mass conservation equation for reactive flows is the same as for non-reactive flows.

(2) Conservation equation of momentum:

The momentum conservation equation, also known as the Navier-Stokes (N-S) equations, describes the motion of fluids under the influence of external forces, as shown in **Eq. (2.2)**:

$$\frac{\partial(\rho \boldsymbol{u})}{\partial t} + \nabla \cdot (\rho \boldsymbol{u}\boldsymbol{u}) = \nabla \cdot \boldsymbol{P} + \rho \sum_{k=1}^{n_s} Y_k \boldsymbol{f_k} \tag{2.2}$$

where $\boldsymbol{P}$ denotes the viscous stress tensor following Stokes hypothesis, given by **Eq. (2.3)**. Y_k represents the mass fraction of species k, and f_k is the volume force acting on species k. For most numerical simulations of turbulent flames, volume force can be neglected.

$$\boldsymbol{P} = - p\boldsymbol{I} + \mu[(\nabla \boldsymbol{u}) + (\nabla \boldsymbol{u})^T - \frac{2}{3}(\nabla \cdot \boldsymbol{u})\boldsymbol{I}] \tag{2.3}$$

where μ is the dynamic viscosity of the mixture; $\boldsymbol{I}$ denote the identity tensor.

(3) Conservation equation of species:

The species conservation equation primarily describes the transport and reaction processes of each chemical component in the reactive flow, as shown in **Eq. (2.4)**:

$$\frac{\partial(\rho Y_k)}{\partial t} + \nabla \cdot (\rho \boldsymbol{u} Y_k) = - \nabla \cdot (\rho Y_k \boldsymbol{V_k}) + \dot{\omega}_k \tag{2.4}$$

where $\dot{\omega}_k$ is the mass reaction rate of species k. $\boldsymbol{V_k}$ represents the diffusion velocity of species k. In practical numerical calculations, to avoid the computationally expensive calculation of diffusion velocities, the mixture-averaged model based on Fick's law can be used to simplify the diffusion velocity term, as shown in **Eq. (2.5)** and **Eq. (2.6)**:

$$\boldsymbol{V_k} = - \frac{D_k}{X_k} \nabla X_k \tag{2.5}$$

$$D_k = \frac{1 - Y_k}{\sum_{\mathrm{j} \neq \mathrm{k}} (X_j / D_{kj})} \tag{2.6}$$

where D_k is the mixture-averaged diffusion coefficient of species k. D_{kj} is the binary diffusion coefficient between species k and j, estimated according to the Takahashi correlation [3]. Additionally, to ensure mass conservation, mixture-averaged diffusion formulations should be further constrained by the **Eq. (2.7)**. This is realized by solving the diffusivities independently for the (n_s - 1) species and use the mass conservation identity to determine the diffusion velocity of the last abundant inert species, such as N_2.

$$\sum_{\mathrm{k}=1}^{\mathrm{n_s}} Y_k V_k = 0 \tag{2.7}$$

(4) Conservation equation of energy:

The energy conservation equation describes the transfer and conversion of energy within a fluid, mainly encompassing heat conduction, convection, radiation, and the heat generated by chemical reactions, as shown in **Eq. (2.8)**:

$$\frac{\partial(\rho h_s)}{\partial t} + \nabla \cdot (\rho \boldsymbol{u} h_s) + \frac{\partial(\rho K)}{\partial t} + \nabla \cdot (\rho \boldsymbol{u} K) = \frac{\partial p}{\partial t} + \nabla \cdot \boldsymbol{q} \tag{2.8}$$

where h_s denotes sensible enthalpy, K represents kinematic energy, and $\boldsymbol{q}$ represents heat flux vector. In this study, for the heat flux term, the heat flux effect caused by component concentration gradients (Dufour effect) is ignored, while the effects of heat conduction, mass diffusion of species, and radiation are considered, as shown in **Eq. (2.9)**:

$$\boldsymbol{q} = - \frac{\lambda}{c_p} \nabla h_s + \sum_{\mathrm{k}=1}^{\mathrm{n_s}} (\frac{\lambda}{c_p} - \rho D_k) h_{s,k} \nabla Y_k - \rho \sum_{\mathrm{k}=1}^{\mathrm{n_s}} h_{c,k} D_k \nabla Y_k - \nabla \cdot \boldsymbol{q_r} \tag{2.9}$$

where λ is the mixture thermal conductivity, and c_p denotes the specific heat capacity at constant pressure. $h_{s,k}$ and $h_{c,k}$ represent the sensible and chemical enthalpy of species k, respectively. q_r represents the radiation term.

Finally, since the governing equations contain multiple unknown variables, to close the equations, the density ρ can also be obtained from the ideal gas law, as shown in **Eq. (2.10)**:

$$\rho = \frac{p}{\mathrm{R}^0(\sum_{\mathrm{k}=1}^{\mathrm{n_s}} \frac{Y_k}{W_k})T} \tag{2.10}$$

where $\mathrm{R}^0 = 8.3145$ J/(mol · K) is universal gas constant, and W_k represents the molecular mass of species k.

Additionally, based on the thermodynamic state equation, the relationship between sensible enthalpy h_s and temperature T can be obtained, as shown in **Eq. (2.11)**:

$$h_{s,k} = \int_{T_0}^{T} c_{p,k} \mathrm{d}T \tag{2.11}$$

The heat capacity at constant pressure depends on temperature and is calculated using NASA polynomial approximations based on the JANAF thermochemical tables for high and low temperature ranges, as shown in **Eq. (2.12)**:

$$\frac{c_{p,k}}{\mathrm{R}^0 T} = \mathrm{a}_1 + \mathrm{a}_2 T + \mathrm{a}_3 T^2 + \mathrm{a}_4 T^3 + \mathrm{a}_5 T^4 \tag{2.12}$$

Similarly, the sensible enthalpy h_s can also be obtained from the NASA polynomials:

$$\frac{h_{s,k}}{\mathrm{R}^0 T} = \mathrm{a}_1 + \mathrm{a}_2 \frac{T}{2} + \mathrm{a}_3 \frac{T^2}{3} + \mathrm{a}_4 \frac{T^3}{4} + \mathrm{a}_5 \frac{T^4}{5} + \frac{\mathrm{a}_6}{T} \tag{2.13}$$

With these additional transport equations, the system is closed and can be solved iteratively.

2.2.2 RANS governing equations

As previously mentioned, considering the industrial application context, the present study will use the RANS method for CFD simulations. The core of the RANS method is to decompose instantaneous flow variables (any quantity f) into time-averaged and fluctuating components, as shown in **Eq. (2.14)**:

$$f = \overline{f} + f' \quad \text{with} \quad \overline{f'} = 0 \tag{2.14}$$

However, when performing Reynolds averaging for compressible flows, many unclosed correlations are introduced between the quantity f and its density fluctuation $\rho' f'$. Therefore, another mass-weighted averaging method called Favre averaging, can be used. Similar to Reynolds averaging, any quantity f can be split into a mean (time-averaged) component and a fluctuating component, as shown in **Eq. (2.15)**:

$$f = \tilde{f} + f'' = \frac{\overline{\rho f}}{\bar{\rho}} + f'' \text{ with } \overline{f''} = \frac{\overline{\rho' f}}{\bar{\rho}} \tag{2.15}$$

After applying Favre averaging to the four instantaneous conservation equations discussed in **Sec. 2.2.1**, the RANS transport equations of mass, momentum, chemical species, and enthalpy in the present research are respectively described by **Eqs. (2.16) – (2.19)**:

$$\frac{\partial(\bar{\rho})}{\partial t} + \nabla \cdot (\bar{\rho}\tilde{\boldsymbol{u}}) = 0 \tag{2.16}$$

$$\frac{\partial(\bar{\rho}\tilde{\boldsymbol{u}})}{\partial t} + \nabla \cdot (\bar{\rho}\tilde{\boldsymbol{u}}\tilde{\boldsymbol{u}}) = -\nabla\bar{p} + \nabla \cdot (\bar{\tau} - \bar{\rho}\widetilde{u''u''}) + \bar{\rho}\boldsymbol{g} \tag{2.17}$$

$$\frac{\partial(\bar{\rho}\tilde{Y}_k)}{\partial t} + \nabla \cdot (\bar{\rho}\tilde{\boldsymbol{u}}\tilde{Y}_k) = \nabla \cdot (\bar{\rho}(D_k + D_t)\nabla\tilde{Y}_k) + \overline{\dot{\omega}_k} \tag{2.18}$$

$$\frac{\partial(\bar{\rho}\tilde{h})}{\partial t} + \nabla \cdot (\bar{\rho}\tilde{\boldsymbol{u}}\tilde{h}) + \frac{\partial(\bar{\rho}\tilde{K})}{\partial t} + \nabla \cdot (\bar{\rho}\tilde{\boldsymbol{u}}\tilde{K}) = \frac{\partial\bar{p}}{\partial t} + \nabla \cdot (\frac{\lambda + \lambda_t}{\bar{c}_p}\nabla\tilde{h}) + \overline{\dot{\omega}_T} + \nabla \cdot \overline{\boldsymbol{q}_r} \tag{2.19}$$

where the overbar and tilde symbols signify the Reynolds and Favre averages, respectively; The variable ρ represents the fluid density, while $\boldsymbol{u}$ represents the fluid velocity vector. Additionally, p and $\boldsymbol{g}$ denote the pressure and gravity force, respectively. In the momentum equation, τ is the viscous stress tensor, $\bar{\rho}\widetilde{u''u''}$ denotes Reynolds stress, which needs to be solved based on the turbulence model. The chemical species equation involves Y_k and $\dot{\omega}_k$, referring to the mass fraction and chemical source term (reaction rate) for species k, respectively. D_k and D_t respectively stand for the mass diffusion coefficient and its turbulent part. In **Eq. (2.19)**, the variables h and K stand for the specific sensible enthalpy and kinetic energy, respectively. λ and λ_t represent the molecular thermal conductivity and its turbulent part, while c_p denotes specific heat capacity at the constant pressure. Heat source terms are denoted as $\dot{\omega}_T$ and $\boldsymbol{q_r}$, encompassing contributions from combustion and radiation.

2.3 Calculation models selection

In the discretization of the four governing equations introduced in **Sec. 2.2**, many unknown terms will arise, leading to unclosed equations that cannot be directly solved. Therefore, it is necessary to introduce turbulence models, combustion models, and radiation models in this section to close the corresponding governing equations.

2.3.1 Turbulence model

(a) Standard k-ε model

Based on the Favre-averaged conservation of momentum equation obtained in **Eq. (2.17)**, the Reynolds stress term cannot be directly solved due to the inclusion of fluctuating velocity

components. Therefore, it is necessary to introduce a turbulence model to close the equation. The Standard k-ε (KE) turbulence model is based on the Boussinesq assumption to simplify the Reynolds stress term, as shown in **Eq. (2.20)**:

$$\bar{\rho}\widetilde{u_i'' u_j''} = \mu_t[(\nabla\tilde{\boldsymbol{u}}) + (\nabla\tilde{\boldsymbol{u}})^T - \frac{2}{3}(\nabla\cdot\tilde{\boldsymbol{u}})\boldsymbol{I}] \tag{2.20}$$

where μ_t represents the turbulent viscosity, which is obtained from **Eq. (2.21)**:

$$\mu_t = \bar{\rho}C_\mu\frac{\tilde{k}^2}{\tilde{\varepsilon}} \tag{2.21}$$

The Boussinesq assumption is a useful simplification, reducing the number of unknowns in the Reynolds stress tensor in 3D calculations from six to one (μ_t). This method calculates the turbulent viscosity by introducing the turbulent kinetic energy k and the turbulent dissipation rate ε, thereby closing the Reynolds stress term. The corresponding transport equations for the turbulent kinetic energy and turbulent dissipation rate are given by **Eqs. (2.22)** and **(2.23)**, respectively:

$$\frac{\partial(\bar{\rho}\tilde{k})}{\partial t} + \nabla\cdot(\bar{\rho}\tilde{\boldsymbol{u}}\tilde{k}) = \nabla\cdot((\mu + \frac{\mu_t}{\sigma_k})\nabla\tilde{k}) + P_k - \bar{\rho}\tilde{\varepsilon} \tag{2.22}$$

$$\frac{\partial(\bar{\rho}\tilde{\varepsilon})}{\partial t} + \nabla\cdot(\bar{\rho}\tilde{\boldsymbol{u}}\tilde{\varepsilon}) = \nabla\cdot((\mu + \frac{\mu_t}{\sigma_k})\nabla\tilde{\varepsilon}) + C_{\varepsilon 1}\frac{\tilde{\varepsilon}}{\tilde{k}}P_k - C_{\varepsilon 2}\bar{\rho}\frac{\tilde{\varepsilon}^2}{\tilde{k}} \tag{2.23}$$

where P_k is the turbulence kinetic energy production due to viscous forces, which can be obtained from **Eq. (2.24)**:

$$P_k = -\mu_t[(\nabla\tilde{\boldsymbol{u}}) + (\nabla\tilde{\boldsymbol{u}})^T - \frac{2}{3}(\nabla\cdot\tilde{\boldsymbol{u}})\boldsymbol{I}] : \nabla\tilde{\boldsymbol{u}} - \frac{2}{3}\bar{\rho}\widetilde{k} : \nabla\tilde{\boldsymbol{u}} \tag{2.24}$$

Since Jones and Launder [4] proposed the related turbulence computation model in 1972, the KE model has been widely applied to many scientific and industrial turbulent flows. This method has high computational efficiency and generality but has certain limitations in simulating strongly anisotropic flows [5]. The KE model includes five adjustable model constants with recommended values given by Ref. [6], namely, $C_{\varepsilon 1} = 1.44$, $C_{\varepsilon 2} = 1.92$, $C_\mu = 0.09$, $\sigma_k = 1.0$, and $\sigma_\varepsilon = 1.3$.

(b) Re-Normalization Group k-ε model

The Re-Normalisation Group k-ε (RngKE) model serves as an advanced version of the KE model, characterized by an additional term in its ε equation that improves its accuracy for rapidly strained flows [7]. Although the RngKE model is regarded as more reliable and precise than the KE model, it has not yet gained widespread adoption in practical applications. The

corresponding transport equations for calculating turbulent kinetic energy and turbulent dissipation rate for RngKE model are shown in **Eqs. (2.25)** and **(2.26)**:

$$\frac{\partial(\bar{\rho}\tilde{k})}{\partial t} + \nabla \cdot (\bar{\rho}\tilde{\boldsymbol{u}}\tilde{k}) = \nabla \cdot ((\mu + \frac{\mu_t}{\sigma_k})\nabla\tilde{k}) + P_k - \bar{\rho}\tilde{\varepsilon} \tag{2.25}$$

$$\frac{\partial(\bar{\rho}\tilde{\varepsilon})}{\partial t} + \nabla \cdot (\bar{\rho}\tilde{\boldsymbol{u}}\tilde{\varepsilon}) = \nabla \cdot ((\mu + \frac{\mu_t}{\sigma_k})\nabla\tilde{\varepsilon}) + C_{\varepsilon 1}\frac{\tilde{\varepsilon}}{\tilde{k}}P_k - C_{\varepsilon 2}\bar{\rho}\frac{\tilde{\varepsilon}^2}{\tilde{k}} + R_\varepsilon \tag{2.26}$$

where the main difference between the RngKE model and KE model lies in the additional term R_ε in the turbulent dissipation rate equation and is given by **Eq. (2.27)**:

$$R_\varepsilon = \frac{C_\mu \bar{\rho}\eta^3(1 - \eta/\eta_0)}{1 + \beta\eta^3}\frac{\tilde{\varepsilon}^2}{\tilde{k}} \tag{2.27}$$

$$\eta = \frac{\tilde{k}}{\tilde{\varepsilon}}[\frac{1}{2}(\nabla\tilde{\boldsymbol{u}} + (\nabla\tilde{\boldsymbol{u}})^T) : (\nabla\tilde{\boldsymbol{u}} + (\nabla\tilde{\boldsymbol{u}})^T)]^{0.5} \tag{2.28}$$

The model constants for the RngKE model used by default and are given as $C_{\varepsilon 1}$ = 1.42, $C_{\varepsilon 2}$ = 1.68, C_μ = 0.0845, η_0 = 4.38, β = 0.012, C_μ = 0.0845, σ_k = 0.72, and σ_ε = 0.72 [8].

(c) Reynolds stress equation model

The Reynolds Stress Model (RSM) is a classic turbulence model consisting of three variants. In this study, the LRR-IP model (hereafter abbreviated as LRR model), developed by Launder et al. [9], will be applied. Unlike the KE and RngKE model, the LRR turbulence model abandons the isotropic eddy-viscosity hypothesis and solves transport equations for the Reynolds stresses, along with an equation for the turbulent dissipation rate, to close the RANS equations. Therefore, in 2D flows, five additional transport equations are required compared to seven in 3D flows. The equations of the LRR model are expressed as follows:

$$\frac{\partial(\bar{\rho}\widetilde{u_i''u_j''})}{\partial t} + \nabla \cdot (\bar{\rho}\tilde{\boldsymbol{u}}\widetilde{u_i''u_j''}) = P_{ij} - \frac{2}{3}\delta_{ij}\bar{\rho}\tilde{\varepsilon} + \phi_{ij} + P_{ij,b} + \nabla \cdot ((\mu + \frac{2}{3}C_s\bar{\rho}\frac{\tilde{k}^2}{\tilde{\varepsilon}})\nabla\widetilde{u_i''u_j''}] \tag{2.29}$$

$$\frac{\partial(\bar{\rho}\tilde{\varepsilon})}{\partial t} + \nabla \cdot (\bar{\rho}\tilde{\boldsymbol{u}}\tilde{\varepsilon}) = \nabla \cdot ((\mu + \frac{\mu_t}{\sigma_t})\nabla\tilde{\varepsilon}) + C_{\varepsilon 1}\frac{\tilde{\varepsilon}}{\tilde{k}}P_k - C_{\varepsilon 2}\bar{\rho}\frac{\tilde{\varepsilon}^2}{\tilde{k}} \tag{2.30}$$

where $P_{ij,b}$ denote the production due to the buoyancy; P_{ij} is the turbulence production term. Φ_{ij} is the pressure-strain correlation influencing the Reynolds stresses redistribution. Detailed expressions of the LRR model can be found in Ref. [10,11].

The default values of the model constants $C_{\varepsilon 1}$ and $C_{\varepsilon 2}$ are 1.44 and 1.92, respectively. Notably, the value of $C_{\varepsilon 1}$ is reported in the literature within the range of 1.44 - 1.5. In the present study, $C_{\varepsilon 1}$ is adjusted to 1.48 and its influence is discussed, with an ultimate aim of identifying the

optimal value for accurate prediction.

2.3.2 Combustion model

According to the Arrhenius law, chemical reaction rates are highly non-linear. Therefore, the average chemical reaction rate cannot be directly obtained from average quantities (such as species mass fractions, temperature, as well as density) and requires closure based on a turbulence combustion model for the chemical source term in the RANS species transport **Eq. (2.18)**. The solver used in this study will introduce two combustion models, the Eddy Dissipation Concept (EDC) and the Partially Stirred Reactor (PaSR), to explore their accuracy in numerical predictions. This section will briefly introduce the numerical computation approaches of these two models.

(a) Eddy dissipation concept

The EDC model was first proposed by Magnussen [12] in 1981 and has been widely applied in turbulent combustion simulations. Compared to more complex methods, such as the conditional moment closure and the transported PDF methods, this model can introduce detailed reaction kinetics parameters at a relatively low computational cost [13]. In the concept of the EDC model, combustion reactions are assumed to occur in small regions of the flow where the dissipation of turbulence kinetic energy takes place, known as fine structures. The fine structures are assumed to be isobaric and adiabatic perfectly stirred reactors. Therefore, the mean cell reaction rate of species k in the transport **Eq. (2.18)** can be obtained according to **Eqs. (2.31)** and **(2.32)**:

$$\overline{\dot{\omega}_k} = \frac{\bar{\rho}(\xi^*)^2}{1 - (\xi^*)^3}\frac{(Y_k^* - \widetilde{Y}_k)}{\tau^*} \tag{2.31}$$

$$\widetilde{Y}_k = (\xi^*)^3 Y_k^* + [1 - (\xi^*)^3]Y_k^0 \tag{2.32}$$

where Y_k^* is the mass fraction of species k in the fine structures; Y_k represents the mean mass fraction of the kth species between the fine structures and the surrounding state (denoted as Y_k^0). ξ^* represents the volume fraction of the fine structures, and τ^* represents the characteristic time of the fine structures. These two characteristic variables of the fine structures can be described based on the energy cascade model [14], given by **Eqs. (2.33)** and **(2.34)**:

$$\xi^* = (\frac{3C_{D2}}{4C_{D1}^2})^{0.25}(\frac{\upsilon\tilde{\varepsilon}}{\tilde{k}^2})^{0.25} = C_\xi(\frac{\upsilon\tilde{\varepsilon}}{\tilde{k}^2})^{0.25} \tag{2.33}$$

$$\tau^* = (\frac{C_{D2}}{3})^{0.5}(\frac{\upsilon}{\tilde{\varepsilon}})^{0.5} = C_\tau(\frac{\upsilon}{\tilde{\varepsilon}})^{0.5} \tag{2.34}$$

where υ is the kinematic viscosity; k and ε represent the turbulent kinetic energy and turbulent dissipation rate, respectively. C_{D1} and C_{D2} are model constants fixed to 0.134 and 0.5, respectively, from which the volume fraction as well as the characteristic time constants C_ξ = 2.1377 and C_τ = 0.4082 of the fine structures can be obtained [15].

(b) Partially stirred reactor model

The PaSR combustion model is similar to the EDC model in the computational approach. In this model, each computational cell is divided into two regions: a reactive zone and a non-reactive region [16]. Therefore, the mean cell reaction rate of species k in the transport equation is obtained based on the mass exchange between these two regions, as shown in **Eq. (2.35)**:

$$\overline{\dot{\omega}_k} = \kappa \frac{\overline{\rho}(Y_k^* - Y_k^0)}{\tau^*} \tag{2.35}$$

where Y_k^0 and Y_k^* represent the mass fractions of species k in the non-reactive region and the reactive zone, respectively. τ^* represents the residence time in the reactive structure. The parameter κ is the volume fraction of the reactive zone and thus provides the partially stirred condition. This parameter can be expressed as the ratio of the chemical time scale τ_c to the sum of the chemical time scale and the mixing time scale ($\tau_c + \tau_{mix}$), as shown in **Eq. (2.36)**:

$$\kappa = \frac{\tau_c}{\tau_c + \tau_{mix}} \tag{2.36}$$

In order to get the value of Y_k^* in **Eq. (2.35)**, a time-splitting approach is used. This method models the reaction region as an ideal reactor (such as the perfectly stirred reactor) and obtains Y_k^* based on Y_k^0 during the residence time τ^*, as indicated in **Eq. (2.37)**:

$$\frac{\mathrm{d}Y_k^*}{\mathrm{d}t} = \frac{\dot{\omega}_k^*}{\overline{\rho}} \tag{2.37}$$

where the term $\dot{\omega}_k^*$ is the instantaneous formation rate of species k. Finally, integrating ($\mathrm{d}Y_k^*/\mathrm{d}t$) with the residence time gives the value of Y_k^*. The residence time τ^* is considered to be the mixing time scale and is also the time over which the ideal reactor is integrated [16,17]. In the present study, this value is chosen as the minimum of the chemical time scale τ_c and the mixing time scale τ_{mix}.

Thus, for the computation based on the PaSR combustion model, only the chemical time scale and the mixing time scale remain unknown. The selection of these two values is also crucial for the accurate prediction. Currently, various methods have been proposed in different papers to estimate these two items [16,18]. In this study, for the chemical time scale, the approach based on the species formation rates by considering the slowest chemical time scale

as the leading one is chosen [19], as shown in **Eq. (2.38)**:

$$\tau_c = \max\left(\frac{Y_k^*}{|\,\mathrm{d}Y_k^*/\mathrm{d}t\,|}\right) \tag{2.38}$$

For the mixing time scale, it is given by **Eq. (2.39)**:

$$\tau_{mix} = C_{mix}\frac{\tilde{k}}{\tilde{\varepsilon}} \tag{2.39}$$

where k is the turbulent kinetic energy, ε is the turbulent dissipation rate, and C_{mix} denotes the mixing constant, ranging from 0.001 to 0.3, In this study, the value is chosen as 0.15. Similar to the EDC model, the PaSR model also provides fast computational speeds in numerical analysis and is widely applied in industrial analysis. Moreover, since the model considers both mixing and chemical time scales, it is suitable for various reactive flows without needing to pre-identify the type of reactive flow [20].

2.3.3 Radiation model

Radiative heat transfer is a crucial factor in turbulent combustion systems, serving as the primary energy transfer mechanism in high-temperature devices. For example, research by Tessé et al. [21] has demonstrated that turbulence-radiation interactions can significantly increase radiative heat loss, accounting for approximately 30% of the total chemical heat release. Radiative heat transfer directly affects the temperature field, consequently affecting chemical kinetics, most notably the formation of thermal NO, which exhibits high sensitivity to temperature variations. Therefore, implementing an accurate radiation model is essential, especially in the context of industrial applications.

In the present study, the Weighted-Sum-of-Gray-Gases (WSGG) model is used to solve the radiation term in the energy equation for the non-gray gas radiative properties [22]. The Finite Volume Discrete Ordinates Method (fvDOM) is adopted to solve the different gray gas Radiative Transport Equations (RTEs) in the WSGG model [23]. Since the subject of this study is the gas mixture, scattering is typically negligible; hence the RTE adopted in this study only accounts for the radiation attenuation and augmentation due to absorption and emission, respectively. The simplified RTE equation is formulated in **Eq. (2.40)**:

$$\frac{\mathrm{d}I_\eta}{\mathrm{d}s} = -\kappa_\eta I_\eta + \kappa_\eta I_{b\eta} \tag{2.40}$$

where I_η is the spectral radiative intensity at wavenumber η and along the path length s; $I_{b\eta}$ is the Planck blackbody spectral radiation intensity, and κ_η is the spectral absorption coefficient of the medium. This parameter is strongly dependent on the wavenumber and contain thousands

or even millions of spectral lines for participating gases. Solving for all spectral lines is very time-consuming, as such, the WSGG model has been developed to solve the RTE quickly [23].

In the WSGG model, the entire spectrum is replaced by several independent gray gases. Each gray gas j has a unique absorption coefficient κ_j and is assumed to occupy a fixed, yet mostly non-contiguous, portion of the spectrum. These parameters are established such that the total emittance of the real gas can be approximated by the weighted sum of the fictitious grey gases [24,25]. Under the application of the WSGG model, the RTE for each gray gas needs to be solved, as shown in **Eq. (2.41)**:

$$\frac{\mathrm{d}I_j}{\mathrm{d}s} = -\kappa_j I_j + \kappa_j a_j(T) I_b(T) \tag{2.41}$$

where I_j represents the local intensity associated with gray gas j, while $I_b(T)$ represents the total blackbody radiation intensity related to the local temperature; $\alpha_j(T)$ is an emission weighted factors representing the fraction of blackbody energy that lies within the portion of the radiation spectrum occupied by gas j [26].

However, the above RTE applies only to instantaneous quantities fluctuating in turbulence, while the RANS turbulence model can only provide time-averaged quantities and possibly their mean square fluctuations [27]. Therefore, in RANS simulations, considering the spectrally integrated form of the RTE and time averaging, the WSGG model in **Eq. (2.41)** can be written as:

$$\frac{\mathrm{d}\overline{I_j}}{\mathrm{d}s} = -\overline{\kappa_j I_j} + \overline{\kappa_j a_j I_b} \tag{2.42}$$

Solving the above RTE equation allows for solving the radiation source term in the energy conservation, as shown in **Eq. (2.43)**:

$$\nabla \cdot \overline{\boldsymbol{q_r}} = 4\pi \overline{\kappa_p(\varphi) I_b(T)} - \sum_{\mathrm{j}=0}^{\mathrm{N}} \overline{\kappa_j G_j} \tag{2.43}$$

where κ_p is the Planck mean radiative absorption coefficient, and the scalar quantities that affect the radiative absorption coefficient are represented by φ, as shown in **Eq. (2.44)**. G_j is the direction-integration incident radiation for the grey gas j, as shown in **Eq. (2.45)**:

$$\kappa_p = \sum_{\mathrm{j}=0}^{\mathrm{N}} (\kappa_j a_j) \text{ with } \varphi = [T, X_{CO_2}, X_{H_2O}, p]^T \tag{2.44}$$

$$G_j = \int_{4\pi} I_j \, \mathrm{d}\Omega \tag{2.45}$$

This section provides a brief overview of the combined fvDOM and WSGG radiation model. For a more detailed solution of the radiation source term in the RANS equations, readers are recommended to refer to the work by Modest and Haworth [28].

2.4 Conjugate heat transfer method

As mentioned in **Sec. 1.3.2**, in numerical analysis of the combustion furnaces, achieving a precise estimation of the thermal boundary conditions at the furnace walls is a crucial factor that significantly influences the accurate prediction of temperature and species distributions. Among the existing methods describing the thermal boundary conditions of furnace walls, the Conjugate Heat Transfer (CHT) method is receiving more attention. It considers the thermal interactions between the fluid and solid domains, offering a more realistic approach compared to other traditional methods that assume constant wall temperatures or heat flux densities [29]. The accuracy of this method in the numerical prediction of combustion furnaces has also been validated in the related work by Xie et al. [30]. Consequently, in the numerical analysis of ammonia combustion furnaces conducted in the present research, the CHT method has been incorporated into the developed solver. This integration aims to describe the thermal boundary conditions more accurately, thereby enhancing the prediction accuracy of the combustion process within the furnace.

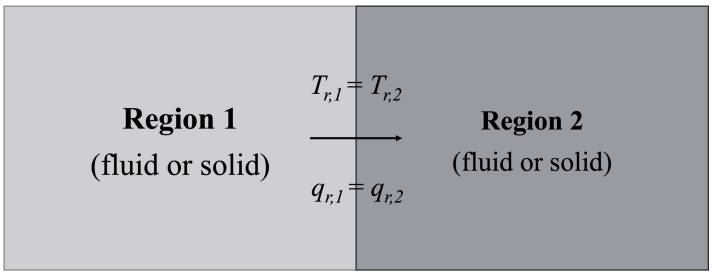

Figure 2.2 Thermal boundary setting at the fluid-solid interface (temperature and heat flow density).

As for the governing equations in the solid domain, only energy transfer needs to be resolved. Since there is no fluid flow within the solid region, the density of the solid remains constant. Therefore, the enthalpy equation can be simplified to a conduction equation without any source terms, as illustrated in **Eq. (2.46)**:

$$\frac{\partial(\bar{\rho}\tilde{h})}{\partial t} = \nabla \cdot (\lambda_s \nabla T_s) \tag{2.46}$$

where λ_s represents the thermal conductivity of the solid region. T_s signifies the temperature of the solid. For the interface between different computational domains, whether fluid-solid or solid-solid, two sets of computational conditions need to be added [31,32]. The first condition

enforces the equality of temperatures at the interface, ensuring thermal continuity between the two regions. The second condition mandates the equivalence of heat flux originating from one side and entering the other region, as demonstrated in **Eqs. (2.47)** and **(2.48)**:

$$T_{region1,\ int} = T_{region2,\ int} \tag{2.47}$$

$$\lambda_{region1} \frac{\partial T_{region1}}{\partial n} = \lambda_{region2} \frac{\partial T_{region2}}{\partial n} \tag{2.48}$$

2.5 Reaction mechanism

Since ammonia has recently begun to be viewed as a potential carbon-free fuel, research on ammonia reaction mechanisms is relatively sparse compared to studies on hydrogen or methane [33]. The earliest studies on ammonia chemical reaction mechanisms can be traced back to 1983 when Miller et al. [34] proposed the first ammonia oxidation kinetics model. Since then, numerous reaction mechanisms related to ammonia combustion have gradually been developed. **Table 2.1** summarizes some of the common chemical reaction mechanisms related to ammonia combustion, organized in chronological order. These mechanisms are mostly validated and evaluated based on parameters such as laminar burning velocity, ignition delay time, flame structure, and NO formation during the ammonia combustion process.

As observed in **Table 2.1**, most currently developed reaction mechanisms focus on the chemical reactions in ammonia/air combustion, with relatively few addressing ammonia/hydrocarbon fuel co-combustion. In 2018, Okafor et al. [35], based on the GRI-Mech 3.0 [36] and the reaction mechanism by Tian et al. [37], proposed a detailed reaction mechanism applicable to ammonia/hydrocarbon fuel co-combustion. This reaction mechanism includes 59 species and 356 elementary reactions, making it suitable in terms of the computational cost. It has been validated for CH_4/NH_3 combustion as well as for ammonia combustion and is capable of accurately capturing the laminar flame speed, ignition time, and emission characteristics at elevated temperatures [38]. Therefore, all calculations in the present study employed the Okafor detailed reaction mechanism.

Additionally, to explore the acceleration capabilities of the integrated acceleration strategy employed in this study for larger reaction mechanisms, in the 3D calculations related to the ammonia co-combustion furnace, a comparison was made between the Okafor detailed reaction mechanism and the detailed reaction mechanism proposed by Sako et al. [39]. The Sako reaction mechanism is based on the nitrogen element-tracking method suitable for ammonia/methane co-combustion, which also allows for the analysis of NO formation sources during the reaction process. This mechanism includes 90 species and 607 sub-reactions and

holds significant relevance for the combustion analysis of industrial furnaces.

Table 2.1 Summary of chemical reaction mechanisms for ammonia-based combustion in published studies.

Reaction mechanism	Year	Number of species/reactions	Mixture composition
Miller et al. [34]	1983	22 species, 98 reactions	NH_3/O_2, $NH_3/H_2/O_2$
Lindstedt et al. [40]	1993	21 species, 95 reactions	$NH_3/H_2/O_2/N_2$
Coppens et al. [41] (Konnov_v0.5 detailed mechanism)	2007	127 species, 1200 reactions	H/C/N/O
Tian et al. [37]	2009	84 species, 703 reactions	$NH_3/CH_4/O_2/Ar$
Song et al. [42]	2016	34 species, 204 reactions	NH_3/air
Nakamura et al. [43]	2017	38 species, 232 reactions	NH_3/air
Okafor et al. [35] (Okafor detailed)	2018	59 species, 356 reactions	NH_3/CH_4/air
Otomo et al. [44]	2018	33 species, 213 reactions	NH_3/air, NH_3/H_2/air
Okafor et al. [45] (Okafor reduced)	2019	42 species, 130 reactions	NH_3/CH_4/air
Mei et al. [46]	2019	38 species, 265 reactions	$NH_3/H_2/N_2$/air
C1-C3 + NOx mechanism [47]	2019	159 species, 2459 reactions	$NH_3/CH_4/O_2/N_2$
Stagni et al. [48]	2020	31 species, 203 reactions	NH_3/air
Cai et al. [49]	2022	20 species, 89 reactions	NH_3/air, NH_3/H_2/air
Sako et al. [39]	2024	90 species, 607 reactions	NH_3/CH_4/air

2.6 Integrated acceleration strategy

As outlined in the introduction, when dealing with finite-rate chemistry problems, the computational challenges predominantly stem from three factors: the size of the reaction mechanism, the load imbalance issue in multi-processor applications, and the grid dimensions. The present study addresses these challenges by introducing an integrated acceleration strategy that incorporates the SpeedCHEM chemistry solver, Dynamic Load Balancing (DLB) code, Open Multi-Processing (OpenMP) method, and Local Time Stepping (LTS) scheme, as illustrated in **Fig. 2.3**. The implementation details of the different acceleration strategies will be presented in this section.

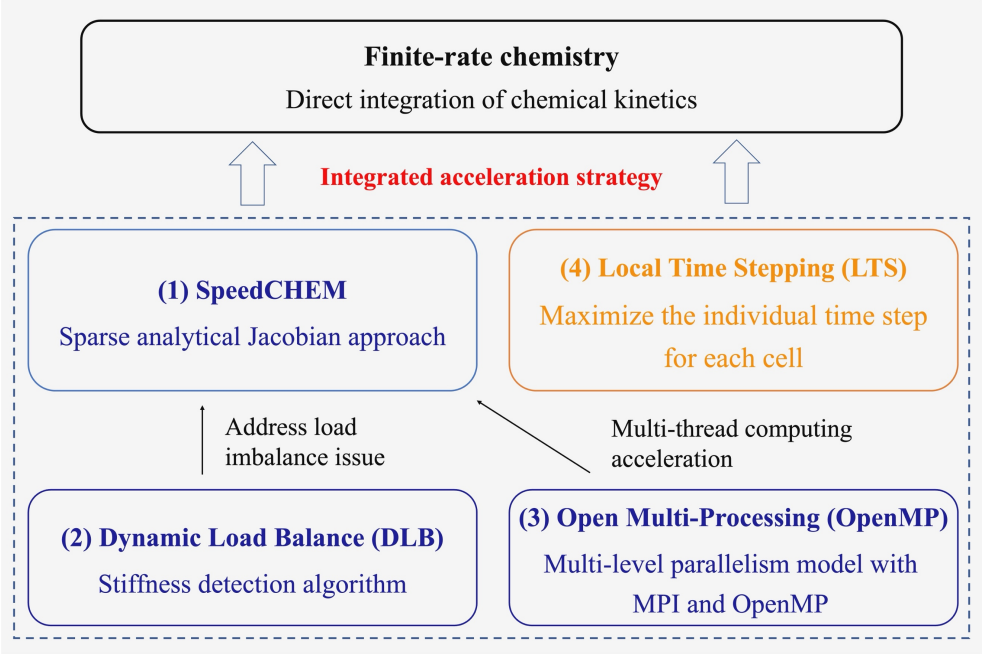

Figure 2.3 Schematic diagram of the integrated acceleration strategy applied in the present thesis.

2.6.1 SpeedCHEM chemistry solver

In the numerical calculation of reactive flows, to mitigate the computational demands associated with utilizing a detailed reaction mechanism, the present research introduced the SpeedCHEM chemistry library and adopted the Livermore Solver for Ordinary Differential Equations with Sparse Jacobian matrix (LSODES) as the ODE solver. This chemistry code, initially developed by Perini et al. [50], is written in the Fortran language. It utilizes a sparse analytical formulation for all chemical and thermodynamic functions involved in depicting the reacting system. This approach significantly reduces computational and storage requirements, thereby enhancing computational efficiency. The advantages of this method become more apparent as the size of the reaction mechanism increases [51].

In the calculation of chemical kinetics, the time evolution of an adiabatic, constant volume, homogeneous gas-phase chemically reacting environment is considered, whose solution is given throughout the integration of a system of ordinary differential equations. The independent variables are the species mass fractions and the average system temperature, as shown in **Eqs. (2.49)** and **(2.50)**:

$$\frac{\mathrm{d}Y_k}{\mathrm{d}t} = \frac{W_k}{\rho}\sum_{i=1}^{n_r}(\nu'_{i,k} - \nu''_{i,k})\,Q_i, \quad k = 1, \ldots, n_s \tag{2.49}$$

$$\frac{\mathrm{d}T}{\mathrm{d}t} = -\frac{1}{\bar{c}_v}\sum_{i=1}^{n_s}\left(\frac{U_k}{W_k}\frac{\mathrm{d}Y_k}{\mathrm{d}t}\right) \tag{2.50}$$

wherein the reaction mechanism is delineated by a set of n_r reactions involving a total of n_s chemical species. Y_k and W_k respectively denote the mass fraction and molecular weight of species k. v' and v'' represent the stoichiometric coefficients of reactants and products before and after different chemical reactions, respectively. Q_i signifies the reaction rates of the progress variable, which typically depend on the temperature T and the species mass fractions of the involved species. c_v represents the mass average mixture specific heat at constant volume, and $U_k = U_k(T)$ are the molar internal energies of the species at temperature T.

$$\mathrm{J} = \begin{array}{|c|c|} \hline \textcircled{4}\ \dfrac{\partial \dot{T}}{\partial T} & \dfrac{\partial \dot{T}}{\partial Y_j}\ \textcircled{2} \\ \hline \dfrac{\partial \dot{Y}_k}{\partial T}\ \textcircled{3} & \dfrac{\partial \dot{Y}_k}{\partial Y_j}\ \textcircled{1} \\ \hline \end{array}$$

Figure 2.4 Structure of the Jacobian matrix for the chemical kinetics ODE system [50].

Figure 2.4 presents the structure of the Jacobian matrix for the chemical kinetics of the ODE system. The matrix elements represent different partial derivatives related to species mass fractions and temperature changes, reflecting the coupling between variables in the system. The first part indicates the derivatives of the rate of change of species mass fraction with respect to other species mass fractions. This represents the interaction between different species due to chemical reactions. This part of the matrix is often sparse in reaction networks, as not all species are directly involved in every reaction. Part 2 illustrates how changes in species mass fractions affect the rate of temperature change. Parts 3 and 4 represent the impact of temperature on the rate of change of species mass fractions and the self-coupling of the temperature rate of change concerning temperature, respectively. In the SpeedCHEM chemistry solver, these four sections are solved as outlined in **Eqs. (2.51) – (2.54)**:

$$J_{k+1,\,j+1} = \frac{\partial}{\partial Y_k}\left(\frac{\mathrm{d}Y_k}{\mathrm{d}t}\right) = \frac{W_k}{\rho}\sum_{i=1}^{n_r}\left(v_{i,k}\frac{\partial Q_i}{\partial Y_k}\right) \tag{2.51}$$

$$J_{1,j+1} = \frac{\partial}{\partial Y_k}\left(\frac{\mathrm{d}T}{\mathrm{d}t}\right) = -\frac{1}{\bar{c}_v}\left[\frac{C_{v,k}}{W_k}\frac{\mathrm{d}T}{\mathrm{d}t} + \sum_{k=1}^{n_s}\frac{U_k}{W_k}\frac{\partial}{\partial Y_k}\left(\frac{\mathrm{d}Y_k}{\mathrm{d}t}\right)\right] \tag{2.52}$$

$$J_{j+1,1} = \frac{\partial}{\partial T}\left(\frac{\mathrm{d}Y_j}{\mathrm{d}t}\right) = \frac{W_k}{\rho}\sum_{i=1}^{n_r} v_{i,k}\frac{\partial Q_i}{\partial T} \tag{2.53}$$

$$\frac{\partial}{\partial T}\left(\frac{\mathrm{d}T}{\mathrm{d}t}\right) = -\frac{1}{\bar{c}_v}\left\{\frac{\mathrm{d}T}{\mathrm{d}t}\frac{\partial c_v}{\partial T} + \sum_{i=1}^{n_r}\left[\frac{1}{W_k}\left(C_{v,k}\frac{\mathrm{d}Y_k}{\mathrm{d}t} + U_k J_{j+1,1}\right)\right]\right\} \tag{2.54}$$

where $v_{i,k} = v''_{i,k} - v'_{i,k}$, and Q_i signifies the reaction rates of the progress variable.

Because only a limited number of species significantly affect the effective molecularity in third-body and pressure-dependent reactions, the Jacobian matrix can be made sparse by storing and computing only the non-zero elements related to these influential species. Consequently, in the SpeedCHEM chemistry solver, an approximation is introduced for constant-volume systems, assuming negligible partial derivatives of total concentration concerning certain species. This assumption further enhances sparsity without compromising the accuracy of the ODE solution. This approach enables the Jacobian matrix to be represented in a much sparser form, effectively reducing computational complexity and improving efficiency, which is especially beneficial for large-scale systems with numerous species and reactions. The approximation minimally impacts integration results, as commonly used stiff ODE solvers typically reuse the Jacobian matrix across Newton iteration steps, thereby maintaining stable and accurate solutions. Further details about this chemistry solver can be found in Ref. [50].

2.6.2 Dynamic load balancing

To mitigate load imbalance issues in multi-processor applications, this study introduced a dynamic load balancing code into the developed solver. The DLB framework has been extensively discussed in previous literature, manifesting numerous diverse variants [52–54]. In the current investigation, the reference point is the DLBFoam solver recently developed by Tekgül et al. [52], as highlighted in **Fig. 2.5**.

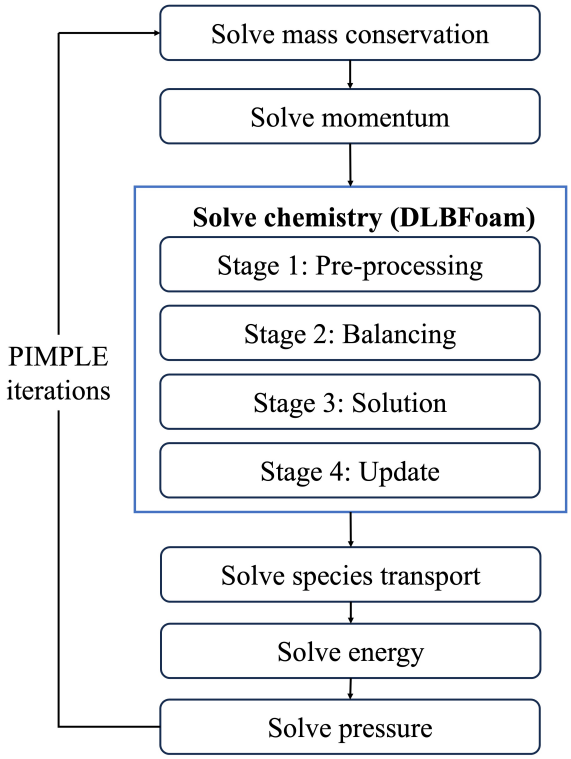

Figure 2.5 Schematic diagram of the main steps of the reactive solver within a single CFD time step (the dynamic load balancing part is highlighted in the blue box) [52].

In multi-processor reactive CFD simulations, the process with the highest computational load will take longer to compute compared to other processes. For instance, as illustrated in **Fig. 2.6(a)**, processor (22) consumes more chemistry computation time in each CFD time step, thereby affecting overall computational efficiency. During the implementation of the DLB code, it employs Message Passing Interface (MPI) routines to redistribute the computational load of chemistry calculations more evenly across processors during the simulation, specifically by transferring some of the chemical problems from overloaded processors to less occupied ones to achieve a more uniform load balance [55]. By controlling the load balance during the computational process, this method can effectively enhance computational efficiency, as shown in **Fig. 2.6(b),** where the computation time for each processor is more evenly distributed.

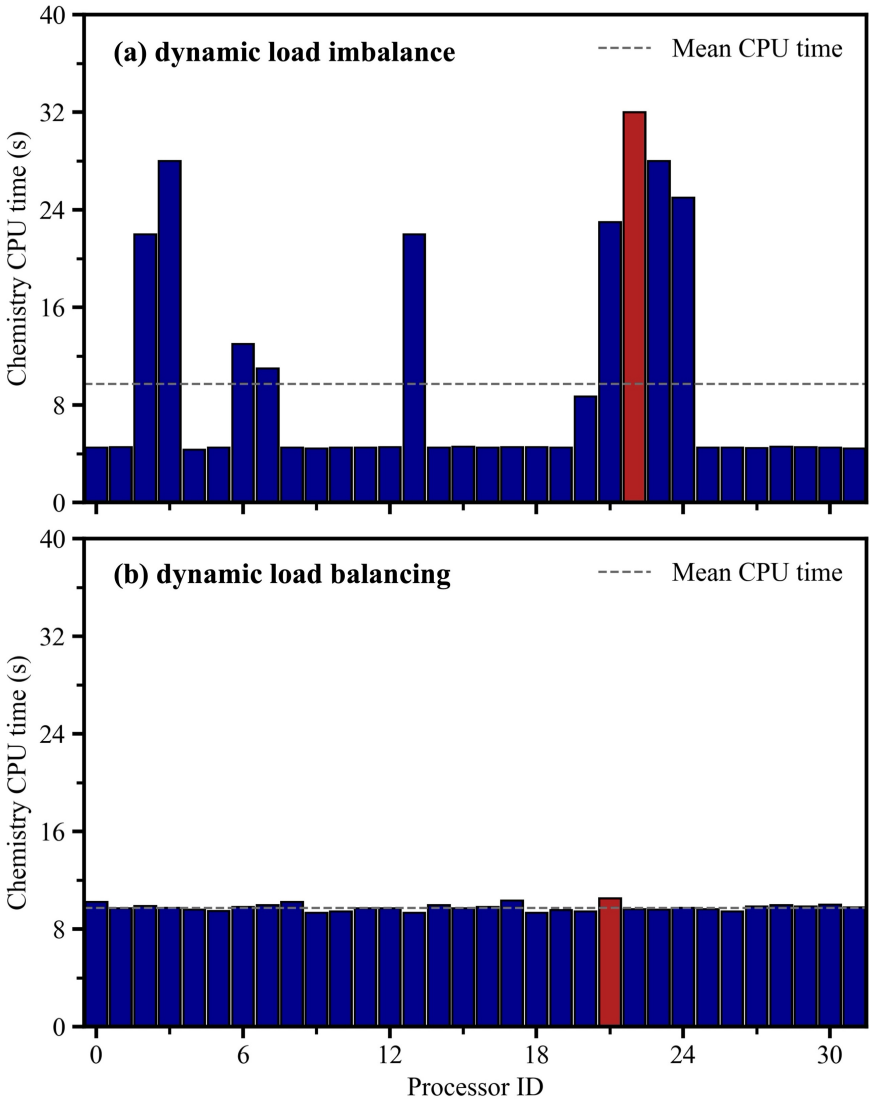

Figure 2.6 An illustration of (a) the computational imbalance and (b) dynamic load balance in reactive CFD simulation

2.6.3 Open multi-processing method and local time stepping scheme

To further enhance the numerical computation capability and convergence speed of the developed solver, two additional acceleration strategies were introduced in the present research. First, the OpenMP technique was incorporated as a means to augment the efficiency of parallel execution through multi-threading for chemical source terms, as shown in **Fig. 2.7**. This approach was motivated by the observation that, while the application of Message Passing Interface (MPI) parallelism can improve computational efficiency in CFD calculations, for some large-scale computational demands, an excessive number of MPI ranks might lead to significant increases in communication bottlenecks between different processors [56]. This scenario can prevent achieving perfect speed-up and might even negatively impact computational efficiency. Therefore, the application of the OpenMP method has the potential

to reduce the need for excessive domain partitioning in high-performance computing environments, offering a strategic complement to MPI parallelism by optimizing parallel execution within shared memory architectures.

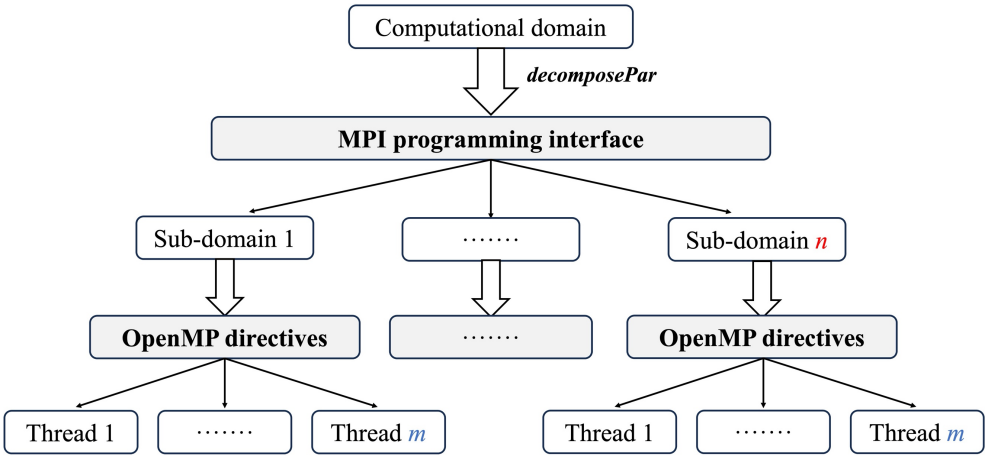

Figure 2.7 The hybrid parallelization strategy (MPI × OpenMP) for the OpenFOAM-based solver [57].

Lastly, the LTS scheme was integrated into the computational framework. This strategy allows for maximizing the individual time step for each computational cell based on the local Courant-Friedrichs-Lewy (CFL) number (for the fluid region) and diffusion number (for solid regions). The LTS method is particularly effective under conditions where significant variations in reactive flow characteristics occur, such as during ignition or at the early stages of reaction. By setting different stability constraints (time steps) according to the reactive characteristics of the mesh, this method effectively prevents a small portion of the grid from imposing a restrictive time step on the entire computational domain [58]. Consequently, this approach reduces the total number of function evaluations, thereby accelerating the overall convergence speed of the simulation. For specific applications of the LTS method, readers are also recommended to refer to the work by Becker [59].

2.7 Implementation details

After introducing the computational model and integrated acceleration strategy used in the present study, the following chapters will explore the computational performance of the solver and the accuracy of the model in predictions. In this study, numerical simulations were conducted on the OpenFOAM platform to address the coupling of flow, combustion, thermodynamics, and heat transfer. The solver used the Pressure-Implicit with Splitting of Operators (PISO) algorithm for pressure-velocity coupling. All governing equations and species transport equations were discretized using a second-order scheme. Convergence criteria

were established to ensure residuals were less than 10^{-6}.

In analyzing the computational performance of the integrated acceleration strategy, four different models were used for performance benchmarking: (1) the numerical Jacobian computation based on the LSODES solver (hereafter referred to as Standard); (2) the Standard model with DLB code (Standard + DLB); (3) the introduction of the SpeedCHEM chemistry solver with DLB code (SpeedCHEM + DLB); (4) the introduction of OpenMP parallel computing strategy based on the third model (SpeedCHEM + DLB + OpenMP). Furthermore, it is noteworthy that, in comparing the acceleration capabilities of these four models, the computational time step for all grids was fixed at 10^{-6} s to ensure uniformity and thus exclude the influence of the LTS method from this comparison. However, in practical scenarios, applying the LTS method can reduce the time required for computational convergence. Thus, faster convergence capabilities of the developed solver can be anticipated.

In this thesis, computational performance analysis was conducted for both the 2D Sandia flames D-F and the 3D 10-kW ammonia co-combustion furnace. For each case, the integrated method were first used to solve the full-scale combustion problem. Then, a time interval considered computationally challenging, for example, where the chemistry ODE problem is stiff in parts of the domain due to ignition, was selected, and 1000 iterations were conducted using the aforementioned four models. During the calculations, the absolute and relative tolerances of the chemistry ODE solver were set to 10^{-10} and 10^{-5}, respectively [52,55].

Finally, the numerical computation work and all performance comparison tasks in this study were carried out using the SQUID supercomputer at the Cybermedia Center at Osaka University. SQUID includes 1520 general-purpose CPU nodes, each equipped with two 38-core 2.4 GHz Intel Xeon Platinum 8368 CPUs. All nodes are interconnected using Mellanox InfiniBand HDR technology with 200 GB/s links [60].

2.8 Summary

This chapter, as the simulation theoretical introduction section of the thesis, describes the details of numerical computation models and the integrated acceleration strategy adopted in this research.

Regarding the selection of numerical computation models, this chapter introduces three turbulence models: KE, RngKE, and LRR. The EDC and PaSR models for the combustion model are discussed. In pursuit of a more precise prediction of temperature distribution and an enhancement in the predictive accuracy of radiative heat transfer, the fvDOM method combined with the WSGG absorption model was utilized. In the simulation of the 3D ammonia co-

combustion furnace, the CHT method was incorporated into the developed solver to more accurately describe the thermal boundary conditions of furnace walls. Lastly, regarding the selection of reaction mechanisms, this thesis will discuss the numerical analysis results based on the Okafor detailed reaction mechanism and the Sako reaction mechanism.

On the other hand, to address the computational challenges posed by the introduction of detailed reaction mechanisms and solid domain calculations, a novel integrated acceleration strategy was developed to enhance the computational efficiency of the solver. This strategy includes four key improvements: the implementation of a sparse analytical Jacobian approach using the SpeedCHEM chemistry library to enhance the efficiency of chemistry ODE solution routines; the utilization of the DLB code for even redistribution of the computational load for chemistry across multiple processes; the incorporation of the OpenMP method to improve parallel computing efficiency; and the integration of the LTS scheme to maximize the time step for each computational cell. Based on the computational models and integration acceleration strategy presented in this chapter, a fast, stable, and accurate solver for reactive flow simulations can be anticipated.

References

[1] A. Valera-Medina, M.O. Vigueras-Zuniga, H. Shi, S. Mashruk, M. Alnajideen, A. Alnasif, J. Davies, Y. Wang, X. Zhu, W. Yang, Y.B. Cheng, Ammonia combustion in furnaces: A review. *International Journal of Hydrogen Energy*, 2024, 49: 1597–1618.

[2] C.J. Greenshields, OpenFOAM User Guide: Version 8. *The OpenFOAM Foundation*, 2020, available from: https://doc.cfd.direct/openfoam/user-guide-v8/.

[3] T. Li, J. Pan, F. Kong, B. Xu, X. Wang, A quasi-direct numerical simulation solver for compressible reacting flows. *Computers & Fluids*, 2020, 213: 104718.

[4] W.P. Jones, B.E. Launder, The prediction of laminarization with a two-equation model of turbulence. *International Journal of Heat and Mass Transfer*, 1972, 15: 301–314.

[5] H. Yilmaz, O. Cam, S. Tangoz, I. Yilmaz, Effect of different turbulence models on combustion and emission characteristics of hydrogen/air flames. *International Journal of Hydrogen Energy*, 2017, 42: 25744–25755.

[6] M. Tajnesaie, E. Jafari Nodoushan, R. Barati, M. Azhdary Moghadam, Performance comparison of four turbulence models for modeling of secondary flow cells in simple trapezoidal channels. *ISH Journal of Hydraulic Engineering*, 2020, 26: 187–197.

[7] Z. Han, R.D. Reitz, Turbulence modeling of internal combustion engines using RNG κ-ε models. *Combustion Science and Technology*, 1995, 106: 267–295.

[8] J. Kim, J. Baik, A numerical study of the effects of ambient wind direction on flow and dispersion in urban street canyons using the RNG k–ε turbulence model. *Atmospheric Environment*, 2004, 38: 3039–3048.

[9] B.E. Launder, G.J. Reece, W. Rodi, Progress in the development of a Reynolds-stress turbulence closure. *Journal of Fluid Mechanics*, 1975, 68: 537–566.

[10] G. Li, B. Naud, D. Roekaerts, Numerical investigation of a bluff-body stabilised non-premixed flame with differential Reynolds-stress models. *Flow, Turbulence and Combustion*, 2003, 70: 211–240.

[11] V. Bianco, A. Khait, A. Noskov, V. Alekhin, A comparison of the application of RSM and LES turbulence models in the numerical simulation of thermal and flow patterns in a double-circuit Ranque-Hilsch vortex tube. *Applied Thermal Engineering*, 2016, 106: 1244–1256.

[12] B. Magnussen, On the structure of turbulence and a generalized eddy dissipation concept for chemical reaction in turbulent flow, in *19th Aerospace Sciences Meeting*, American Institute of Aeronautics and Astronautics, 1981, A81-0042.

[13] A. Parente, M.R. Malik, F. Contino, A. Cuoci, B.B. Dally, Extension of the Eddy Dissipation Concept for turbulence/chemistry interactions to MILD combustion. *Fuel*, 2016, 163: 98–111.

[14] I.S. Ertesvåg, B.F. Magnussen, The eddy dissipation turbulence energy cascade model. *Combustion Science and Technology*, 2000, 159: 213–235.

[15] I.R. Gran, B.F. Magnussen, A numerical study of a bluff-body stabilized diffusion flame.

Part 2. Influence of combustion modeling and finite-rate chemistry. *Combustion Science and Technology*, 1996, 119: 191–217.

[16] S. Iavarone, A. Péquin, Z.X. Chen, N.A.K. Doan, N. Swaminathan, A. Parente, An a priori assessment of the Partially Stirred Reactor (PaSR) model for MILD combustion. *Proceedings of the Combustion Institute*, 2021, 38: 5403–5414.

[17] A. Péquin, S. Iavarone, R. Malpica Galassi, A. Parente, The partially stirred reactor model for combustion closure in large eddy simulations: Physical principles, sub-models for the cell reacting fraction, and open challenges. *Physics of Fluids*, 2022, 34: 055122.

[18] S. Iavarone, M. Cafiero, M. Ferrarotti, F. Contino, A. Parente, A multiscale combustion model formulation for NO predictions in hydrogen enriched jet flames. *International Journal of Hydrogen Energy*, 2019, 44: 23436–23457.

[19] Z. Li, M. Ferrarotti, A. Cuoci, A. Parente, Finite-rate chemistry modelling of non-conventional combustion regimes using a Partially-Stirred Reactor closure: Combustion model formulation and implementation details. *Applied Energy*, 2018, 225: 637–655.

[20] F. Delic, Three dimensional numerical simulation of combustion in a jet engine combustion chamber, Master thesis, University of Zagreb, 2019.

[21] L. Tessé, F. Dupoirieux, J. Taine, Monte Carlo modeling of radiative transfer in a turbulent sooty flame. *International Journal of Heat and Mass Transfer*, 2004, 47: 555–572.

[22] S.C. Mishra, H.K. Roy, Solving transient conduction and radiation heat transfer problems using the lattice Boltzmann method and the finite volume method. *Journal of Computational Physics*, 2007, 223: 89–107.

[23] F.R. Centeno, C.V. da Silva, R. Brittes, F.H.R. França, Numerical simulations of the radiative transfer in a 2D axisymmetric turbulent non-premixed methane–air flame using up-to-date WSGG and gray-gas models. *Journal of the Brazilian Society of Mechanical Sciences and Engineering*, 2015, 37: 1839–1850.

[24] Y. Sun, H. Shen, S. Zheng, L. Jiang, A hybrid non-gray gas radiation heat transfer solver based on OpenFOAM. *Journal of Quantitative Spectroscopy and Radiative Transfer*, 2022, 281: 108105.

[25] J. Lin, H. Zhou, E.R. Hawkes, M. Ma, G.H. Yeoh, Numerical investigation on turbulence-radiation interaction in the UMD turbulent line fires. *Fire Safety Journal*, 2023, 141: 103970.

[26] R.M. da Silva, G.C. Fraga, F.H. Ramos França, Improvement of the efficiency of the superposition method applied to the WSGG model to compute radiative transfer in gaseous mixtures. *International Journal of Heat and Mass Transfer*, 2021, 179: 121662.

[27] L.D. Lemos, L.A.Q. Llanos, F.M. Pereira, F.R. Centeno, F.H.R. França, Comparison between numerical and experimental data of the radiative heat transfer in a natural gas/CO_2/H_2 turbulent flame. *Fuel*, 2020, 281: 118740.

[28] M.F. Modest, D.C. Haworth, Radiative heat transfer in turbulent combustion systems, Springer, Cham, 2016.

[29] B. John, P. Senthilkumar, S. Sadasivan, Applied and theoretical aspects of conjugate heat

transfer analysis: A review. *Archives of Computational Methods in Engineering*, 2019, 26: 475–489.

[30] M. Xie, Y. Tu, Q. Peng, Numerical study of NH_3/CH_4 MILD combustion with conjugate heat transfer model in a down-fired lab-scale furnace. *Applications in Energy and Combustion Science*, 2023, 14: 100144.

[31] Y. Li, S. Kong, Coupling conjugate heat transfer with in-cylinder combustion modeling for engine simulation. *International Journal of Heat and Mass Transfer*, 2011, 54: 2467–2478.

[32] M. Abbassi, D. Lahaye, K. Vuik, Modelling turbulent combustion coupled with conjugate heat transfer in OpenFOAM, in *Numerical Mathematics and Advanced Applications ENUMATH 2019*, Springer, Cham, 2021, pp. 1137–1145.

[33] T. Cai, D. Zhao, E. Gutmark, Overview of fundamental kinetic mechanisms and emission mitigation in ammonia combustion. *Chemical Engineering Journal*, 2023, 458: 141391.

[34] J.A. Miller, M.D. Smooke, R.M. Green, R.J. Kee, Kinetic modeling of the oxidation of ammonia in flames. *Combustion Science and Technology*, 1983, 34: 149–176.

[35] E.C. Okafor, Y. Naito, S. Colson, A. Ichikawa, T. Kudo, A. Hayakawa, H. Kobayashi, Experimental and numerical study of the laminar burning velocity of CH_4–NH_3–air premixed flames. *Combustion and Flame*, 2018, 187: 185–198.

[36] G.P. Smith, D.M. Golden, M. Frenklach, N.W. Moriarty, B. Eiteneer, M. Goldenberg, C.T. Bowman, R.K. Hanson, S. Song, W.C. Gardiner, V.V. Lissianski, Z. Qin, GRI Mech 3.0. *Gas Research Institute*, 2000, available from: http://www.me.berkeley.edu/gri_mech.

[37] Z. Tian, Y. Li, L. Zhang, P. Glarborg, F. Qi, An experimental and kinetic modeling study of premixed $NH_3/CH_4/O_2$/Ar flames at low pressure. *Combustion and Flame*, 2009, 156: 1413–1426.

[38] X. Han, Z. Wang, Y. He, Y. Liu, Y. Zhu, A.A. Konnov, The temperature dependence of the laminar burning velocity and superadiabatic flame temperature phenomenon for NH_3/air flames. *Combustion and Flame*, 2020, 217: 314–320.

[39] N. Sako, J. Hayashi, T. Sako, H. Kawanabe, M. Katsuki, Nitrogen-origin-determination in NOx formation under ammonia/methane/air co-combustion using a nitrogen-tagged reaction model. *Combustion and Flame*, 2024, 259: 113210.

[40] R.P. Lindstedt, F.C. Lockwood, M.A. Selim, Detailed kinetic modelling of chemistry and temperature effects on ammonia oxidation. *Combustion Science and Technology*, 1994, 99: 253–276.

[41] F. Coppens, J. Deruyck, A. Konnov, The effects of composition on burning velocity and nitric oxide formation in laminar premixed flames of $CH_4 + H_2 + O_2 + N_2$. *Combustion and Flame*, 2007, 149: 409–417.

[42] Y. Song, H. Hashemi, J.M. Christensen, C. Zou, P. Marshall, P. Glarborg, Ammonia oxidation at high pressure and intermediate temperatures. *Fuel*, 2016, 181: 358–365.

[43] H. Nakamura, S. Hasegawa, T. Tezuka, Kinetic modeling of ammonia/air weak flames in a micro flow reactor with a controlled temperature profile. *Combustion and Flame*, 2017,

185: 16–27.

[44] J. Otomo, M. Koshi, T. Mitsumori, H. Iwasaki, K. Yamada, Chemical kinetic modeling of ammonia oxidation with improved reaction mechanism for ammonia/air and ammonia/hydrogen/air combustion. *International Journal of Hydrogen Energy*, 2018, 43: 3004–3014.

[45] E.C. Okafor, Y. Naito, S. Colson, A. Ichikawa, T. Kudo, A. Hayakawa, H. Kobayashi, Measurement and modelling of the laminar burning velocity of methane-ammonia-air flames at high pressures using a reduced reaction mechanism. *Combustion and Flame*, 2019, 204: 162–175.

[46] B. Mei, X. Zhang, S. Ma, M. Cui, H. Guo, Z. Cao, Y. Li, Experimental and kinetic modeling investigation on the laminar flame propagation of ammonia under oxygen enrichment and elevated pressure conditions. *Combustion and Flame*, 2019, 210: 236–246.

[47] Y. Song, L. Marrodán, N. Vin, O. Herbinet, E. Assaf, C. Fittschen, A. Stagni, T. Faravelli, M.U. Alzueta, F. Battin-Leclerc, The sensitizing effects of NO_2 and NO on methane low temperature oxidation in a jet stirred reactor. *Proceedings of the Combustion Institute*, 2019, 37: 667–675.

[48] A. Stagni, C. Cavallotti, S. Arunthanayothin, Y. Song, O. Herbinet, F. Battin-Leclerc, T. Faravelli, An experimental, theoretical and kinetic-modeling study of the gas-phase oxidation of ammonia. *Reaction Chemistry & Engineering*, 2020, 5: 696–711.

[49] T. Cai, D. Zhao, S.H. Chan, M. Shahsavari, Tailoring reduced mechanisms for predicting flame propagation and ignition characteristics in ammonia and ammonia/hydrogen mixtures. *Energy*, 2022, 260: 125090.

[50] F. Perini, E. Galligani, R.D. Reitz, An analytical Jacobian approach to sparse reaction kinetics for computationally efficient combustion modeling with large reaction mechanisms. *Energy & Fuels*, 2012, 26: 4804–4822.

[51] F. Perini, E. Galligani, R.D. Reitz, A study of direct and Krylov iterative sparse solver techniques to approach linear scaling of the integration of chemical kinetics with detailed combustion mechanisms. *Combustion and Flame*, 2014, 161: 1180–1195.

[52] B. Tekgül, P. Peltonen, H. Kahila, O. Kaario, V. Vuorinen, DLBFoam: An open-source dynamic load balancing model for fast reacting flow simulations in OpenFOAM. *Computer Physics Communications*, 2021, 267: 108073.

[53] Y. Shi, W.H. Green, H.-W. Wong, O.O. Oluwole, Accelerating multi-dimensional combustion simulations using GPU and hybrid explicit/implicit ODE integration. *Combustion and Flame*, 2012, 159: 2388–2397.

[54] J. Muela, R. Borrell, J. Ventosa-Molina, L. Jofre, O. Lehmkuhl, C.D. Pérez-Segarra, A dynamic load balancing method for the evaluation of chemical reaction rates in parallel combustion simulations. *Computers & Fluids*, 2019, 190: 308–321.

[55] I. Morev, B. Tekgül, M. Gadalla, A. Shahanaghi, J. Kannan, S. Karimkashi, O. Kaario, V. Vuorinen, Fast reactive flow simulations using analytical Jacobian and dynamic load balancing in OpenFOAM. *Physics of Fluids*, 2022, 34: 021801.

[56] A. Amritkar, S. Deb, D. Tafti, Efficient parallel CFD-DEM simulations using OpenMP. *Journal of Computational Physics*, 2014, 256: 501–519.

[57] S. Zou, Y.F. Lin, J. Chen, Q. Wang, Y. Cao, The performance analysis and parallel optimization of the OpenFOAM-based viscoelastic solver for heterogeneous HPC platforms. *Applied Mechanics and Materials*, 2014, 670–671: 873–880.

[58] L. Krivodonova, An efficient local time-stepping scheme for solution of nonlinear conservation laws. *Journal of Computational Physics*, 2010, 229: 8537–8551.

[59] M. Becker, dhcaeLTSThermoParcelSolver. *DHCAE Tools*, 2012, available from: https://www.dhcae-tools.com/images/dhcaeLTSThermoParcelSolver.pdf.

[60] S. Date, Y. Kido, Y. Katsuura, Y. Teramae, S. Kigoshi, Supercomputer for quest to unsolved interdisciplinary datascience (SQUID) and its five challenges, in *Sustained Simulation Performance 2021*, Springer, Cham, 2023, pp. 1–19.

Chapter 3

Model validation

3.1 Introduction

In performing three-dimensional numerical analysis for large-scale combustion furnaces, the large number of computational grids leads to substantial computational costs and time to achieve the converged solution. This poses significant challenges in selecting different computational models and parameters. In **Chapter 2**, various turbulence and combustion models were introduced; however, their accuracy in numerical predictions based on the solver developed for this thesis remains unknown. Therefore, before conducting the three-dimensional numerical analysis on the ammonia co-combustion furnace, it is essential to establish a reliable two-dimensional benchmark experiment. This benchmark should allow for exploring the predictive accuracy of the solver under different computational models while maintaining lower computational costs and grid numbers.

On that basis, the benchmark experiment for validating the CFD solver in the present study should fulfill the following requirements. First, the experimental results should be reliable and widely accepted by the turbulence combustion community. Second, the experiment should offer extensive measurements of critical parameters such as the temperature field, velocity field, and combustion reactants, with specific focus on NO distribution. Third, the burner size should not vary significantly (exponential order) from that of the ammonia co-combustion furnace, and various fuel jet velocity conditions should be available. Accordingly, the Sandia flames D, E, and F (hereafter abbreviated as flames D-F) were selected for the present study as a validation of the customized solver [1]. This type of turbulent partially premixed methane/air flame has been widely investigated and is seen as essential for various studies [2,3].

In summary, the present chapter will serve as a model validation part, using two-dimensional numerical analysis of the Sandia flames D-F to explore the capabilities of the customized solver in terms of numerical prediction and the computational acceleration of the integrated acceleration strategy. Three distinct turbulence models, including the Standard k-ε (KE), Re-Normalization Group k-ε (RngKE), and Launder-Reece-Rodi (LRR) models, were selected to evaluate their accuracy in predicting temperature and velocity fields, as well as species distribution. Additionally, the impact of turbulent Prandtl number and model constants on the predicted results will be investigated, and optimal numerical results will be proposed for various experimental conditions. Finally, the validated optimal models from this chapter will also be

applied to the subsequent three-dimensional numerical predictions for the ammonia co-combustion furnace.

3.2 Sandia flames D-F

3.2.1 Experimental setup

As previously mentioned, Sandia flames D-F were selected to validate the acceleration capacity and prediction accuracy of the customized solver. The Sandia flame is a partially turbulent premixed flame, primarily composed of three parts: the central fuel jet zone, the high-temperature pilot flame zone, and the air co-flow zone. **Table 3.1** summarizes the flow parameters at the inlet boundary for the three flames. Apart from differences in jet and pilot inlet velocities, flames D-F have identical burner structures and inlet fuel compositions. For the combustion mixture parameters, the fuel inlet consists of a mixture of methane (CH_4) and air, composed of 25% and 75% by volume, respectively. This mixture is used to reduce the problem of fluorescence interference due to soot and shorten the flame length while producing a more robust flame than pure CH_4. The pilot flame is composed of a mixture of C_2H_2, H_2, air, CO_2, and N_2, with a combustion state comparable to methane burning at an equivalence ratio of 0.77. The energy released for flames D-F by the pilot amounted to about 6% of the main jet flame with a gas temperature of 1880 K, and its primary role is to stabilize the jet flame.

Table 3.1 Experimental flow parameters of Sandia flames D-F.

	Sandia flame D	**Sandia flame E**	**Sandia flame F**
Reynolds number in the jet zone	22400	33400	44800
Velocity in the jet zone (m/s)	49.6	74.4	99.2
Velocity in the pilot zone (m/s)	11.4	17.1	22.8
Velocity in the co-flow zone (m/s)	0.9	0.9	0.9

Figure 3.1 uses flame D as an example to illustrate the overview of the burner used for the three flames and the corresponding details of the pilot flame. As can be observed, the pilot flame forms a blue triangular shape surrounding the fuel jet. The tall flame from the fuel jet has a blue boundary that rises upwards. The pilot and the fuel jet are separated by a wall, and there is also an outer wall surrounding the pilot jet. Additionally, it is important to note that during the transition from flame D to F, as the fuel and pilot jet velocities gradually increase, the probability of local extinction at the flame front also increases. Flame D has a low probability of local extinction, whereas extinction becomes more prominent in flames E and F. The velocity field and scalar data for flames D-F were measured by the Technical University of Darmstadt and the Sandia National Laboratory, respectively. The calculations obtained will be compared

to the reference data mentioned above. For more experimental details on the Sandia flames, readers can refer to the work of Barlow and Frank [1,4].

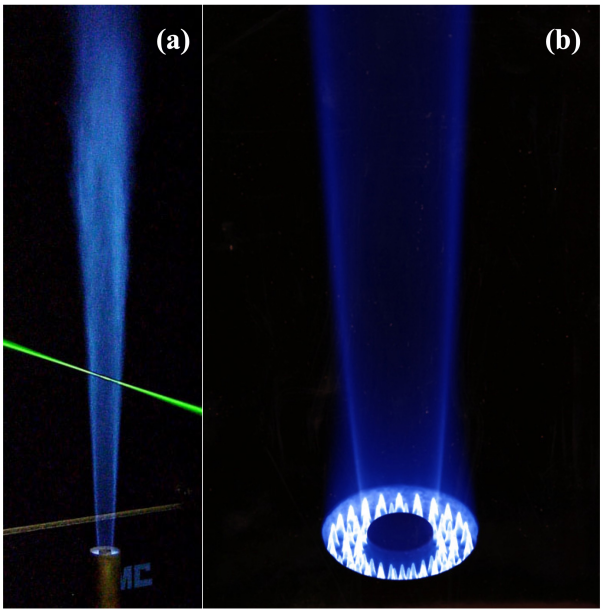

Figure 3.1 (a) General view of Sandia flame D, and (b) close-up of the pilot flame [1].

3.2.2 Computational domain details

After introducing the relevant parameters of the Sandia flame experiment, it is necessary to proceed with the mesh generation for the Sandia flame burner structure. **Figure 3.2(a)** depicts the schematic of the Sandia flame burner. Specifically, the burner is composed of a jet nozzle with a diameter of D = 7.2 mm, surrounded by a wide pilot nozzle with inner and outer diameters of 7.7 mm and 18.2 mm, respectively. In the present study, pre-inlet nozzles for both the jet and pilot were taken into consideration in the computational domain to obtain a fully developed turbulent velocity profile at the burner inlet where its length extends up to approximately 15 D. According to the recommended model dimension from Ref. [3,5], the axial and radial dimensions of the computational domain after the inlet were set to 76.5 D and 20.83 D, respectively. Calculations were conducted in a two-dimensional domain as a sector of 5°. The lower dimensionality simulations were performed with a mesh having a thickness of one cell. Details of the computational domain are displayed in **Fig. 3.2(b)**, where mesh refinement was applied in the jet and pilot regions, totaling approximately 3×10^4 cells. Additionally, a mesh independence study was conducted in advance, with a refinement ratio of approximately 1.5 between meshes. The number of meshes is appropriate for conducting two-dimensional numerical validation calculations.

It is important to note that during the numerical calculations, the present study calibrated the turbulent Prandtl number for different flame types (D-F) and turbulence models. Notably, the

optimal range for the turbulent Prandtl number in non-isothermal circular jets has been reported to be within the interval of 0.7 to 1 in previous literature [6,7]. For flame D, the recommended value of 0.82, as given by Chua and Antonia [8], was used in the present study for the KE and RngKE turbulence models. However, due to the significant increase in inlet jet velocity of flames E and F compared to flame D, which enhances the momentum eddy diffusivity, it becomes necessary to increase the turbulent Prandtl number during the transition from flame D to F to control the relationship between momentum and heat diffusion eddy diffusivity. Additionally, it was found that decreasing the turbulence Prandtl number by 0.1 for flames D and E, compared to the values employed in the other two turbulence models, can yield more accurate predictions when adopting the LRR turbulence model. Specifically, in the numerical calculations of this chapter, the turbulent Prandtl numbers for flames D, E, and F were set to 0.82, 0.92, and 1 for the KE and RngKE turbulence models. For the LRR turbulence model, the turbulent Prandtl numbers were adjusted to 0.72, 0.82, and 1. The turbulent Schmidt number was fixed at 0.7 in all cases. The influence of the turbulent Prandtl number on numerical prediction results will be discussed in detail in **Sec. 3.6.2**.

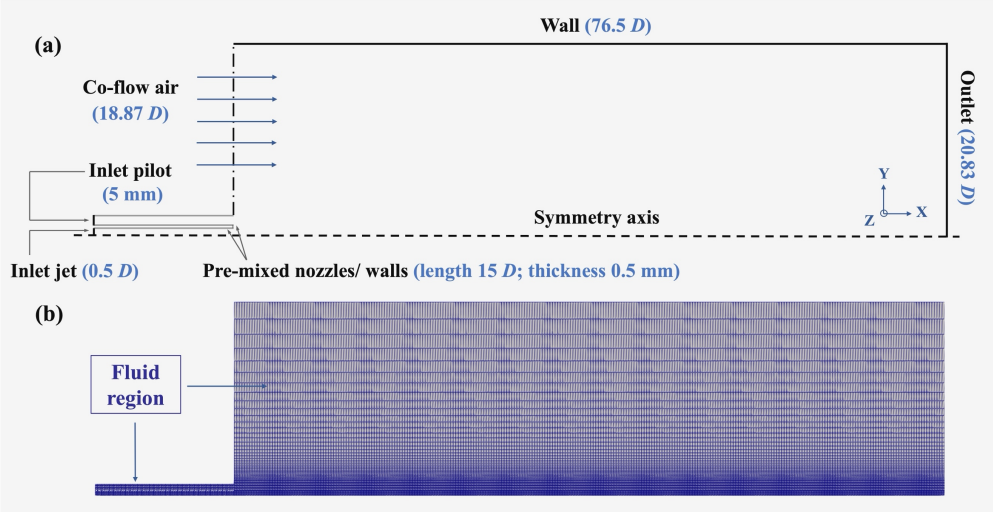

Figure 3.2 (a) Schematic diagram and (b) general view of the computational domain of Sandia flames D-F (D = 7.2 mm).

3.3 Computational efficiency comparison

Before validating the accuracy of different calculation models, the present section first conducted a performance analysis based on flame D to verify the effectiveness of acceleration strategies. **Figure 3.3** displays the parallel computing efficiency provided by the solver after integrating the DLB code and applying the SpeedCHEM algorithm. It is well-known in CFD calculations that increasing the number of sub-domains can effectively reduce computation time. However, with the increase in the number of MPI ranks, achieving perfect scaling still becomes

challenging due to communication bottlenecks between different processors and load imbalance issues. As shown in the figure, the Standard model demonstrates poor parallel scaling, whereas, with the introduction of the DLB code, the solver approximates perfect scaling below 16 processors, showing a clear advantage over the Standard model. However, as the number of processors continues to increase, the communication overhead between different processors significantly rises. When the number of processors reaches 64, for the SpeedCHEM + DLB model, it only approximates about 61% of perfect scaling but is still significantly higher than that of the Standard model.

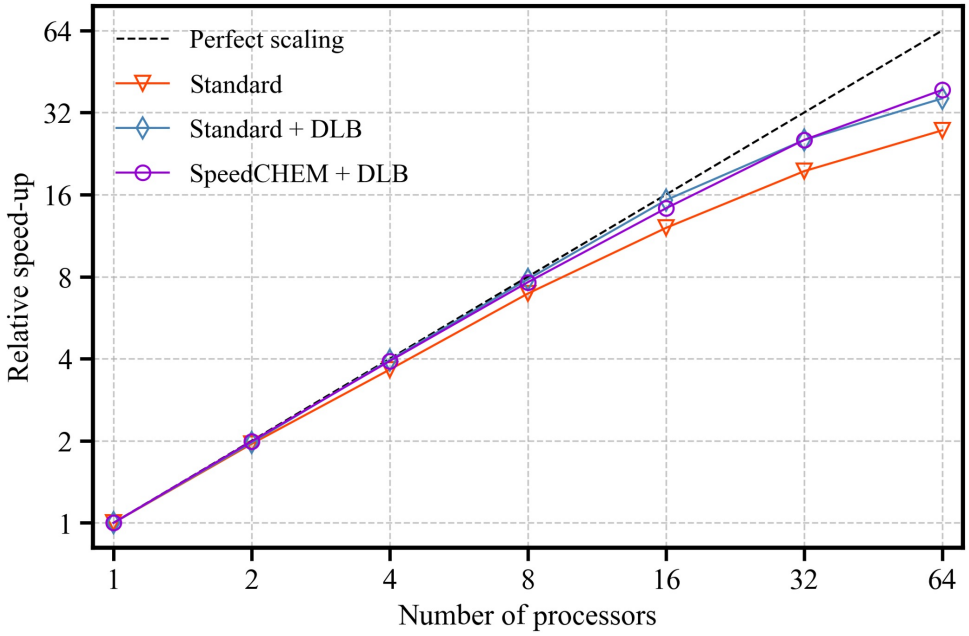

Figure 3.3 Strong scaling performance of different acceleration methods for Sandia flame D simulation.

In light of this, introducing the OpenMP method on the base of the DLB + SpeedCHEM model, which involves distributing tasks across multiple processors for parallel processing, can effectively enhance computational efficiency while reducing the number of sub-domains. Additionally, the introduction of OpenMP also helps prevent the issue of generating a large number of files when increasing the sub-domains. To identify the optimal combination of OpenMP threads and MPI ranks, **Table 3.2** compares the execution time under different combinations of OpenMP threads and MPI ranks. During the testing process, the computing nodes were fixed at two, thus keeping the total number of OpenMP threads × MPI ranks constant at 128. As shown in **Table 3.2**, when the case is divided into 8 sub-domains, using 16 OpenMP threads achieves the optimal solution for controlling communication between different processors, resulting in a computational speed increase of nearly 3 times compared to the condition without using the OpenMP method (1 × 128). Therefore, subsequent Sandia

flames-related calculations will be based on this setup.

Table 3.2 Comparison of time spent under different combinations of MPI and OpenMP (2 nodes are used in all cases).

OpenMP × MPI rank	Time spent over 1000 iterations (s)
1 × 128	1302
2 × 64	620
4 × 32	711
8 × 16	435
16 × 8	397
32 × 4	512
64 × 2	793

Figure 3.4 illustrates the computational speed-up achieved when simulating flame D with different acceleration strategies. Following the analysis results, the computational domain was divided into 8 sections, and all speed-up tests were conducted for 1000 iterations with constant global time steps of 10^{-6} s after ignition. The figure reveals that using the Standard model requires a significant amount of time, around 12000 seconds. Introducing the DLB code offers a modest speed-up factor of approximately 1.2. This improvement, which is not as significant as the speed-up reported in the previous results by Tekgül et al. [9], can be attributed to the absence of an additional zonal reference cell mapping approach in the code [10]. This method could optimize computation time by grouping and solving once for cells with similar thermochemical state vectors in low reaction zones, but it might affect the computational accuracy. Implementing the SpeedCHEM + DLB method results in a considerable speed-up by a factor of 4.69, affirming the robustness of such a chemistry solver. The addition of the OpenMP method further accelerates computations, with the integrated acceleration strategy achieving a speed-up nearly 30 times greater than the Standard conditions. These findings demonstrate the significant performance improvement of the integrated approach in enhancing computational speed.

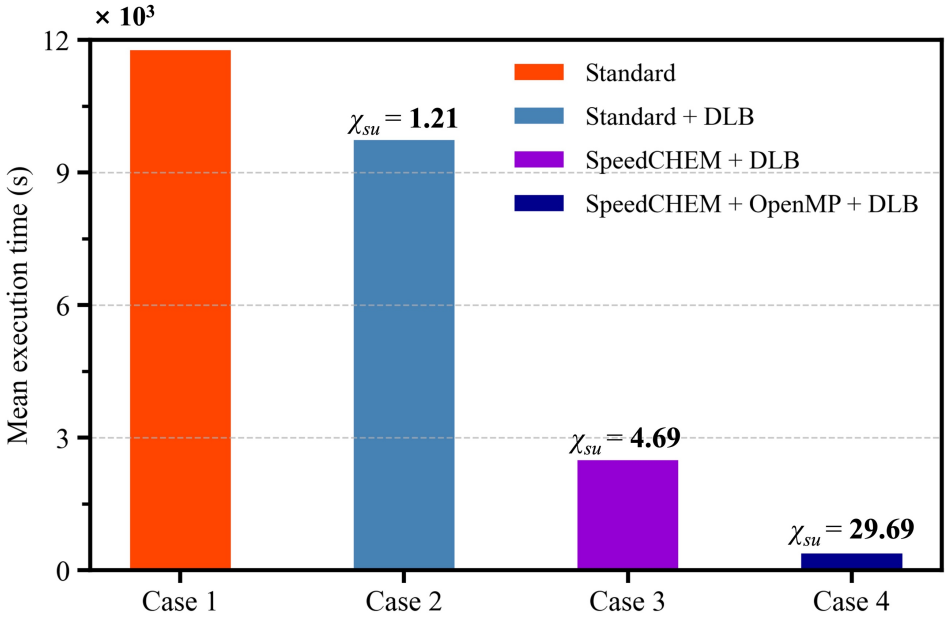

Figure 3.4 Mean execution times over 1000 iterations for the flame D simulation under 8 computational sub-domains (χ_{su} is the speed-up factor).

3.4 Accuracy prediction

Since **Sec. 3.3** verified the effectiveness of the integrated acceleration strategy in enhancing computational speed. Therefore, this section will utilize the integrated acceleration strategy to conduct calculations and discuss the accuracy of the developed solver in predictions under different turbulence models. The EDC model is used as the combustion model.

3.4.1 Inlet boundary conditions

When evaluating the accuracy of a customized solver, it is common practice to compare the predicted values with the experimental values. Generally, the employed combustion models, turbulence models, or reaction mechanisms are held responsible for any discrepancies between the computed and experimental values. However, Lewandowski al. [11] noted that other factors also contribute to these discrepancies. For instance, the accuracy of the predicted results is also influenced by the inlet boundary conditions. Therefore, it is crucial to carefully consider all the relevant factors when interpreting the results of a numerical simulation.

In the present study, to ensure a fully developed turbulent velocity profile at the burner inlet, pre-inlet nozzles with an approximate length of 15 D for the jet and pilot were incorporated in the computational domain. However, the presence of pre-inlet walls significantly affects turbulent flows, with regions affected by viscosity experiencing alterations in the flow. When translated to CFD calculations, differences in the inlet wall function type can influence the velocity field predictions, resulting in deviations from the actual results. Consequently, a precise

near-wall region representation is critical for accurately predicting wall-bounded turbulent flows. To assist the researchers in validating their prediction results, the official documentation from the Sandia National Laboratories provided correction velocity profiles at the burner inlet of flame D.

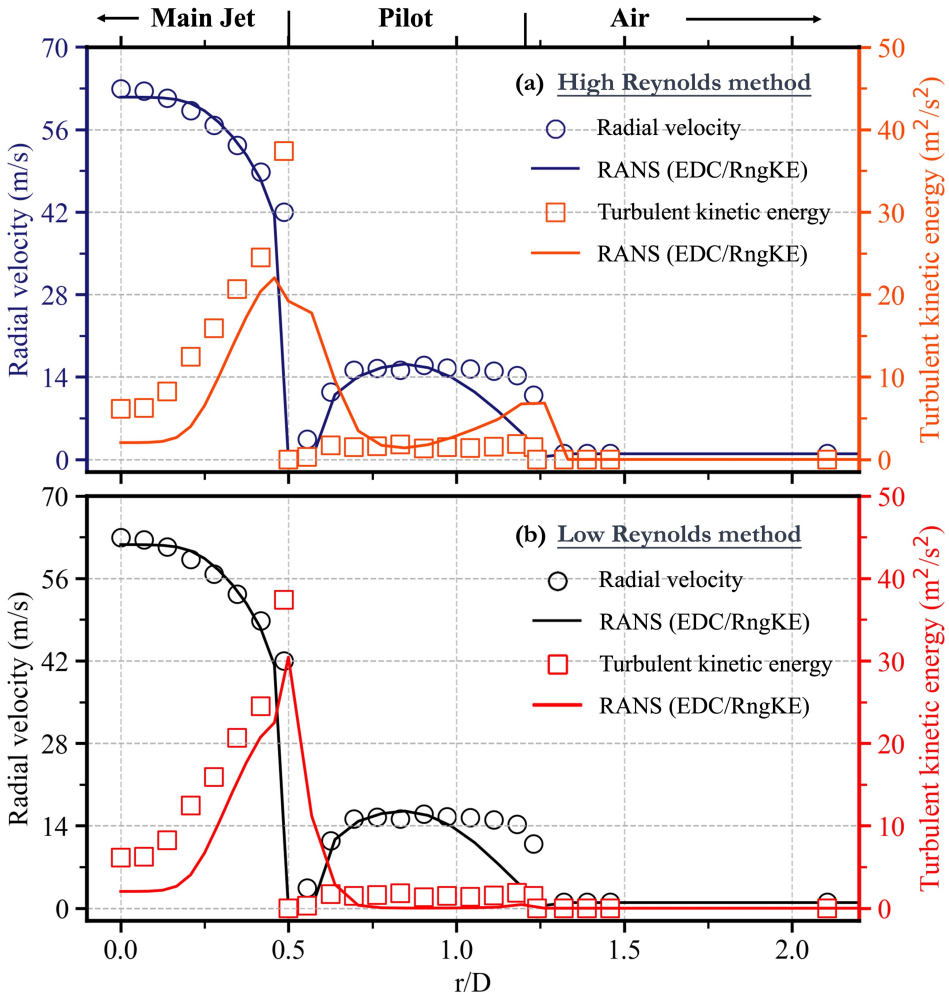

Figure 3.5 Comparison of experimental and predicted velocity profiles using (a) high and (b) low Reynolds methods for flame D at the inlet boundary (X/D = 0).

Generally speaking, most turbulence models are only valid in areas where turbulence is fully developed, and they tend to perform poorly in regions near the wall. Therefore, in different simulation cases, it is necessary to select an appropriate wall function model based on the fluid flow conditions near the wall. In CFD analysis, y-plus (y^+) is a key dimensionless parameter that can effectively assess the choice of wall functions, as shown in **Eq. (3.1)**:

$$y^+ = \frac{yu_t}{v} \tag{3.1}$$

where y is the absolute distance from the wall; v is the kinematic viscosity and u_t represents

the friction velocity, which can be obtained based on wall shear stress and fluid density. y^+ value can be interpreted as a local Reynolds number, indicating that its magnitude can be expected to determine the relative importance of viscous and turbulent processes. When this value exceeds 30, it suggests that the flow in that region is primarily dominated by turbulence, allowing for the application of coarse meshes and High Reynolds methods to simulate turbulent effects.

The examination of the y^+ values in flame D reveals that the flow near the pre-inlet wall is not fully turbulent ($y^+ < 30$). Consequently, based on the OpenFOAM platform, the Low Reynolds (LowRe) method, which can handle a flow that is not fully turbulent, yields better predictions compared to the high Reynolds number wall functions. **Figure 3.5** provides a comparison of experimental and predicted results utilizing these two different types of wall functions. Notably, the implementation of the LowRe method led to significant improvements in the velocity fields, particularly the turbulent kinetic energy at the burner inlet. Although some discrepancies with experimental results still exist, utilizing the LowRe method in the wall function enhanced the predictive capability for flame D. The prediction results of flame D based on the above wall function will be addressed in the subsequent section.

3.4.2 Central axis prediction

Figures 3.6, **3.7**, and **3.8** present the centerline profiles of temperature, mean mixture value, velocity, major species (CO_2, O_2, CH_4, N_2), and minor species (CO, NO) for flames D-F, respectively. Notably, the KE model was not used to calculate flame F through the customized solver due to its quenched state during the calculation. One explanation is that the flame F is close to global extinction, resulting in high sensitivity of certain numerical parameters such as the turbulent Prandtl number during transport calculations [12].

In terms of temperature field prediction, all three turbulence models exhibit a minor overestimation of the peak value along the central axis. The peak temperature differences between the RngKE and KE models were 66 K and 68 K for flame D, and 104 K and 115 K for flame E. In contrast, the peak temperature difference for flames D and E employing the LRR model is closer to the experimental value at roughly 22 K and 78 K, respectively. Concerning the flame structure, the RngKE model closely aligns with experimental values in the flame developing and combustion region ($X/D < 45$), whereas the LRR and KE models overestimate the temperature. Nonetheless, as the flame develops, an underestimation of temperature near the flame front is observed when employing the RngKE and KE models. This discrepancy could be attributed to the implementation of the radiation model [13]. Collectively, good agreements with the experimental values can be observed based on the RngKE turbulence model. Reasonable temperature field predictions lead to good predictions of the species distribution.

As shown in **Fig. 3.7**, the RngKE model offers higher accuracy in predicting major species than the other two turbulence models.

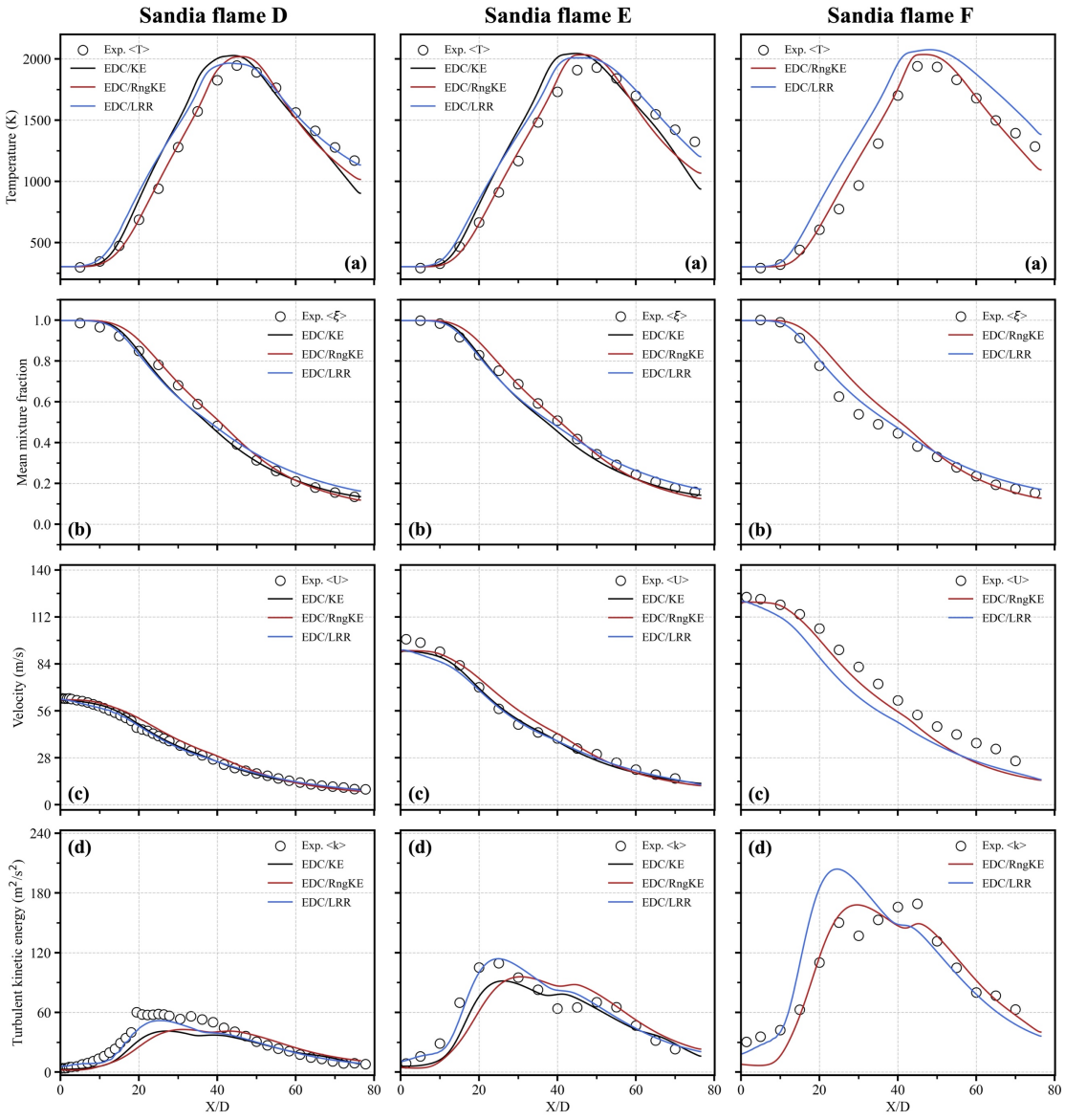

Figure 3.6 Centerline profiles of (a) temperature, (b) mean mixture value (c) normalized velocity, and (d) turbulent kinetic energy for flames D-F.

Regarding the velocity field predictions for flames D and E, the RngKE model exhibits significant discrepancies in the turbulent kinetic energy values despite capturing some experimental trends. Conversely, the LRR model provides superior predictions for turbulent flow owing to its ability to solve transport equations for each component of the Reynolds stress tensor, and accounts for the history and anisotropy of turbulence [14]. In summary, the velocity field predictions generated by the LRR model are more closely aligned with the actual experimental values.

Nonetheless, the prediction accuracy for flame F diminishes when employing the RngKE and LRR turbulence models, particularly in the velocity field. Given that flame F has significant local extinction, the severity of local extinction substantially complicates the RANS prediction. Therefore, it poses a substantial challenge in reproducing the correct amount of extinction compared to the more precise Large Eddy Simulation (LES) and Direct Numerical Simulation (DNS) approaches. Apart from the inaccuracies in the velocity field, the RngKE model is generally capable of reproducing the distribution of major species in flame F.

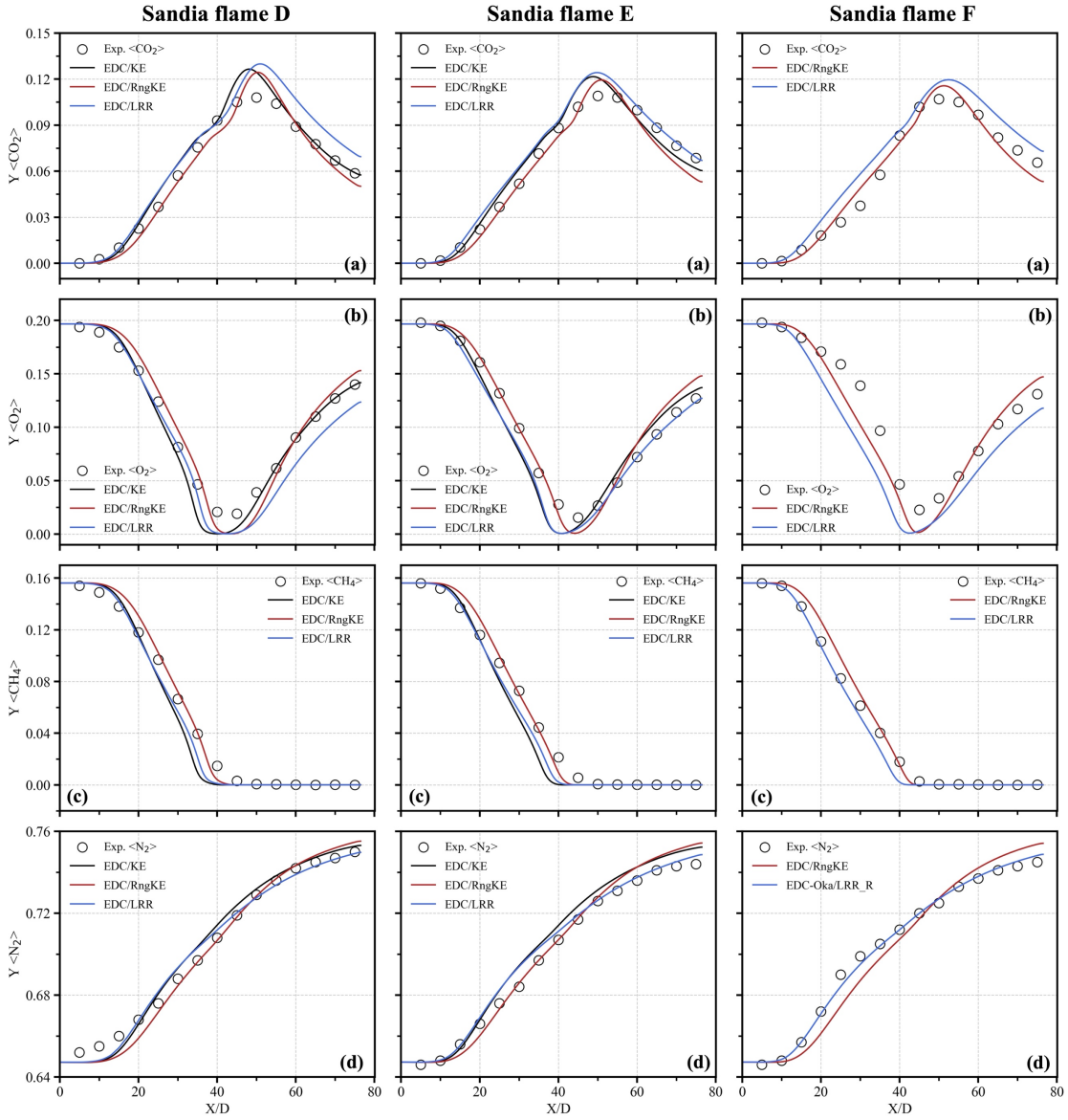

Figure 3.7 Centerline profiles of (a) carbon dioxide, (b) oxygen, (c) methane, and (d) nitrogen for flames D-F.

Accurate simulation of minor species, particularly those affected by transient effects, remains a challenge in recent studies. As can be observed in **Fig. 3.8**, three turbulence models show an

overprediction in peak values regarding the minor species, with such a phenomenon particularly pronounced in the prediction of NO. To calculate CO, employing the RngKE model results in the peak values for flames D and E being overestimated by approximately 0.34, and 0.35 times, respectively. The predictions for the LRR model display a marginal improvement over the RngKE model, at approximately 0.28 and 0.34 times. Saini et al. [15] attributed the intermediate CO discrepancy to the inadequate mixing time scale in the EDC combustion model. With respect to NO prediction, although all three turbulence models overestimate the NO prediction, the centerline NO profiles with the LRR model are observed to be closer to the experimental results. Compared to the RngKE model, the LRR model demonstrates enhanced prediction accuracy, overestimating flame D by 0.69 times and flame E by 1.13 times, as opposed to 1.41 and 1.86 times overestimation, respectively. The numerical predictions for the KE turbulence model are similar to those of the RngKE model; however, the NO peak position is further from the flame front, significantly deviating from the experimental results.

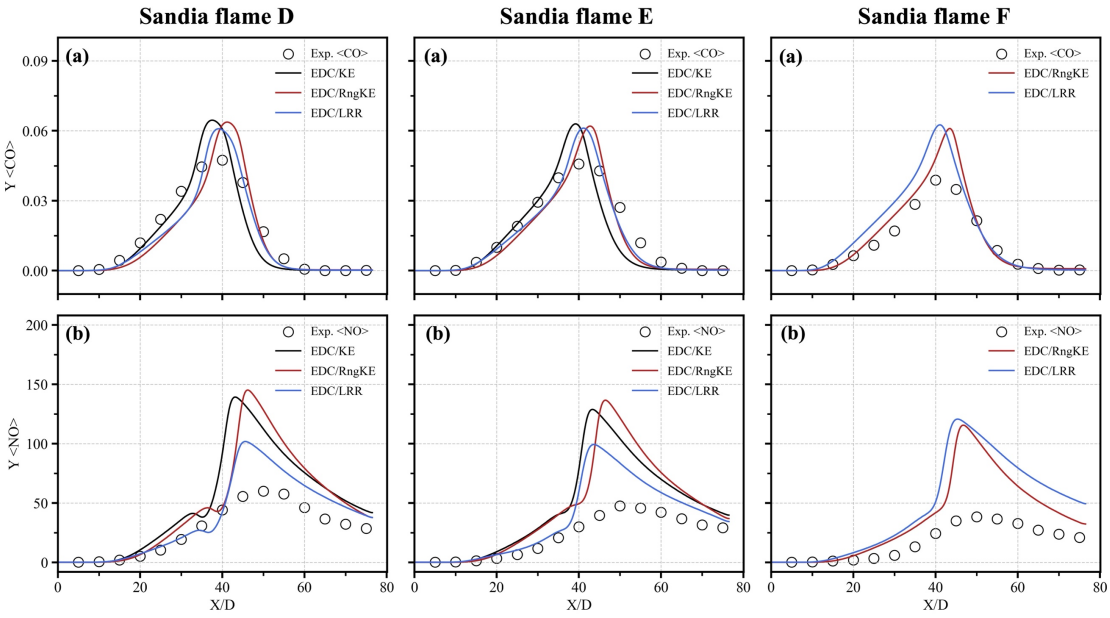

Figure 3.8 Centerline profiles of (a) carbon monoxide, and (b) nitric oxide for flames D-F.

Fundamentally, the primary NO formation in gaseous combustion systems includes three mechanisms, namely, thermal NO, prompt NO, and fuel NO. Roomina and Bilger [16] studied flame D and reported that a skeletal mechanism including only thermal NO formation chemistry significantly underpredicted the NO mass fraction. They concluded that the predominant route for NO formation in the flame developing and combustion region with $X/D < 45$ is prompt NO. Overpredictions of NO in the present study can be related to the above theory due to the poor prediction of the prompt NO along the central axis. Further downstream near the flame front,

where X/D > 45, thermal NO formation becomes the dominant process, and therefore reasonable agreement for the LRR turbulence model is achieved. The accuracy improvement in LRR turbulence model prediction can be linked to the precise prediction of peak flame temperature values, as shown in **Fig. 3.6**. Given that thermal NO is the predominant source of NO under most hydrocarbon fuel combustion, accurate estimation of the high-temperature field is essential for precise NO predictions.

3.4.3 Radial distribution prediction

Figures 3.9 and **3.10** present the detailed radial profiles (X/D = 3, 7.5, 15, 30, 45, and 60) of temperature, mean mixture value, velocity, and turbulent kinetic energy for flame D. Take the RngKE turbulence model as an example, in the flame developing region ($X/D \leq 7.5$), the predictions are basically in good agreement with the experimental data, demonstrating that the inlet boundary condition settings are appropriate. As the flame develops, the average axial velocity observed in the jet spreading is slightly overestimated at X/D = 15, resulting in the prediction of large temperature values. Similar overestimations are observed in other RANS-related studies applying the Standard k–ε [15], Realizable k–ε [17], and Reynolds stress model [18] respectively. Moreover, from the observation of Ref. [3], the LES approach exhibits a similar trend as the RANS results in the present study. At the flame front where X/D = 45 and 60, although temperature field overestimations persist, the prediction of jet spreading becomes accurate, and turbulent kinetic energy profiles are reasonably well predicted at both locations. Overall, the aforementioned findings demonstrate that the RngKE turbulence model is appropriate for the flame D prediction.

Regarding the predictions of the other two KE and LRR turbulence models, differences in jet spreading exhibit little deviation from the RngKE predictions, and experimental results are well reproduced at most radial locations. However, the problem of the temperature field overestimation is more pronounced, especially at the axial positions of X/D = 7.5, 15, and 30, where the predictions for the temperature distribution are significantly higher than the experimental values. One explanation for this deviation is the selection of empirical coefficients in the LRR model, as it typically requires variable case-specific empirical data. Differences in these empirical coefficients could constrain the prediction accuracy and impose a limitation on the practical application of the LRR model [14].

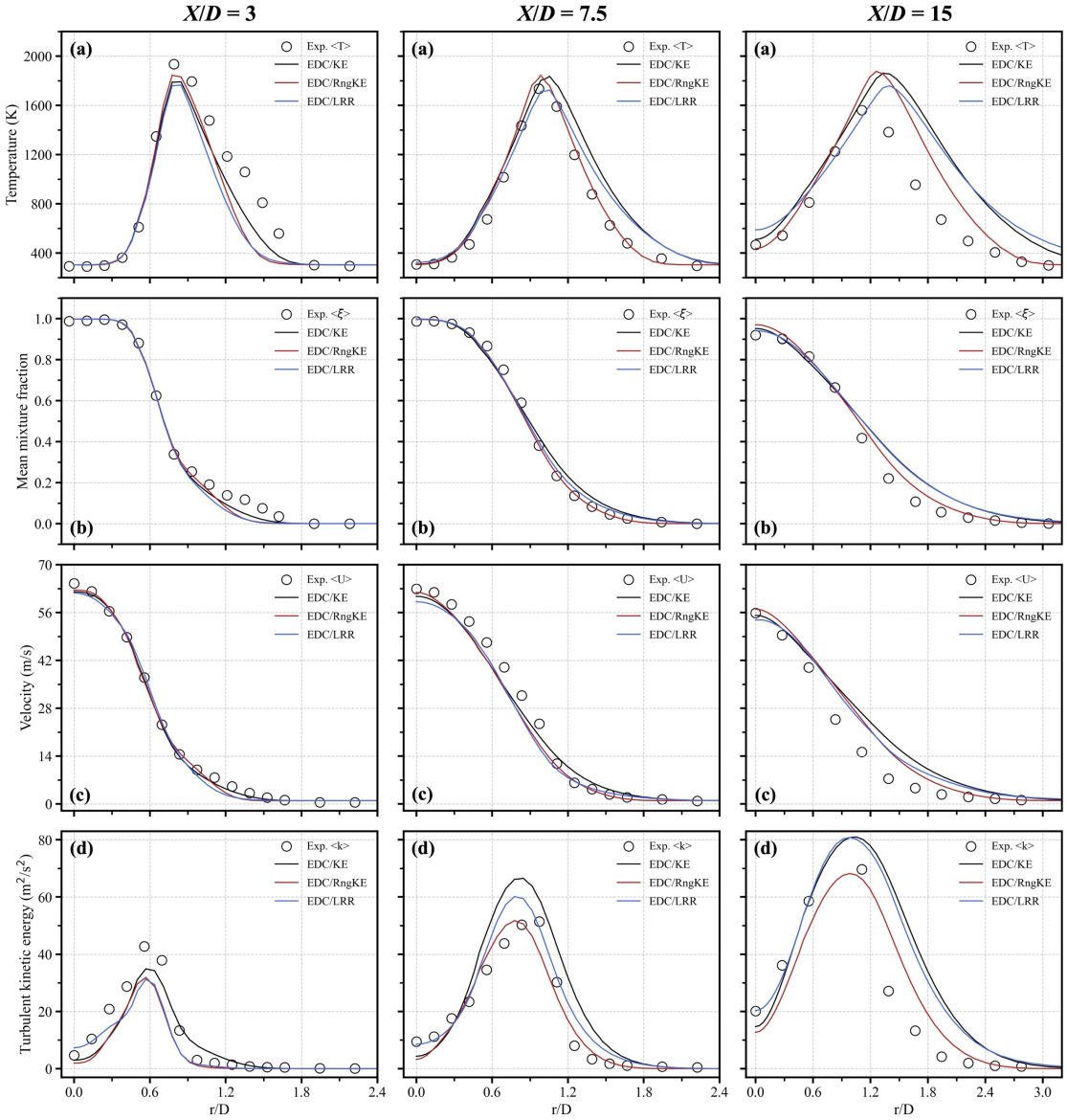

Figure 3.9 Radial profiles of (a) temperature, (b) mean mixture value, (c) normalized velocity, and (d) turbulent kinetic energy at X/D = 3 (left), X/D = 7.5 (middle), and X/D = 15 (right) for flame D.

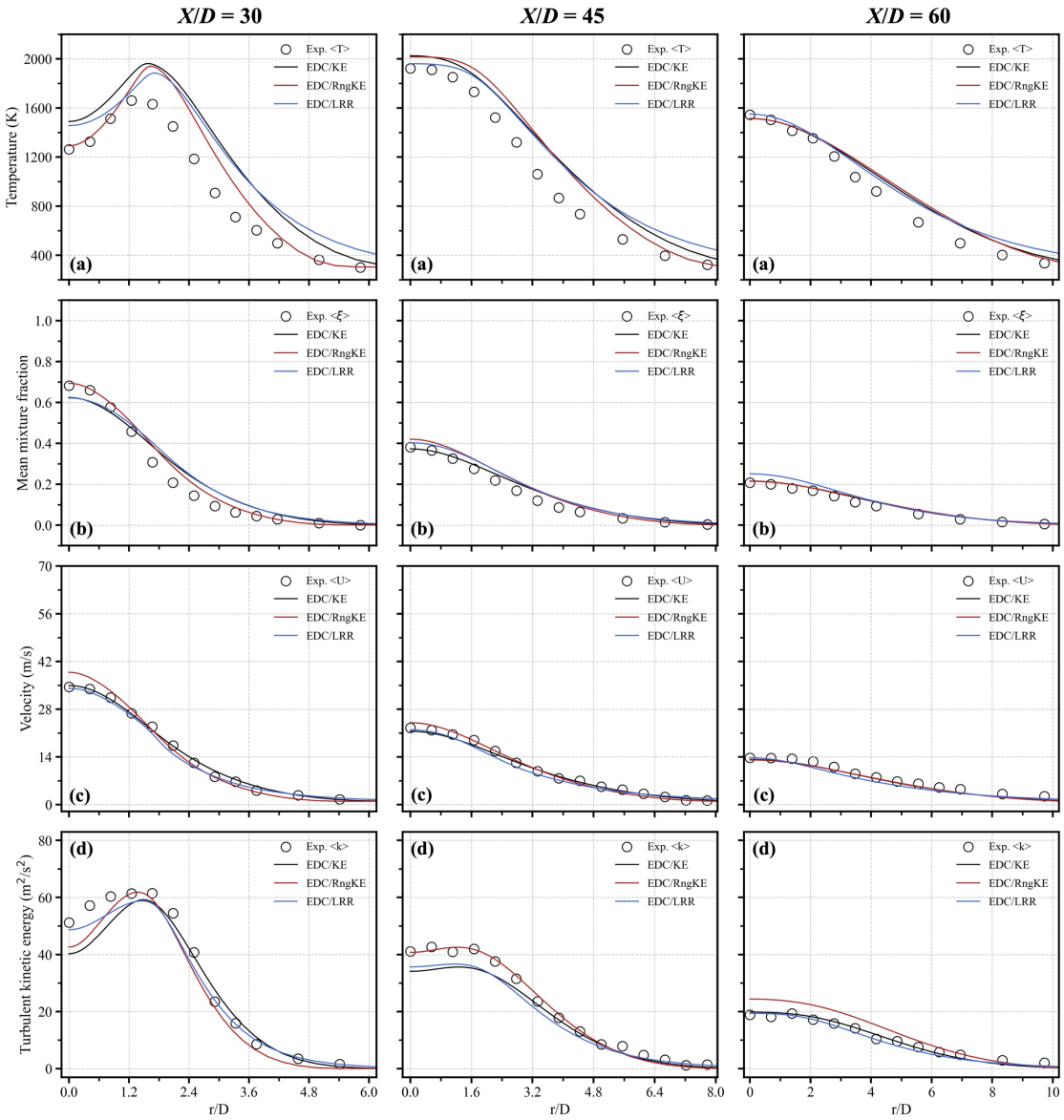

Figure 3.10 Radial profiles of (a) temperature, (b) mean mixture value, (c) normalized velocity, and (d) turbulent kinetic energy at X/D = 30 (left), X/D = 45 (middle), and X/D = 60 (right) for flame D.

Figure 3.11 displays the radial profiles of the mean mixture fraction for flame D to flame F at three axial positions. Mirroring the results obtained in flame D, predictions applying the three turbulence models exhibit an identical trend to the experimental values in the flame developing region. At the axial location of X/D = 15, over-spreading in the radial extent is also observed in both flames E and F due to their high-velocity prediction. Overall, compared to the other two turbulence models, the RngKE model provides a reasonably good agreement with experimental values concerning jet spreading predictions.

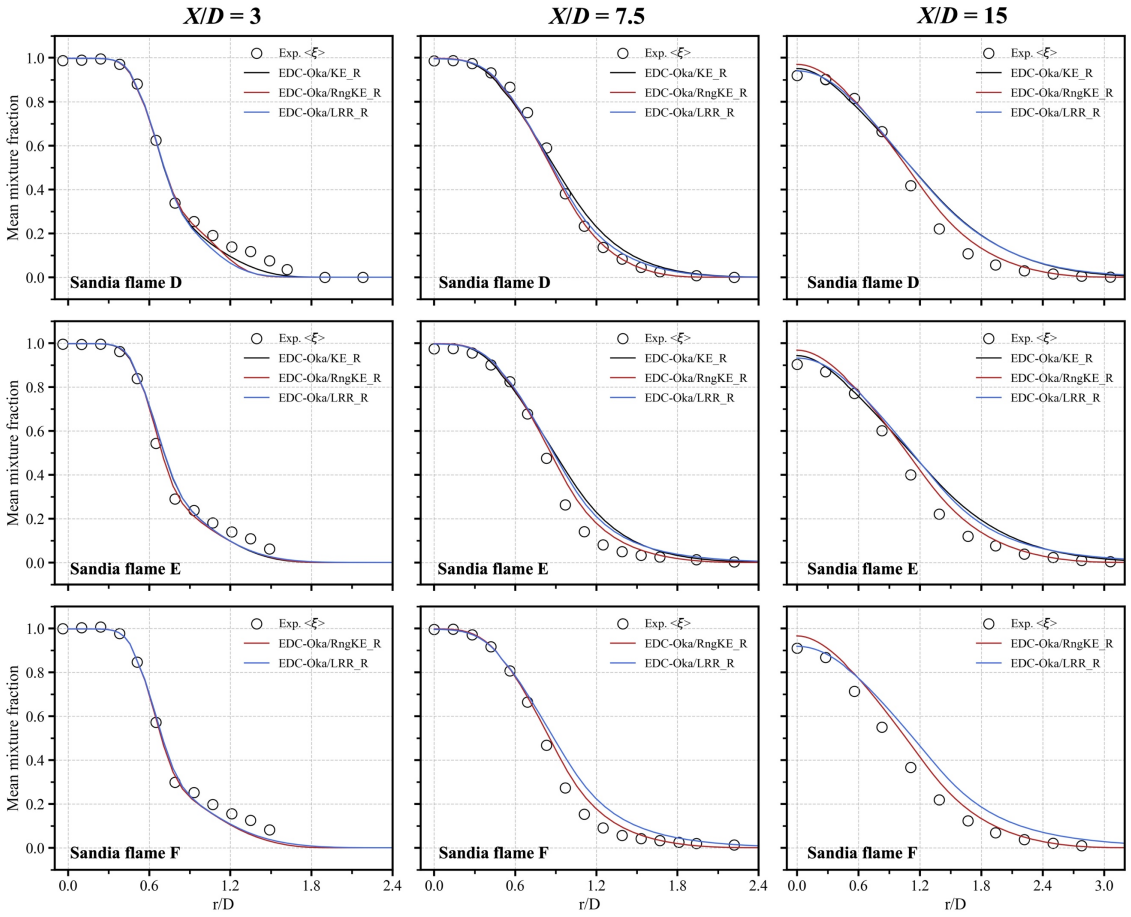

Figure 3.11 Radial profiles of mean mixture value for flame D to flame F at X/D = 3 (left), X/D = 7.5 (middle), and X/D = 15 (right).

Figure 3.12 presents the radial profiles of the NO for flame D to flame F at three different axial locations. Similar to the predictions near the centerline, in terms of radial distribution, the LRR model also demonstrates higher accuracy in NO prediction, while results based on the RngKE and KE models are considerably overestimated. In various jet burning studies concerning hydrocarbon or carbon-free fuels, controlling the inlet velocity of the fuel or oxidizer is a common strategy to reduce NO emissions. This method enhances the recirculation of the fuel in the reaction regions, thereby strengthening the NO reduction reaction. This technique can effectively reduce NO formation in ammonia co-combustion furnaces and has been experimentally validated [19]. The three turbulence models applied in the present study reproduce that phenomenon well through the flow velocity transition (from flame D to flame F), except for a slight overestimation of flame F. This discrepancy could be attributed to the limited precision in simulating severe local extinction and consequently increased over-prediction of mean temperatures within that region, which in turn promotes the generation of additional thermal NO.

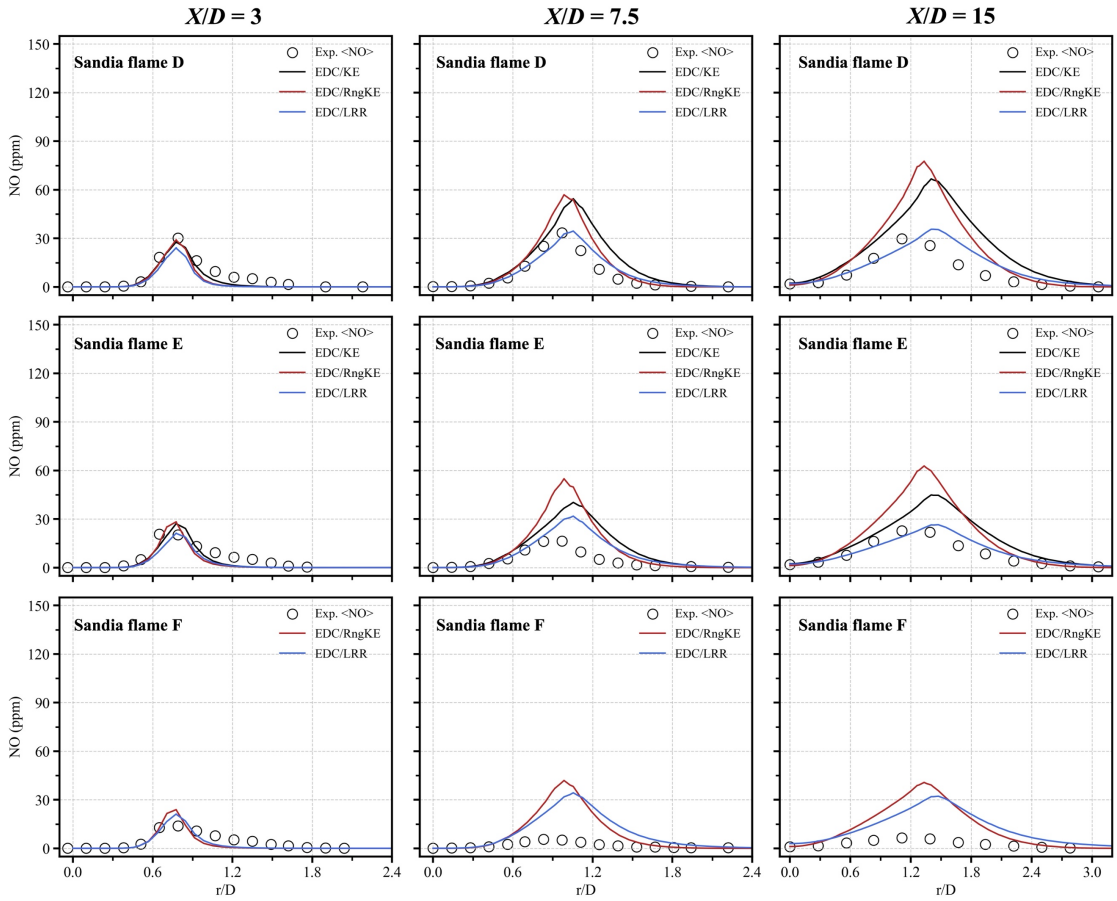

Figure 3.12 Radial profiles of NO for flame D to flame F at X/D = 3 (left), X/D = 7.5 (middle), and X/D = 15 (right).

3.5 LRR model constant assessment

It is known that several variables can affect the prediction accuracy in CFD calculations, including the reaction mechanism [2], combustion model [3,12], and as previously discussed, inlet boundary conditions and turbulence models. In the case of turbulence models, the optimization of turbulence model constants plays a crucial role in achieving accurate predictions, especially to the $C_{\varepsilon 1}$ (related to the dissipation rate). One underlying reason is that the default constant of the turbulence model fails to provide accurate predictions of the spreading rate and dissipation rate under different combustion conditions. Currently, many researchers have put forth recommended values for the $C_{\varepsilon 1}$ within the KE turbulence model according to their customized solver [20,21]. However, there is currently a lack of research related to the constants in the LRR turbulence model. Therefore, in this section, different turbulence model constants ($C_{\varepsilon 1}$) for the LRR model will be examined, based on the solver applied in the present study to determine the optimal prediction solution for the round jet flow.

Figure 3.13 displays a comparison of the mean temperature distribution for flame D under different model constants using the LRR model as well as the RngKE model. The predicted

scalar data for the central axis, $X/D = 7.5$ (flame developing region), and $X/D = 60$ (flame front), are respectively presented in **Fig. 3.14**. It can be observed that, as the $C_{\varepsilon 1}$ gradually increases from the default value (1.44) to 1.5, the turbulence dissipation rate is enhanced, and more turbulence is converted to heat through molecular viscosity, which is particularly evident at the flame front. In the flame developing region, different cases all over-predict the temperature field, with a pronounced effect when $C_{\varepsilon 1}$ is equal to 1.44. At the flame front, an increase in the $C_{\varepsilon 1}$ significantly improves the energy transfer efficiency, resulting in a higher temperature distribution. When $C_{\varepsilon 1}$ equals 1.48, predictions correspond well with experimental data, while the temperature field becomes overestimated as the value increases to 1.5. Therefore, the model constant $C_{\varepsilon 1}$ greater than 1.5 was not examined in the present study. However, for the velocity field, an opposite trend was observed. As $C_{\varepsilon 1}$ changes from 1.44 to 1.5, the dissipation rate increases, accompanied by an enhanced conversion of turbulence into heat. This conversion consistently acts to reduce the turbulent kinetic energy, resulting in a higher deviation of the turbulent kinetic energy from the experimental value at $C_{\varepsilon 1} = 1.5$.

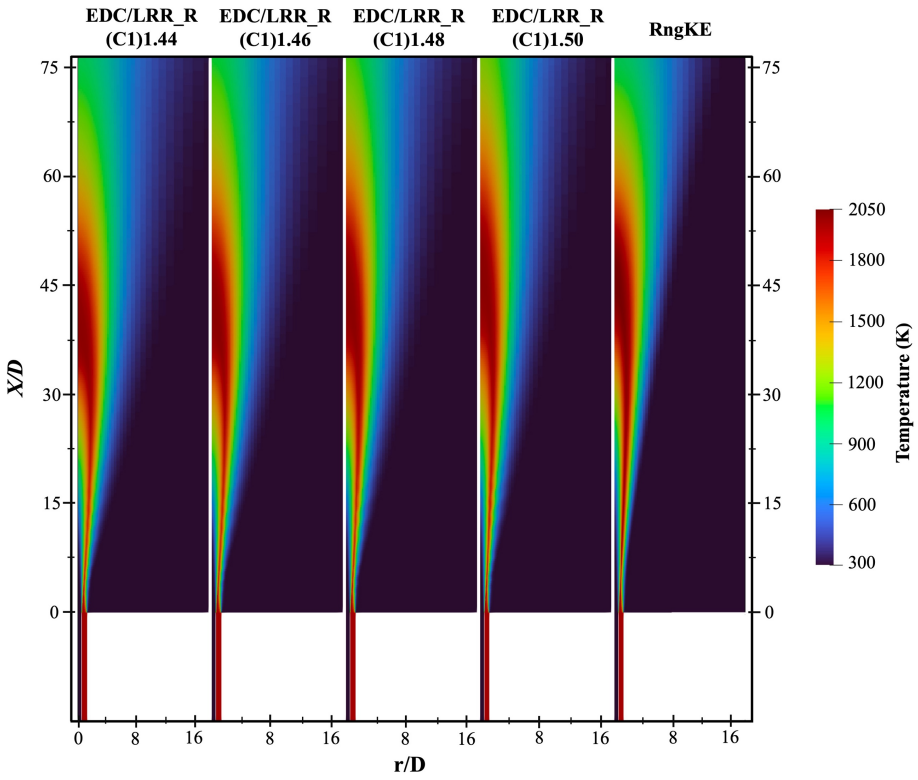

Figure 3.13 Mean temperature distribution of the flame D under different model constants of the LRR model and RngKE model.

In summary, based on the customized solver applied in this thesis, adjusting the $C_{\varepsilon 1}$ from 1.44 to 1.48 in the LRR model achieves better prediction results. A comprehensive analysis of the quantitative prediction performance concerning different model constants will be elaborated

upon in **Sec. 3.6.1**. However, it should be noted that although accurate predictions can be obtained after adjusting the $C_{\varepsilon 1}$, the adjustment of the model constants is of limited value and the notion of generality is lost. As Pope [20] stated, adjusting the model constant value might yield the desired predictions, but in doing so, will simultaneously lose the sense of generality.

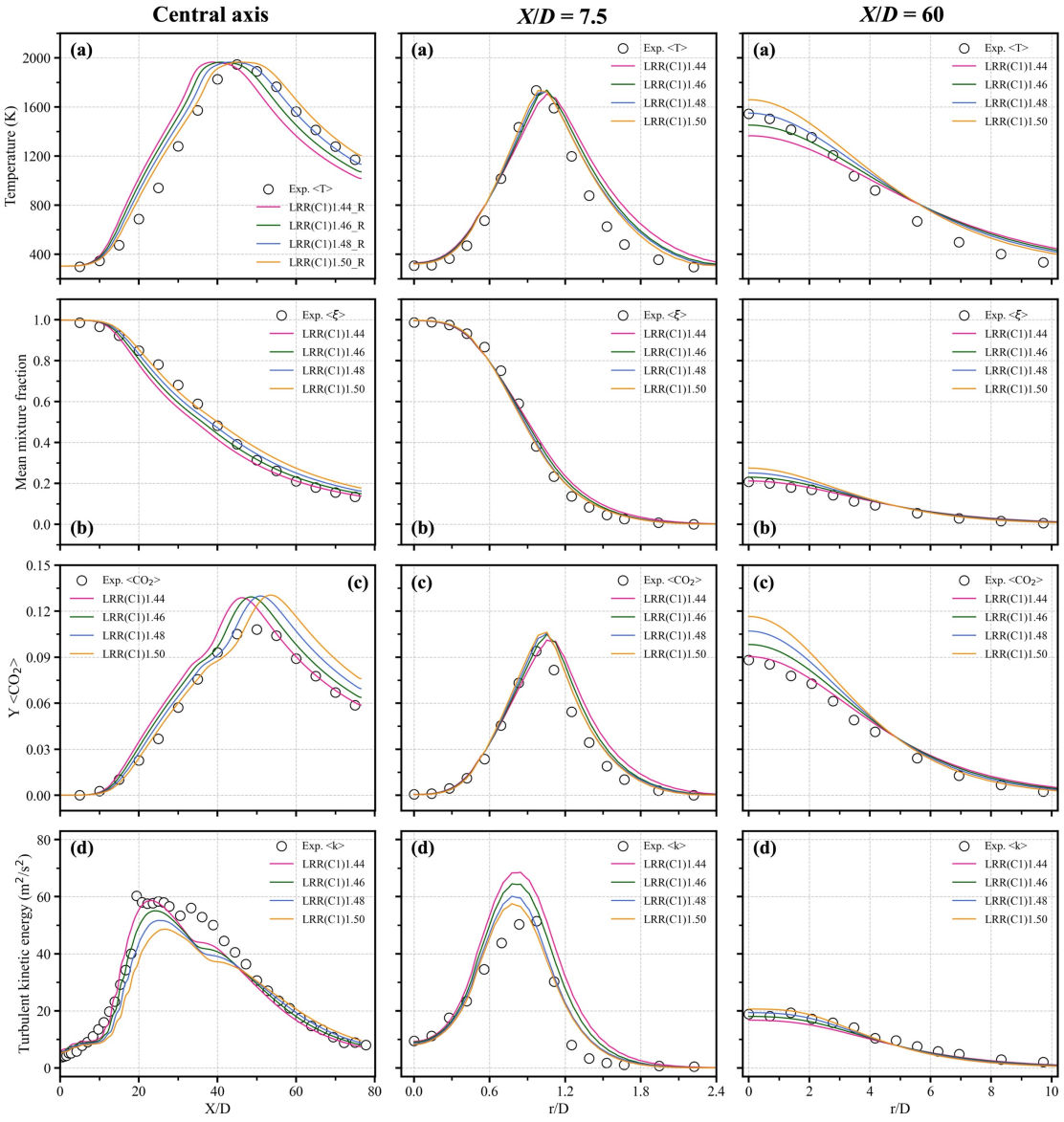

Figure 3.14 Influence of LRR model constant ($C_{\varepsilon 1}$) to the prediction results of flame D.

3.6 Computational model evaluation

3.6.1 Turbulence-combustion models

The assessment of generality and accuracy of various turbulence models has been a crucial topic in combustion predictions, especially when the results cannot be visually discerned. Consequently, the present section quantifies the prediction results derived from an array of turbulence and combustion models to demonstrate their prediction performance. Owing to the

high quality of results from flame D, the analysis will predominantly focus on the prediction performance of flame D.

The Root Mean Square Error (RMSE) serves as an effective method for assessing prediction accuracy and is frequently employed as a performance metric [22]. The RMSE can be regarded as an uncertainty metric when different calculation models are used as a predictor, and its value can be expressed by **Eq. (3.2)**:

$$\mathrm{RMSE} = \frac{1}{\tilde{\Omega}} \sqrt{\frac{1}{n} \sum_{i=1}^{n} [f(x_i) - y_i]^2} \tag{3.2}$$

where n is the number of experimental points, $f(x_i)$ and y_i are the predicted and experimental results, respectively. $\tilde{\Omega}$ is the normalization constant, which can be obtained from the experimental results, as delineated in **Eq. (3.3)**:

$$\tilde{\Omega} = \sqrt{\frac{1}{n} \sum_{i=1}^{n} y_i^2} \tag{3.3}$$

The calculated RMSE values for flame D of various cases along the central axis are shown in **Table 3.3**. In light of the synthesis of prediction results across different cases, three primary conclusions can be drawn. First, the RngKE and LRR turbulence models yield satisfactory predictions. Specifically, the RngKE model provides accurate predictions of the temperature field and major species (CO_2, CH_4, O_2). While the LRR model, better reproduces turbulence effects, thus exhibiting higher accuracy in terms of velocity and turbulent kinetic energy. Additionally, with the LRR model constant $C_{\varepsilon 1}$ set to 1.48, the RMSE value is most reasonable, validating the accuracy of the model constant selection.

Second, for the NO predictions, although the RMSE values for all three types of turbulence models display significant deviations from the experimental values, the LRR model offers superior prediction accuracy compared to the other two models. One explanation pertains to the LRR model accurately predicting the high-temperature field at the flame front, which reduces the thermal NO production. Third, the present study compares differences between the Okafor detailed reaction mechanism and the GRI-3.0. Despite slightly better predictions for the GRI-3.0, the RMSE values obtained under GRI-3.0, and the Okafor detailed mechanism are approximately identical.

For the third point, it should be mentioned that, usually, reaction mechanisms have the most pronounced effects on emission predictions, and the NO is especially sensitive to different reaction mechanisms. It is unclear as to why the difference is not prominent. Given that the Okafor detailed mechanism was built based on GRI-3.0 and is intended for the prediction of

ammonia combustion [23]. The comparable results to GRI-3.0 validates its prediction accuracy. Therefore, more attention can be given to the Okafor detailed mechanism in the simulation of ammonia co-combustion furnace-related cases.

Table 3.3 RMSE values comparison of various calculation cases for major and minor species of Sandia flame D along the central axis.

Case	T	CO_2	F	U	k	CH_4	O_2	NO	N_2
EDC/RngKE	4.60	8.98	4.12	5.97	40.13	7.53	10.21	92.46	0.68
EDC/RngKE (GRI 3.0)	4.71	8.92	4.03	5.87	39.74	7.41	10.13	92.01	0.66
EDC/LRR _(C1)1.44	16.22	15.25	9.34	5.63	11.39	18.46	12.25	40.72	1.03
EDC/LRR _(C1)1.46	12.3	14.28	6.91	3.54	12.68	14.43	11.14	39.34	0.74
EDC/LRR _(C1)1.48	8.61	16.13	5.72	2.01	16.92	9.31	13.87	48.86	0.56
EDC/LRR _(C1)1.50	6.98	20.54	6.76	2.53	23.74	5.56	19.98	56.09	0.64
EDC/KE	10.88	9.68	4.65	2.13	32.99	13.13	9.78	89.35	0.66
PaSR/RngKE	9.49	15.02	7.39	7.48	50.39	7.98	13.26	184.54	0.93

3.6.2 Turbulent Prandtl number

In most CFD modeling studies, an accurate turbulent Prandtl number setting poses a considerable impact on predictions. In other words, the turbulent Prandtl number is a concept pertinent to turbulent heat transfer, and thus, it significantly affects the temperature field. **Figure 3.15** illustrates the influence of turbulent Prandtl numbers on the temperature field. As can be observed, optimal turbulent Prandtl numbers vary when employing different turbulence models. Low RMSE values and low temperature deviations are achieved when the turbulent Prandtl number is set to 0.72 and 0.82 for the LRR and RngKE models, respectively. Nevertheless, the influence of turbulent Prandtl number in combustion prediction research often goes beyond that. Typically, the combustion models assume that the turbulent field transports all scalars, such as CH_4, and CO_2, in a similar way as heat [6]. Moreover, reactions of thermal NO are highly temperature dependent, rendering these species highly sensitive to the turbulent Prandtl number. Combining **Figs. 3.8**, **3.12**, **3.15**, and **Table 3.3**, the above conclusion explains why the LRR model outperforms the other two turbulence models in terms of NO prediction, which is

attributed to the lowered turbulent Prandtl number setting.

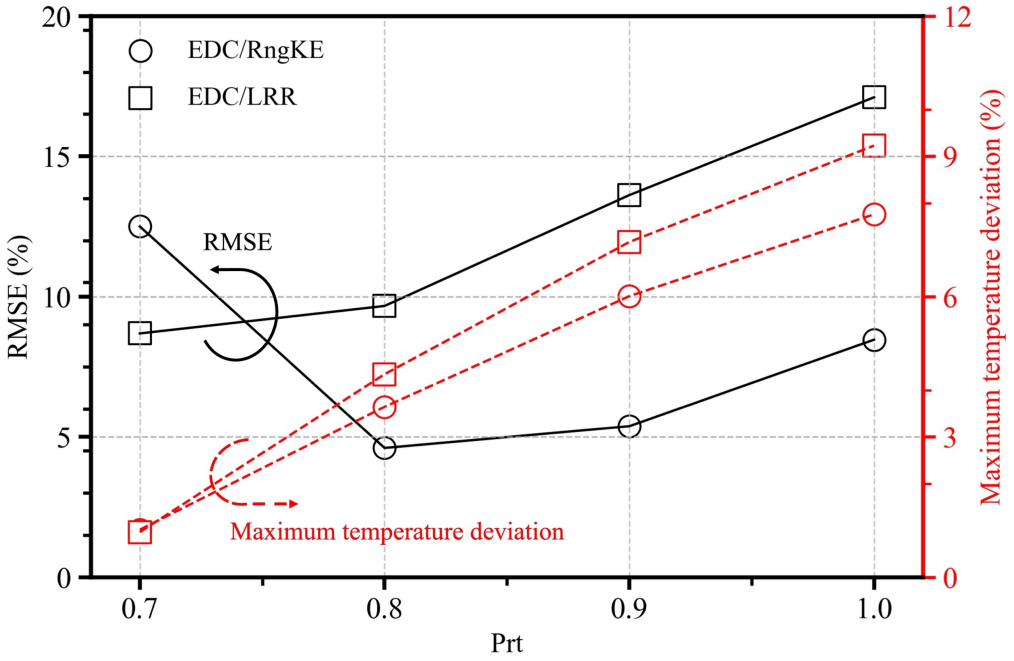

Figure 3.15 Influence of the turbulent Prandtl number on the temperature field for flame D simulation.

3.7 Influence of the integrated acceleration method on prediction results

So far, this chapter has validated the effectiveness of the solver in both computational acceleration and numerical prediction. For the completeness of model validation, it is also necessary to investigate whether introducing the integrated acceleration strategy affects the numerical prediction results. Therefore, this section aims to display the differences in numerical prediction results for Sandia flames D-F before and after implementing the integrated acceleration strategy. Based on the numerical prediction results, the RngKE turbulence model and EDC combustion model, which provided better prediction results, were used for comparison, and the turbulent Prandtl number was adjusted accordingly.

Figure 3.16 compares the centerline profiles of temperature, mean mixture value, and velocity based on the Standard model versus after incorporating the integrated acceleration strategy. It is observed that the numerical predictions achieve the same results as the Standard model. However, the adoption of the integrated acceleration strategy significantly improves computational performance, demonstrating its effectiveness in enhancing the efficiency of simulations without affecting the accuracy of predictions. Therefore, in the subsequent three-dimensional numerical simulations of the ammonia co-combustion furnace, the computational acceleration strategy will be employed for simulation.

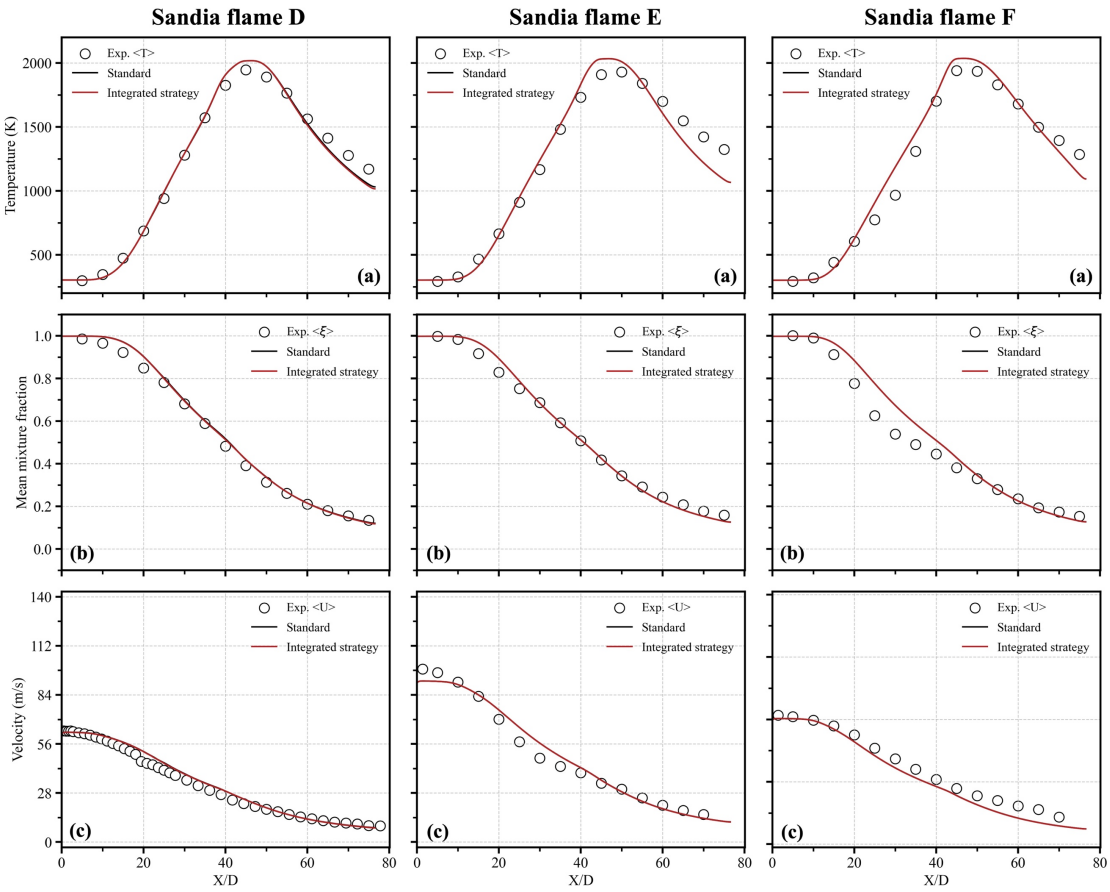

Figure 3.16 Comparison of numerical prediction results before and after the introduction of integrated acceleration strategy.

3.8 Summary

To validate the accuracy of the solver proposed in this thesis for numerical calculations and to assess the computational speed-up achieved by the integrated acceleration strategy, the present chapter selected three distinct partially turbulent premixed flames (Sandia flames D, E, and F) for two-dimensional numerical analysis. The following results were obtained:

First, for the numerical simulation of flame D, a comparison of different acceleration strategies showed that the strong scaling performance of the customized solver significantly improved after introducing the DLB + SpeedCHEM method. The further introduction of the OpenMP method reduced communication bottlenecks between processors, resulting in nearly a 30-fold increase in computational speed compared to the Standard model when using the optimal OpenMP × MPI combination. Moreover, introducing this integrated acceleration strategy to the solver did not significantly affect the prediction accuracy.

Subsequently, through a comprehensive comparative analysis involving various turbulence models, turbulent Prandtl numbers, and model constants, optimal numerical parameters were identified for various conditions. Overall, the prediction results demonstrate that all three

turbulence models, after the appropriate selection of wall functions, are capable of reasonably reproducing the experimental outcomes. Regarding the flame D calculation, the LRR model achieves better prediction results when the model constant and turbulent Prandtl number are set to 1.48 and 0.72, respectively. In contrast, increasing the turbulent Prandtl number by 0.1 for RngKE and KE models yields improved results. The RngKE turbulence model demonstrates higher accuracy in the temperature field and major species predictions, while the LRR model exhibits superior precision in velocity field predictions.

Concerning the NO prediction, the LRR model provides noticeably better results than the other two turbulence models, as it predicts the peak temperature with improved accuracy, which reduces the formation of thermal NO. The investigation particularly focused on the impact of the turbulent Prandtl number on the NO prediction, revealing that increasing the turbulent Prandtl number in scenarios with increased inlet jet velocities yielded improved results.

Overall, the customized solver developed in the present study has been verified and can be implemented in the subsequent three-dimensional ammonia co-combustion furnace analysis.

References

[1] R. Barlow, J. Frank, Piloted CH_4/air flames C, D, E, and F – Release 2.1. *TNF Workshop*, 2007, available from: https://tnfworkshop.org/data-archives/pilotedjet/ch4-air/.

[2] B. Lilleberg, D. Christ, I.S. Ertesvåg, K.E. Rian, R. Kneer, Numerical simulation with an extinction database for use with the eddy dissipation concept for turbulent combustion. *Flow, Turbulence and Combustion*, 2013, 91: 319–346.

[3] D.A. Lysenko, I.S. Ertesvåg, K.E. Rian, Numerical simulations of the Sandia flame D using the eddy dissipation concept. *Flow, Turbulence and Combustion*, 2014, 93: 665–687.

[4] R.S. Barlow, J.H. Frank, Effects of turbulence on species mass fractions in methane/air jet flames. *Symposium (International) on Combustion*, 1998, 27: 1087–1095.

[5] S.M. Rassoulinejad-Mousavi, Y. Mao, Y. Zhang, Reducing greenhouse gas emissions in Sandia methane-air flame by using a biofuel. *Renewable Energy*, 2018, 128: 313–323.

[6] U.C. Goldberg, S. Palaniswamy, P. Batten, V. Gupta, Variable turbulent Schmidt and Prandtl number modeling. *Engineering Applications of Computational Fluid Mechanics*, 2010, 4: 511–520.

[7] M.T. Lewandowski, Z. Li, A. Parente, J. Pozorski, Generalised Eddy Dissipation Concept for MILD combustion regime at low local Reynolds and Damköhler numbers. Part 2: Validation of the model. *Fuel*, 2020, 278: 117773.

[8] L.P. Chua, R.A. Antonia, Turbulent Prandtl number in a circular jet. *International Journal of Heat and Mass Transfer*, 1990, 33: 331–339.

[9] B. Tekgül, P. Peltonen, H. Kahila, O. Kaario, V. Vuorinen, DLBFoam: An open-source dynamic load balancing model for fast reacting flow simulations in OpenFOAM. *Computer Physics Communications*, 2021, 267: 108073.

[10] M. Raju, M. Wang, M. Dai, W. Piggott, D. Flowers, Acceleration of detailed chemical kinetics using multi-zone modeling for CFD in internal combustion engine simulations, in *SAE 2012 World Congress & Exhibition*, SAE International, 2012, 2012-01-0135.

[11] M.T. Lewandowski, P. Płuszka, J. Pozorski, Influence of inlet boundary conditions in computations of turbulent jet flames. *International Journal of Numerical Methods for Heat & Fluid Flow*, 2018, 28: 1433–1456.

[12] V. Jaganath, M. Stoellinger, Transported and presumed probability density function modeling of the Sandia flames with flamelet generated manifold chemistry. *Physics of Fluids*, 2021, 33: 045123.

[13] A. Habibi, B. Merci, D. Roekaerts, Turbulence radiation interaction in Reynolds-averaged Navier–Stokes simulations of non-premixed piloted turbulent laboratory-scale flames. *Combustion and Flame*, 2007, 151: 303–320.

[14] V. Bianco, A. Khait, A. Noskov, V. Alekhin, A comparison of the application of RSM and LES turbulence models in the numerical simulation of thermal and flow patterns in a double-circuit Ranque-Hilsch vortex tube. *Applied Thermal Engineering*, 2016, 106: 1244–1256.

[15] R. Saini, S. Prakash, A. De, R. Yadav, Investigation of NOx in piloted stabilized methane-air diffusion flames using finite-rate and infinitely-fast chemistry based combustion models. *Thermal Science and Engineering Progress*, 2018, 5: 144–157.

[16] M.R. Roomina, R.W. Bilger, Conditional moment closure (CMC) predictions of a turbulent methane-air jet flame. *Combustion and Flame*, 2001, 125: 1176–1195.

[17] D. He, Y. Yu, Y. Kuang, C. Wang, Model comparisons of flow and chemical kinetic mechanisms for methane–air combustion for engineering applications. *Applied Sciences*, 2021, 11: 4107.

[18] V. Raman, R.O. Fox, A.D. Harvey, Hybrid finite-volume/transported PDF simulations of a partially premixed methane–air flame. *Combustion and Flame*, 2004, 136: 327–350.

[19] K. Kikuchi, R. Murai, T. Hori, F. Akamatsu, Fundamental study on ammonia low-NOx combustion using two-stage combustion by parallel air jets. *Processes*, 2021, 10: 23.

[20] S.B. Pope, An explanation of the turbulent round-jet/plane-jet anomaly. *AIAA Journal*, 1978, 16: 279–281.

[21] G. Li, B. Naud, D. Roekaerts, Numerical investigation of a bluff-body stabilised non-premixed flame with differential Reynolds-stress models. *Flow, Turbulence and Combustion*, 2003, 70: 211–240.

[22] Y. Ögren, P. Tóth, A. Garami, A. Sepman, H. Wiinikka, Development of a vision-based soft sensor for estimating equivalence ratio and major species concentration in entrained flow biomass gasification reactors. *Applied Energy*, 2018, 226: 450–460.

[23] E.C. Okafor, Y. Naito, S. Colson, A. Ichikawa, T. Kudo, A. Hayakawa, H. Kobayashi, Experimental and numerical study of the laminar burning velocity of CH_4–NH_3–air premixed flames. *Combustion and Flame*, 2018, 187: 185–198.

Chapter 4

Development of low-NO ammonia co-combustion furnace

4.1 Introduction

As mentioned in the introduction of **Chapter 1**, when ammonia is introduced as a fuel in power systems, two major challenges are inevitably encountered during combustion: low laminar burning velocity (resulting in combustion instability) and high NO emissions [1–3]. The former issue can typically be addressed by co-firing ammonia with some traditional hydrocarbon fuels, which not only increases the laminar burning velocity of ammonia but also effectively controls carbon dioxide emissions [4–6]. However, controlling NO emissions is relatively more difficult and often requires specific adjustments to the burner structure.

Among the current methods for controlling NO emissions in ammonia co-combustion furnaces, introducing the air-staged strategy is seen as a highly economical and effective approach. This method creates a fuel-rich region within the furnace, utilizing ammonia as an effective NO reduction agent to achieve the reduction of NO. Therefore, in the 10-kW ammonia co-combustion furnace explored in this thesis, the burner is also equipped with a secondary injection system, as shown in **Fig. 4.1**. In this secondary injection system, secondary air, fuel, and primary air are injected into the furnace from the same wall, thereby applying the internal air-staged combustion method.

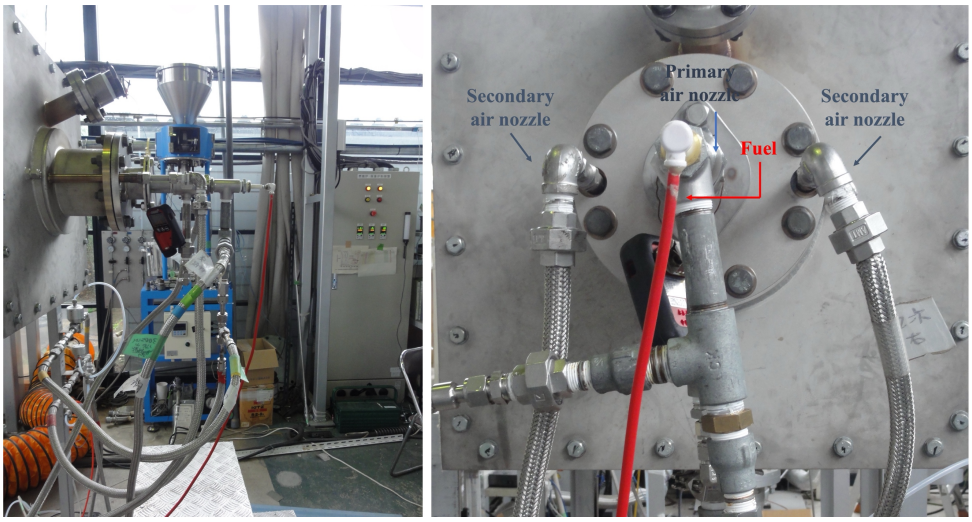

Figure 4.1 Photograph of the 10-kW co-combustion furnace and parallel injection system.

Within the scope of internal air-staged combustion, another common approach to effectively reduce the formation of NO inside the furnace is to decrease the total air ratio injected. However, this operation can significantly increase the risk of ammonia leakage, leading to secondary

accidents and potential secondary pollution [7,8]. In the previous research on the 10-kW ammonia co-combustion furnace, Kikuchi et al. [9] set the total air ratio at 1.2 for each operating condition, achieving a relative balance between controlling NO emissions and preventing ammonia leakage.

Under a fixed total air ratio inside the furnace, adjusting the primary and secondary air ratio allows for different forms of combustion within the same burner structure. As previously mentioned, for ammonia co-firing systems, creating a slightly fuel-rich region through airflow control is desirable. However, based on the majority of current published research, for the ammonia co-combustion equipped with a parallel injection system, there is no definitive conclusion on how to adjust the primary and secondary air ratios to maximize suppression of NO formation. In other words, the impact of the air-staging ratio on NO formation and emission inside the furnace remains unclear.

Additionally, for the secondary injection system using the internal air-staged combustion method, many other parameters can also influence the combustion characteristics within the furnace. For example, the distance between the primary and secondary nozzles can affect the formation of the fuel-rich region inside the furnace, thereby impacting NO emissions. The diameter of the secondary nozzles, while influencing the velocity of secondary air entering the furnace, also indirectly affects the flow field distribution inside the furnace, thereby impacting NO formation and emission. Therefore, in exploring the optimal value for the air-staging ratio, the present chapter will also investigate these two parameters to explore the optimal conditions for controlling NO formation in the ammonia co-combustion furnace.

In summary, the present chapter aims to comprehensively elucidate the combustion and emission characteristics of ammonia co-firing in a 10-kW combustion furnace under varying conditions of the secondary injection system. After verifying the numerical prediction accuracy of the solver in **Chapter 3**, this chapter will use the solver as a numerical tool to conduct a three-dimensional numerical analysis of the combustion furnace to explore the optimal solutions for controlling NO emissions under different air-staging ratios, nozzle distances, and secondary nozzle diameters, providing references for future industrial applications.

4.2 10-kW combustion furnace

4.2.1 Combustion furnace specifications

The present chapter focuses on a 10-kW lab-scale combustion furnace designed for ammonia co-firing [9]. This furnace is outfitted with a secondary air injection system inside the burner, facilitating air-staged combustion to minimize NO production. The combustion chamber has internal dimensions of 1200 mm in length (X-axis), 300 mm in width (Y-axis), and 300 mm in

height (Z-axis). Its exterior is covered with a 100 mm thick layer, consisting of 92 mm of ceramic fiber insulation and an 8 mm steel plate for thermal insulation. During the experiments, a flue gas analyzer is installed near the furnace outlet to measure and alert for NO and unburned ammonia. Data acquisition is performed when the combustion reaches stability and after confirming the absence of ammonia leakage, typically below 1 ppm.

As mentioned previously, in the present study, the burner structure differs from common designs that introduce air through the side walls of the combustion chamber. Instead, this burner is equipped with a parallel injection system. **Figure 4.2** shows the detailed simulated geometry of the 10-kW ammonia co-combustion furnace. It is evident from the figure that the primary and secondary air nozzle, along with the fuel nozzle, are all positioned on the same wall. The secondary nozzles are symmetrically installed at both sides of the primary nozzle. During the combustion process, air-staged combustion is realized by simultaneously supplying air through both the primary and secondary nozzles.

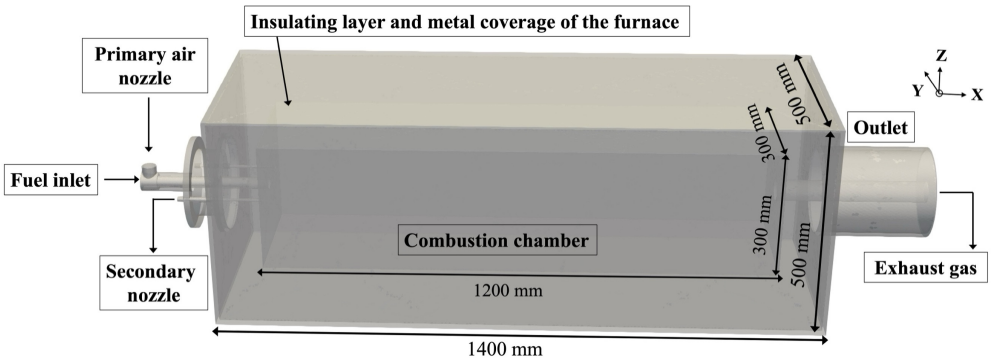

Figure 4.2 The simulated geometry of the 10-kW ammonia co-combustion furnace with parallel injection system.

Figure 4.3 (a) – (c) respectively illustrate the dimensional details of the combustion furnace along the Z-plane cross-section, the details of the parallel injection system, and the burner configuration along the X-plane cross-section. The burner incorporates multiple adjustable parameters, allowing for altering the combustion state within the furnace to achieve optimal conditions. Since the focus of the present chapter is on the effects of air-staging ratio, secondary nozzle diameter (D_2), and the distance between the primary and secondary nozzle diameters (L) on NO formation and combustion behavior. Hence, other parameters are kept constant. Specifically, the fuel nozzle diameter (D_f) is fixed at 16.7 mm, and the primary air nozzle diameter (D_1) at 27.2 mm. Moreover, as outlined in **Sec. 4.1**, the total air ratio (λ_{total}) injected into the furnace is set at 1.2 to balance unburned ammonia and NO emissions. Therefore, in numerical calculations, adjusting the injection ratio between primary (λ_1) and secondary (λ_2) air can determine the impact of the air-staging ratio on the combustion state within the furnace.

During the experiments, the reaction air flow for the non-staged combustion was entirely supplied by the primary air nozzle ($\lambda_1 = 1.2$, $\lambda_2 = 0$)

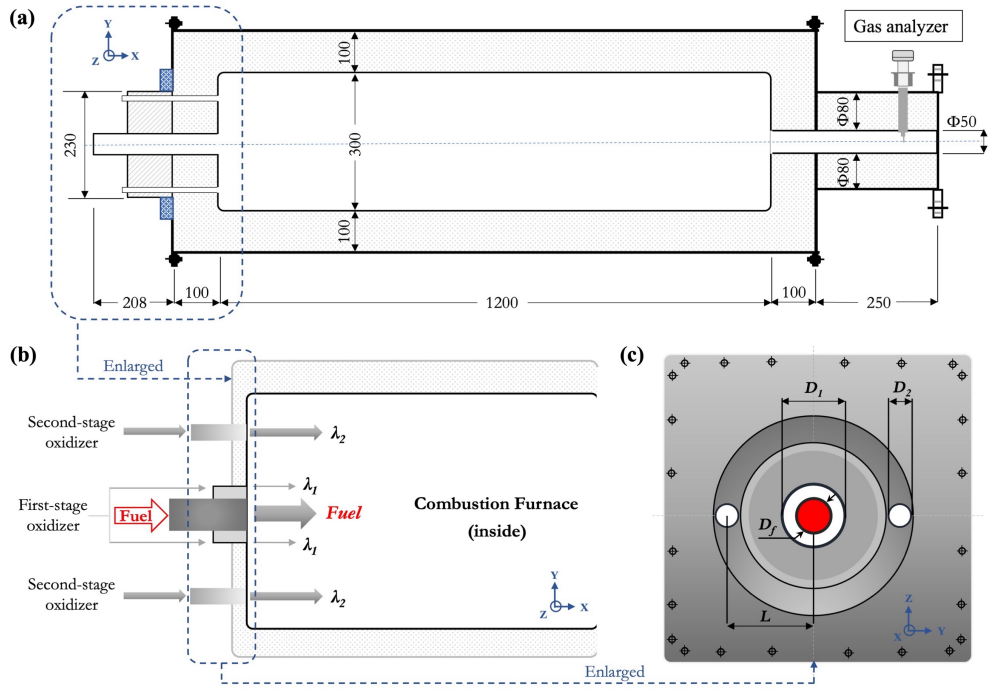

Figure 4.3 Schematic diagram of (a) Z-plane cross-section of the 10-kW combustion furnace; (b) parallel injection system; (c) burner configuration.

4.2.2 Experimental and modeling conditions

Considering the industrial purposes, the conducted experiments utilized a blend of ammonia and City gas 13A as the fuel for co-combustion. City gas 13A is a composite fuel comprising various hydrocarbons, predominantly consisting of methane (CH_4) at 88.9%, ethane (C_2H_6) at 6.8%, propane (C_3H_8) at 3.1%, and butane (C_4H_{10}) at 1.2% by volume fraction [9]. It is a commonly utilized city gas in Japan, characterized by its higher Lower Heating Value (LHV) of 40.65 MJ/Nm³ and higher adiabatic flame temperature compared to methane. The division of the ammonia co-firing ratio (E_{NH3}) was determined based on the LHV of the two fuels, as indicated by **Eq. (4.1)**. The two fuels are pre-mixed and adjusted to the required proportions after pressure reduction by regulators to a co-firing ratio of 10% (in all computational conditions explored in this chapter, the ammonia co-firing ratio is fixed at this value). Subsequently, at room temperature, the mixed fuel is supplied to the combustion chamber through a mass flow controller. The discussion regarding the combustion characteristics at higher ammonia co-firing ratios will be conducted in the next chapter.

$$E_{NH3}[\%] = \frac{X_{NH3} \times LHV_{NH3} \times 100}{X_{NH3} \times LHV_{NH3} + (1 - X_{NH3}) \times LHV_{13A}} \tag{4.1}$$

Table 4.1 summarizes the numerical calculation conditions employed in this chapter. A total of sixteen cases were considered and simulated to investigate the effect of the air-staging ratio, air nozzle distance (L), and secondary nozzle diameter (D_2) on NO emission characteristics. First, the air-staging ratio, subsequently referred to as the primary air ratio (λ_1), describes the relative relationship between the primary and secondary air ratios. The total air ratio (λ_{total}), representing the sum of the primary and secondary air ratios, was fixed at 1.2. During the experiment, the primary air ratio was increased from 0 to 1.2 in increments of 0.2, while the corresponding secondary air ratio decreased from 1.2 to 0. This complementary variation formed seven different gradients to explore the impact of the primary air ratio on the combustion characteristics within the furnace.

In the calculations, except for the condition where non-staged combustion (λ_1 = 1.2, case 1) negates the need to consider the impact of the secondary nozzle diameter, two sets of secondary nozzle diameters, 6.6 and 7.8 mm, were set for different primary air ratios to identify common patterns during the combustion process, as shown in cases (4.1) - (4.13). Additionally, to investigate the effect of different secondary nozzle diameters on NO formation, an extra calculation was performed for a primary air ratio of 0.6 with D_2 = 4.2 mm, as depicted in case (4.14). Finally, cases (4.15) and (4.16) will discuss the variations in combustion characteristics within the furnace under different air nozzle distances. The quantities of fuel and air supplied for the numerical calculations were aligned with the experimental conditions, maintaining a consistent combustion power of 11.63-kW. The inlet temperatures for primary air, secondary air, and fuel were maintained at 300 K.

Table 4.1 Summary of the calculation conditions in the present chapter.

Case	L (mm)	D_2 (mm)	E_{NH3} (%)	λ_1	λ_2	Mass flow velocity ×10^{-3} (kg/s)		
						Fuel	1st air	2nd air
(4.1)	-	-		1.2	0		4.7548	-
(4.2)		7.8		1.0	0.2		3.9623	0.7925
(4.3)		6.6		1.0	0.2			
(4.4)		7.8		0.8	0.4		3.1698	1.5849
(4.5)		6.6		0.8	0.4			
(4.6)	100	7.8	10	0.4	0.8	0.2712	1.5849	3.1698
(4.7)		6.6		0.4	0.8			
(4.8)		7.8		0.2	1.0		0.7925	3.9623
(4.9)		6.6		0.2	1.0			
(4.10)		7.8		0	1.2		-	4.7548

Table 4.1 Summary of the calculation conditions in the present chapter (continued).

Case	L (mm)	D_2 (mm)	E_{NH3} (%)	λ_1	λ_2	Mass flow velocity $\times 10^{-3}$ (kg/s)		
						Fuel	1st air	2nd air
(4.11)	100	6.6	10	0	1.2	0.2712	-	4.7548
(4.12)		7.8		0.6	0.6		2.3774	2.3774
(4.13)		6.6		0.6	0.6			
(4.14)		4.2		0.6	0.6			
(4.15)	50	6.6		0.6	0.6			
(4.16)	140	6.6		0.6	0.6			

Figure 4.4 presents the grid layout for the Y-plane and Z-plane sections of the 10-kW combustion furnace, with the secondary nozzle diameter and air nozzle distance set at 6.6 mm and 100 mm, respectively. Since the CHT method was introduced in the three-dimensional numerical calculations, the computational domain includes a fluid region and four different solid regions, with grids refined near the burner. The combustion furnace grid was generated using ANSYS Fluent Meshing, employing an unstructured poly-hexcore mesh as the grid type for three-dimensional simulations. Compared to the traditional tetrahedral or polyhedral grids, this type of mesh significantly reduces the number of grid cells required without compromising computational accuracy, thereby enhancing computational efficiency. The total number of grid cells in the computational domain is approximately two million. The same meshing parameters were used for cases with different air nozzle distances and secondary nozzle diameters.

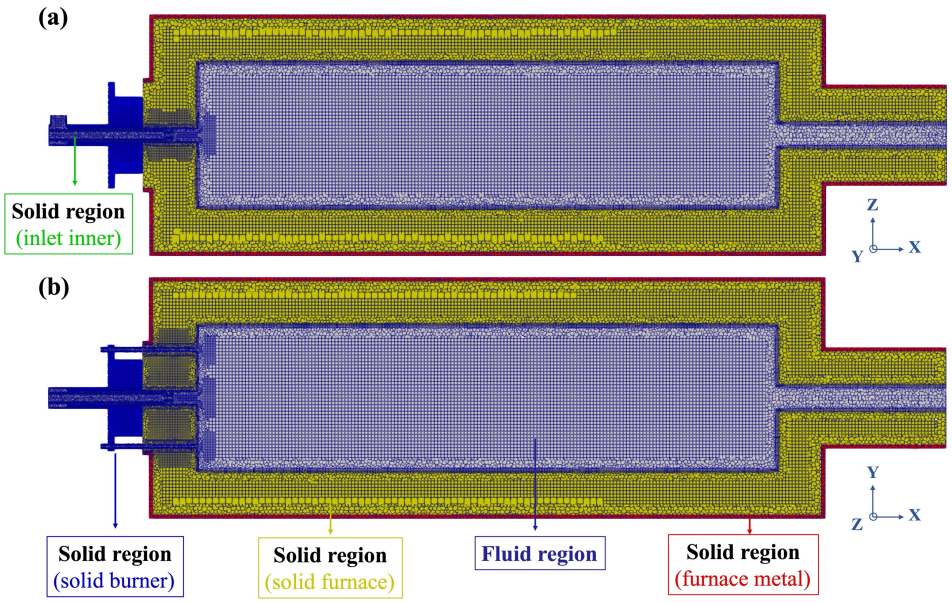

Figure 4.4 Computational domain and grid information of the combustion furnace, where (a) is the Y-plane section and (b) is the Z-plane section.

4.3 Computational efficiency comparison

The present section will discuss the computational acceleration capabilities of the integrated acceleration strategy when extended to three-dimensional calculations. In finite-rate chemistry, the reaction mechanism significantly influences the prediction accuracy of numerical calculations. Detailed chemical reaction mechanisms help better understand the combustion characteristics within the furnace and NO emissions. Along with introducing the Okafor detailed reaction mechanism in **Sec. 2.5**, the Sako reaction mechanism was also introduced [10]. Sako reaction mechanism is based on the nitrogen element-tracking method suitable for ammonia-methane co-combustion, which also allows for the analysis of NO formation sources during the reaction process. This mechanism includes 90 species and 607 sub-reactions and holds significant relevance for the combustion analysis of industrial furnaces. Therefore, in this section, in addition to exploring the acceleration capabilities of the integrated acceleration strategy based on the Okafor detailed reaction mechanism (comprising 59 species and 356 sub-reactions), the acceleration capabilities of the customized solver extended to Sako reaction mechanism will also be examined, providing a reference for the future application of more detailed reaction mechanisms.

Figure 4.5 presents the computational speed-up achieved when simulating the 10-kW ammonia co-combustion furnace under the Okafor detailed and Sako reaction mechanism. The test conditions are based on a secondary nozzle diameter of 6.6 mm and the distance between the primary and secondary air nozzle of 100 mm. Same as the calculations for flame D, all speed-up tests were conducted for 1000 iterations under the constant time steps of 10^{-6} s after ignition. However, due to a significant increase in computational grid cells, the computational domain was expanded to 256 sections. All cases utilized 32 nodes during the computation, and the distribution of OpenMP threads × MPI ranks was set to 8 × 256.

For the performance analysis results of the Okafor detailed reaction mechanism in **Fig. 4.5**, similar to the results for flame D, the speed-up performance for the 3D combustion furnace calculation was not very significant after introducing the DLB code, resulting in approximately 1.29 times increase. Incorporating the SpeedCHEM chemistry solver also led to a more than 4 times increase in computational performance, confirming the universality and robustness of this chemistry solver in computations. However, due to the notable increase in grid cells and the division into more computational sub-domains, the communication overhead among different MPI ranks increased. Therefore, the performance improvement brought by the OpenMP method was noticeably less than that for the 2D flame D calculation, around 7.06 times. Interestingly, regarding the Sako reaction mechanism, using the integrated acceleration strategy improved the

acceleration factor to 13.88 compared to the Standard model, which can be due to the benefits of the sparse analytical Jacobian and the efficient utilization of the OpenMP method [11,12]. Overall, the integrated acceleration strategy introduced in the present thesis can also significantly enhance computational performance in 3D larger-scale simulations. As the reaction mechanism becomes more complex, the advantages of the combined acceleration strategy become more apparent, facilitating the use of more precise and detailed reaction mechanisms in future research.

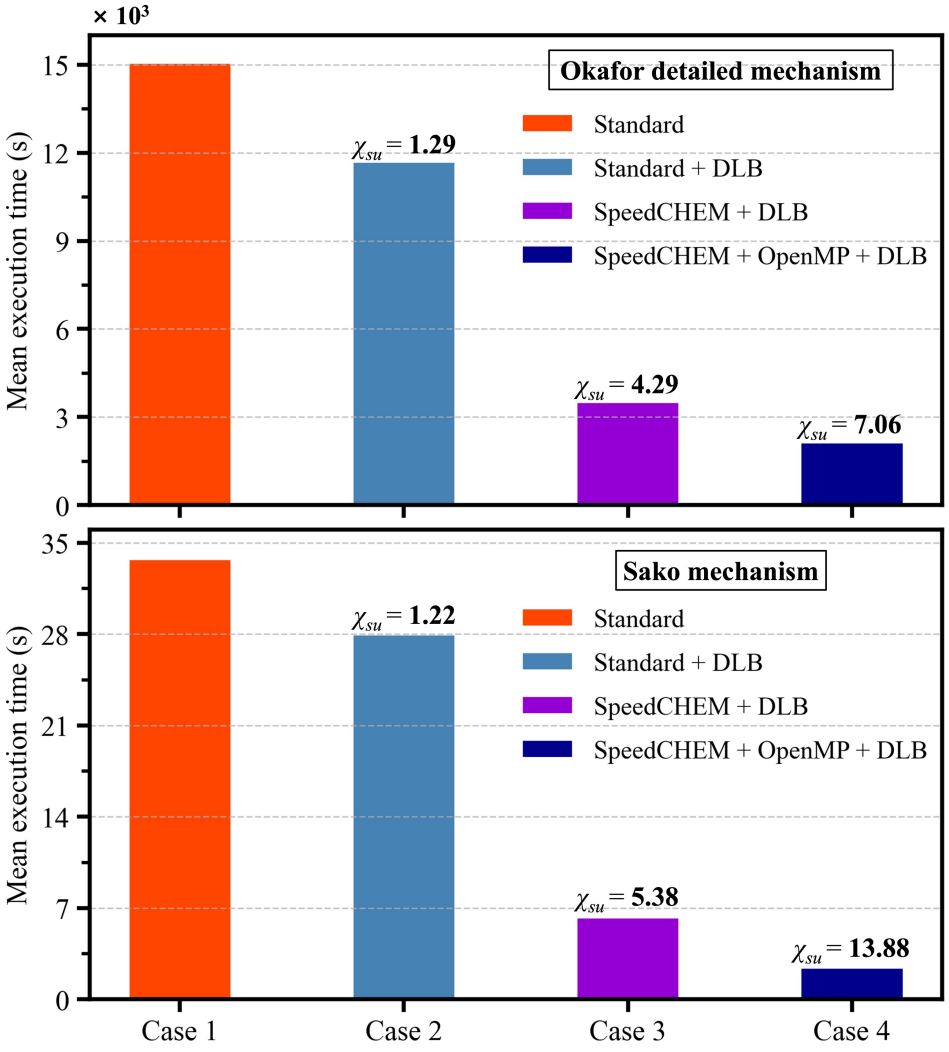

Figure 4.5 Mean execution times over 1000 iterations for the 10-kW ammonia co-combustion furnace simulation under 256 computational sub-domains using Okafor detailed (up) and Sako (down) reaction mechanism.

4.4 Influence of the primary air ratios on NO emission

4.4.1 Trends and model validation of NO emissions

The integration of a secondary injection system in the ammonia combustion furnace aims to

divert part of the air through a secondary nozzle, enabling the adjustment of the air injection ratio between the primary and secondary nozzles. Such adjustments modify the equivalence ratio in specific zones, creating a fuel-rich region near the fuel nozzle outlet to manage NO formation. Consequently, understanding the distribution of fuel-rich regions within the furnace at various air ratios is crucial before exploring the effects of the primary air ratio on NO formation and emissions. The Global Equivalence Ratio (GER) serves as a critical parameter representing the fuel-to-air ratio in the combustion process across different furnace regions. When this value is greater than 1, it indicates a fuel-rich region. Conversely, when it is less than 1, it means insufficient fuel and incomplete combustion. The GER is highly effective for characterizing the distribution of the fuel-rich region under varying conditions.

Figures 4.6 and **4.7** depict the GER distribution within the furnace along the Z-plane section at different primary air ratios, with the secondary nozzle diameters of 6.6 mm and 7.8 mm, respectively. The corresponding secondary air ratio is calculated by subtracting the primary air ratio from the total air ratio of 1.2. It is noted that during the transition from complete air supply by the primary nozzle (λ_1 = 1.2) to complete air supply by the secondary nozzle (λ_1 = 0), a distinctly fuel-rich region (far rich equivalence ratio) forms in the central area of the furnace, which we subsequently refer to as the Primary Air (PA) zone. The area near the outlet of the secondary nozzle is referred to as the Secondary Air (SA) zone.

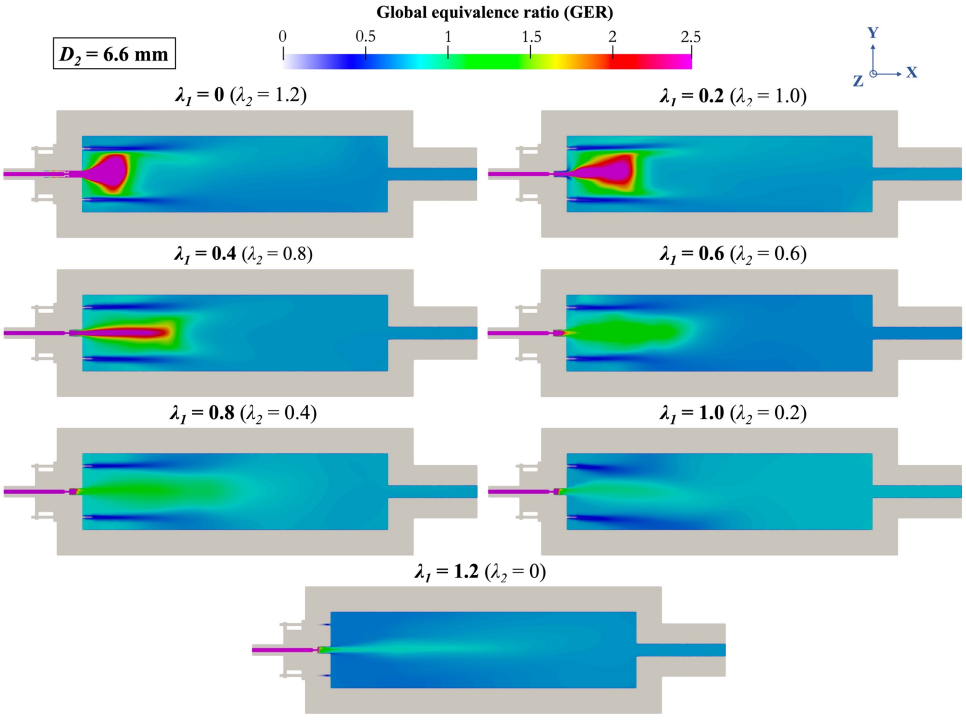

Figure 4.6 GER distribution at different primary air ratios along the Z-plane section at the secondary nozzle diameter of 6.6 mm.

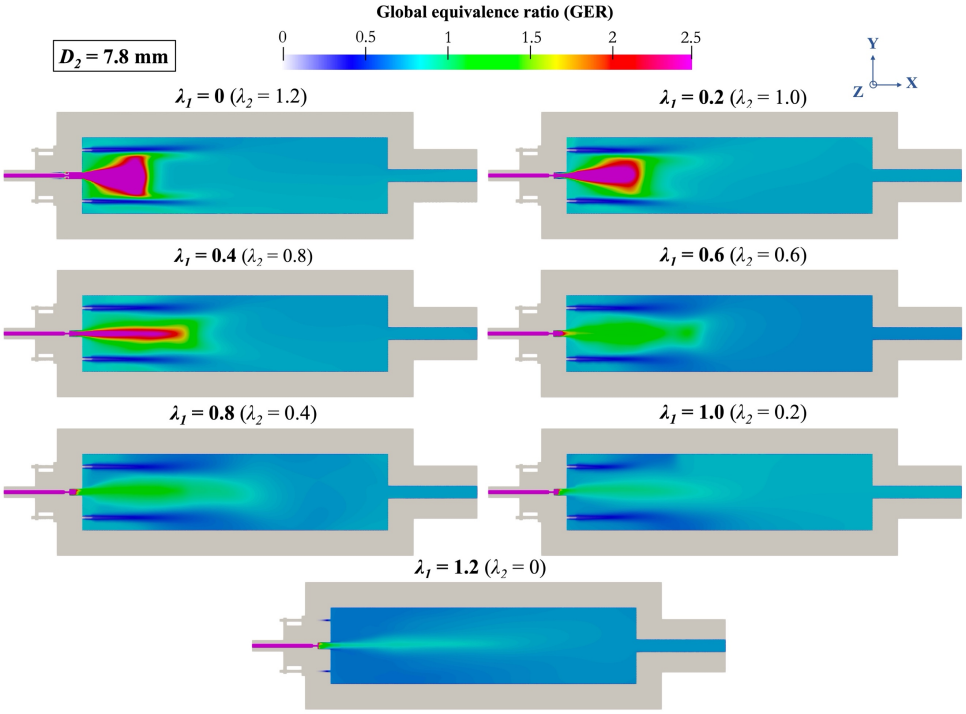

Figure 4.7 GER distribution at different primary air ratios along the Z-plane section at the secondary nozzle diameter of 7.8 mm.

Figure 4.8 (a) and **(b)** respectively represent the variation in NO emission rates under different primary air ratios, with secondary nozzle diameters of 6.6 mm and 7.8 mm. In the scenario with D_2 = 6.6 mm, the figure also contrasts simulation results with experimental data. It is crucial to note that the experimental NO measurement results were obtained after removing the influence of water vapor by cooling the flue gas. Consequently, the numerical comparisons in this section also eliminate the impact of water vapor in the exhaust (dry gas). The uncertainty in NO measurements during the experiments was approximately 10%. The error bars in the figure are derived by calculating the ratios of maximum potential experimental deviations at each primary air ratio condition. Specifically, the upper limit of the error bar indicates the ratio of the increased experimental NO emission value (by 10% to accommodate measurement uncertainty) at a specific primary air ratio to the decreased experimental NO emission value (by 10%) at the reference condition (non-staged combustion). Conversely, the lower limit of the error bar represents the ratio of the decreased experimental NO emission value (by 10%) at the specific primary air ratio condition to the increased reference condition value (by 10%). The comparison reveals that all calculated results align well within the error range, effectively reflecting the experimental trend and thereby validating the accuracy of the customized solver used in this thesis for the three-dimensional simulation.

As previously mentioned, for ammonia co-firing systems, adjusting the air injection ratios

within the furnace to create a fuel-rich region near the primary nozzle is instrumental in controlling NO generation and emission. However, the experimental and numerical results presented in **Fig. 4.8** reveal that under a constant total air ratio, simply reducing the primary air ratio does not lead to a linear decrease in NO emissions at the furnace outlet. Instead, such a reduction leads to a V-shaped trend. The minimum emission level, showing a reduction of approximately 89.9% compared to the non-staged combustion, is achieved when both primary and secondary air ratios are equal to 0.6. This phenomenon indicates the existence of a threshold for the air ratio supplied to the primary combustion zone. Concerning the effect of secondary nozzle diameter, the NO emission rate in the combustion furnace follows a similar V-shaped pattern across different diameters. Notably, increasing the secondary nozzle diameter to 7.8 mm results in marginally lower overall NO emissions compared to a 6.6 mm scenario. The following parts will discuss these findings.

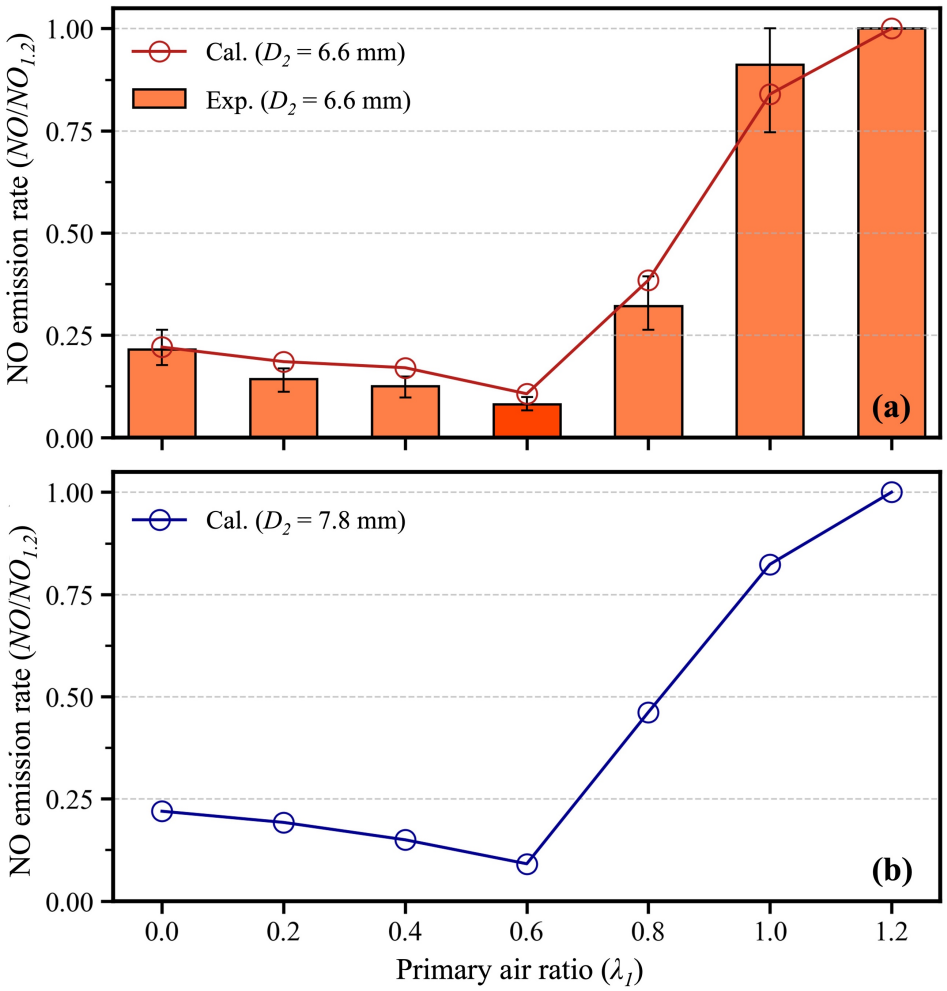

Figure 4.8 The effect of primary air ratio on NO emission rate with secondary nozzle diameters of (a) 6.6 mm and (b) 7.8 mm. The subscript 1.2 denotes non-staged combustion.

4.4.2 Temperature and NO distribution within the combustion furnace

Figures 4.9 and **4.11** respectively demonstrate the distribution of temperature and NO inside the combustion furnace under varying primary air ratios. **Figure 4.10** further explores the influence of the primary air ratio on the temperature field, presenting trends in peak and outlet temperatures within the furnace under two sets of secondary nozzle diameters (6.6 mm, and 7.8 mm). Integrating the data from **Figs 4.9** and **4.10** reveals a significant upward trend in the peak flame temperature within the furnace when gradually increasing the air flow rate injected through the primary nozzle. The highest value is reached under stoichiometric scenarios in the PA zone ($\lambda_1 = 1.0$), approximately 460 K higher than under the condition at $\lambda_1 = 0$. Subsequently, although there is a decline in peak temperature under non-staged combustion, it remains notably higher than in other air-staged combustion scenarios.

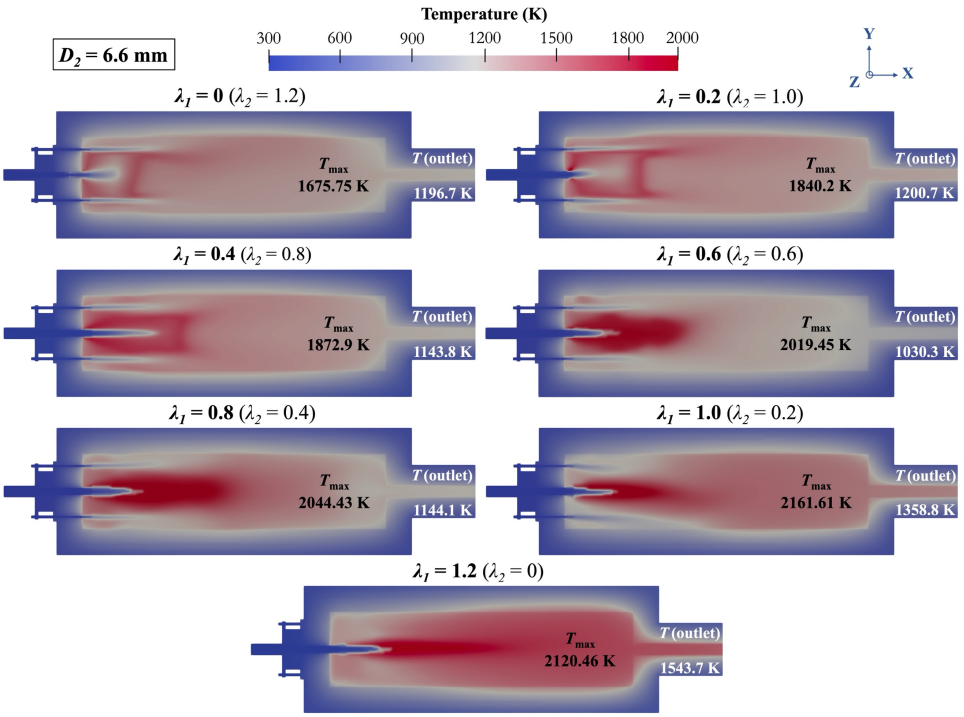

Figure 4.9 Temperature distribution at different primary air ratios along the Z-plane section at the secondary nozzle diameter of 6.6 mm.

As the primary air ratio changes, significant differences in the shape of the flame within the furnace are also observed. Specifically, when the oxidant is primarily supplied through the primary nozzle (for instance, λ_1 = 1.0 or 1.2), the combustion predominantly occurs in the PA zone. This condition results in an elongated flame, extensive high-temperature regions, and the flame front nearing the furnace outlet, which correlates with a significant increase in the outlet temperature of the exhaust gases. Additionally, in this thesis, the vertical injection of fuel and oxidizer through nozzles means that increasing the primary air ratio substantially raises the

velocity of the injected air stream, causing flame lift-up inside the furnace. This phenomenon can impact flame stability [13]. Conversely, when λ_1 is 0, since the oxidant is entirely supplied through the secondary nozzle, it represents another non-staged combustion mode, where fuel and oxidizer mix only after entering the furnace, through molecular and turbulent diffusion, resembling the form of a turbulent diffusion flame. Here, the reaction temperature is relatively lower, which hinders efficient thermal energy utilization but is beneficial for suppressing the formation of thermal NO inside the furnace. More interestingly, the outlet temperature also displays a V-shaped pattern as λ_1 increases, as shown in **Fig. 4.10**, mirroring the trends observed in NO emissions. This suggests that the exhaust gas temperature could serve as a potential indicator for predicting NO emissions during the experiments.

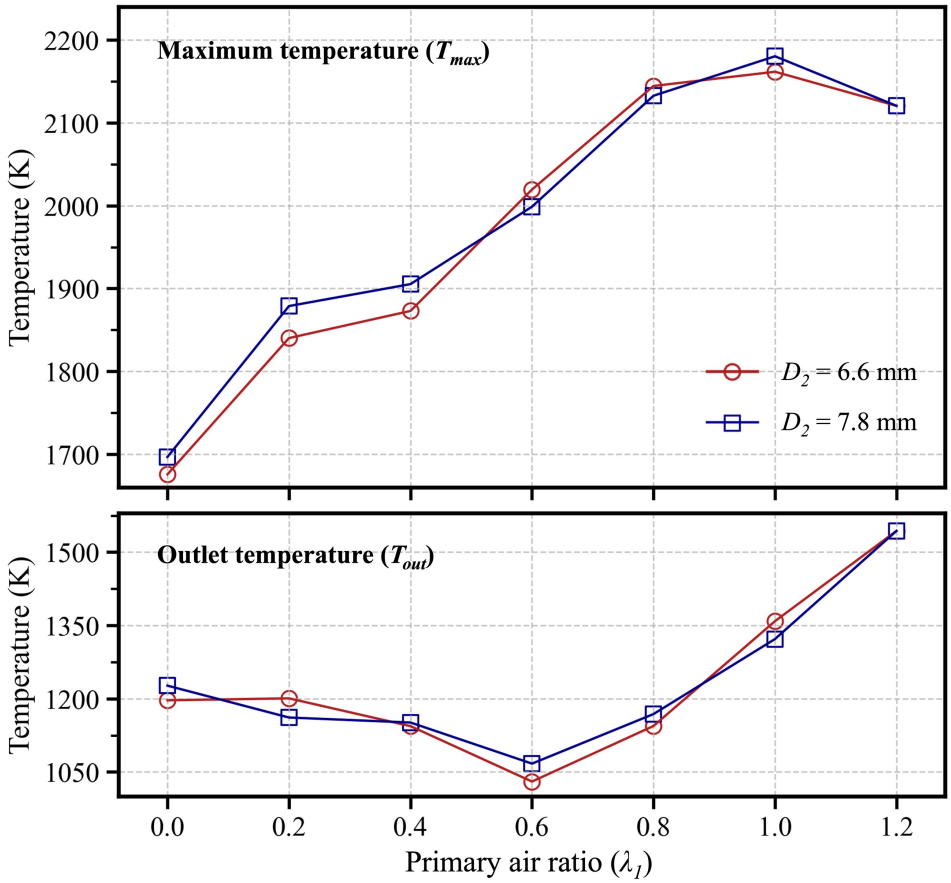

Figure 4.10 Variations of the maximum temperature and outlet temperature within the furnace under different primary air ratios.

Figure 4.11 elucidates that the primary air ratio also significantly influences NO distribution within the furnace. An optimal value for controlling NO formation is identified at λ_1 = 0.6. As the primary air ratio exceeds 0.6, transitioning the PA zone from fuel-rich to fuel-lean conditions, there is a marked rise in NO formation and emission. This phenomenon can be attributed to two main reasons. Firstly, under fuel-lean conditions, there is an abundance of oxygen atoms

available to combine with nitrogen atoms to form NO, and the reduced quantity of nitrogen atoms is not conducive to the homogeneous reduction of NO. Secondly, as λ_1 increases, the injection intensity of the primary nozzle augments, increasing the velocity of the primary air. This reduces the residence time of fuel in the furnace, which is unfavorable for the reduction reactions of NO. Conversely, when $\lambda_1 < 0.6$, that is, continuously increasing the equivalence ratio in the PA zone to strengthen the formation of a fuel-rich region, the formation and emission of NO still exhibit a slowly increasing trend. However, the temperature inside the furnace drops significantly, and the NO content in the exhaust gases is considerably lower than in conditions where $\lambda_1 > 0.6$. When $\lambda_1 = 0$, NO emissions are equivalent to 20.8% of those at $\lambda_1 = 1.2$. In these scenarios, it is observed that the NO formation in the PA zone is not significant, resulting in a low-NO area. As the primary air ratio decreases, this area expands to the SA zone, indicating that the main combustion reaction may not be occurring in the PA zone.

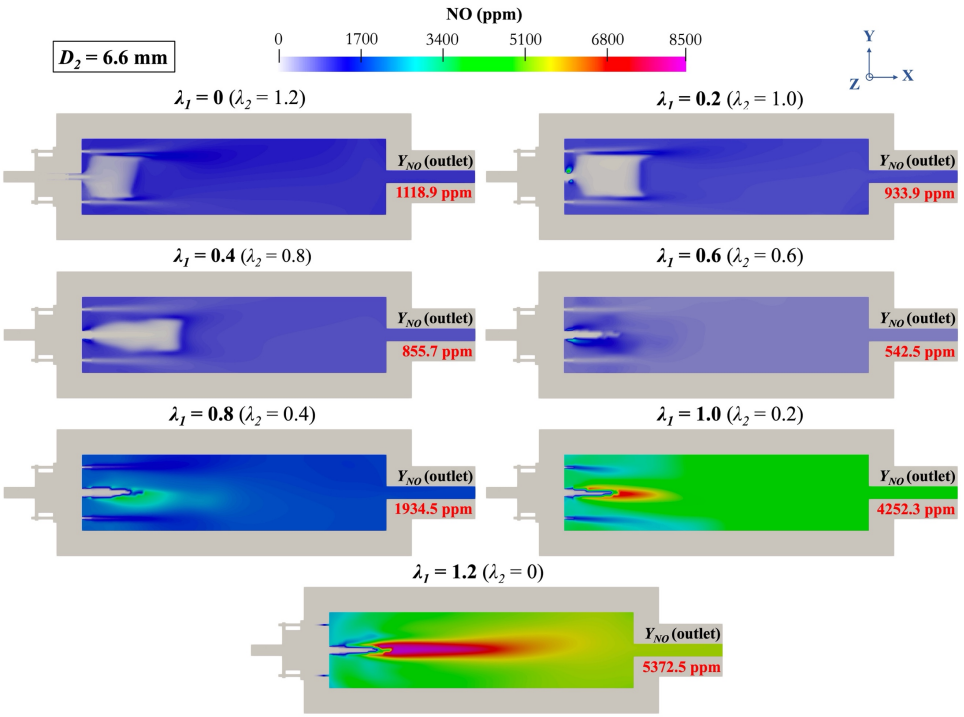

Figure 4.11 NO distribution at different primary air ratios along the Z-plane section at the secondary nozzle diameter of 6.6 mm.

To substantiate the above conclusion, **Fig. 4.12** presents the heat release rate (dQ) along the Z-plane section of the furnace under different primary air ratios. From the figure, it can be observed that when λ_1 is greater than or equal to 0.6, the heat release is concentrated in the PA region, while as λ_1 decreases from 0.6 to 0.4, reactions occur simultaneously in both the PA and SA areas. When λ_1 further decreases to 0.2 and 0, the heat release zone shifts to the area near the secondary nozzle, with almost no heat release reaction occurring in the fuel-rich region.

Figure 4.13 provides the gas temperature distribution along the central axis of the combustion furnace at varying primary air ratios. It is observed that under two different secondary nozzle diameters, the temperature curves exhibit similar trends, displaying two distinct patterns of change. When $\lambda_1 \geq 0.6$, a rapid rise in flue gas temperature is observed, reaching a peak approximately 200 mm from the fuel nozzle outlet. This peak temperature is close to the peak temperature inside the furnace. Further downstream in the furnace, the temperature gradually decreases and stabilizes, indicating that the reaction is transitioning into the burnout stage. Under these conditions, as fuel and most of the oxidizers are injected through the primary nozzle, reactions predominantly occur within the PA zone, resulting in overall higher reaction temperatures. In contrast, when $\lambda_1 < 0.6$, the change in flue gas temperature along the central axis is relatively slow, with the peak temperature of the central axis occurring further back and significantly lower than the peak temperature under corresponding conditions within the furnace. This observation indicates that when the secondary air flow begins to exceed the primary air flow, the combustion reaction does not exclusively take place in the central region of the furnace. Instead, the main reaction process likely occurs between the PA and SA zones. That is to say, as the primary air ratio varies, two different combustion modes arise within the combustion furnace, directly influencing the formation and emission of NO.

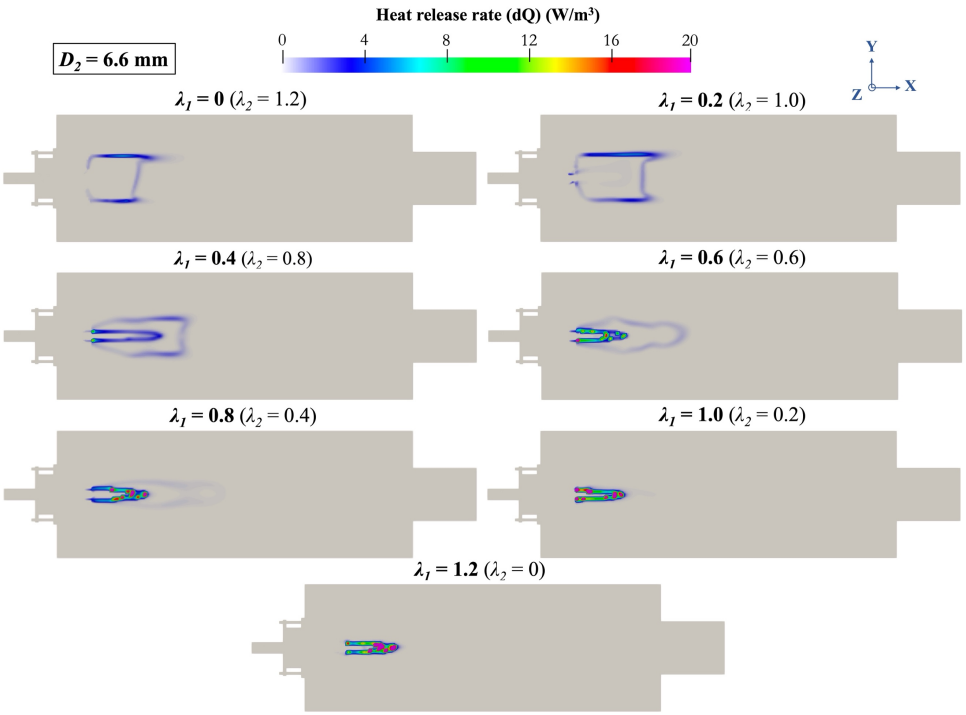

Figure 4.12 Heat release rate at different primary air ratios along the Z-plane section at the secondary nozzle diameter of 6.6 mm.

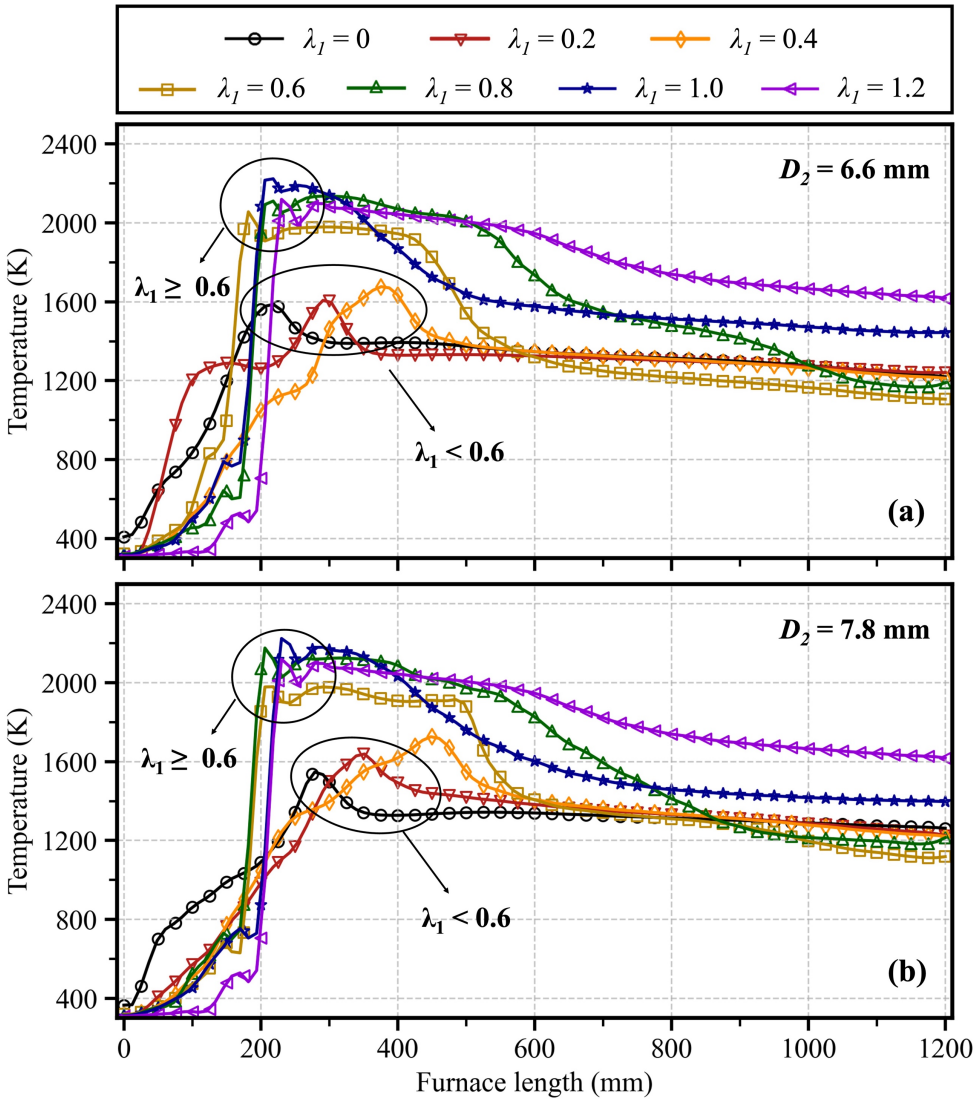

Figure 4.13 Temperature distribution under different primary air ratios along the central axis (X-axis) with secondary nozzle diameters of (a) 6.6 and (b) 7.8mm.

4.4.3 Mechanisms of NO formation and reduction

(a) The effectiveness of air-staged strategy

Sec. 4.4.2 briefly describes the V-shaped variation trend of NO emissions and the differences in temperature distribution within the furnace when the air-staging ratio changes. This section will provide a more detailed discussion of such phenomena. Before delving into this discussion, it is essential to understand the effectiveness of the air-staged strategy and its mechanism for controlling NO emissions within the furnace.

Figure 4.14 displays the NO distribution within the combustion furnace in both the Y-plane and Z-plane sections. Taking the condition with a secondary nozzle diameter of 6.6 mm as an example, it compares the application of an air-staged strategy with a non-staged condition. It is important to note that the Y_{NO} (outlet) values depicted in the figure represent predicted values

that include the influence of water content. As can be observed, after applying the air-staged strategy, there is a substantial reduction in NO distribution within the combustion furnace. The length of the peak NO region is correspondingly shortened, primarily concentrating in the upstream section of the furnace, near the burner inlet. Simultaneously, the NO concentration at the exhaust is reduced by approximately 89.9%. This numerical simulation reproduces the effectiveness of air-staged combustion and underscores the necessity of implementing an air-staged strategy in the parallel injection system.

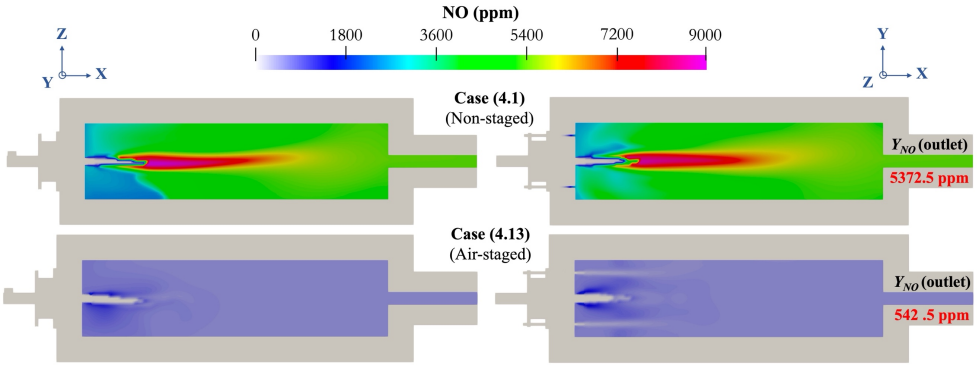

Figure 4.14 NO distribution with (down) and without (up) the application of air-staged strategy at the secondary nozzle diameter of 6.6 mm.

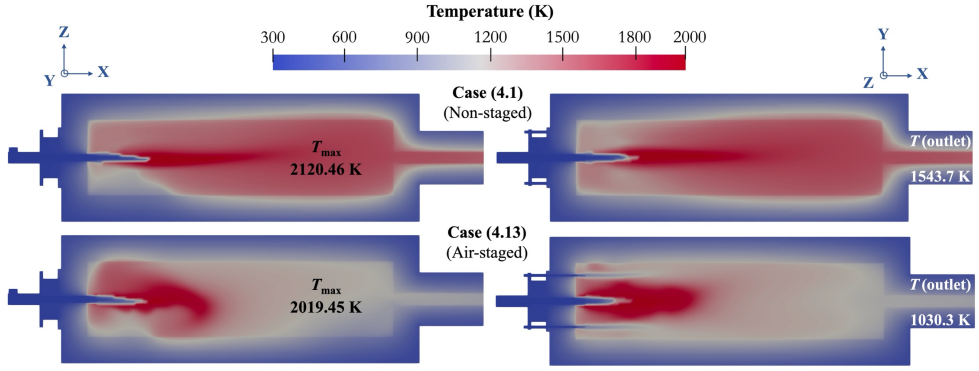

Figure 4.15 Temperature distribution with (down) and without (up) the application of air-staged strategy at the secondary nozzle diameter of 6.6 mm.

To gain a clearer understanding of the mechanism behind the reduction in NO emissions following the application of an air-staged strategy, **Fig. 4.15** presents the corresponding temperature distribution within the combustion furnace for two different conditions. Similar to the NO emissions results, with the implementation of the air-staged strategy, there is a noticeable reduction in the high-temperature region within the furnace. Moreover, as discussed in **Sec. 4.4.2**, due to the utilization of the air-staged strategy, a portion of the combustion air is introduced through the secondary nozzle, leading to a reduction in the mass flow rate at the primary air nozzle (inlet injection velocity decreases). This significantly shortens the flame

length, eliminating the formation of a distinct high-temperature jet flame that was characteristic in the non-staged combustion. Since the flame top is further away from the furnace exit, the outlet temperature of the exhaust gases decreases by approximately 500 K compared to the condition without the application of the air-staged strategy. The peak temperature within the furnace is also notably lower, by approximately 100 K.

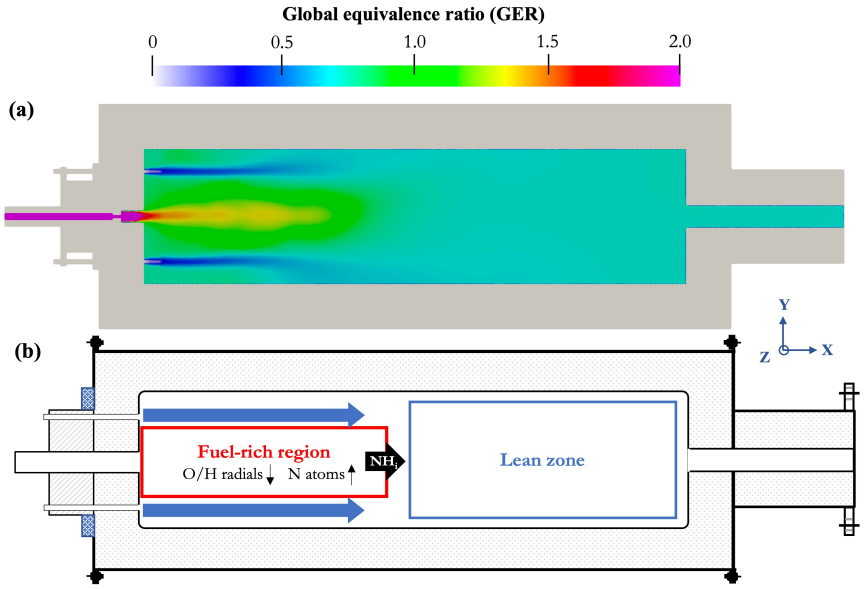

Figure 4.16 (a) Global equivalence ratio distribution, and (b) the schematic diagram of the combustion region distribution with the application of air-staged strategy.

Figure 4.16(a) presents the numerical distribution of the GER within the combustion furnace following the application of the air-staged strategy at the primary air ratio of 0.6. A brief description of the process for achieving air-staged combustion in the parallel injection system is given in **Fig. 4.16(b)**. In short, the air-staged strategy is accomplished by adjusting the air injection ratio between the primary and secondary air nozzles, creating a fuel-rich region near the primary nozzle outlet (PA zone). This approach capitalizes on both the stability and low NO emissions associated with the fuel-rich region. To further investigate the transformation of reaction pathways in the furnace after applying the air-staged strategy, a kinetic analysis of the Rate of Production (ROP) of NO was conducted, with the main elementary reactions contributing to the production and reduction of NO in the Z-plane section presented in **Fig. 4.17**. Combining the results from **Figs. 4.16** and **4.17**, it can be observed that under fuel-rich conditions, there is a limited supply of oxygen available for NO formation, leading to an abundance of N atoms. This significantly enhances the intensity of reaction R220, establishing it as the primary reduction step in air-staged combustion. On the other hand, the concentration of O/H radicals noticeably decreases, which also promotes the reduction of NO by NH

intermediates (R241, R242, R256, R257) [1].

Another significant factor in reducing the distribution of NO is temperature control. In the air-staged combustion configuration, the formation of a fuel-rich region helps avoid the high temperature of a stoichiometric flame. The overall temperature within the furnace also decreases significantly, thereby reducing the generation of thermal NO [14]. Additionally, since the secondary air required to complete the combustion of ammonia-mixed fuel is added on both sides of the primary combustion zone, the lower secondary inlet air temperature facilitates the minimization of the formation of additional NO in low-temperature reaction gases. In summary, the air-staged strategy applied in the present thesis could effectively control the generation and emission of NO within the furnace.

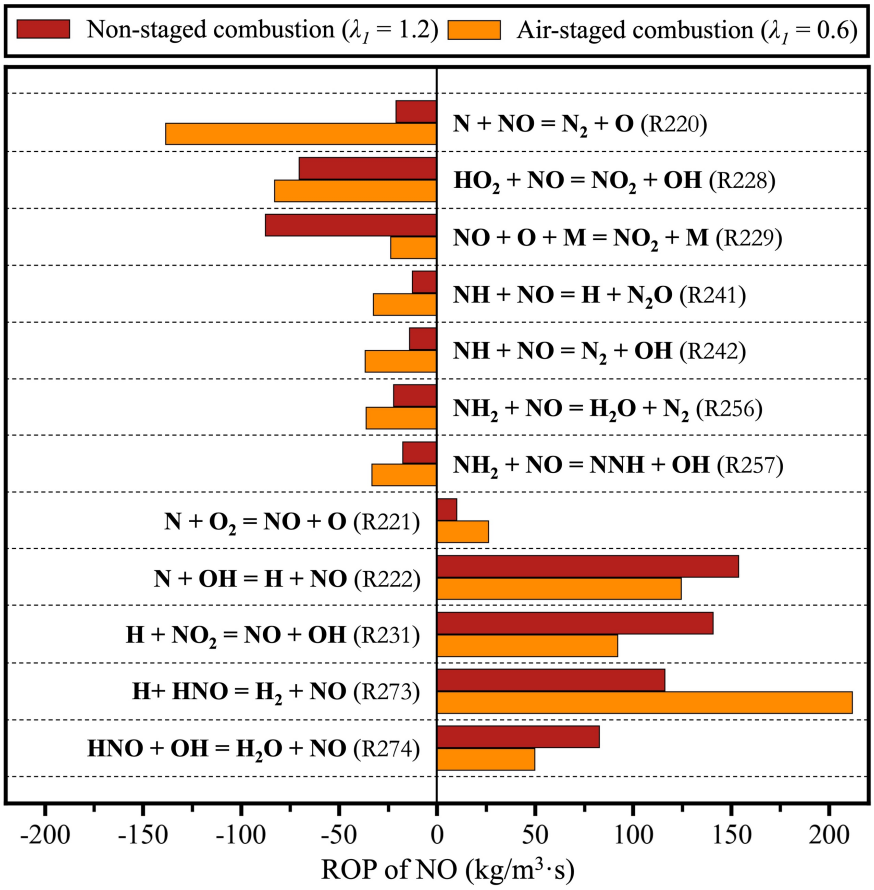

Figure 4.17 Contributions of elementary reactions for NO production and reduction under the condition of non-staged and air-staged combustion.

(b) The effect of primary air ratios

Based on the analysis in the previous section, applying the air-staged strategy to form a fuel-rich region in the PA zone can effectively promote the NO reduction reaction within the furnace. However, despite the necessity of creating a fuel-rich region in the PA zone, the experimental

and numerical results obtained indicate the existence of a threshold when adjusting the primary air ratio. Specifically, setting the primary air ratio to 0.6 yields the optimal solution for controlling NO emissions, as any deviation from this value results in increased NO in the exhaust gases. As suggested in **Fig. 4.13**, as the primary air ratio changes, there is a noticeable shift in the combustion mode within the furnace. Specifically, when the primary air ratio is below 0.6, the main combustion reaction shifts away from the fuel-rich region (PA zone). This shift is likely the primary reason for the observed threshold.

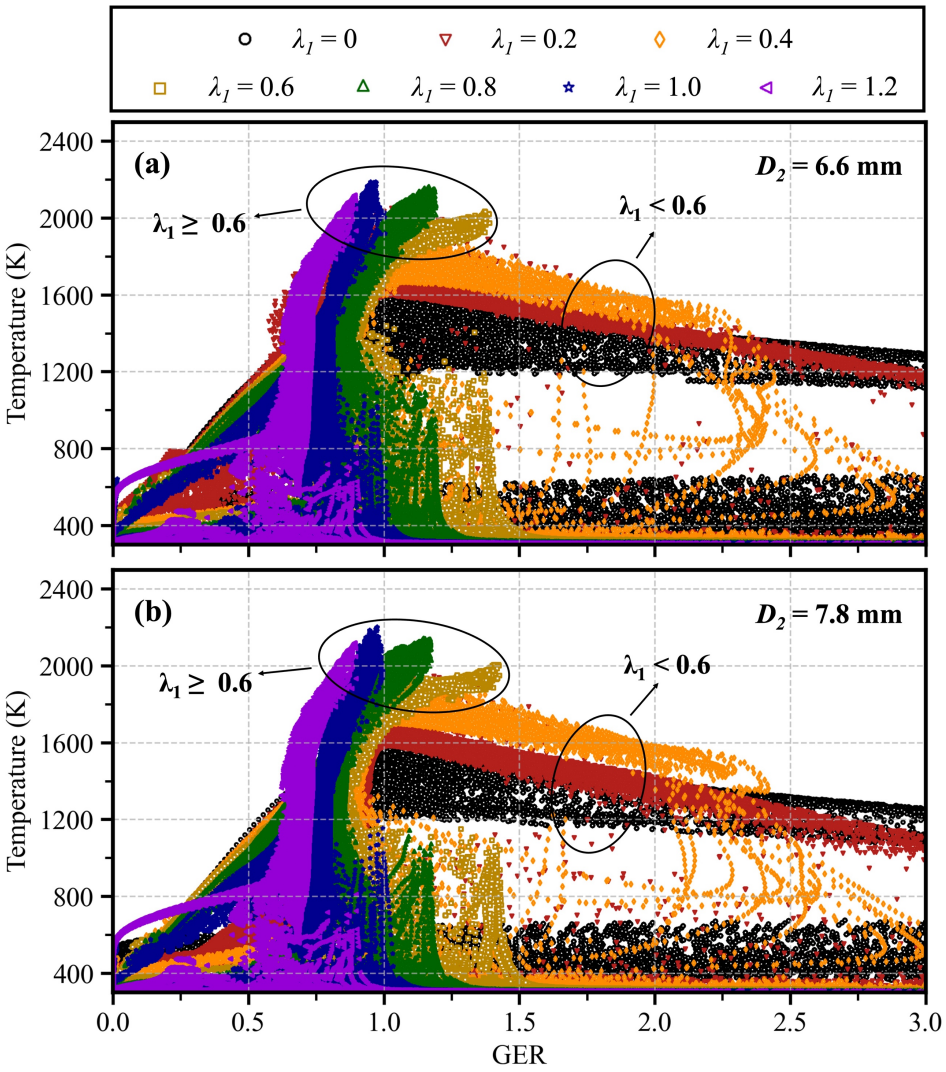

Figure 4.18 Local temperature distribution concerning GER value inside the combustion furnace under different primary air ratios with secondary nozzle diameters of (a) 6.6 mm and (b) 7.8 mm.

To validate the above conclusion, **Fig. 4.18** elucidates the correlation between the GER and the corresponding reaction temperatures at various locations within the combustion furnace across different primary air ratios. Typically, the highest flame temperature corresponds to the center of the combustion reaction. When combined with the GER distribution from **Fig. 4.6**, it

is apparent that for $\lambda_1 \geq 0.6$, the highest flame temperatures basically coincide with the peak GER values. This suggests that the combustion reaction predominantly occurs in the PA zone. In contrast, when $\lambda_1 < 0.6$, a discrepancy emerges: peak flame temperatures do not match the highest GER values. The GER values at these peak temperatures are notably lower than those observed at $\lambda_1 = 0.6$. Furthermore, with the primary air ratio decreasing, the peak temperatures corresponding to the GER values continue to decline, resulting in a shift of the GER-temperature distribution towards the lower left. This shift implies that under lower primary air ratios, the reaction zone is changed, occurring between the PA and SA zones.

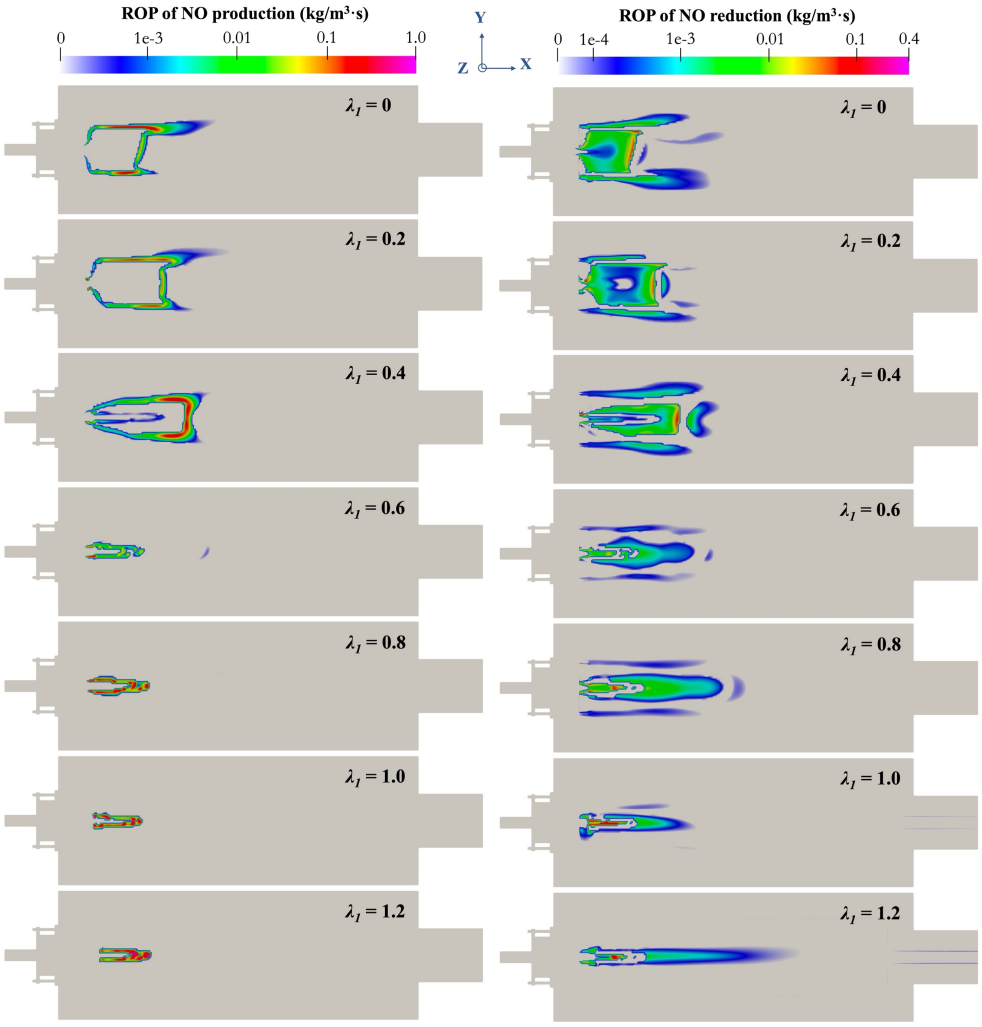

Figure 4.19 Overview of the main production and reduction of NO under different primary air ratios at the secondary nozzle diameter of 6.6mm.

Figure 4.19 illustrates the primary regions of NO production and reduction within the Z-plane section for different primary air ratios, with a secondary nozzle diameter of 6.6 mm. First, regarding the NO production, it is noticeable that at $\lambda_1 \geq 0.6$, the NO production areas are very similar, mainly occurring in the PA zone. As the primary air ratio decreases, the NO production

in the furnace decreases significantly, with the reduction reactions being enhanced. When λ_1 continues to decrease beyond 0.6, the NO production gradually transitions to the secondary nozzle area, and at $\lambda_1 = 0$, the reaction occurs almost entirely in the SA zone. Under these conditions, even though the reduction reaction of NO is intensified due to the reduced intensity of primary injection, the main combustion reaction area is not in the PA zone, resulting in GER values at peak temperatures lower than those at $\lambda_1 = 0.6$. These observations explain why a continuous reduction in the primary air ratio leads to a V-shaped pattern in NO emissions rather than a linear decrease, as the main combustion reaction does not occur in the intended fuel-rich region when the primary air ratio is below 0.6.

4.4.4 Discussion on emission variations

The previous discussion primarily addressed the formation and emission of NO, given its adverse impacts on environmental and human health [3,8]. However, as discussed in **Sec. 1.2.3**, in the process of co-firing with ammonia, fuel-bonded nitrogen inevitably leads to the formation of not only NO but also additional byproducts of NO_2 and N_2O. Among these, NO_2, together with NO, constitutes NOx, which also poses significant ecological threats. N_2O is currently considered a potent greenhouse gas with a global warming potential significantly higher than CO_2 [15]. Therefore, in emissions from combustion furnaces, it is crucial not only to control the emissions of NO and unburned ammonia as much as possible but also to minimize the emissions of N_2O.

Figure 4.20 displays the emissions variation trends of the exhaust gases under different primary air ratios. Notably, since the ammonia is combusted completely, the discussion does not include ammonia in the exhaust gases. First, it is observed that for different secondary nozzle diameters, the emissions of various substances follow similar trends. For NO_2 emissions, the minimum value is reached at $\lambda_1 = 0.6$, with the maximum value at $\lambda_1 = 1.0$, but the overall emission values are significantly lower than corresponding NO emissions. For N_2O, when $\lambda_1 \geq 0.6$, the emissions approach zero, becoming negligible. However, as the primary air ratio is lower than 0.6, N_2O emissions exhibit a rapid increase, reaching a maximum at $\lambda_1 = 0$. Research by Hayakawa et al. [16] suggests that a decrease in flame temperature inhibited the reduction of N_2O through the reaction $N_2O + (M) = N_2 + O + (M)$, which is highly temperature-dependent. Therefore, the noticeable increase in N_2O emissions with a decrease in primary air ratio is likely due to the rapid drop in reaction temperatures within the furnace. These findings indicate that introducing an air-staged strategy and adjusting the primary air ratio to 0.6 can also achieve optimal control of NOx formation, demonstrating the effectiveness of air-staged combustion in controlling pollutants.

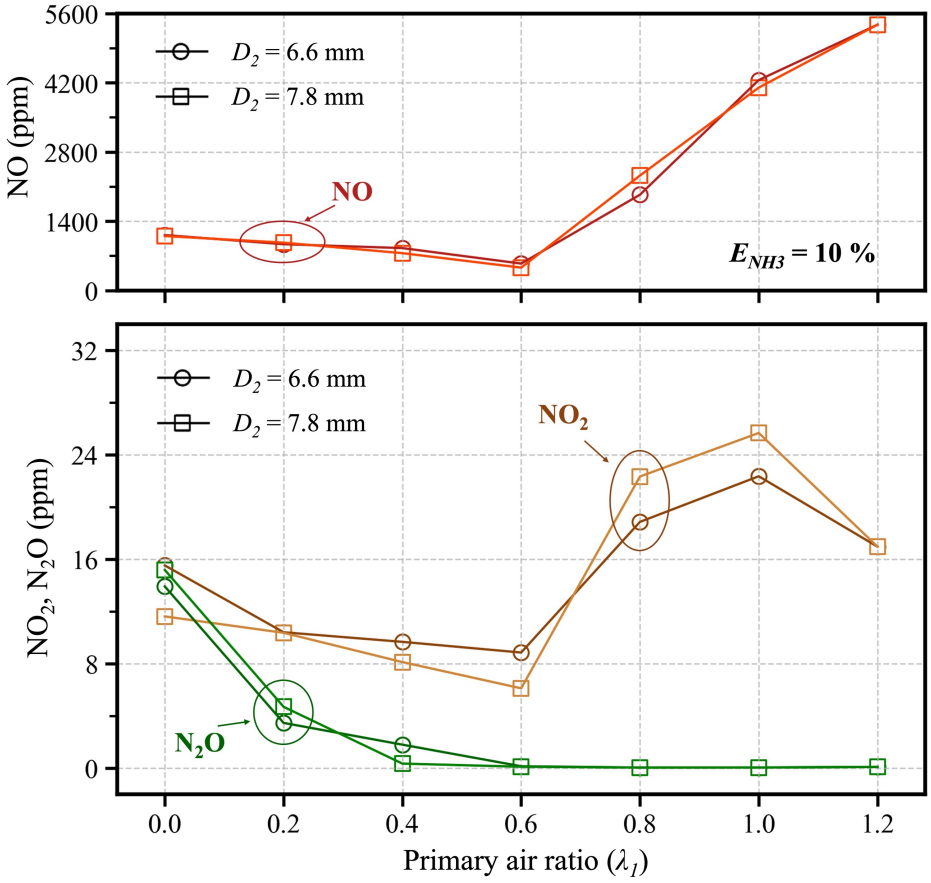

Figure 4.20 Variations of emissions of the exhaust gases under different primary air ratios.

4.5 Influence of the nozzle distances on NO emission

Section 4.4 discussed the impact of the air-staging ratio on NO emissions, revealing that the optimal NO control solution is achieved at a primary air ratio of $\lambda_1 = 0.6$. Therefore, this section will discuss the variation in NO generation and emissions when the distance between the primary air nozzle and the secondary nozzle changes under the application of the air-staged strategy, based on cases (4.13), (4.15), and (4.16) from **Table 4.1**.

4.5.1 Trends and model validation of NO emissions

Figure 4.21 compares the experimental and numerical results of normalized NO emissions under scenarios where the distances between the primary and secondary nozzles were 0 (non-staged combustion), 50, 100, and 140 mm, respectively. Similar to the numerical comparison results in **Fig. 4.8**, the NO experimental measurements when investigating the effect of air nozzle distance were also obtained by cooling the exhaust gas to eliminate the influence of water vapor, so the numerical results also excluded the impact of water vapor. During the experimental measurement, the uncertainty in NO measurements is around 10%. Error bars in the figure are calculated based on the ratios of maximum potential experimental deviations for

each condition, as discussed in **Sec. 4.4.1**. From the figure, it can be observed that the calculation results also fit well within the error intervals, effectively reproducing the experimental trend on NO emissions.

The findings from **Fig. 4.21** demonstrate that maintaining a constant air ratio between the primary and secondary nozzles while transitioning from non-staged combustion to the air-staged combustion scenario with L = 50 mm can lead to a reduction in NO emissions by approximately 85%. This underscores the effectiveness of air-staged strategies in significantly lowering NO emissions within combustion furnaces. As the distance between the primary and secondary nozzles further increased, a continued decrease in NO emissions was observed. Specifically, for scenarios with L = 100 mm and L = 140 mm, NO emissions were reduced by approximately 90% and 92%, respectively, in comparison to the non-staged combustion scenario. These results highlight that within the parallel injection system, increasing the distance between the nozzles can further diminish NO emissions.

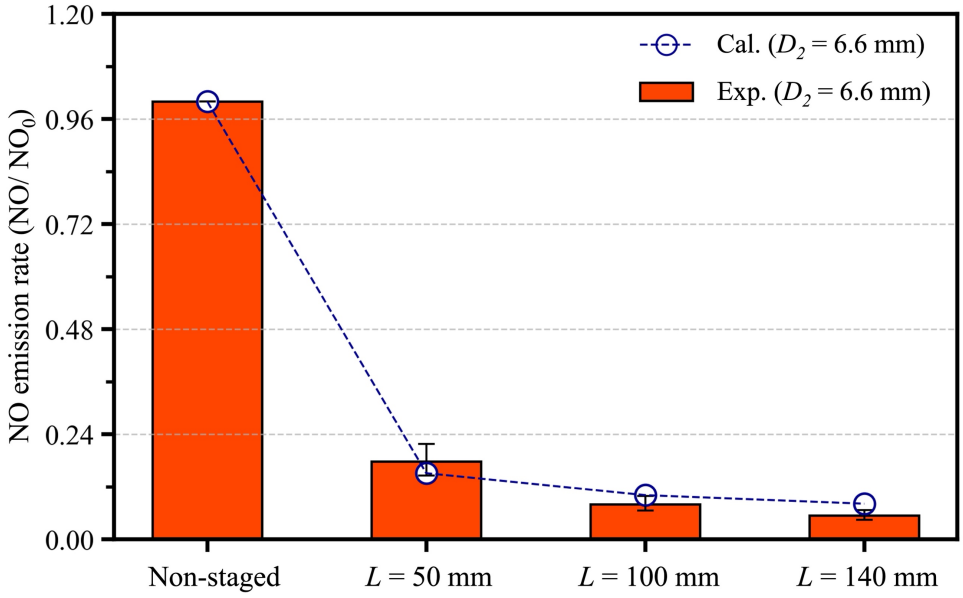

Figure 4.21 Effect of the distance between the primary and secondary nozzles on NO emissions. The subscript 0 indicates that under the condition of non-staged combustion.

4.5.2 Combustion characteristics analysis

Figure 4.22 displays the temperature and NO distribution along the Z-plane section for the four scenarios, respectively. Since the non-staged combustion scenario was discussed in detail earlier, it will not be explored further here. For the other three air-staged combustion scenarios, as the distance between the primary and secondary nozzles increases, the area of high-temperature regions near the burner outlet expands, indicating an enlarged reaction area. However, the peak temperatures within the furnace slightly decrease, with a corresponding

trend of lower exhaust gas temperatures at the furnace outlet. Regarding the NO distribution trend, for the air-staged combustion scenarios, the peak areas of NO concentration are mainly located on both sides of the primary nozzle outlet. This phenomenon is primarily related to the low ammonia co-firing ratio (E_{NH3} = 10 %) used in this chapter. At a lower co-firing ratio, the limited amount of ammonia in the fuel undergoes swift combustion upon entering the furnace, leading to the rapid conversion of N radicals into NO. As the distance between the primary and secondary nozzles increases, the reaction area expands, showing a trend of reduced NO distribution within the furnace. This indicates that the reduction reactions for NO within the furnace gradually strengthen.

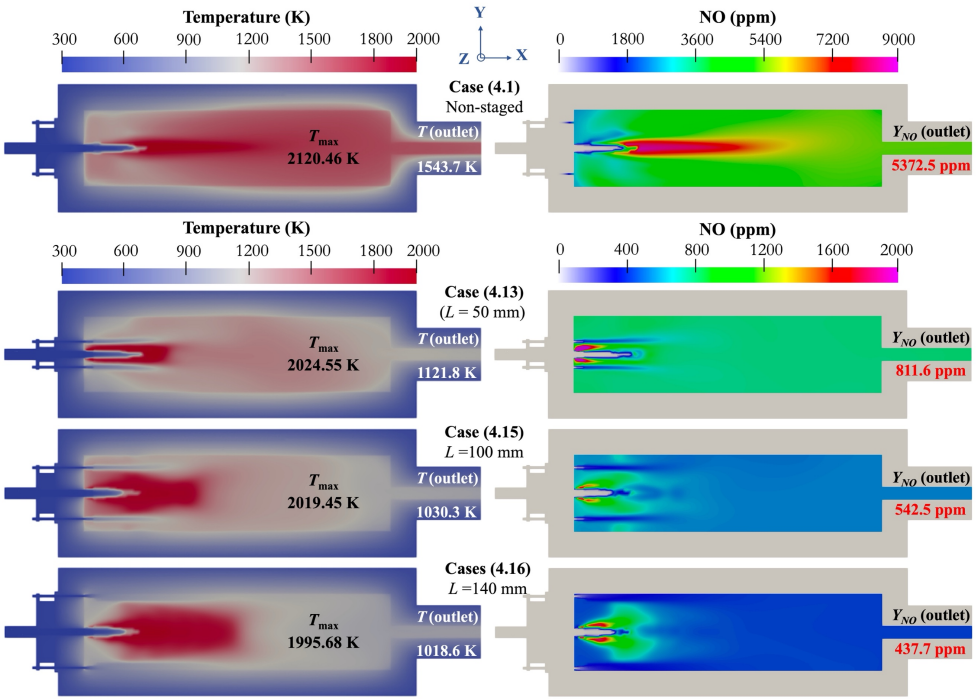

Figure 4.22 Overview of the temperature (left) and NO (right) distribution along the Z-plane section at different nozzle distances.

Through the ROP analysis of NO within the furnace, **Fig. 4.23** further illustrates the primary regions of NO production and reduction within the Z-plane section of the combustion furnace under different nozzle distances. It can be observed from the figure that in the non-staged combustion, NO production is quite significant. However, when applying the air-staged strategy, NO production decreases markedly across the three operating conditions. Although the primary production regions change slightly, the reaction intensities are similar. Regarding NO reduction, as the distance between the primary and secondary nozzle increases, the NO reduction region expands significantly, and the NO reduction rate is greatly enhanced, indicating the reduction of NO is a major factor contributing to the lower NO emissions observed at L = 140 mm.

However, regarding the impact of the air nozzle distance on NO emissions, Liu et al. [17]

highlighted that in air-staged combustion, if the combustion products generated in the fuel-rich region do not mix well with the secondary air, the reduction reactions within the furnace are weakened, which can lead to significant NO emissions. Applying this insight to the air-staged combustion configuration in this section, when L = 50 mm, the smaller area of the fuel-rich zone leads to weaker reduction effects on NO. Therefore, gradually increasing the distance between the two nozzles can effectively promote the reduction reactions of NO within the furnace. However, limited by the size of the combustion furnace used in the present thesis, the maximum distance (L) could only reach 140 mm. Kikuchi et al. [9] argued that merely increasing the distance between the primary and secondary nozzles does not linearly reduce NO formation, because if the mixing speed of ammonia-mixed fuel with the secondary air is too slow, diffusion combustion reactions approaching stoichiometric air-fuel ratios may continue downstream in the furnace, failing to achieve the desired effect to suppress NO. Furthermore, it is important to note that the conclusions obtained in this section are based on scenarios with lower ammonia co-firing ratios. With an increase in the ammonia co-firing ratio, the injection intensity of the fuel nozzle would significantly increase, altering both the flow field and flame shape within the furnace [4]. Therefore, at lower ammonia co-firing ratios, it is advisable to moderately increase the distance between the primary and secondary nozzles to control the generation of NO more effectively.

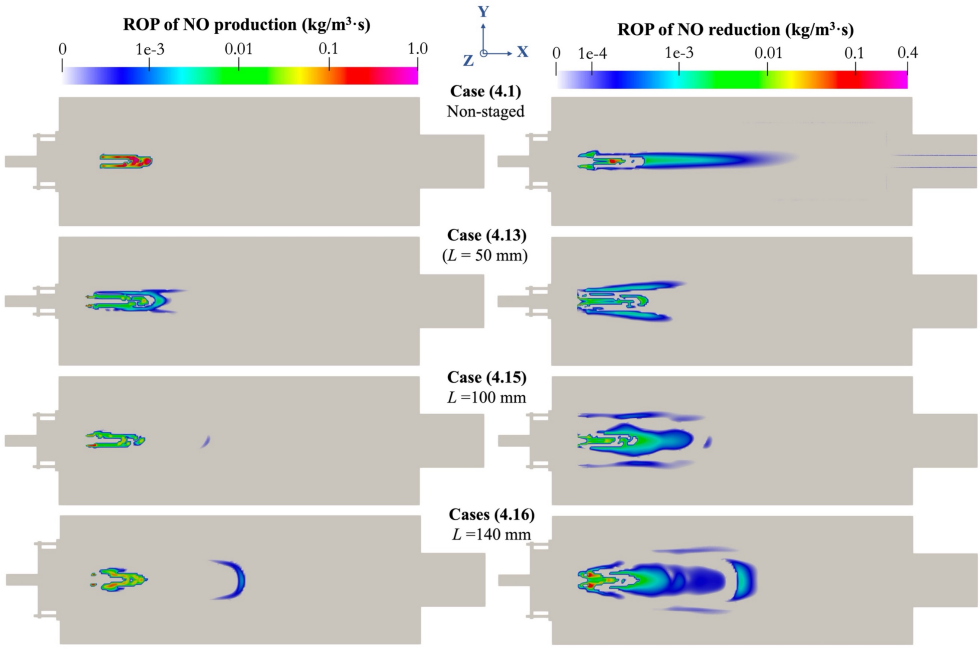

Figure 4.23 Overview of the main production and reduction of NO in the 10-kW combustion furnace along the Z-plane section at different nozzle distances.

4.6 Secondary nozzle diameter selection

The last critical parameter to consider for secondary injection systems is the selection of the secondary nozzle diameter. Generally, under a fixed primary air ratio, adjusting the nozzle diameter will affect the inlet velocity of the secondary air entering the furnace, thereby affecting the distribution of the internal flow field. **Figure 4.24** demonstrates the distribution of NO and temperature within the furnace under three different secondary nozzle diameters (7.8 mm, 6.6 mm, and 4.2 mm, corresponding to cases (4.12) - (4.14) in **Table 4.1**), at $\lambda_1 = 0.6$, $L = 100$ mm and with an ammonia co-firing ratio of 10%. It can be observed that at lower ammonia co-firing ratios, increasing the secondary nozzle diameter effectively reduces the formation and emission of NO. When D_2 increases from 4.2 mm to 7.8 mm, NO emissions at the furnace outlet are reduced by approximately 32.8%. Additionally, the area of the high-temperature zone in the PA zone significantly increases. This is because enlarging the secondary nozzle diameter strengthens the internal recirculation flow in the PA zone, prolongs the residence time of fuel and oxidant in the furnace, allows sufficient time for fuel reactions, and also enhances the reduction reactions of NO [18].

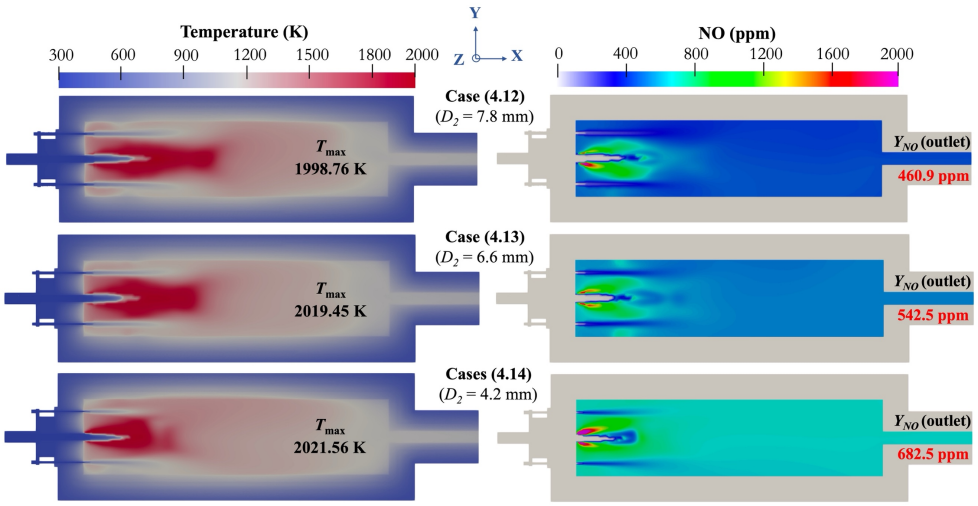

Figure 4.24 Overview of the temperature (left) and NO (right) distribution along the Z-plane section at different secondary nozzle diameters.

However, it is important to note that the impact of secondary nozzle parameters on NO emissions can vary according to changes in the ammonia co-firing ratio. Kikuchi et al. [9] found that NO emissions significantly decrease with the increase of the secondary nozzle diameter when the ammonia co-firing ratio is below 40%. But if the ammonia co-firing ratio is further increased, the impact of the secondary nozzle diameter on NO emissions gradually weakens and may even show an opposite trend to that at lower ammonia co-firing ratios, that is, increasing with the augmentation of D_2. This phenomenon could be related to changes in the

flow field of the PA zone. According to the numerical investigation from Zhang et al. [4], as the ammonia co-firing ratio increases, the injection intensity of the fuel nozzle significantly increases, and the shape as well as flow field of the flame in the furnace undergo considerable changes. Therefore, the selection of secondary nozzle parameters is crucial for combustion furnaces equipped with secondary injection systems. Depending on the intended ammonia co-firing ratio, it is necessary to adjust the secondary nozzle diameter to obtain an optimal solution for controlling NO formation. At lower ammonia co-firing ratios, larger secondary nozzles are recommended, as they can control the NO formation more effectively.

4.7 Summary

This chapter focuses on a 10-kW ammonia co-combustion furnace, utilizing 3D numerical analysis to investigate the effects of the primary air ratio (λ_1), air nozzle distance (L), and secondary nozzle diameter (D_2) on NO emissions within the furnace. The CHT model, which incorporates both solid materials and reacting flow regions, was employed to accurately represent the thermal conditions of the furnace walls. Validation of the computational accuracy with experimental results led to the following noteworthy findings:

First, regarding the computational acceleration capabilities of the solver, for three-dimensional ammonia co-combustion furnace calculations, the acceleration performance of the integrated acceleration strategy was reduced due to increased communication overhead between different MPI ranks, achieving up to 7.06 times speed-up. However, when applying a more detailed Sako reaction mechanism, the acceleration factor increased to 13.88, indicating the promising application potential of this acceleration strategy when extended to larger-size reaction mechanisms.

Second, concerning the impact of the air-staging ratio within the secondary injection system, numerical results indicated that maintaining a constant total air ratio of 1.2, merely reducing the primary air ratio does not linearly decrease NO emissions at the furnace outlet. Instead, this reduction results in a V-shaped curve. The optimum solution for controlling NO generation is achieved when the primary air ratio reaches 0.6, with NO emissions decreasing by approximately 90% compared to non-staged combustion, indicating a threshold in controlling NO generation and emissions through adjusting the primary air ratio.

As the primary air ratios changes, two distinct combustion modes manifest. When $\lambda_1 \geq 0.6$, the main combustion reactions occur in the primary air zone. As the primary air ratio decreases, a fuel-rich region forms near this area, enhancing reduction reactions and decreasing NO formation and emissions. Conversely, when $\lambda_1 < 0.6$, the flow of oxidizers from the secondary nozzle gradually exceeds that from the primary nozzle, shifting the main combustion reactions

toward the secondary air zone, and is accompanied by a significant decrease in furnace temperature. The main combustion reactions do not occur as anticipated in the fuel-rich region, resulting in an increase in NO emissions.

In the analysis of other related pollutant emissions, an analysis of the emission characteristics shows that under a primary air ratio of 0.6, not only is the optimal solution for controlling NO, but it also exhibits favorable characteristics in controlling NO_2 and N_2O emissions. When the primary air ratio falls below 0.6, the reduction in flame temperature within the combustion furnace weakens the reduction reactions for N_2O, leading to a rapid increase in N_2O emissions. Therefore, to control emissions effectively in air-staged combustion, it is essential to avoid excessively fuel-rich combustion conditions.

Third, regarding the impact of the distance between the primary and secondary nozzles on NO generation and emissions within the furnace, numerical results indicate that at an ammonia co-firing ratio of 10%, increasing the distance between the two nozzles from 50 mm to 140 mm leads to an expanded fuel-rich region and intensified reduction reactions, resulting in a 46.1% decrease in NO emissions at the furnace outlet. During this process, NO formation within the furnace does not significantly decrease, but the reduction reactions are notably enhanced. Consequently, for furnaces equipped with parallel injection systems and operating at lower ammonia co-combustion ratios, it is advisable to moderately increase the distance between the primary and secondary nozzles.

Finally, for an ammonia co-firing ratio at 10%, increasing the secondary nozzle diameter effectively reduces the formation and emissions of NO within the furnace. When this value increases from 4.2 mm to 7.8 mm, the NO in the exhaust can be reduced by about 32.8%. Therefore, larger secondary nozzles are recommended under lower ammonia co-combustion conditions.

In summary, the present chapter validates the feasibility of controlling NO generation through adjustments in the secondary injection system parameters without extensive modifications to the existing infrastructure of the combustion furnace. The above results can provide references for parameter design and selection for future low-NO ammonia co-combustion furnaces.

References

[1] H. Kobayashi, A. Hayakawa, K.D.K.A. Somarathne, E.C. Okafor, Science and technology of ammonia combustion. *Proceedings of the Combustion Institute*, 2019, 37: 109–133.

[2] L. Kang, W. Pan, J. Zhang, W. Wang, C. Tang, A review on ammonia blends combustion for industrial applications. *Fuel*, 2023, 332: 126150.

[3] J. Tian, L. Wang, Y. Xiong, Y. Wang, W. Yin, G. Tian, Z. Wang, Y. Cheng, S. Ji, Enhancing combustion efficiency and reducing nitrogen oxide emissions from ammonia combustion: A comprehensive review. *Process Safety and Environmental Protection*, 2024, 183: 514–543.

[4] J. Zhang, T. Ito, H. Ishii, S. Ishihara, T. Fujimori, Numerical investigation on ammonia co-firing in a pulverized coal combustion facility: Effect of ammonia co-firing ratio. *Fuel*, 2020, 267: 117166.

[5] K.D.K.A. Somarathne, E.C. Okafor, D. Sugawara, A. Hayakawa, H. Kobayashi, Effects of OH concentration and temperature on NO emission characteristics of turbulent non-premixed CH_4/NH_3/air flames in a two-stage gas turbine like combustor at high pressure. *Proceedings of the Combustion Institute*, 2021, 38: 5163–5170.

[6] M. Xie, Y. Tu, Q. Peng, Numerical study of NH_3/CH_4 MILD combustion with conjugate heat transfer model in a down-fired lab-scale furnace. *Applications in Energy and Combustion Science*, 2023, 14: 100144.

[7] P. Berwal, S. Kumar, B. Khandelwal, A comprehensive review on synthesis, chemical kinetics, and practical application of ammonia as future fuel for combustion. *Journal of the Energy Institute*, 2021, 99: 273–298.

[8] R. Murai, N. Nakatsuka, H. Higashino, F. Akamatsu, Review of fundamental study on ammonia direct combustion in industrial furnaces, in *CO_2 Free Ammonia as an Energy Carrier*, Springer, Singapore, 2022, pp. 627–640.

[9] K. Kikuchi, R. Murai, T. Hori, F. Akamatsu, Fundamental study on ammonia low-NOx combustion using two-stage combustion by parallel air jets. *Processes*, 2021, 10: 23.

[10] N. Sako, J. Hayashi, T. Sako, H. Kawanabe, M. Katsuki, Nitrogen-origin-determination in NOx formation under ammonia/methane/air co-combustion using a nitrogen-tagged reaction model. *Combustion and Flame*, 2024, 259: 113210.

[11] F. Perini, E. Galligani, R.D. Reitz, An analytical Jacobian approach to sparse reaction kinetics for computationally efficient combustion modeling with large reaction mechanisms. *Energy & Fuels*, 2012, 26: 4804–4822.

[12] F. Perini, E. Galligani, R.D. Reitz, A study of direct and Krylov iterative sparse solver techniques to approach linear scaling of the integration of chemical kinetics with detailed combustion mechanisms. *Combustion and Flame*, 2014, 161: 1180–1195.

[13] E.C. Okafor, K.D.K.A. Somarathne, A. Hayakawa, T. Kudo, O. Kurata, N. Iki, H. Kobayashi, Towards the development of an efficient low-NOx ammonia combustor for a micro gas turbine. *Proceedings of the Combustion Institute*, 2019, 37: 4597–4606.

[14] X. Wang, W. Fan, J. Chen, G. Feng, X. Zhang, Experimental study on effects of air-staged

strategy and NH_3 co-firing ratios on NO formation characteristics in ammonia/coal co-firing process. *Fuel*, 2023, 332: 126217.

[15] Y. Park, B. Kim, Catalytic removal of nitrogen oxides (NO, NO_2, N_2O) from ammonia-fueled combustion exhaust: A review of applicable technologies. *Chemical Engineering Journal*, 2023, 461: 141958.

[16] A. Hayakawa, M. Hayashi, M. Kovaleva, G.J. Gotama, E.C. Okafor, S. Colson, S. Mashruk, A. Valera-Medina, T. Kudo, H. Kobayashi, Experimental and numerical study of product gas and N_2O emission characteristics of ammonia/hydrogen/air premixed laminar flames stabilized in a stagnation flow. *Proceedings of the Combustion Institute*, 2023, 39: 1625–1633.

[17] H. Liu, W. Qian, M. Zhu, S. Li, Kinetics modeling on NOx emissions of a syngas turbine combustor using rich-burn, quick-mix, lean-burn combustion method. *Journal of Engineering for Gas Turbines and Power*, 2020, 142: 021005.

[18] K. Kikuchi, T. Motegi, T. Hori, F. Akamatsu, Influence of nozzle design parameters on exhaust gas characteristics in practical-scale flameless hydrogen combustion. *International Journal of Hydrogen Energy*, 2022, 47: 21287–21297.

Chapter 5

Ammonia co-firing at different ratios

5.1 Introduction

Chapter 4 investigated the NO emission characteristics of the secondary injection system in the 10-kW ammonia co-combustion furnace, revealing that at lower ammonia co-firing ratios, adjusting the primary and secondary air ratio to 0.6, along with moderately increasing the secondary nozzle diameter and air nozzle distance, effectively reduces NO formation and emissions within the furnace. These adjustments also promote NO reduction reactions, which are beneficial for advancing the application of ammonia co-combustion in power generation.

To further promote the use of carbon-free fuels and control carbon dioxide emissions, increasing the utilization of ammonia in combustion processes is necessary, especially at higher ammonia co-firing ratios. This requires a detailed investigation into the combustion and emission characteristics under such conditions. Some researchers have already studied NO emission characteristics across different ammonia co-firing ratios. For example, in 2017, Kurata et al. [1] successfully demonstrated pure ammonia combustion power generation using a 50-kW micro gas turbine system, showing that adjusting the inlet temperature effectively controlled NO and unburned ammonia emissions. In ammonia/methane co-firing systems, NO emissions increased significantly with a higher ammonia ratio, though the NO conversion ratio decreased. Li et al. [2] optimized combustion in an ammonia/methane gas turbine, confirming that NO emissions below 30 ppm could be achieved even when the volumetric ratio of the ammonia reached 40%. Somarathne et al. [3] studied the effects of OH concentration and temperature on NO emissions in an air-staged combustion micro-gas turbine, finding that NO emissions peaked between 20% and 30% ammonia co-firing ratios, after which they gradually declined. Similarly, Okafor et al. [4] conducted systematic research on micro-gas turbines, providing insights for developing low-NO combustors at higher ammonia co-firing ratios.

In boiler applications within power systems, most research has focused on ammonia/coal co-firing. Tamura et al. [5] conducted experimental investigations on a 1.2-MW ammonia/coal co-firing horizontal furnace and found that NO emissions only significantly increased when the ammonia co-firing ratio exceeded 30%. Nagatani et al.[6] from IHI Japan tested ammonia co-firing in a 10-MW coal-fired furnace with a single swirl burner, demonstrating that with a well-implemented air-staged strategy, NO emissions could be controlled to pure coal combustion levels when ammonia co-firing ratios below 20%. Zhang et al. [7] extended this work by

performing three-dimensional numerical investigations on a similar furnace, exploring combustion characteristics at ammonia co-firing ratios ranging from 0 to 80%. Their results showed that combustion intensity peaked and unburned carbon reached its minimum at a 10% ammonia co-firing ratio, while NO emissions at the furnace outlet were highest. When the ammonia co-firing ratio exceeded 40%, the risk of ammonia leakage increased significantly. Similarly, Jin et al. [8] performed a three-dimensional numerical analysis on a 1050-MW coal-fired boiler under different ammonia/coal co-firing conditions. They found that due to the dominance of the oxidation of ammonia over its NO reduction capability, NO emissions increased linearly with higher ammonia co-firing ratios. Additionally, the risk of low-temperature corrosion in the furnace increased with higher ammonia ratios, necessitating specific design considerations for furnaces at elevated ammonia co-firing ratios.

By summarizing the majority of current studies, it is evident that research on ammonia co-firing power generation can be broadly divided into two main categories: studies focusing on ammonia/methane co-firing in small gas turbines, and research on ammonia/coal co-firing in boilers. Due to the higher power output in the latter case, air-staged combustion strategies predominantly utilize side-wall injection systems. Therefore, there is a notable lack of analysis concerning the combustion characteristics of furnaces at different ammonia co-firing ratios employing the parallel injection system. Additionally, as discussed in **Sec. 2.4**, accurately describing the thermal boundary conditions of the furnace walls is crucial in the three-dimensional numerical analysis of combustion furnaces. Hence, it is essential to incorporate the conjugate heat transfer method.

In summary, the primary objective of the present chapter was to conduct a detailed investigation into the co-firing characteristics of a 10-kW ammonia co-combustion furnace through numerical simulations. A three-dimensional numerical simulation utilizing the CHT method was employed to provide precise insights into the effects of ammonia co-firing ratios with parallel injection systems on temperature distributions and NO emissions within the combustion furnace. The insights gained from this research can serve as valuable references for the design and application of larger-scale ammonia co-firing furnaces.

5.2 Experimental and modeling conditions

Since the present chapter aims to investigate the combustion characteristics within the 10-kW ammonia co-combustion furnace at different ammonia co-firing ratios, the furnace configuration remains identical to that introduced in **Sec. 4.2.1**. In terms of the secondary injection system parameters, the secondary nozzle diameter and air nozzle distance were set at 6.6 mm and 100 mm, respectively, to ensure numerical stability during simulations. The total

air ratio across all conditions was kept constant at 1.2, balancing the prevention of ammonia leakage and minimizing NO emissions. As demonstrated in **Chapter 4**, the application of the air-staged combustion strategy employing the parallel injection system is effective in controlling NO emissions. Therefore, this strategy is applied in all cases for the current chapter, with an equal mass flow rate of air through the primary and secondary air nozzles ($\lambda_1 = \lambda_2 =$ 0.6). The fuel used for co-firing is a mixture of ammonia and City gas 13A, and the ammonia co-firing ratio was calculated based on **Eq. (4.1)**.

Regarding the setup for numerical calculations, simulations were also conducted using OpenFOAM to couple flow, combustion, thermodynamics, and heat transfer processes. The PISO algorithm was employed for pressure-velocity coupling calculations. All governing equations and species transport equations were discretized using a second-order scheme, with convergence criteria ensuring residuals were below 10^{-6}. The turbulent Prandtl number and Schmidt number were set at 0.82 and 0.7, respectively, based on the results from the numerical validations presented in **Chapter 3**.

Table 5.1 Summary of the calculation conditions in the present chapter.

Case	L (mm)	D_2 (mm)	E_{NH3} (%)	λ_1	λ_2	Mass flow velocity $\times 10^{-3}$ (kg/s)		
						Fuel	1st air	2nd air
(5.1)	100	6.6	0	0.6	0.6	0.232	2.3896	2.3896
(5.2)			10			0.2712	2.3774	2.3774
(5.3)			20			0.31	2.3651	2.3651
(5.4)			30			0.3495	2.353	2.353
(5.5)			40			0.3887	2.3406	2.3406
(5.6)			50			0.4278	2.3284	2.3284
(5.7)			60			0.467	2.3161	2.3161
(5.8)			70			0.506	2.3039	2.3039
(5.9)			80			0.5453	2.2917	2.2917
(5.10)			90			0.5845	2.2794	2.2794
(5.11)			100			0.6237	2.2672	2.2672

Table 5.1 summarizes the numerical conditions employed in this chapter. A total of eleven combustion scenarios were simulated to investigate the effects of the ammonia co-firing ratio on the combustion characteristics within the lab-scale ammonia co-combustion furnace. Specifically, cases (5.1) to (5.11) cover the range from pure City gas 13A combustion ($E_{NH3} =$ 0) to pure ammonia combustion ($E_{NH3} =$ 100%), with increments of 10%. As the LHV of

ammonia is significantly lower than that of City gas 13A, the mass flow rate of fuel increased proportionally with the rise in the ammonia co-firing ratio. The quantities of fuel and air supplied for numerical calculations were consistent with the experimental conditions, maintaining a combustion power of 11.63-kW. The inlet temperatures for the primary air, secondary air, and fuel were kept at 300 K.

5.3 NO emission under various ammonia co-firing ratios

5.3.1 Trends and model validation of NO emissions

Figure 5.1 illustrates the comparison between experimental and numerical results of normalized NO emissions under different ammonia co-firing ratios in the case of air-staged combustion. The numerical results separately investigate the Okafor detailed and Sako reaction mechanisms. The reference condition (NO_0) corresponds to pure City gas 13A combustion (E_{NH3} = 0). Similar to the experimental setup in **Chapter 4**, the margin of error (uncertainty) for NO measurements was approximately 10%, and the effect of water vapor was eliminated by condensing the exhaust gas during the NO measurements [9]. Therefore, in the numerical comparisons presented in this section, the influence of water is similarly excluded. The error bars in the figure are also derived by calculating the ratios of maximum potential experimental deviations at each ammonia co-firing ratio condition. Specifically, regarding **Fig. 5.1**, the upper limit of the error bar represents the ratio of the experimental NO emission value at a specific ammonia co-firing ratio increased by 10% (to account for the measurement uncertainty) to the experimental NO emission value at the reference condition decreased by 10%. Conversely, the lower error bar limit represents the ratio of the experimental NO emission value at the ammonia co-firing ratio decreased by 10% to the reference condition value increased by 10%. As can be observed, for both reaction mechanisms, the computational results are well within the potential error range, effectively reproducing the observed trend of NO emissions under various ammonia co-firing ratios. This consistency underscores the accuracy of the solver in predictive simulations.

Because ammonia is a nitrogen-containing fuel, the introduction of ammonia during co-firing inevitably leads to an increase in NO emissions. However, it is observed that NO emissions resulting from ammonia co-firing do not exhibit a linear increase with an increase in ammonia co-firing ratio, displaying a parabolic-like trend instead. Taking the computational results based on the Okafor detailed reaction mechanism as an example, in the case of pure City gas combustion, the lowest NO emissions in the exhaust gas are observed. With the introduction of ammonia co-firing, there is a pronounced escalation in NO emissions, peaking at an ammonia co-firing ratio of 50%, which represents an approximately 12-fold increase compared to the

scenario of pure City gas combustion. As the ammonia co-firing ratio continues to rise beyond 50%, the trend in NO emissions gradually moves toward reduction. In the case of pure ammonia combustion, the expected NO emissions in the exhaust gas experience a significant reduction, numerically decreasing by approximately 40%. However, this value remains roughly 7.3 times higher than those observed in pure City gas combustion.

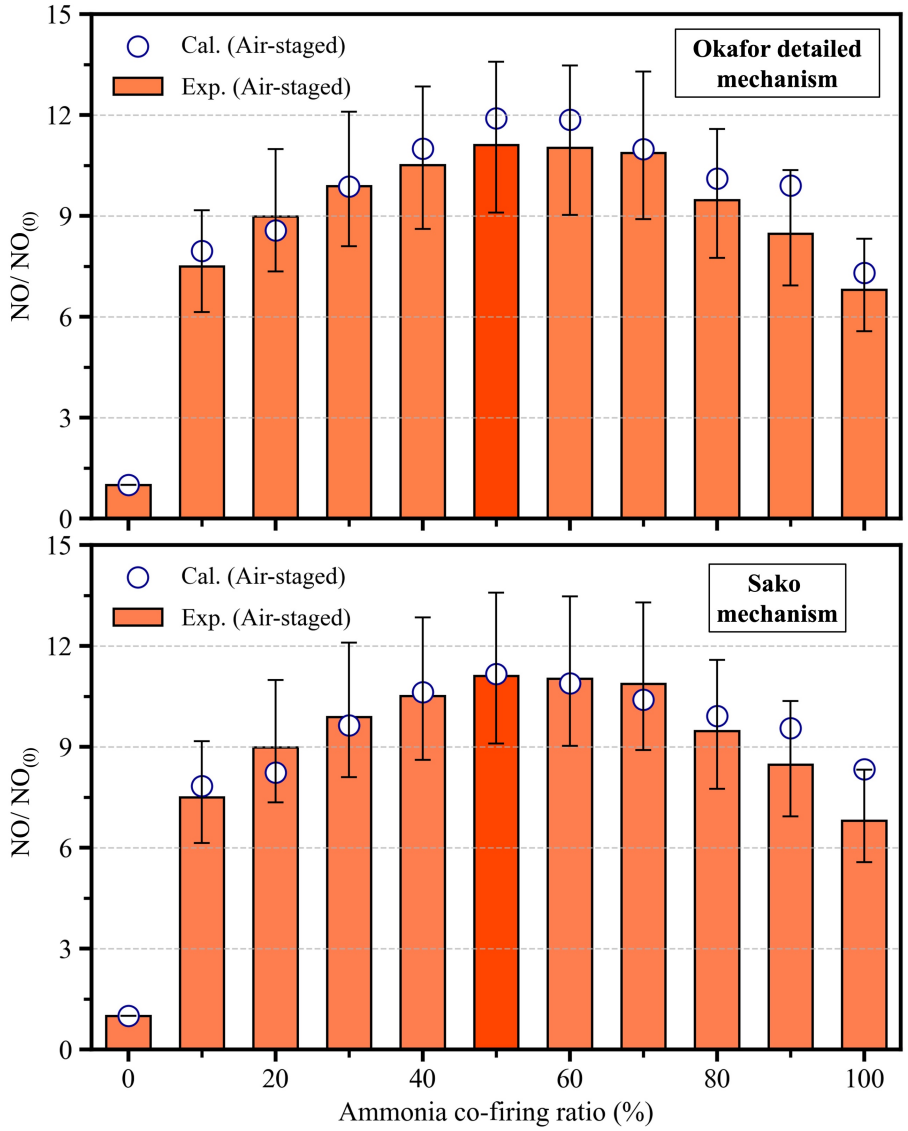

Figure 5.1 Comparison between the experimental results and prediction results using the Okafor detailed (up) and Sako reaction mechanism (down) under air-staged combustion. The subscript 0 indicates that under the case of ammonia co-firing ratio of 0 % (pure City gas 13A combustion).

5.3.2 Nitrogen origin determination

Figure 5.2 illustrates the trends of fuel NO and thermal NO emissions under different ammonia co-firing ratios, based on calculations using the Sako reaction mechanism. The Sako

mechanism, which incorporates the nitrogen element-tracking method, allows for a clear distinction between fuel-originated nitric oxide (fuel NO) and oxidizer-originated nitric oxide (thermal NO) emissions [10].

As shown in the figure, regarding fuel NO emissions at the furnace outlet, during pure City gas 13A combustion, the formation of fuel NO is nearly zero. However, as the ammonia co-firing ratio slightly increases to 10%, fuel NO emissions rise rapidly. This is followed by a pattern where fuel NO initially increases and then decreases as ammonia injection continues, peaking at a co-firing ratio of 50%. On the other hand, thermal NO formation shows a distinct decreasing trend as the ammonia co-firing ratio increases. When the ammonia co-firing ratio exceeds 40%, thermal NO emissions at the furnace outlet become almost negligible. Therefore, at higher ammonia co-firing ratios, controlling the formation of fuel NO becomes the primary factor in reducing overall NO emissions within the furnace.

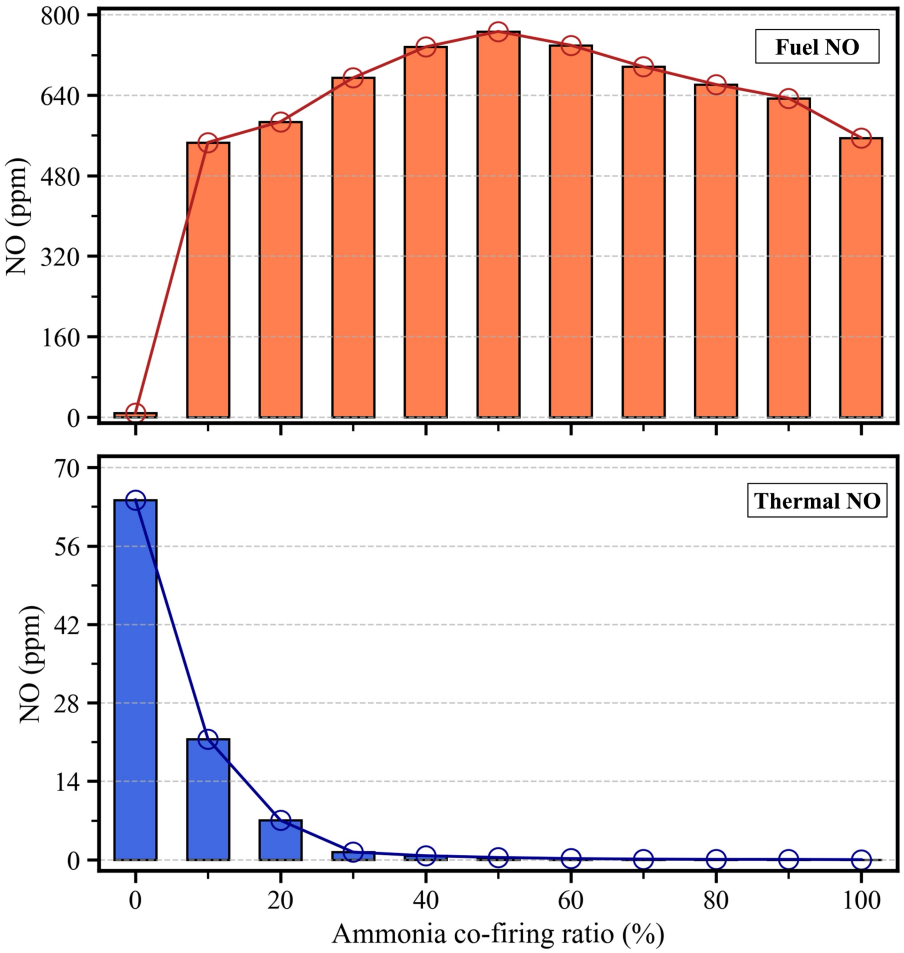

Figure 5.2 Fuel NO (up) and thermal NO (down) emission under different ammonia co-firing ratio using the Sako reaction mechanism.

5.4 Effect of ammonia co-firing ratio

In **Sec. 5.3.1**, both experimental and numerical results have indicated that as the ammonia co-firing ratio increases, the NO concentration in the exhaust gases follows a parabolic trend of initially increasing and then decreasing. Therefore, the present section will explore the potential reasons for this phenomenon through numerical analysis.

5.4.1 Temperature distribution

Figure 5.3 presents the temperature distribution within the furnace at different ammonia co-firing ratios, ranging from 10% to 90%. It can be observed that an increase in the ammonia co-firing ratio leads to an overall reduction in furnace temperature. This phenomenon can be attributed to two main factors. First, the theoretical flame temperature of ammonia is lower than that of traditional hydrocarbon fuels [8]. Second, given that the LHV of ammonia is 14.1 MJ/Nm^3, which is substantially lower than the LHV of City gas 13A at 40.65 MJ/Nm^3, an increase in the mass flow rate of the injected fuel is necessary to maintain a consistent combustion power (11.63-kW) under increased ammonia co-firing ratios. As a result, when the ammonia co-firing ratio is increased, the volume of flue gas also increases. This increase in flue gas volume further dissipates a significant amount of heat, leading to a reduction in furnace temperature. In summary, as the ammonia co-firing ratio increases from 10% to 90%, the maximum temperature in the furnace decreases by approximately 300 K. Additionally, a noticeable extension in the length of the low-temperature jets from the primary nozzle is observed when the ammonia co-firing ratio reaches to a higher level, bringing the reaction region closer to the downstream of the furnace. Therefore, in the design of industrial furnaces for future scenarios with high ammonia co-firing ratios or pure ammonia combustion, it is necessary to consider appropriate extensions in furnace length compared to traditional hydrocarbon fuel combustion.

Additionally, it should be noted that **Figure 5.3** shows cross-sections of the combustion furnace along both the Y-plane (left) and Z-plane (right). The temperature distribution on the Y-plane section exhibits noticeable asymmetry, primarily attributed to the influence of gravity. In the present study, gravity acts in the (-z) direction. As a result, for the Y-plane section (left side of **Fig. 5.3**), when the fuel and air enter the combustion furnace, since the hot-gas density is lower than that of the cold-gas, the hot gases will rise due to buoyancy after the fuel burns and generates heat, leading to this asymmetrical rising trend of the flame within the furnace. In air-staged combustion, the oxidizer enters the furnace in stages through primary and secondary nozzles, further complicating the flow field, yet the overall convection pattern remains influenced by natural convection.

For the Z-plane section on the right side of **Fig. 5.3**, where gravity does not have a directional influence, the temperature distribution within the furnace appears more symmetrical. The slight deviations from perfect symmetry could be attributed to minor asymmetries in the furnace mesh during the grid generation process. Nonetheless, this asymmetry does not significantly impact the overall predictive accuracy of the numerical simulations.

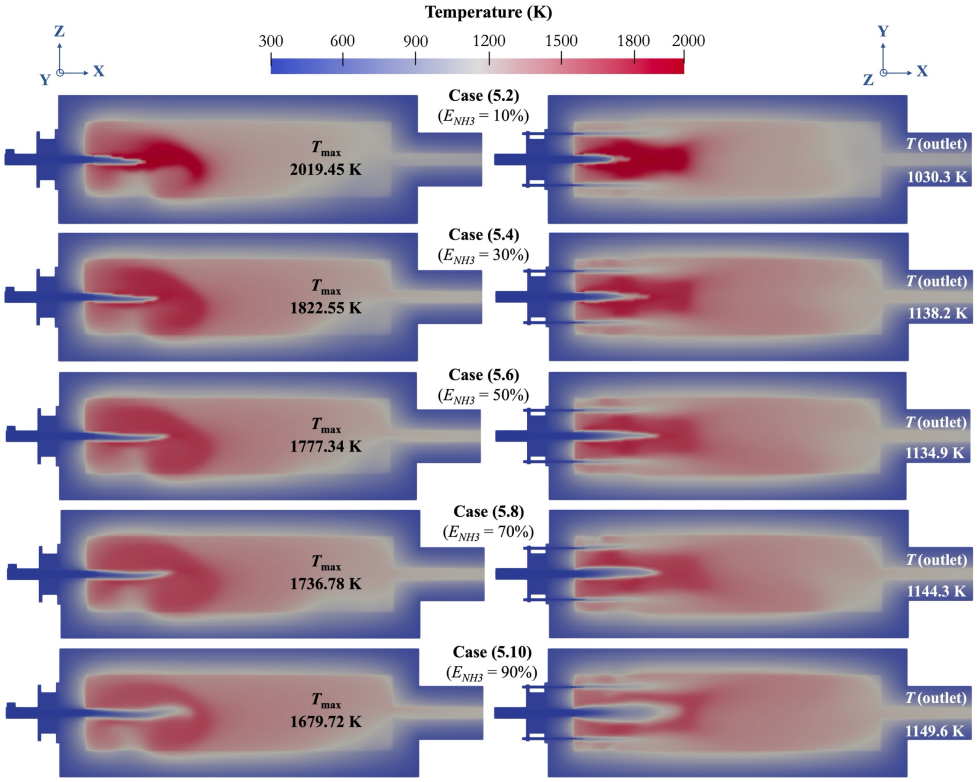

Figure 5.3 Effect of ammonia co-firing ratio on temperature distribution.

To further investigate the impact of the ammonia co-firing ratio on the combustion characteristics within the furnace, the gas temperature along the central axis is presented in **Fig. 5.4**. And **Fig. 5.5** provides the peak temperature and their corresponding X-axis locations for eleven different ammonia co-firing ratio scenarios. The data reveals that at lower ammonia co-firing ratios (E_{NH3} = 10% or 30%), a rapid temperature increase occurs around 200 mm from the fuel nozzle outlet, which is attributed to the ignition of the ammonia-mixed fuel. Subsequently, the reaction enters the main reaction zone, maintaining high-temperature combustion for a certain duration. As reactions progress downstream in the furnace, the temperature gradually decreases and then stabilizes, signifying the transition into the burned-out stage. However, as the ammonia co-firing ratio continues to increase, the length of the low-temperature jet notably extends, causing the main reaction zone to shift closer to the downstream region of the furnace. In these conditions, the central temperature axis exhibits a two-stage temperature rise process. The reactivity within the furnace diminishes, leading to a

significant ignition delay effect. Furthermore, the flame front fails to sustain high-temperature combustion for an extended period and rapidly transitions to the burned-out stage.

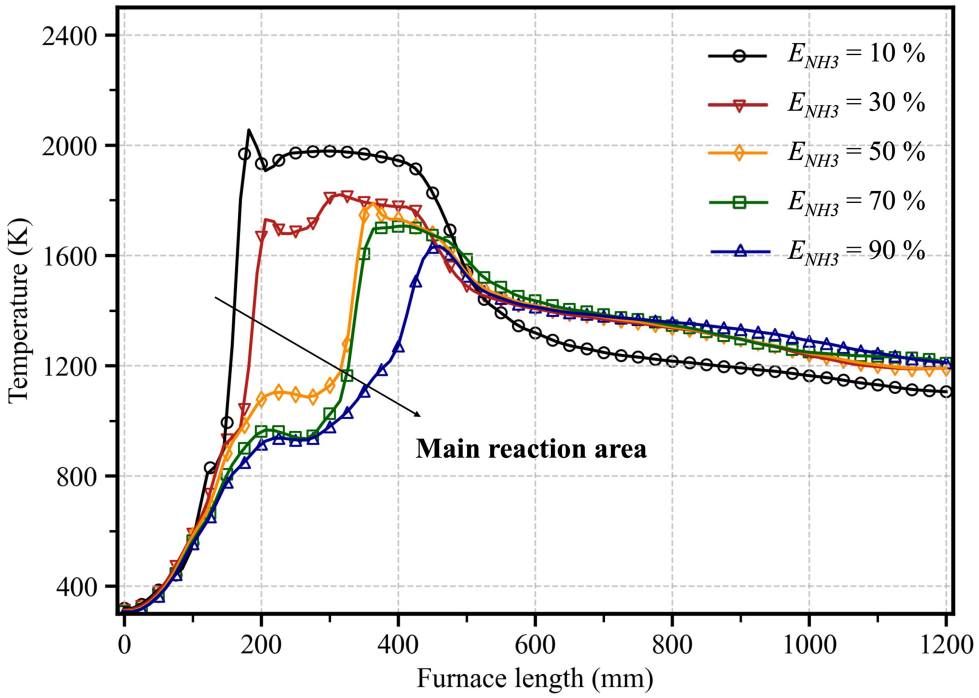

Figure 5.4 Effect of ammonia co-firing ratio on the gas temperature along the central axis (X-axis of the combustion furnace).

In summary, for the air-staged ammonia co-combustion furnace, increasing the ammonia co-firing ratio in terms of furnace temperature distribution may introduce two potential drawbacks. First, such an increase requires elevating the fuel velocity to maintain a constant combustion power, which significantly extends the length of the low-temperature jets. This could result in the ignition of ammonia-mixed fuel at a greater distance from the burners, leading to undesirable delayed ignition and potential adverse effects on combustion stability. Second, an increase in the ammonia co-firing ratio can lead to a reduction in flue gas temperature, and the high-temperature regions within the furnace become significantly reduced, which is unfavorable to radiative heat transfer.

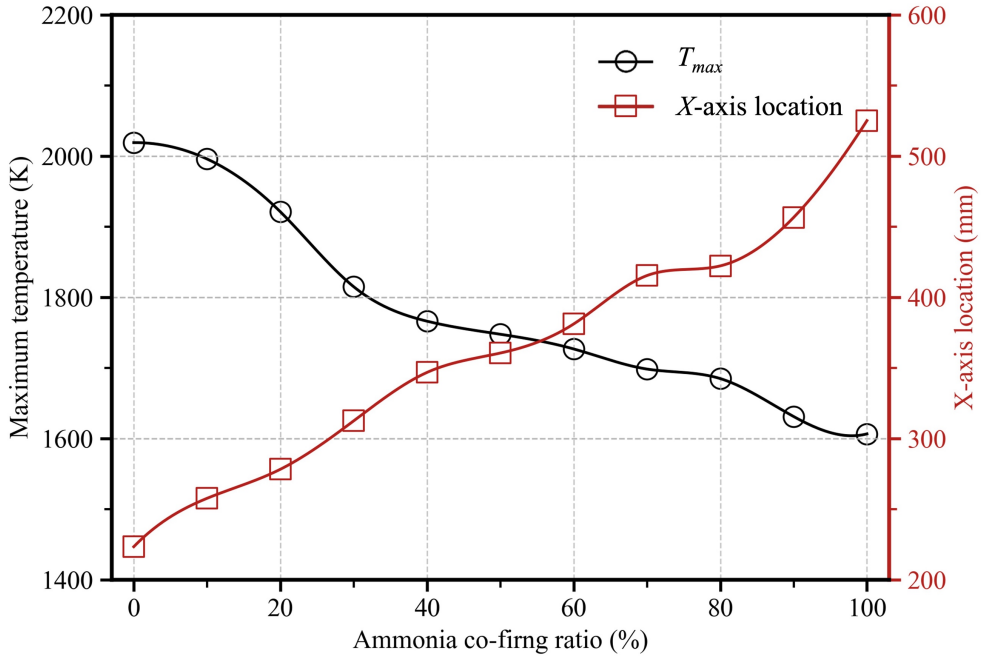

Figure 5.5 Maximum temperature and its corresponding X-axis location under different ammonia co-firing ratios.

5.4.2 NO distribution

Figure 5.6 presents numerical results concerning the distribution of NO within the furnace under various ammonia co-firing ratios. It is evident from the figure that the ammonia co-firing ratio significantly influences the NO distribution. Combining the temperature distribution data in **Fig. 5.4** with the NO distribution data in **Fig. 5.6** reveals that when the ammonia co-firing ratio is below 50%, an increase in the ammonia co-firing ratio results in higher NO concentrations in the exhaust gases. This can be attributed to the low ammonia concentration in low co-firing ratio scenarios. Consequently, the limited ammonia in the fuel quickly undergoes combustion upon entering the furnace, resulting in the rapid conversion of N radicals into NO. This effect is particularly pronounced near the furnace entrance, as highlighted by the red dashed box in **Fig. 5.6**, where a noticeable NO-enriched region forms, contributing to higher NO concentrations in the exhaust gases. This interpretation is supported by the ammonia distribution along the central axis (X-axis) under various ammonia co-firing ratios, as presented in **Fig. 5.7**. In the cases of 10% and 30%, ammonia is mainly consumed during the ignition process within the first 200 mm of the furnace. Typically, in NH_3/air flames, N radicals primarily originate from the fuel stream, while in CH_4/air flames, N is generated from the air stream at high temperatures [11]. Additionally, based on the Sako reaction mechanism calculations, in these two scenarios, the elevated furnace temperature primarily contributes to the formation of thermal NO and fuel NO.

As previously mentioned, when the ammonia co-firing ratio continues to rise, the length of the low-temperature jet inside the combustion furnace increases, and the main reaction area gradually shifts toward the downstream region, with reactivity decreasing. Additionally, **Fig. 5.7** shows a significant increase in the concentration of unburned ammonia at the primary nozzle outlet. That is to say, following the ignition process, which generates NO, the deNOx reaction is also markedly enhanced in this area. Consequently, it is observed that, as the ammonia co-firing ratio is higher than 50%, the region of NO enrichment near the burner outlet gradually diminishes. The high NO generation zone moves further away from the burner and is observed outside the central cold air jet counterpart, which is in the post-flame zone, as indicated by the solid red box in **Fig. 5.6**. In this range of conditions, due to a notable reduction in the furnace temperature, the generation of thermal NO becomes restricted, and the dominance shifts to fuel-NO production. However, it can be seen from **Fig. 5.7** that a second rapid ammonia consumption process in the post-flame zone occurs, indicating there are some incompletely burned ammonia molecules as well as NH intermediates resulting from ammonia reactions, will recombine with NO, and thus promoting the NO reduction process. This results in an overall lower distribution of NO within the furnace compared to conditions with lower ammonia co-firing ratios, and the NO emissions in the exhaust gases also exhibit a decreasing trend.

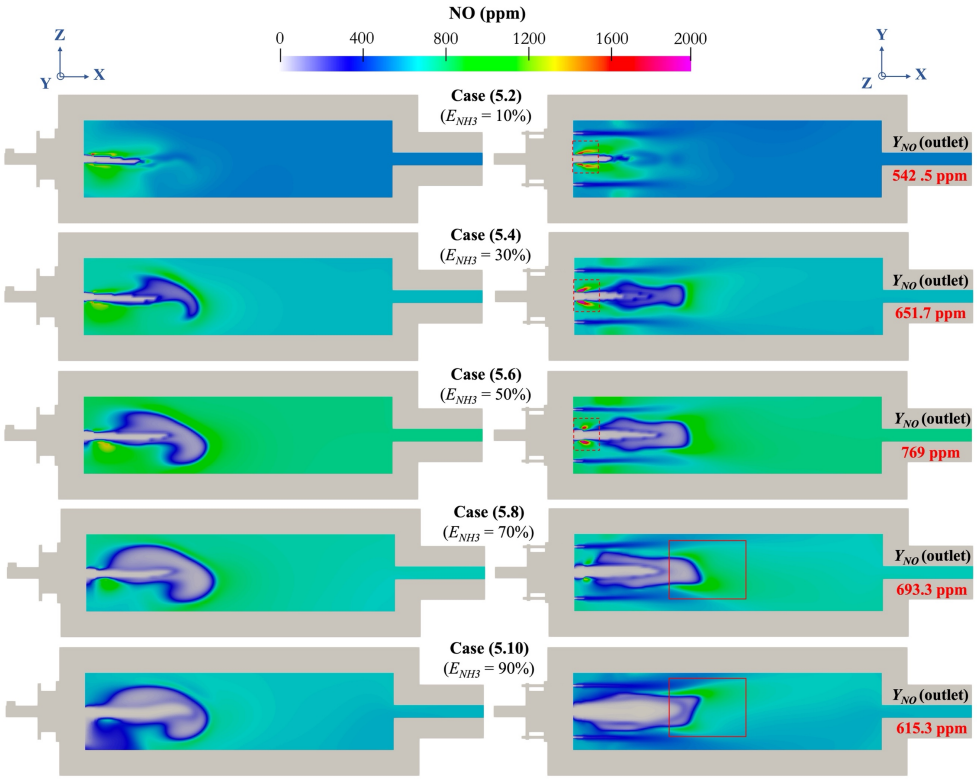

Figure 5.6 Effect of ammonia co-firing ratio on NO distribution.

Finally, concerning the ammonia leakage of the combustion furnace, as observed in **Fig. 5.7**,

even under conditions with higher ammonia co-firing ratios, ammonia is rapidly consumed in the primary reaction zone and approaches near-zero levels in the downstream region beyond 500 mm along the furnace length. Moreover, since the temperature of the flue gas exceeds the ignition points of ammonia (924 K), the ammonia content in the exhaust gas is almost negligible in the simulation results, highlighting the excellent combustion characteristics of ammonia. Therefore, concerning the current combustion furnace design, ammonia can be safely employed in co-firing experiments.

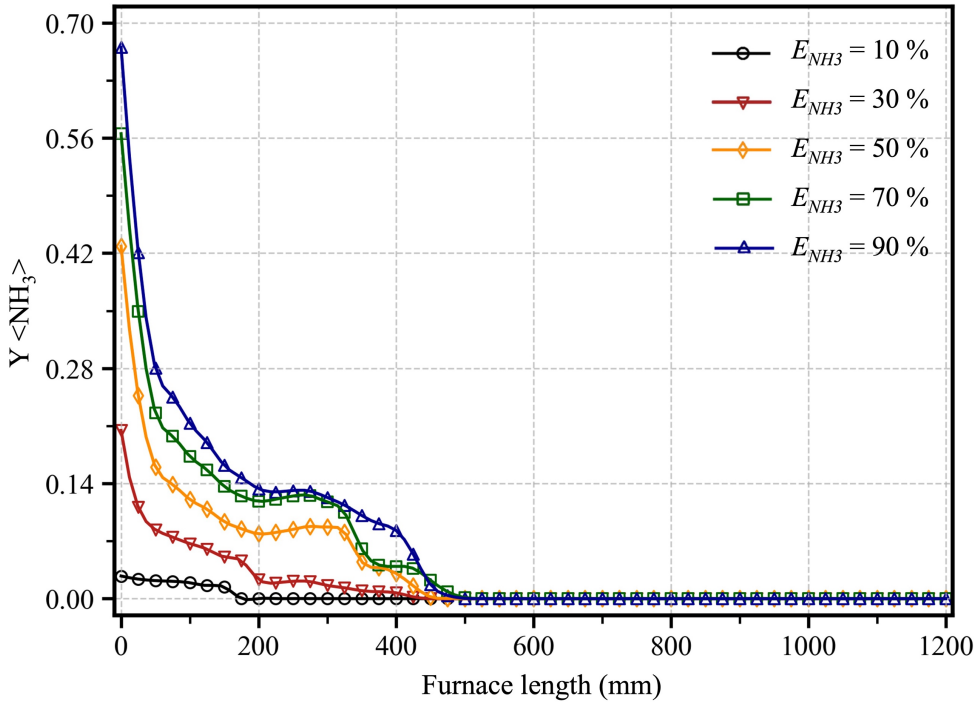

Figure 5.7 Ammonia distribution under various ammonia co-firing ratio along the central axis (X-axis of the combustion furnace).

5.4.3 Combustion characteristics analysis

To further explore the mechanisms governing the generation and reduction of NO within the combustion furnace under different ammonia co-firing ratios, as well as the transition of reaction pathways, the present section conducts the NO ROP analysis at ammonia co-firing ratios of 10%, 50%, and 90%. **Figure 5.8** illustrates the primary regions of NO generation and reduction within the Z-plane section for the three distinct ammonia co-firing ratios. The main elementary reactions contributing to NO generation and reduction in the Z-plane section are displayed in **Fig. 5.9**.

First, regarding the production of NO, when the ammonia co-firing ratio is at 10%, it is evident that a substantial amount of NO is generated near the primary nozzle outlet in the combustion furnace. In this scenario, the dominant mechanisms encompass thermal NO

reactions (R221, R222) and fuel NO reactions (R273), with the principal origin of NO in the fuel NO reactions being HNO. However, as the ammonia co-firing ratio increases, a noticeable decrease in furnace temperature occurs. At this point, the production of thermal NO weakens, and fuel NO reactions begin to predominate. The HNO intermediate channel remains the dominant pathway for NO production, with reactions R271 and R274 showing a marked intensification. Simultaneously, sub-reaction R237 related to the NH intermediate is gradually enhanced.

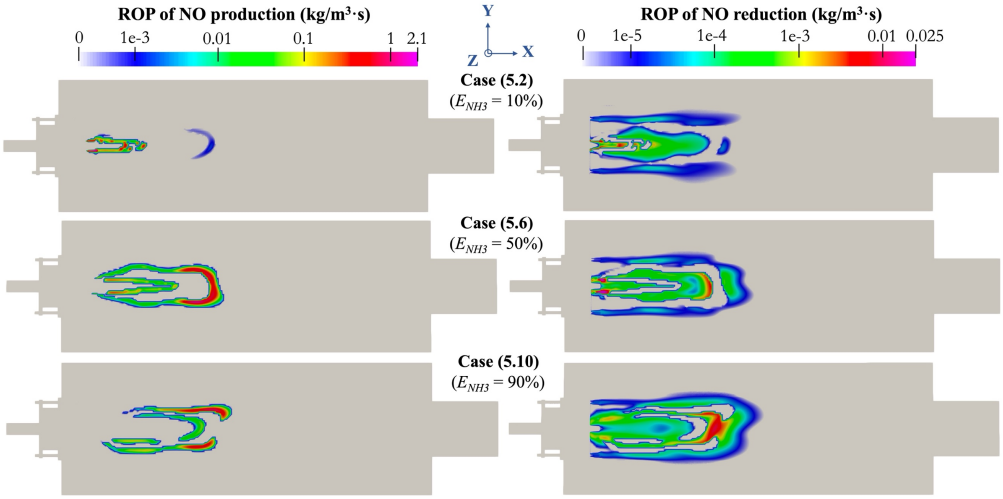

Figure 5.8 Overview of the main production and reduction of NO under the ammonia co-firing ratio of 10%, 50% and 90%.

On the other hand, regarding the reduction of NO, as the ammonia co-firing ratio increases, there is a noticeable expansion in the range of NO reduction. From **Fig. 5.8**, it can be observed that under the condition with an ammonia co-firing ratio of 90%, NO reduction primarily occurs in the post-flame zone. In this scenario, After the NO generation, the excessive NH intermediates within the furnace engage in reduction reactions with NO, yielding more stable N_2 (R242, R256). This leads to a pronounced reduction in the overall NO generation within the combustion furnace. The above finding indicates that at higher ammonia co-firing ratios, ammonia acts both as a reducing agent and a fuel for effective heat release. As strong deNOx reactions occur within the combustion furnace, the NO emissions in the exhaust gases do not increase linearly with the ammonia content. Instead, they exhibit a parabolic trend of initially increasing and then decreasing.

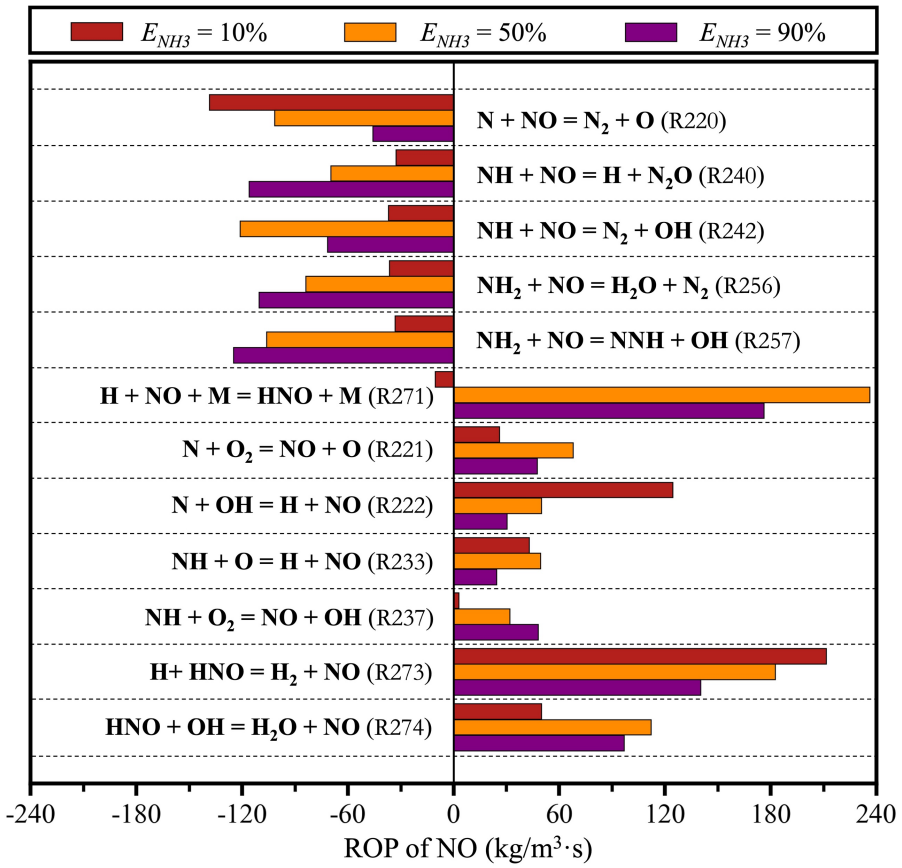

Figure 5.9 Contributions of elementary reactions for NO production or reduction under the ammonia co-firing ratio of 10%, 50% and 90%.

Figure 5.10 demonstrates the impact of the ammonia co-firing ratio on N_2O emissions, as well as normalized CO_2 and H_2O emissions of the combustion furnace. Firstly, regarding CO_2 emissions at the furnace outlet, the incorporation of ammonia into traditional hydrocarbon fuel combustion significantly reduces CO_2 emissions by eliminating carbon. With an ammonia co-firing ratio of 50%, CO_2 emissions decrease by approximately 46%. However, while CO_2 emissions decrease, due to the high mass fraction of nitrogen in ammonia molecules, N_2O emissions exhibit a notable exponential increase. Although the overall emissions of N_2O remain significantly lower than those of NO, some studies suggest that N_2O could have a more severe impact on the formation of the greenhouse effect [12]. Therefore, future applications of ammonia co-firing combustion furnaces must also consider strategies for N_2O removal. It is crucial to avoid excessively increasing the ammonia co-firing ratio, in light of the exponential growth characteristics of N_2O emissions.

Elevating the ammonia co-firing ratio produces another adverse effect. As discussed earlier, an increase in this ratio, while keeping combustion power constant, requires an increased mass flow rate of the mixed fuel. This increase in ammonia injection substantially raises the number

of hydrogen atoms entering the furnace, leading to a marked increase in H_2O content in the exhaust gases. At a co-firing ratio of 50%, the rate of this increase is approximately 58%. The resultant high levels of H_2O emissions can cause corrosion on low-temperature heating surfaces. Therefore, effective surface corrosion prevention measures are also crucial for the design of industrial furnaces employing ammonia combustion.

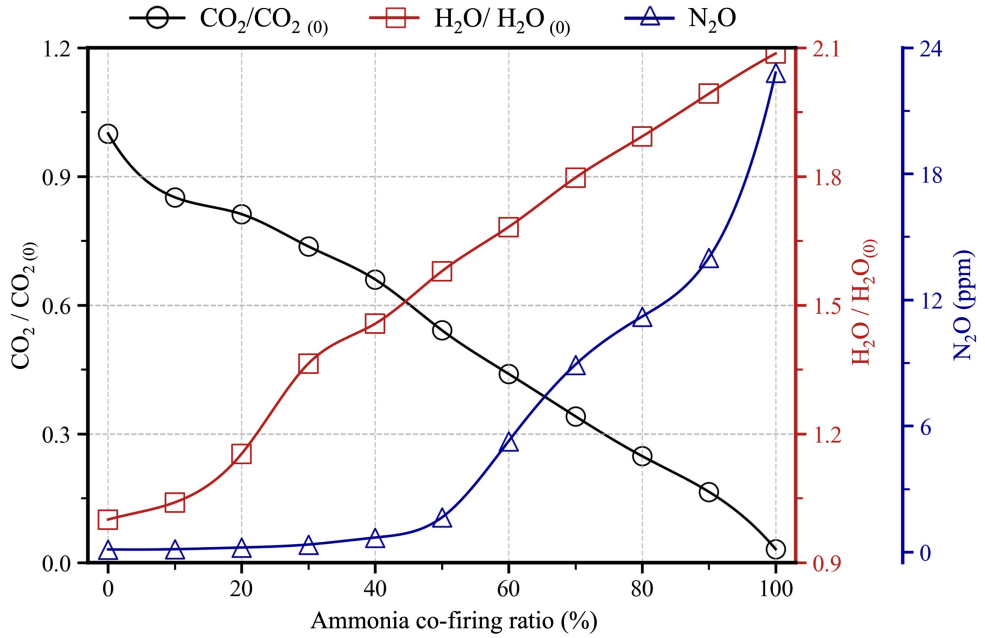

Figure 5.10 Effect of ammonia co-firing ratio on normalized CO_2 and H_2O emissions as well as N_2O emissions of the exhaust gas. The subscript 0 indicates that under the case of ammonia co-firing ratio of 0 % (Pure city gas combustion).

5.5 Summary

In the present chapter, a 10-kW industrial ammonia co-combustion furnace was investigated by employing three-dimensional numerical simulations to assess the effects of ammonia co-firing ratios on combustion characteristics. To accurately represent the thermal conditions at the furnace walls, the CHT model encompassing both solid materials and reacting flow regions was utilized, which eliminates the commonly used fixed temperature or fixed heat flux assumptions for furnace walls. By comparing the numerical simulation results derived from the Okafor detailed and Sako reaction mechanisms with experimental data, the present chapter yielded the following conclusions:

First, an analysis was conducted to examine the influence of ammonia co-firing ratios on the NO emissions. Results indicate that as the ammonia co-firing ratio increases from 0% to 100%, NO emissions at the furnace outlet exhibit a parabolic trend, initially increasing and then decreasing, peaking at 50%. Meanwhile, the temperature distribution within the furnace follows

a linear decline. According to the Sako reaction mechanism results, when the ammonia co-firing ratio exceeds 40%, thermal NO emissions at the furnace outlet become negligible due to the reduced furnace temperature, with fuel NO dominating the reaction process.

Subsequently, an analysis of the ROP of NO within the furnace provides insights into this behavior. At lower ammonia co-firing ratios ($E_{NH3} < 50\%$), ammonia entering the furnace from the primary nozzle is rapidly consumed. In these conditions, NO generation primarily originates from thermal NO and fuel NO (R273). This results in the formation of a conspicuous NO-enriched region near the primary nozzle outlet. However, as the ammonia co-firing ratio increases ($E_{NH3} \geq 50\%$), the primary source of NO generation shifts to fuel NO, with HNO (R271, R274) and NH intermediates (R237) reaction pathway becoming the predominant. The NO-enriched region moves further to the post-flame region. Although the N radicals increase, the post-flame region experiences strong NO reduction reactions, leading to the production of more stable N_2. This ultimately contributes to the reduction in NO emissions. These findings indicate that at higher ammonia co-firing ratios, ammonia serves a dual role as both a reducing agent and a fuel for effective heat release, explaining the parabolic trend observed in NO emissions with increasing ammonia co-firing ratios.

While increasing the ammonia co-firing ratio can effectively reduce carbon dioxide emissions, two associated drawbacks of this change should not be overlooked. Firstly, a higher ammonia co-firing ratio significantly extends the length of the low-temperature jets, which can lead to undesirable delayed ignition and potentially have adverse effects on combustion stability. Secondly, as the ammonia co-firing ratio increases, there is a noticeable elevation in the water vapor content in the exhaust gases, which poses a corrosion risk to some low-temperature heating surfaces within the combustion furnace.

References

[1] O. Kurata, N. Iki, T. Matsunuma, T. Inoue, T. Tsujimura, H. Furutani, H. Kobayashi, A. Hayakawa, Performances and emission characteristics of NH_3–air and NH_3-CH_4–air combustion gas-turbine power generations. *Proceedings of the Combustion Institute*, 2017, 36: 3351–3359.

[2] S. Li, S. Zhang, H. Zhou, Z. Ren, Analysis of air-staged combustion of NH_3/CH_4 mixture with low NOx emission at gas turbine conditions in model combustors. *Fuel*, 2019, 237: 50–59.

[3] K.D.K.A. Somarathne, E.C. Okafor, D. Sugawara, A. Hayakawa, H. Kobayashi, Effects of OH concentration and temperature on NO emission characteristics of turbulent non-premixed CH_4/NH_3/air flames in a two-stage gas turbine like combustor at high pressure. *Proceedings of the Combustion Institute*, 2021, 38: 5163–5170.

[4] E.C. Okafor, K.D.K.A. Somarathne, R. Ratthanan, A. Hayakawa, T. Kudo, O. Kurata, N. Iki, T. Tsujimura, H. Furutani, H. Kobayashi, Control of NOx and other emissions in micro gas turbine combustors fuelled with mixtures of methane and ammonia. *Combustion and Flame*, 2020, 211: 406–416.

[5] M. Tamura, T. Gotou, H. Ishii, D. Riechelmann, Experimental investigation of ammonia combustion in a bench scale 1.2 MW-thermal pulverised coal firing furnace. *Applied Energy*, 2020, 277: 115580.

[6] G. Nagatani, H. Ishii, T. Ito, E. Ohno, Y. Okuma, Development of co-firing method of pulverized coal and ammonia to reduce greenhouse gas emissions. *IHI Engineering Review*, 2020, 53: 1-10.

[7] J. Zhang, T. Ito, H. Ishii, S. Ishihara, T. Fujimori, Numerical investigation on ammonia co-firing in a pulverized coal combustion facility: Effect of ammonia co-firing ratio. *Fuel*, 2020, 267: 117166.

[8] W. Jin, F. Si, Y. Cao, C. Yu, J. Wang, Numerical research on ammonia-coal co-firing in a 1050 MW coal-fired utility boiler under ultra-low load: Effects of ammonia ratio and air staging condition. *Applied Thermal Engineering*, 2023, 233: 121100.

[9] K. Kikuchi, R. Murai, T. Hori, F. Akamatsu, Fundamental study on ammonia low-NOx combustion using two-stage combustion by parallel air jets. *Processes*, 2021, 10: 23.

[10] N. Sako, J. Hayashi, T. Sako, H. Kawanabe, M. Katsuki, Nitrogen-origin-determination in NOx formation under ammonia/methane/air co-combustion using a nitrogen-tagged reaction model. *Combustion and Flame*, 2024, 259: 113210.

[11] K.D.K.A. Somarathne, E. C. Okafor, A. Hayakawa, T. Kudo, O. Kurata, N. Iki, H. Kobayashi, Emission characteristics of turbulent non-premixed ammonia/air and methane/air swirl flames through a rich-lean combustor under various wall thermal boundary conditions at high pressure. *Combustion and Flame*, 2019, 210: 247–261.

[12] Y. Park, B. Kim, Catalytic removal of nitrogen oxides (NO, NO_2, N_2O) from ammonia-fueled combustion exhaust: A review of applicable technologies. *Chemical Engineering Journal*, 2023, 461: 141958.

Chapter 6

Conclusions and recommendations

6.1 Research conclusions

In global power and energy systems, carbon dioxide emissions from traditional hydrocarbon fuel combustion are a primary driver of global warming and environmental degradation. Therefore, reducing carbon dioxide emissions has become a central objective of the worldwide energy transition. With the advancement toward carbon neutrality, carbon-free fuels such as ammonia have received increasing attention and are regarded as critical pathways to achieve a low-carbon future. To facilitate the broader adoption of ammonia, addressing challenges such as its low laminar burning velocity and ignition delay during combustion has become essential. Researchers in academic and industrial communities are exploring ammonia co-combustion with conventional hydrocarbon fuels as a transitional strategy. Moreover, high NO emissions of ammonia during combustion pose another significant challenge for large-scale industrial applications. Therefore, it is essential to investigate the combustion behavior of ammonia under different operating conditions to develop combustion systems with low NO emissions.

Within this background, the present thesis introduced a rapid and accurate customized solver developed on the OpenFOAM platform to investigate the combustion characteristics of a 10-kW lab-scale ammonia co-combustion furnace under various secondary injection system configurations and ammonia co-firing ratios. To accelerate the three-dimensional numerical analysis, a novel integrated acceleration strategy was developed to enhance the computational efficiency of the solver. The strategy included: (1) implementing a sparse analytical Jacobian approach using the SpeedCHEM chemistry library to improve the efficiency of solving chemistry ODEs; (2) utilizing the DLB code to redistribute the computational load for chemistry across multiple processes evenly; (3) incorporating the OpenMP method to enhance parallel computing efficiency; and (4) integrating the LTS scheme to maximize the time step for each computational cell.

First, to verify the computational acceleration capabilities of the integrated acceleration strategy, as well as the prediction accuracy of the customized solver, Sandia flames D-F were selected for two-dimensional numerical analysis. The following two conclusions were drawn:

- **Computational acceleration**: The application of the DLB + SpeedCHEM method demonstrated better strong scaling performance. With the subsequent introduction of the OpenMP method, communication bottlenecks between processors were significantly reduced.

Under the optimal combination of OpenMP × MPI, computational speed for flame D calculations increased by nearly 30 times compared to the standard model, with minimal impact on the prediction accuracy.

- **Prediction accuracy**: Numerically, the calculations achieved reasonable predictions for flame temperature and combustion reactants along the central and axial distribution, validating the accuracy of the solver. For the flame D calculations, the LRR model yielded better prediction results when the model constant and turbulent Prandtl number were set to 1.48 and 0.72, respectively. In contrast, for the RngKE model, increasing the turbulent Prandtl number by 0.1 produced better results. The RngKE turbulence model demonstrated higher accuracy in temperature field and major species predictions, while the LRR model exhibited superior precision in velocity field predictions.

Subsequently, the present thesis focuses on a three-dimensional numerical analysis of a 10-kW ammonia co-combustion furnace to investigate the combustion characteristics under a parallel injection system. Variables such as the primary air ratio, air nozzle distance, secondary nozzle diameter, and different ammonia co-firing ratios were explored. To accurately represent the thermal conditions at the furnace walls, the conjugate heat transfer method, which includes both solid materials and reacting flow regions, was utilized. This approach eliminates the commonly used fixed temperature or heat flux assumptions for furnace walls. Through the comparison with experimental results, the following conclusions were drawn from the numerical analysis:

- **Computational acceleration**: In three-dimensional ammonia co-combustion furnace simulations, the acceleration performance of the integrated strategy was diminished due to increased communication overhead between MPI ranks, achieving a speed increase of up to 7.06 times. However, when using a more detailed Sako reaction mechanism, the acceleration factor improved to 13.88, highlighting the promising potential of this acceleration strategy when applied to larger reaction mechanisms.
- **Influence of the primary air ratio on NO emissions**: While maintaining a total air ratio of 1.2, simply reducing the primary air ratio to create a fuel-rich region near the primary nozzle exit does not linearly decrease NO emissions at the furnace outlet. Instead, a V-shaped trend is observed. The optimal NO emission reduction is achieved when the primary air ratio is reduced to 0.6, resulting in approximately a 90% decrease in NO emissions compared to non-staged combustion. This indicates a threshold for controlling NO emissions by adjusting the primary air ratio.
- **Influence of the air nozzle distance on NO emissions**: At an ammonia co-firing ratio of

10%, increasing the distance between the primary and secondary nozzles from 50 mm to 140 mm enlarges the fuel-rich region in the furnace and intensifies the reduction reactions. Consequently, NO emissions at the furnace outlet decreased by about 46.1%. However, the amount of NO generated inside the furnace does not significantly change, though the reduction reactions are enhanced. Therefore, for furnaces with parallel injection systems and operating at lower ammonia co-firing ratios, it is recommended to moderately increase the distance between the primary and secondary nozzles.

- **Influence of the secondary nozzle diameter on NO emissions**: For an ammonia co-firing ratio of 10%, increasing the secondary nozzle diameter effectively reduces the NO formation and emission within the furnace. When the nozzle diameter is increased from 4.2 mm to 7.8 mm, NO emissions in the exhaust decrease by approximately 32.8%. Hence, larger secondary nozzles are recommended under lower ammonia co-firing conditions.
- **Influence of ammonia co-firing ratio on NO emissions**: As the ammonia co-firing ratio increases from 0 to 100%, NO emissions at the furnace outlet exhibit a parabolic trend, initially increasing and then decreasing, peaking at a 50% ammonia co-firing ratio. Simultaneously, the temperature distribution inside the furnace decreases linearly. When the ammonia co-firing ratio exceeds 40%, thermal NO emissions become negligible, and fuel NO dominates the reaction process. At ammonia co-firing ratios above 50%, intense NO reduction reactions occur in the post-flame zone of the furnace, leading to the formation of more stable N_2. Under these conditions, ammonia serves a dual role as both a reducing agent and a fuel for efficient heat release, explaining the parabolic trend in NO emissions as the ammonia co-firing ratio increases.
- **Potential drawbacks at higher ammonia co-firing ratio**: Although increasing the ammonia co-firing ratio reduces CO_2 emissions, this change presents two drawbacks. Firstly, a higher ammonia co-firing ratio significantly extends the length of low-temperature jets, which may cause delayed ignition and negatively impact combustion stability. Secondly, as the ammonia co-firing ratio increases, the water vapor content in the exhaust gases rises, posing a corrosion risk to some low-temperature heating surfaces within the combustion furnace.

In summary, this thesis provides a systematic analysis of the combustion characteristics in ammonia co-combustion furnaces under different secondary injection system configurations and ammonia co-firing ratios. The feasibility of controlling NO formation by adjusting furnace configuration parameters was verified, and the results offer valuable insights for the design of industrial ammonia combustion furnaces in the future.

6.2 Future recommendations

The present thesis proposes an effective integrated acceleration strategy and conducts a systematic three-dimensional numerical analysis of a 10-kW ammonia co-combustion furnace using the CHT method, marking a step forward in advancing ammonia combustion toward industrial applications. However, due to the various interacting factors in practical applications, the ammonia combustion process is highly complex. The author recognizes several limitations in this study that merit further improvement, including but not limited to:

- The turbulence model used for numerical analysis and validation of the solver is relatively outdated. In future work, it would be beneficial to extend the study by employing more commonly used models, such as the k-ω (SST) turbulence model.
- Due to constraints in computational cost and time, the parameters for the secondary injection system were kept fixed when investigating the effects of different ammonia co-firing ratios. These fixed values were a primary air ratio of 0.6, air nozzle spacing of 100 mm, and secondary nozzle diameter of 6.6 mm. Future work could explore different secondary nozzle diameters and air nozzle spacings under high ammonia co-firing ratios to better inform the development of low-NO ammonia co-combustion furnaces.
- The present research focused on a 10-kW ammonia co-combustion furnace, which is limited to a laboratory scale for facilitating experimental and numerical analysis under various conditions. In practical industrial applications, scalability becomes crucial, accordingly, future research should investigate the scalability of such furnaces to larger-scale industrial systems.

Appendix

A.1 Prediction accuracy under different ammonia co-firing ratios

In **Chapters 4** and **5** of this study, the comparative trends between numerically predicted NO emissions and experimental values were presented. This section aims to provide a direct numerical comparison of NO emissions at the furnace outlet between experimental measurements and numerical predictions. **Figure A.1** illustrates the comparison of predicted and measured NO emissions under various ammonia co-firing ratios, with the experimental measurement uncertainty being approximately 10%.

As observed in the figure, similar to the results for Sandia flames D-F, the current model exhibits a notable tendency to overpredict NO emissions. The possible reasons for this overestimation relate to the combustion model, the boundary conditions of the CHT model, and the quality of the computational grid. While the computational model employed in this study effectively captures the trends in NO variation, further improvements are needed to enhance the accuracy of numerical predictions for precise NO values in future research.

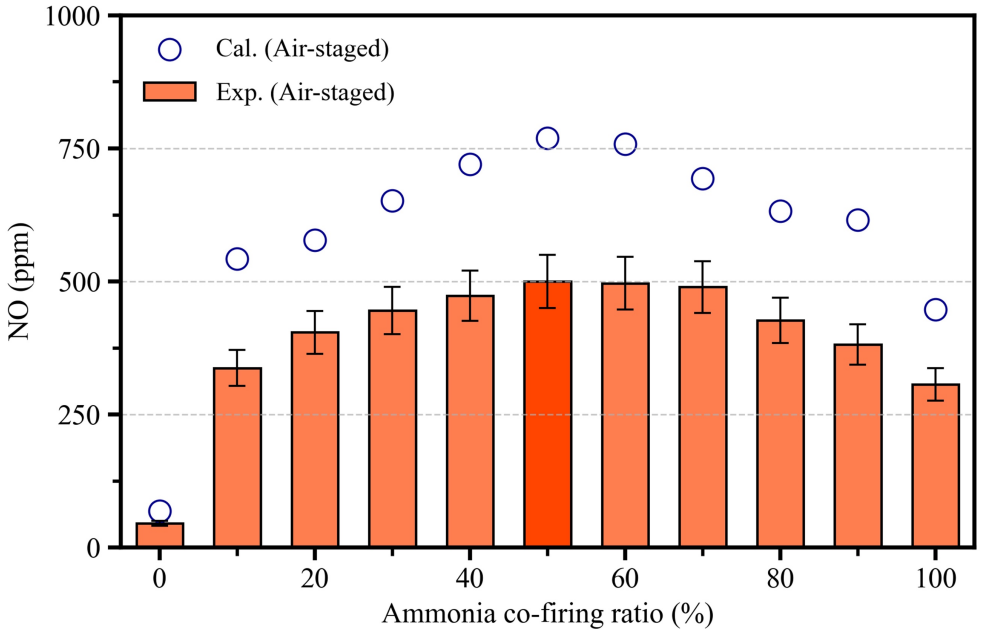

Figure A.1 Comparison of NO emission values under different ammonia co-firing ratio.

Publications related to this thesis

Journal articles

[1] **Y. Yang**, T. Hori, S. Sawada, F. Akamatsu. Accurate and rapid reactive flow simulations using dynamic load balancing and sparse analytical Jacobian approach. *Physics of Fluids*, 2024, 36(8): 085194.

[2] **Y. Yang**, T. Hori, S. Sawada, F. Akamatsu. Toward the development of low-NO ammonia cofiring furnaces: Numerical investigation into the secondary injection system using the conjugate heat transfer method. *Energy & Fuels*, 2024, 36(11): 10357-10369.

[3] **Y. Yang**, T. Hori, S. Sawada, F. Akamatsu. Numerical investigation on the effects of air-staged strategy and ammonia co-firing ratios on NO emission characteristics using the Conjugate heat transfer method. *Fuel*, 2024, 368: 131591.

Conference proceedings with peer review

[1] **Y. Yang**, T. Hori, S. Sawada, F. Akamatsu. Numerical determination of nitrogen sources in NO formation under varying ammonia co-firing ratios in a 10-kW co-combustion furnace, in *2024 International Symposium on Clean Energy and Advanced Materials (CEAM2024)*, 2024, No. 21.

[2] **Y. Yang**, T. Hori, S. Sawada, F. Akamatsu. Effects of primary and secondary air nozzle distance on NO emission characteristics in an ammonia co-combustion furnace with parallel injection system, in *3rd Symposium on Ammonia Energy (SoAE)*, 2024, A0114.

[3] **Y. Yang**, T. Hori, S. Sawada, F. Akamatsu. Numerical investigation of secondary injection system in developing low-NO ammonia co-combustion furnaces with detailed chemistry and conjugate heat transfer, in *19th International Conference on Numerical Combustion (ICNC)*, 2024, ICNC2024-1044.

[4] **Y. Yang**, Z. Bai, T. Hori, S. Sawada, F. Akamatsu. Towards accurate simulation on a three-dimensional turbulent partially premixed flame with detailed chemistry and radiative heat transfer, in *14th Asia-Pacific Conference on Combustion (ASPACC)*, 2023, No. 86.

Domestic presentations

[1] **Y. Yang**, T. Nakai, T. Hori, S. Sawada, F. Akamatsu. Numerical analysis of NO emission characteristics in a 10-kW lab-scale combustion furnace with ammonia co-Firing, in *61st Symposium (Japanese) on Combustion*, 2023, D121.

[2] **Y. Yang**, T. Nakai, T. Hori, S. Sawada, F. Akamatsu. Numerical simulation of conjugate heat transfer for exploring NO Emission characteristics in a 10-kW ammonia combustion furnace with two-stage combustion, in *2023 Japan Society of Mechanical Engineers Thermal Engineering Conference*, 2023, E122.

[3] **Y. Yang**, Z. Bai, T. Hori, S. Sawada, F. Akamatsu. Case study on the Sandia flame D simulation and verification - influence on the reaction mechanisms and thermal radiation, in *60th Symposium (Japanese) on Combustion*, 2022, C325.

[4] D. Talukdar, **Y. Yang**, T. Hori, S. Sawada, F. Akamatsu. Comparative study to evaluate performance of ODE solvers for CFD based combustion analysis, in *62nd Symposium*

(Japanese) on Combustion, 2024, D125.

[5] T. Nakai, **Y. Yang**, K. Nonomura, T. Hori, S. Sawada, F. Akamatsu. Analysis of NO emission characteristics in ammonia and city gas co-firing furnaces using a nitrogen-tagged reaction model, in *62nd Symposium (Japanese) on Combustion*, 2024, A332.

[6] K. Nonomura, T. Hori, **Y. Yang**, T. Nakai, S. Sawada, F. Akamatsu. Effect of reaction mechanism on exhaust NO from ammonia combustion furnace simulation, in *2024 Japan Society of Mechanical Engineers Thermal Engineering Conference*, 2024, M42.

[7] Z. Bai, **Y. Yang**, N. Nakatsuka, T. Hori, J. Hayashi, F. Akamatsu. Effect of adding diluents to oxidizer on soot formation in inverse diffusion flame of the producer gas of woody biomass, in *60th Symposium (Japanese) on Combustion*, 2022, B312.

Awards

[1] **Best paper award** in the 2024 International Symposium on Clean Energy and Advanced Materials (CEAM2024).

Y. Yang, T. Hori, S. Sawada, F. Akamatsu. Numerical determination of nitrogen sources in NO formation under varying ammonia co-firing ratios in a 10-kW co-combustion furnace, in *2024 International Symposium on Clean Energy and Advanced Materials (CEAM2024)*, 2024, No. 21.

Acknowledgment

As I reach the completion of my doctoral studies, I would like to express my heartfelt gratitude to all the professors and fellow students who have supported me along the way.

First and foremost, I wish to express my deepest gratitude to my supervisor, Prof. Fumiteru Akamatsu, for giving me the opportunity to pursue my Ph.D. at the Combustion Engineering Lab. From the beginning of my studies to the end, Prof. Akamatsu has provided me with unwavering guidance and support, both in my research and personal life. His meticulous and kind nature, coupled with his outstanding leadership, has taught me a great deal over these three years. I sincerely wish Prof. Akamatsu continued success and good health in the future.

I would also like to extend my most sincere thanks to Lecture Tsukasa Hori, who has been my academic advisor throughout my research. From initiating the research to conducting numerical analysis, The dedication and input from Lecture Hori have been invaluable. His approachable, patient, and generous nature made the preparation of my doctoral thesis and journal submissions a much smoother process. His guidance greatly enriched the scope of my research. I wish Lecture Hori all the best in his future endeavors.

I am also sincerely grateful to Prof. Shohji Tsushima and Prof. Masahiko Shibahara for their insightful suggestions and guidance on my dissertation. I am also deeply grateful to Assistant Professor Shinya Sawada for his extensive help and guidance while I was writing the thesis. My thanks also go to Researcher Ryuichi Murai, for providing valuable information regarding combustion furnace experiments, and to Researcher Noriaki Nakatsuka, for his assistance in my research. Moreover, I would also like to express my sincere appreciation to Ms. Megumi Yamada, our lab secretary, for her tremendous help with both my work and daily life.

I am very thankful to Dr. Zhiren Bai and Dr. Shuo Tian for their immense support and guidance, particularly in helping me adjust to my studies and life in Japan. My heartfelt thanks go to Mr. Yu Imahashi for his academic guidance during the COVID-19 when I could not reach Japan. I am also grateful to all my fellow lab members, who have been my companions and partners in this journey, sharing challenges and triumphs along the way.

Finally, I owe a deep debt of gratitude to my parents and my girlfriend, Lin Fu, for their boundless care and encouragement. Their unwavering support, understanding, and companionship helped me through the most challenging times.

Yinan Yang
2024.10